Advances in the Environmental Biogeochemistry of Manganese Oxides

In Advances in the Environmental Biogeochemistry of Manganese Oxides; Sparks, et al.;
ACS Symposium Series; American Chemical Society: Washington, DC, 2015.

In Advances in the Environmental Biogeochemistry of Manganese Oxides; Sparks, et al.;
ACS Symposium Series; American Chemical Society: Washington, DC, 2015.

ACS SYMPOSIUM SERIES **1197**

Advances in the Environmental Biogeochemistry of Manganese Oxides

Xionghan Feng, Editor
Huazhong Agricultural University, Wuhan, China

Wei Li, Editor
Nanjing University, Nanjing, China

Mengqiang Zhu, Editor
University of Wyoming, Laramie, Wyoming, United States

Donald L. Sparks, Editor
University of Delaware, Newark, Delaware, United States

Sponsored by the
ACS Division of Geochemistry

American Chemical Society, Washington, DC

Distributed in print by Oxford University Press

In Advances in the Environmental Biogeochemistry of Manganese Oxides; Sparks, et al.;
ACS Symposium Series; American Chemical Society: Washington, DC, 2015.

Library of Congress Cataloging-in-Publication Data

Names: Feng, Xionghan, editor. | American Chemical Society. Division of Geochemistry.
Title: Advances in the environmental biogeochemistry of manganese oxides / Xionghan Feng, editor, Huazhong Agricultural University, Wuhan, China [and three others] ; sponsored by the ACS Division of Geochemistry.
Description: Washington, DC : American Chemical Society, [2015] | [Oxford] : Distributed in print by Oxford University Press | Series: ACS symposium series : 1197 | Includes bibliographical references and index.
Identifiers: LCCN 2015039378| ISBN 9780841230965 | ISBN 9780841230958
Subjects: LCSH: Manganese oxides. | Manganese--Environmental aspects. | Biogeochemistry.
Classification: LCC TN490.M3 A27 2015 | DDC 577/.14--dc23 LC record available at http://lccn.loc.gov/2015039378

The paper used in this publication meets the minimum requirements of American National Standard for Information Sciences—Permanence of Paper for Printed Library Materials, ANSI Z39.48n1984.

Distributed in print by Oxford University Press

PRINTED IN THE UNITED STATES OF AMERICA

Foreword

The ACS Symposium Series was first published in 1974 to provide a mechanism for publishing symposia quickly in book form. The purpose of the series is to publish timely, comprehensive books developed from the ACS sponsored symposia based on current scientific research. Occasionally, books are developed from symposia sponsored by other organizations when the topic is of keen interest to the chemistry audience.

Before agreeing to publish a book, the proposed table of contents is reviewed for appropriate and comprehensive coverage and for interest to the audience. Some papers may be excluded to better focus the book; others may be added to provide comprehensiveness. When appropriate, overview or introductory chapters are added. Drafts of chapters are peer-reviewed prior to final acceptance or rejection, and manuscripts are prepared in camera-ready format.

As a rule, only original research papers and original review papers are included in the volumes. Verbatim reproductions of previous published papers are not accepted.

ACS Books Department

In Advances in the Environmental Biogeochemistry of Manganese Oxides; Sparks, et al.;
ACS Symposium Series; American Chemical Society: Washington, DC, 2015.

Preface

Manganese (Mn) oxides are among the most reactive minerals in the earth's surface environment, and play a significant role in adsorption, co-precipitation and redox reactions, affecting biogeochemical cycles of numerous nutrients and contaminants. In addition, Mn oxides are widely applied as absorbents, ion sieves, chemical oxidants and catalysts for environmental remediation and pollution control. In the past, significant advances in Mn oxide geochemistry were achieved on the occurrence and mineralogy of Mn oxides in various geological settings, and greatly improved our ability to decipher the evolution processes, reactivity and environmental behavior of Mn oxides. There are, however, still many aspects poorly understood in terms of the environmental geochemistry of Mn oxides, such as biogenic formation mechanisms, detailed crystal structure of nanocrystalline phases, electron transfer paths in redox reactions, adsorption mechanisms of contaminants on surfaces, physiochemical factors controlling the contents of structural Mn(III) and vacant sites that largely determine Mn oxide reactivity, and the role of Mn(III) in the above processes. It is increasingly recognized that such knowledge is critical for better understanding both biogeochemical processes and environmental applications of Mn oxides.

To better address the above knowledge gaps and present current advances on geochemistry of Mn oxides in multiple scientific disciplines, we organized a symposium entitled "*Advances in Understanding the Environmental Geochemistry of Manganese (Mn) Oxides*" at the 247th American Chemistry Society National Meeting in Dallas on March 16-20, 2014. The full proceedings of the symposium are available at http://geochemistrydivision.sites.acs.org/acsspring2014sessions.htm. The symposium attracted approximately 100 scientists from the international environmental chemistry and geochemistry communities. Thirty two speakers, including 20 distinguished invited speakers gave presentations over two full-day oral sessions. Many cutting-edge findings and novel methodologies were reported, representing the state-of-the-art in the field of Mn oxide geochemistry.

This book is based on the invited papers presented at the symposium, and aims to bring together advances on Mn oxide environmental biogeochemistry from leading scientists in multiple disciplines, e.g., mineralogy, geochemistry, soil science and environmental engineering. A number of frontier research topics are included in the book, such as *in-situ* characterization of Mn oxide reactivity with As and Cr, kinetics and molecular-scale mechanisms of metal oxidation by Mn oxides, mechanistic understanding of metal sorption through density function theory, the role of surface edge sites of birnessites in metal(loid) sorption, reactivity of natural crytomelane, pathways of phyllomanganate transformation

In Advances in the Environmental Biogeochemistry of Manganese Oxides; Sparks, et al.;
ACS Symposium Series; American Chemical Society: Washington, DC, 2015.

to todorokite, water-oxidation catalysis by Mn oxides, *in situ* As immobilization using stabilized Fe-Mn binary oxides, and synthesis of Li ion-sieves from biogenic oxides and stability of colloidal Mn oxides. To the best of our knowledge, no ACS symposium series has been published on a similar topic in the past 30 years.

The book should be of interest to scientists and engineers in a broad range of disciplines, such as geochemistry, soil science, mineralogy, microbiology, materials science, and environment engineering, as well as graduate students who are engaged in research on Mn oxide biogeochemistry and the engineering application of Mn-bearing materials. It is also targeted for libraries in the above disciplines.

The editors would like to acknowledge all the authors of the chapters for their excellent contribution and the anonymous reviewers for their excellent evaluation of the manuscripts. We are also grateful to the ACS Books editors, Tim Marney, Bob Hauserman and Lindsey Watson, for their kind assistance and patience throughout the publication process. We would like to thank all the speakers who participated in the symposium.

Xionghan Feng
Key Laboratory of Arable Land Conservation (Middle and Lower Reaches of Yangtse River), Ministry of Agriculture
College of Resources and Environment, Huazhong Agricultural University
Wuhan 430070, China
+86-27-87280271 (telephone)
+86-27-87282138 (fax)
fxh73@mail.hzau.edu.cn (e-mail)

Wei Li
Key Laboratory of Surficial Geochemistry, Ministry of Education
School of Earth Sciences and Engineering, Nanjing University
Nanjing 210093, China
+86-25-89680700 (telephone)
+86-25-83686016 (fax)
liwei_isg@nju.edu.cn (e-mail)

Mengqiang Zhu
Department of Ecosystem Science and Management
University of Wyoming
1000 E. University Ave., Laramie, WY 82071
+1-307-766-5523 (telephone)
+1-307-766-6403 (fax)
mzhu6@uwyo.edu (e-mail)

In Advances in the Environmental Biogeochemistry of Manganese Oxides; Sparks, et al.;
ACS Symposium Series; American Chemical Society: Washington, DC, 2015.

Donald L. Sparks
Delaware Environmental Institute (DENIN)
Department of Plant and Soil Science, University of Delaware
221 Academy St., Suite 250
Newark, DE 19716
+1-302-831-3436 (telephone)
+1-302-831-6840 (fax)
dlsparks@udel.edu (e-mail)

In Advances in the Environmental Biogeochemistry of Manganese Oxides; Sparks, et al.;
ACS Symposium Series; American Chemical Society: Washington, DC, 2015.

Editors' Biographies

Xionghan Feng

Xionghan Feng, a Professor of Soil Chemistry, received a Ph.D. in soil science and joined the faculty at the Huazhong Agricultural University in 2003. He spent more than two years at the University of Delaware in the Delaware Environmental Institute (DENIN) as a visiting scientist through 2007 to 2012. His research focuses on mineralogy, reactivity and environmental behaviors of Fe, Mn and Al (hydr)oxides in soils. Projects include mineralization and evolution of active Fe/Mn oxides, interfacial reactions of contaminants and nutrients at the surface of minerals and soil chemical processes regulating coupled cycling of phosphorus and iron.

Wei Li

Wei Li is a Professor of geochemistry at the Nanjing University in the Department of Earth Sciences. His research focuses on mineral-water interfacial geochemistry and soil metal biogeochemistry as well as the application of fundamental principles of geochemistry in soil remediation and water decontamination. Projects include exploring the mechanism of transition metals precipitation on clay and Al oxides surface using quick-scanning EXAFS, the use of limestone minerals and clay minerals for metal sequestration for contaminated soils in Southern China, and designing new materials for fluoride removal. He is also interested in studying the soil phosphorus chemistry using both ^{31}P liquid-state and solid-state NMR spectroscopy. He has published 26 papers in peer-reviewed journals such as Nature Communications, Environmental Science & Technology, and Geochemical Cosmochimical Acta.

Li holds a B.S. in chemistry from the Wuhan University, a M.S in environmental chemistry at the Research Center of Eco-Environmental Sciences of Chinese Academy of Sciences, and a Ph.D. in mineralogy and geochemistry from the State University of New York at Stony Brook. He performed a postdoc at the University of Delaware in the Delaware Environmental Institute (DENIN).

Mengqiang Zhu

Mengqiang Zhu is an assistant professor at the University of Wyoming in the Department of Ecosystem Science and Management. His research include 1) structure, formation and reactivity of environmental minerals, including manganese and iron oxides, 2) mineral-water interfacial processes, and 3) phosphorus and sulfur cycling in natural and agricultural ecosystems.

In Advances in the Environmental Biogeochemistry of Manganese Oxides; Sparks, et al.;
ACS Symposium Series; American Chemical Society: Washington, DC, 2015.

Mengqiang Zhu holds a B.S. in Environmental Engineering from North China Electric Power University, M.S. in Environmental Chemistry from the Research Center for Eco-Environmental Sciences, Chinese Academy of Sciences, and Ph.D. in Environmental Soil Chemistry at the University of Delaware. After postdoctoral research at the Lawrence Berkeley National Laboratory, he joined the faculty at the University of Wyoming in 2013.

Donald L. Sparks

Donald L. Sparks is the S. Hallock du Pont Chair in Soil and Environmental Chemistry, Francis Alison Professor and Director of the Delaware Environmental Institute at the University of Delaware. He is internationally recognized for research on the kinetics of soil chemical processes, sorption mechanisms of metal(loid)s and nutrients at the mineral/water interface, and speciation of contaminants in soils. Sparks is the author of three textbooks, editor of several books, and author of numerous book chapters and 235 refereed papers. He has received numerous honors and awards including Fellow of five professional societies, the Liebig Medal from IUSS, Einstein Professor from the Chinese Academy of Sciences, the Soil Science Research Award, and the Geochemistry Medal from the American Chemical Society.

In Advances in the Environmental Biogeochemistry of Manganese Oxides; Sparks, et al.;
ACS Symposium Series; American Chemical Society: Washington, DC, 2015.

Chapter 1

Advances in Understanding Reactivity of Manganese Oxides with Arsenic and Chromium in Environmental Systems

J. S. Fischel, M. H. Fischel, and D. L. Sparks*

Department of Plant and Soil Sciences, Delaware Environmental Institute, ISE Lab, 221 Academy Street, Suite 250, University of Delaware, Newark, Delaware 19716

***E-mail: dlsparks@udel.edu**

In the past several years, through the use of molecular scale techniques, particularly those that are in-situ, advances have been made in determining the reactivity of manganese oxides with arsenic (As) and chromium (Cr). Of particular note is an enhanced understanding of the kinetics and mechanisms of As(III) and Cr(III) oxidation on Mn-oxides over a range of time scales, from milliseconds to days. This is in large part due to the employment of novel, synchrotron-based techniques, such as Quick X-ray absorption spectroscopy (Q-XAS) and bench-scale attentuated total reflectance Fourier transform infrared (ATR-FTIR) spectroscopy. This review will focus on these advances, and rely heavily on the published research of Sparks and his group, both present and former members. Undoubtedly these advancess were greatly facilitated by a large number of previous investigations by numerous authors, some of which are cited in the review.

Manganese Oxide Reactivity with Arsenic

Manganese-oxide minerals (Mn-oxides) are robust oxidizing agents that play an important role in many redox processes in the natural environment, such as oxidation of arsenic (As) (*1*). Previous studies have suggested that many Mn-oxides found in terrestrial environments are poorly-crystalline and biogenic (*2*, *3*) and extremely reactive (*3*). The reactivity of Mn-oxide minerals depends on

In Advances in the Environmental Biogeochemistry of Manganese Oxides; Sparks, et al.;
ACS Symposium Series; American Chemical Society: Washington, DC, 2015.

their mineralogy. Layered Mn-oxide minerals (i.e. phyllomanganates) are more reactive oxidizing As^{III} than other types of Mn-oxides (*4–8*).

Arsenic (As) is a toxic element in the environment, originating from both geogenic and anthropogenic sources. Its toxicity and mobility are determined by its speciation or form. Arsenite (As^{III}) is more toxic than arsenate (As^{V}) (*9*), and the sorption of As on oxide minerals depends on pH and speciation (*10*, *11*). Manganese-oxides, including phyllomanganates, can oxidize As^{III} to As^{V} (*5–8*, *12–14*), and since As^{III} is more toxic than As^{V} the oxidation process helps detoxify As in the environment. Additionally, As^{III} oxidation by Mn-oxides can decrease the mobility of As mobility (*10*, *15*).

Mechanisms of As^{III} oxidation by Mn-oxides are complex, involving several simultaneous reactions. For example, As^{III} oxidation by birnessite produces As^{V} and Mn^{II} as products. Both As^{V} and Mn^{II} can be adsorbed by birnessite (*4*, *5*). A Mn^{III} intermediate also can form during As^{III} oxidation by Mn-oxides (*7*, *16*). During the reaction with As^{III}, phyllomanganates become passivated, i.e. As^{III} oxidization initially proceeds rapidly, after which there is a decrease in oxidation rate (*5–7*, *12–14*, *17*, *18*). Two potential mechanisms for Mn-oxide passivation are possible. One is the sorption of Mn^{II}, produced by reduction of Mn^{IV} in the mineral structure, which serves to block reactive sites on the mineral surface (*5*, *18*, *19*). A second mechanism is the formation of Mn^{III} on Mn-oxide surfaces, which while less reactive than Mn^{IV} sites, can decrease the As^{III} oxidation rate (*7*, *16*, *20*).

In previous studies passivation of the Mn-oxide surface (represented by $>Mn^{IV}O_2$ in Equation 1) was attributed to sorption of Mn^{II} (Equation 1), which forms during As^{III} oxidation (Equation 2) (*1*, *5*). A Mn^{III} intermediate, produced during As^{III} oxidation by phyllomanganates (*16*), is thought to be another cause of Mn-oxide passivation (Equations 3 and 4) (*7*, *16*).

$$Mn^{II} + >Mn^{IV}O_2 \rightarrow >Mn^{IV}O_2\text{-}Mn^{II} \quad [1]$$

$$Mn^{IV}O_2 + H_3As^{III}O_3 + H^+ \rightarrow Mn^{II} + H_2As^{V}O_4^- + H_2O \quad [2]$$

The Mn^{III} reactive site ($Mn^{III}OOH$ in Equations 3 and 4) on the Mn-oxide surface should be less reactive than a Mn^{IV} reactive site, in oxidizing As^{III} (*20*). While much of the As^{V} produced during As^{III} oxidation by phyllomanganates is released into solution, As^{V} is also sorbed on the solid phase which can also cause passivation of the mineral surface (*6*, *20*, *21*). Passivation of phyllomanganates may also result due to the formation of a Mn/As precipitate under certain reaction conditions (*7*).

$$2Mn^{IV}O_2 + H_3As^{III}O_3 + H_2O \rightarrow 2Mn^{III}OOH + H_2As^{V}O_4^- + H^+ \quad [3]$$

$$2Mn^{III}OOH + H_3As^{III}O_3 + 3H^+ \rightarrow 2Mn^{II}(aq) + H_2As^{V}O_4^- + 3H_2O \quad [4]$$

There are four possible pathways for the oxidation of As^{III} by δ-MnO_2. Each pathway employs a different combination of Mn reactive sites on the δ-MnO_2 surface for As^{III} oxidation (*19*). In the first pathway, one As^{III} molecule reacts with one Mn^{IV} reactive site (represented by $>Mn^{IV}$-OH in Equations 5 – 7; protonation states based on Peacock and Sherman (*22*)) producing one As^{V} molecule and one

In Advances in the Environmental Biogeochemistry of Manganese Oxides; Sparks, et al.;
ACS Symposium Series; American Chemical Society: Washington, DC, 2015.

Mn^{II} molecule (Equation 5). One As^{III} molecule could also react with two Mn^{IV} reactive sites producing one As^{V} molecule and two Mn^{III} reactive sites (represented by $>Mn^{III}\text{-}OH_2$ in Equations 6 - 8; protonation state based on Ramstedt et al.) (Equation 6) (*23*).

$$>Mn^{IV}\text{-}OH + H_3As^{III}O_3(aq) \rightarrow Mn^{II}(aq) + HAs^{V}O_4^{2-}(aq) + 3H^+ \quad [5]$$

$$2(>Mn^{IV}\text{-}OH) + H_3As^{III}O_3(aq) + H_2O \rightarrow 2(>Mn^{III}\text{-}OH_2) + HAs^{V}O_4^{2-}(aq) + 2H^+ \quad [6]$$

The third and fourth possible As^{III} oxidation pathways necessitate that the $\delta\text{-}MnO_2$ surface first contain Mn^{III} reactive sites. One proposed mechanism for Mn^{III} formation is directly through As^{III} oxidation (Equations 3 and 6) (*16*). Some recent studies show that Mn^{III} can form by conproportionation of Mn^{II} and Mn^{IV} at the $\delta\text{-}MnO_2$ surface. In this reaction, Mn^{II} is oxidized, Mn^{IV} is reduced, and the resulting product is Mn^{III} (*24*, *25*). Mn^{III} resulting from conproportionation of Mn^{II} and Mn^{IV} could produce soluble Mn^{III}, however, if there is no ligand to stabilize Mn^{III} in the reactions discussed here, soluble Mn^{III} should rapidly disproportionate back into Mn^{II} and Mn^{IV} (*26*). Thus one can assume that all Mn^{III} in these reactions is associated with the $\delta\text{-}MnO_2$ surface.

One possibility for As^{III} to be oxidized by Mn^{III} is via the reaction of one As^{III} molecule with one Mn^{III} reactive site and one Mn^{IV} reactive site, resulting in one As^{V} molecule, one Mn^{II} molecule and one Mn^{III} reactive site (Equation 7). The other possible pathway for As^{III} oxidation by $\delta\text{-}MnO_2$ is for one As^{III} molecule to react with two Mn^{III} reactive sites creating one As^{V} molecule and two Mn^{II} molecules (Equation 8) (*15*, *19*).

$$>Mn^{IV}\text{-}OH + >Mn^{III}\text{-}OH_2 + H_3As^{III}O_3(aq) \rightarrow Mn^{II}(aq) + >Mn^{III}OH_2 + HAs^{V}O_4^{2}(aq) + 3H^+ \quad [7]$$

$$2(>Mn^{III}\text{-}OH_2) + H_3As^{III}O_3(aq) \rightarrow 2Mn^{II}(aq) + HAs^{V}O_4^{2-}(aq) + H_2O + 4H^+ \quad [8]$$

Advances in Time-Resolved Molecular Scale Techniques To Elucidate Reactions at the Mineral/Water Interface

In soil environments, chemical reactions at the mineral/water interface occur over a range of time scales, from microseconds to years. Many important processes (e.g., adsorption, oxidation-reduction, precipitation) at mineral surfaces are characterized by a rapid, initial reaction that occurs from milliseconds to minutes (*13*, *27–31*). In fact, in some reaction processes, a large part of the reaction process is complete before the first experimental measurement can be made using traditional batch and flow techniques. An understanding of these initial reaction rates, where back reactions and secondary reaction products are minimized, allows one to obtain "chemical kinetic" rate constants and reaction mechanisms, both of which are needed to understand environmental chemical processes. Chemical relaxation techniques e.g., pressure jump (p-jump) and concentration jump (c-jump such as stopped-flow), provide rapid data collection on time scales of milliseconds. However, with these methods, rate “constants” are calculated from linearized rate equations that include parameters that were

In Advances in the Environmental Biogeochemistry of Manganese Oxides; Sparks, et al.;
ACS Symposium Series; American Chemical Society: Washington, DC, 2015.

determined via macroscopic equilibrium and modeling studies. Thus, the rate "constants" are not directly determined (*13*, *32*, *33*).

Direct, in situ, molecular-scale measurement of rapid reactions has been limited. Fendorf et al. (*34*) employed stop-flow electron paramagnetic resonance (SF-EPR) spectroscopy to determine Mn(II) sorption on birnessite (δ-MnO_2) at a time scale of milliseconds. Recently, Parikh et al. (*14*) used in situ, Fourier Transform infrared (FTIR) spectroscopy to determine As(III) oxidation rates on hydrous manganese(IV) oxide (HMO) at a time resolution of ~2.5 s. Unfortunately, both of these techniques have limitations. EPR can only be used to measure EPR active nuclei, while FTIR requires both IR active functional groups and relatively high concentrations of reactants (*14*).

These are not limitations with quick-scanning X-ray absorption spectroscopy (Q-XAS). Q-XAS is a synchrotron-based technique that allows one to collect a X-ray absorption near edge structure (XANES) or extended X-ray absorption fine structure (EXAFS) spectrum on ms time scales (*35*).

Depending on beamline instrumentation and photon flux, Q-XAS, can probe elements with atomic numbers >20 and at low concentrations (*36*). Most of the quick-scanning beamlines allow for collection of a complete EXAFS scan in ~ 1 min or less, by slewing the monochromator from low energy to high energy and repeating the process (*37*). Another way to rapidly collect EXAFS data is to conduct energy-dispersive measurements; however, this technique often has poor sensitivity and since transmission mode is used, it may be unsuitable for mineral/ water studies (*35*).

Ginder-Vogel et al. (*13*), for the first time, employed Q-XAS to measure the kinetics of As(III) oxidation on hydrous manganese oxide (HMO). A cam-operated, continuously scanning monochromator (Figure 1) was used at beamline X18B at the National Synchrotron Light Source (NSLS) at Brookhaven National Laboratory. The constant rocking motion enabled the collection of X-ray fluorescence spectra as the monochromator moved from low to high and from high to low energy. This enabled greater time resolution of the XAS measurements.

Q-XAS has been employed over the past several years to study metal sorption/ precipitation (*31*) and redox kinetics (*13*, *30*) using both batch and flow apparatus.

Kinetics and Mechanisms of As(III) Oxidation on Mn-Oxides

While the mobility and toxicity of elements such as As and Cr is dependent on redox state and the redox conditions of the environment, the kinetics of the processes also play an important role. XAS is an ideal tool for determining the local coordination environment of an element and its oxidation state and for following changes in speciation and reaction mechanisms over time (*38*).

In Advances in the Environmental Biogeochemistry of Manganese Oxides; Sparks, et al.;
ACS Symposium Series; American Chemical Society: Washington, DC, 2015.

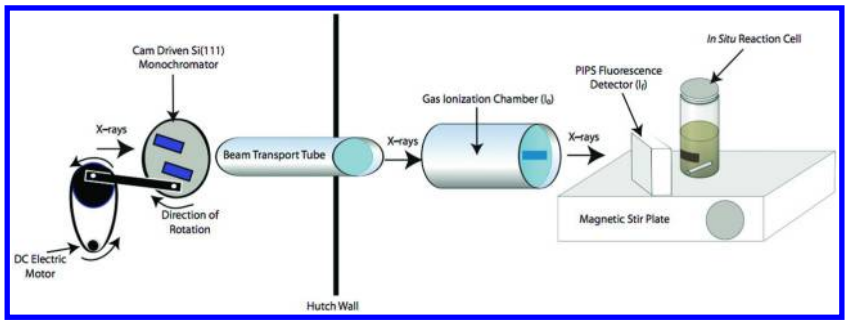

Figure 1. Experimental setup used to collect Q-XAS data. Reproduced with permission from Ginder-Vogel et al. PNAS 106, 16124–16128. Copyright (2009) National Academy of Sciences.

Parikh et al. (*39*), using single bounce, rapid scan attenuated total reflectance Fourier transform infrared (ATR-FTIR) spectroscopy, demonstrated that As(III) oxidation on HMO was extremely rapid. In the research of Ginder-Vogel et al. (*13*), using Q-XAS, a complete XANES spectrum was collected in 980 ms (Figure 2). In this study the oxidation states in both the solution and at the mineral/water interface were probed. The average oxidation state was then determined by fitting each individual XANES spectra with a linear combination of As(III) and As(V) standard solutions (in this experiment, 5 mM standards were used). The fits yielded the molar ratio of As in solution, from which the concentrations of As(III) and As(V) could be calculated, using the initial As concentration. In Figure 3 one sees the XANES spectra for the reaction of As(III) with HMO over time scales ranging from 0.98 to 298.9 sec. There is a rapid transformation of As(III) to As(V) on the HMO surface. Complementary solution and surface concentrations for both Q-XAS and separate batch experiments show that after 1 sec, the As(V) concentration reaches 0.37 mM (Figure 3) and increases precipitously for 45 sec to attain a concentration of 1 mM, and then slowly reaches 1.5 mM after 300s. Based on biphasic kinetics, rate constants were determined from first-order plots for both the Q-XAS and batch experiments (Table 1). For both methods, a rate constant for As(III) depletion was obtained that was an order of magnitude larger during the initial portion of the reaction that in the later segment (Table 1). The initial rate constant of As(III) depletion, obtained using Q-XAS was nearly twice as large (4.7 X 10^{-3} /sec) as the rate constant determined with the batch method (2.5 X 10^{-3}/sec, Table 1).

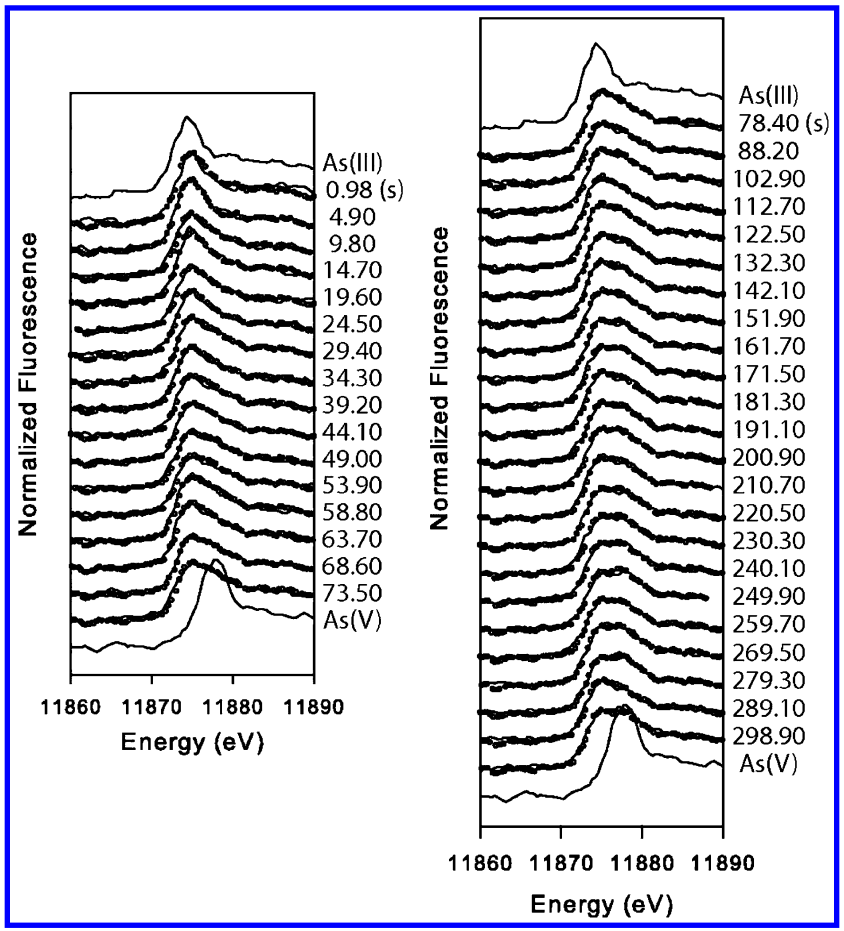

Figure 2. Data (solid) and linear combination fits (dots) of individual As K-edge XANES spectra used to determine As(III) and As(V) concentrations during the batch reactions. Each spectrum was collected in approximately 980 ms, with the time (in s) next to each spectrum indicating the time the last data point of each spectrum was collected. Reproduced with permission from Ginder-Vogel et al. PNAS 106, 16124–16128. Copyright (2009) National Academy of Sciences.

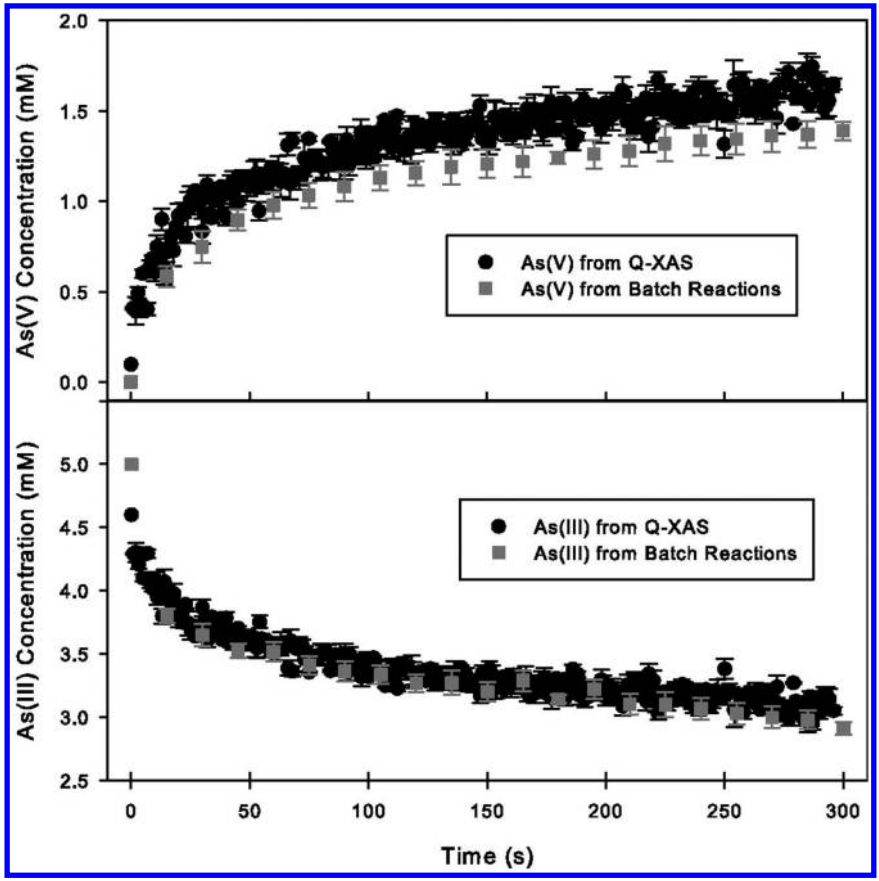

Figure 3. As(V) and As(III) concentrations determined from traditional batch and Q-XAS reactions. Error bars represent the SD of 3 measurements made at each time point. XANES spectra and fits used to calculate Q-XAS As concentrations are shown in Figure 12. Reproduced with permission from Ginder-Vogel et al. PNAS 106, 16124–16128. Copyright (2009) National Academy of Sciences.

Table 1. Apparent, first-order rate constants determined from batch and Q-XAS experiments[a]

Experiment type	*Time period (s)*	*No. of data points*	*k* (s^{-1})	r^2
As(III)–Batch	1–60	4	2.5 (3) × 10^{-3}	0.96
As(III)–Batch	135–300	14	6.1 (4) × 10^{-4}	0.82
As(III)–Q-XAS	1–30	30	4.7 (4) × 10^{-3}	0.91
As(III)–Q-XAS	135–300	168	4.9 (4) × 10^{-4}	0.74

[a] The rate constants of As(III) depletion were determined by linear regression analysis of the noted time-periods.vReproduced with permission from Landrot et al. Environ. Sci. Technol. *44*, 143–149. Copyright (2010) American Chemical Society.

Lafferty et al. (*15*, *40*), using a combined kinetic and molecular scale approach, determined the rates and mechanisms of As(III) oxidation and As desorption on hydrous manganese oxide (HMO), a high surface area, amorphous Mn-oxide. A stirred-flow technique was employed to follow the kinetics of As(III) oxidation over a time scale of days (Figure 4). During the first 0.4 hour no As or Mn appeared in the effluent solutions, indicating that all the As(III) was oxidized to As(V) since the EXAFS data did not show any sorption of As(III) on the HMO. Up until 6.4 hours, only As(V) appeared in the effluent solution suggesting that all the As(III) was oxidized to As(V) and bound to the HMO or was desorbed into the solution phase. After 6.4 hours, As(V), as well as Mn(II) and As(III), appeared in the effluent. This was also when As(III) oxidation decreased. Synchrotron-based XRD and XAS analyses of Mn revealed that initially Mn was sorbed into vacancy sites of the HMO as both Mn^{2+} and Mn^{3+}, and at between 4 and 10 hours the vacancy sites were filled and Mn^{2+} began to compete with As(V) for edge sites, causing a decrease in As(IIII) oxidation. Additionally, the data indicated that Mn^{3+} could be sorbing on edge sites via conproportionation. This results when Mn^{2+} is oxidized and Mn^{4+} is reduced. Thus, passivation of the HMO surface was significantly affected not only by As(V) but most importantly, Mn^{2+} and Mn^{3+}. As time proceeded, passivation of the surface was enhanced. XAS of As speciation showed that only As(V) species were present on the surface, but that the type of As(V) species changed as reaction time proceeded (Figure 5). Up to 4 hours of reaction time, the predominant inner-sphere adsorption complexes were bidentate binuclear and monodentate mononuclear but between 4 and 10 hours, when passivation ensued, there were two predominant species, bidentate binuclear and a bidentate mononuclear. A schematic showing the overall mechanism of As(III) oxidation on HMO is shown in Figure 6. The data clearly show, once again, the importance of following reaction processes over time and at the molecular scale.

Effect of Competitive Ions and Bacteria on As(III) Oxidation on Mn-Oxides

Some studies have been published on the competitive effects of elements and bacteria on the kinetics of As(III) oxidation on Mn-oxides (*41*, *42*). Ion competition does impact As(V) sorption on minerals (*41*, *43–45*), but few studies have appeared on the effect of ion competition on As(III) oxidation kinetics on Mn-oxides (*8*, *41*). Chiu and Hering (*9*) showed that reactions with manganite were slower than what was observed for As(III) oxidation on poorly crystalline Mn(IV) oxides (*13*, *39*). Parikh et al. (*41*) studied the effects of Fe and phosphate competition on the rapid, initial kinetics of As(III) oxidation on δ-Mn-oxide. Phosphate caused decreased total As sorption on Mn-oxide (Figure 7). This could be ascribed to the similar chemical structure and reactivity of As(V) and phosphate (*41*, *44*, *46*). There was also decreased retention of both anions (Figure 7). The reduced As sorption in the presence of phosphate is advantageous in environments where animal waste containing both As and P is land applied (*41*).

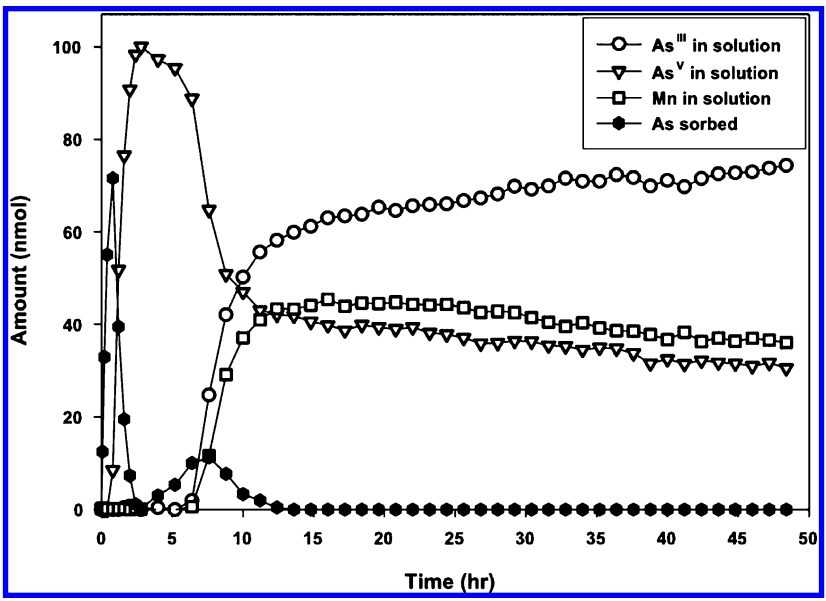

Figure 4. The amount (nmol) of As sorbed as well as amounts (nmol) of AsIII, AsV, and MnII in the effluent of a stirred-flow experiment reacting 1 g/L δ-MnO2 with 100 μM AsIII flowing at 1 mL/min for 48 h. Reproduced with permission from Lafferty et al., Environ. Sci. Technol. 44, 8460-8466. Copyright (2010) American Chemical Society.

In Advances in the Environmental Biogeochemistry of Manganese Oxides; Sparks, et al.;
ACS Symposium Series; American Chemical Society: Washington, DC, 2015.

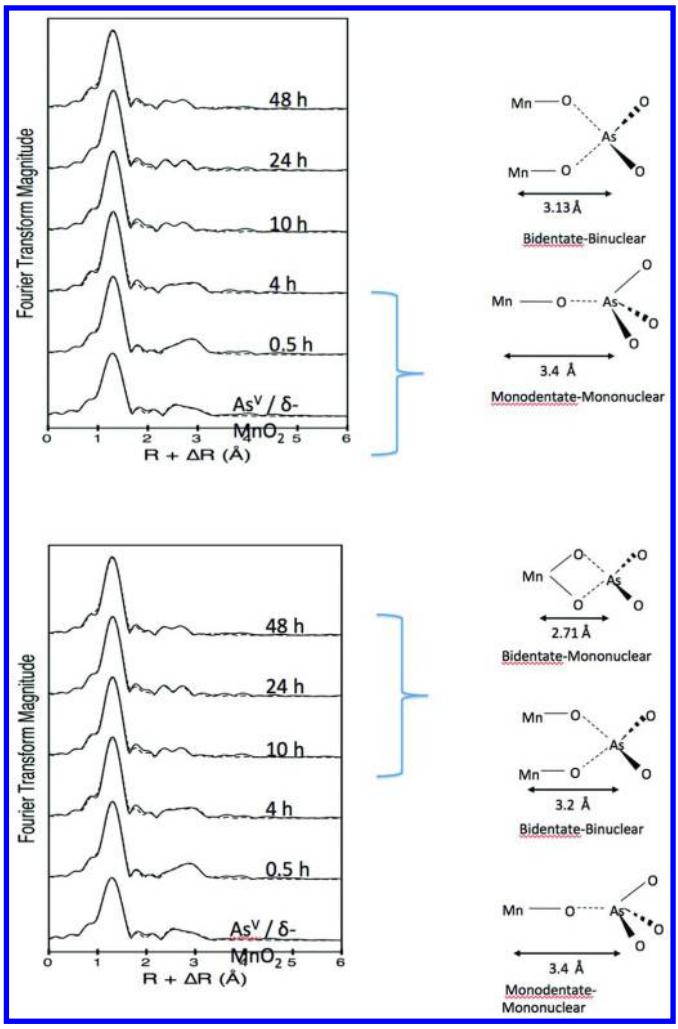

Figure 5. Time 0 through 4 h AsV is bound in Bidentate-Binuclear and Monodenate-Mononuclear. This is the time when Mn is primarily sorbing at vacancy sites. Time 10 through 48 h AsV is bound in Bidentate-Binuclear, Monodenate-Mononuclear, and Bidentate-Mononuclear. Bidentate-binuclear As-Mn length increases. Mn(III) is present when AsV bonding changes. This is the time when Mn has filled all vacancy sites and begins to compete with As for edge sites. Reproduced with permission from Lafferty et al., Environ. Sci. Technol. 44, 8467–8472. Copyright (2010) American Chemical Society.

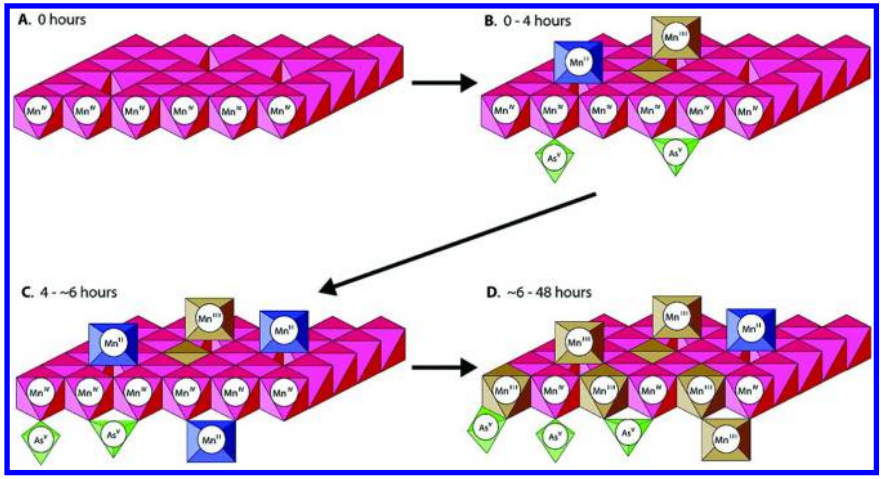

Figure 6. Proposed reaction mechanism for AsIII oxidation by δ-MnO2 over 48 h in a stirred-flow reactor. Throughout the reaction, AsIII is oxidized by MnIV at δ-MnO2 edge sites, producing MnII and AsV. (A) Unreacted δ-MnO2 octahedral layers consist of primarily Mn4+ and have reaction sites at layer edges (edge sites) and vacancy sites. (B) During the first 4 h of AsIII oxidation, MnII sorbs at δ-MnO2 vacancy sites, and AsV sorbs at edge sites in bidentate−binuclear and monodentate−mononuclear complexes. Also, a portion of sorbed MnIIreacts with MnIV at vacancy sites to form MnIII. (C) Between 4 and 6 h of reaction, vacancy sites become filled with MnII/III, MnII begins to sorb at δ-MnO2 edge sites, and AsV sorption continues in the same sorption complexes. (D) Beyond 6 h of reaction, MnII at edge sites (and probably vacancy sites) reacts with MnIII in δ-MnO2 octahedral layers to form MnIII. The resulting MnIII changes the bonding environment of AsV, which begins to sorb in bidentate−mononuclear complexes, and the As−Mn distance in AsV bidentate−binuclear complexes increases slightly. Reproduced with permission from Lafferty et al., Environ. Sci. Technol. 44, 8467–8472. Copyright (2010) American Chemical Society.

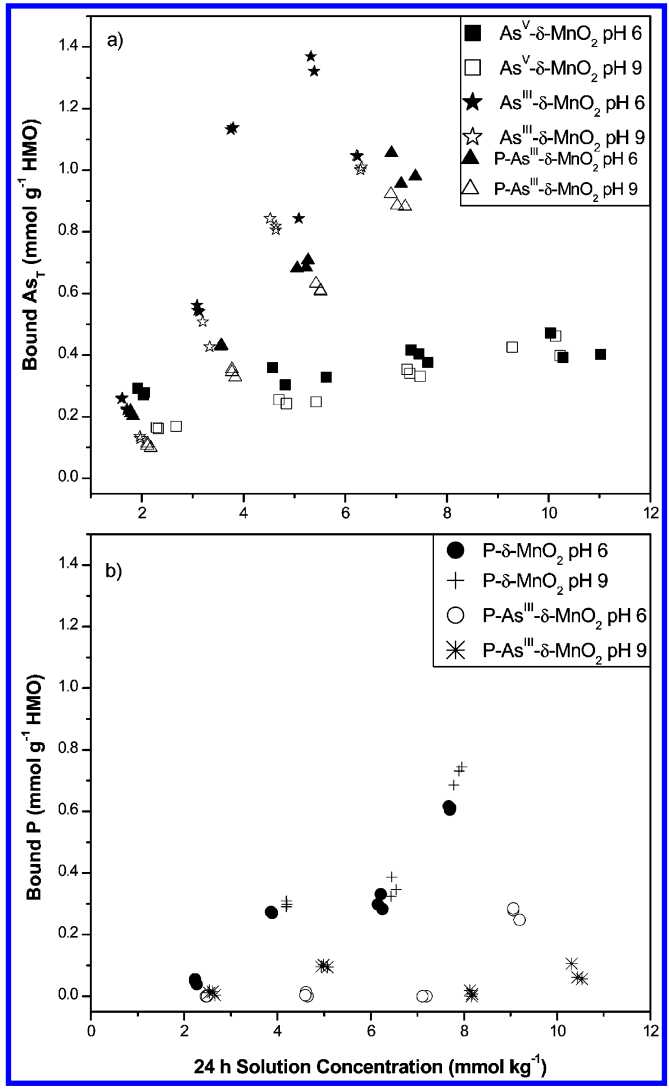

Figure 7. Sorption isotherms from batch experiments at pH 6 (solid symbols) and 9 (open symbols) in 5 mmol kg−1 NaCl for a) As sorption to δ-MnO2 when added as AsV and AsIII (including oxidation) in the presence and absence of phosphate (P) and b) phosphate sorption to δ-MnO2 in the presence and absence of AsIII. Reproduced with permission from Parikh et al., Environ. Sci. Technol. 44, 3772-377. Copyright (2010) American Chemical Society.

Figure 8 shows the percent of initial As [As(III) and As(V)] and phosphate in solution after reaction with Mn-oxide over time at pH 6 and 9. An increased rate of As(III) oxidation on manganite was previously observed with decreased pH (6.3 to 4); however, the current data, and the study of Parikh et al. (*14*) showed no significant effect of pH on the initial As(III) oxidation on Mn-oxide (Figure 8). The concentration of As(III) in solution rapidly dropped to near zero, with full removal from solution occurring between 5 and 30 minutes. At 24 h, both phosphate and As concentrations were stable, with solution As(V) concentrations higher when phosphate was present. When the As(V) concentrations were increased from 5 to 960 minutes reactions are still occurring at the solid-liquid interface. There were still high phosphate concentrations in solution, which indicated that As release was not due to phosphate exchange reactions (*41*).

Figure 9 shows the effect of phosphate and γ-Fe-oxide on As(III) oxidation on Mn-oxides using rapid scan ATR-FTIR. In every case the addition of phosphate reduced the total amount of As(III) oxidation. The initial slope and half times were similar for all reactions, except for the addition of 25 mmol kg-1 phosphate (the slope decreased and half time increased). Although phosphate and α-FeOOH concentrations reduced the amount of As(V) produced, the initial oxidation rate was not affected. Since the initial reaction rates were not strongly influenced by concentration of reactants, including other ions and surfaces, the reaction did not appear to be transport limited, which suggests that primarily chemically controlled kinetics were measured (*41*).

Under certain conditions, As(III) can be oxidized by Fe-oxides (*47*) however, no oxidation by α-FeOOH was observed during 15 minutes of reaction (Figure 9). When δ-Mn-oxide was reacted with As(III) and 4 g kg-1 α-FeOOH, the amount of As(V) detected decreased. However, with increasing α-FeOOH concentration the amount of As(V) increased. At the highest α-FeOOH concentration the amount of As(V) produced exceeded what was observed for δ-Mn-oxide alone (Figure 9). The reduced As(III) oxidation in the presence of α-FeOOH is ascribed to competition between δ-Mn-oxide and α-FeOOH for As(III). Increasing α-FeOOH increased competition for As(V), and with high α-FeOOH concentrations, some As(V) released from δ-Mn-oxide during oxidation binded to the α -FeOOH instead of δ-Mn-oxide. Therefore, passivation of δ-Mn-oxide was reduced. In this case, the Fe-oxide was promoting and hindering As(III) oxidation on δ-Mn-oxide. This result was observed when As(III) was oxidized by birnessite, todorokite, and hausmannite in the presence of α-FeOOH (*41*, *48*). Another study showed an increase in As attenuation via simultaneous oxidation of As(III) and Fe(III) by Mn-oxides, whereby coprecipitation of Fe(III)-oxides with As(V) sequestered As and prevented Mn-oxide passivation (*41*, *49*).

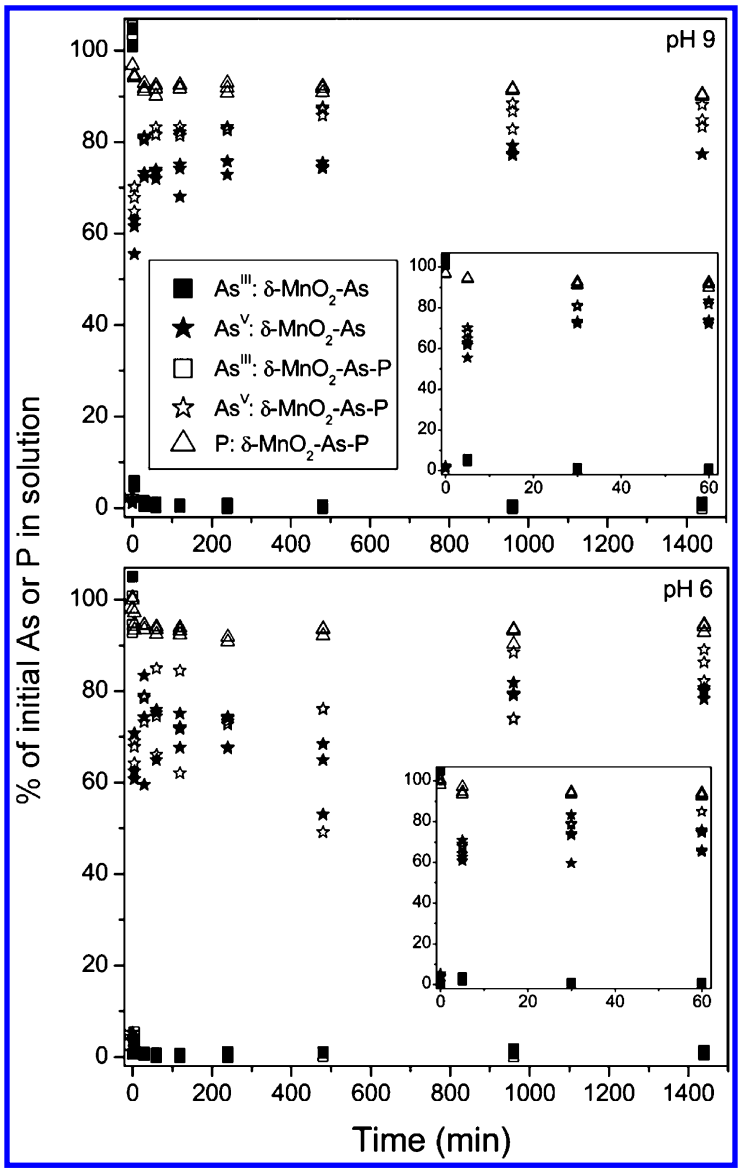

Figure 8. Kinetic plots of batch experiments showing percent of initial As (5 mmol L−1 AsIII), as solution AsIII and AsV, and phosphate in solution during the course of reaction with δ-MnO2 at a) pH 9 and b) pH 6 in 5 mmol kg−1 NaCl. Insets are included to allow viewing of data within the first 60 min of reaction. Solid symbols correspond to experiments where δ-MnO2 was reacted with AsIII, and open symbols correspond to experiments where AsIII and phosphate were simultaneously reacted with δ-MnO2. Reproduced with permission from Parikh et al., Environ. Sci. Technol. 44, 3772-377. Copyright (2010) American Chemical Society.

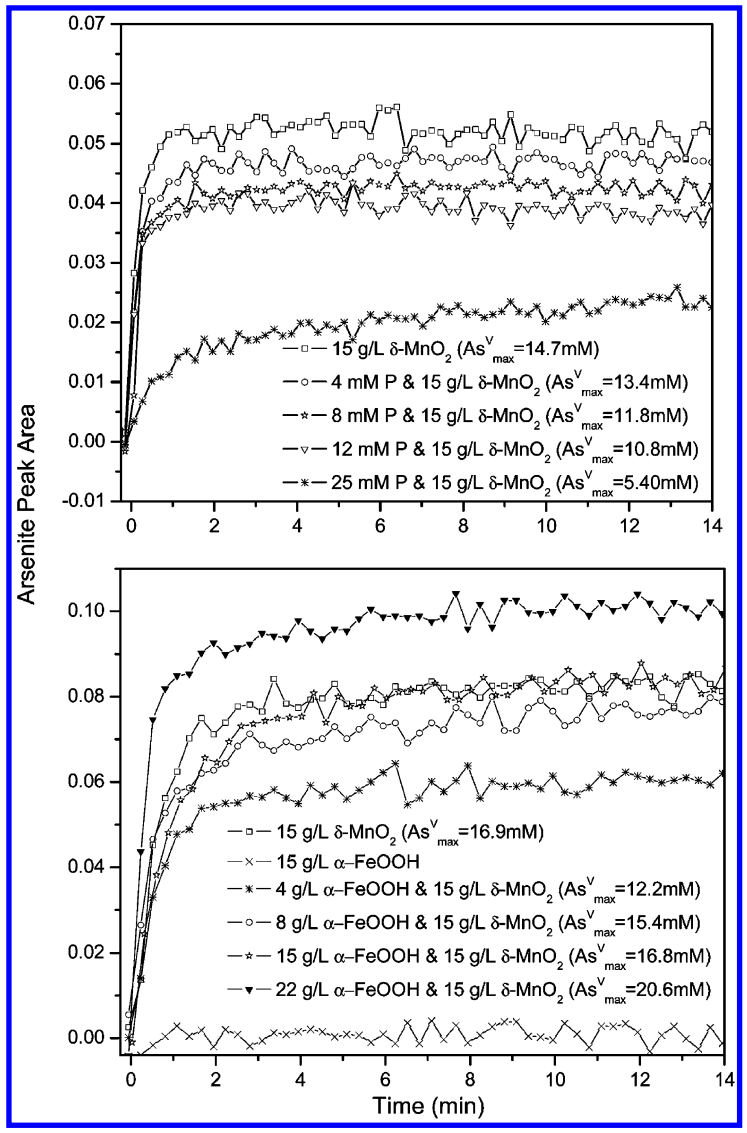

Figure 9. Rapid-scan ATR-FTIR plots of AsV IR peak area as a function of reaction time for 25 mmol kg−1 AsIII (pH 6, 5 mmol kg−1 NaCl) reacted with varying concentrations of a) phosphate (P) and b) α-FeOOH (experiments conducted on a different FTIR and with different batches of δ-MnO2 and α-FeOOH). Reproduced with permission from Parikh et al., Environ. Sci. Technol. 44, 3772-377. Copyright (2010) American Chemical Society.

Parikh et al. (*41*) also studied the effect of bacteria on As(III) oxidation on Mn-oxide. Solution As(III) and As(V) concentrations, over a 48 hour reaction period, showed that the bacteria completely oxidized 1 mmol kg-1 As(III) in about 24 hours. The data also showed that the bacteria oxidize a maximum of about 5 mmol kg-1 As(III) in 48 hours, with the highest oxidation rate occuring after 24 hours of reaction. Rapid-scan ATR-FTIR experiments did not show detectable As(III) oxidation by either *P. fluorescens* or *A. faecalis* alone during the 15 min reaction time (Figure 10) and rapid As(III) oxidation was observed only when Mn-oxide was present. When bacteria were bound to only α-FeOOH, no As(V) was detected; however, if δ-Mn-oxide was present with bacteria, a small IR peak corresponding to As(V) was observed.

The As(V) max for *P. fluorescens* with Mn-oxide was 3.05 mmol kg-1 and 4.41 mmol kg-1 for *A. faecalis* with Mn-oxide; with α-FeOOH also present the values dropped to 0.79 and 2.14, respectively. The half-time values were less than when δ-Mn-oxide reacted with As(III) alone, with values ranging from 0.64 to 0.88; however, the slope values were much less with a value of 0.01. Bacterial adhesion to minerals blocks access to Mn(IV) and reduces the As(V) maximum. Bacteria bound to δ-Mn-oxide impede As(V) production much more than reaction with phosphate or α-FeOOH. Reaction rates were significantly reduced, based on half-times (0.9802.81) and m30 s (0.01) values, which suggest that the reaction was transport limited. Exchange of bacteria or biopolymers for As(III) at Mn(IV) sites was not likely. Rather, the As(III) diffusion and transport through bacteria extracellular material (biofilm) proabley retarded As(III) oxidation (*41*).

Jones et al. (*42*) studied the kinetics of As(III) oxidation by two heterotrophic soil bacteria (*Agrobacterium tumefaciens* and *Pseudomonas fluorescens*) and poorly crystalline manganese oxide (δ-Mn-oxide) using batch experiments. The apparent rate of As(V) appearance in solution was higher for the combined batch experiments in which bacteria and δ-Mn-oxide were oxidizing As(III) at the same time than for either component alone. The additive effect of the mixed bacteria and δ-Mn-oxide system was consistent for short (<1 h) and long (24 h) term coincubation showing that mineral surface inhibition by cells had little effect on the As(IIII) oxidation rate. Surface interactions between cells and the mineral surface were indicated by sorption and pH-induced desorption data. Total sorption of As on the mineral was lower with bacteria present (16.1 t- 0.8% As sorbed) and higher with δ-Mn-oxide alone (23.4+- 1%). Arsenic was more easily desorbed from the cell- δ-Mn-oxide system than from δ-Mn-oxide alone. Therefore, the presence of bacteria inhibited As sorption and decreased the stability of sorbed As on δ-Mn-oxide even though As(III) was oxidized most rapidly in a mixed cell- (δ-Mn-oxide system. The additive effect of biotic (As-oxidizing bacteria) and abiotic (δ-Mn-oxide mineral) oxidation processes in a system containing both oxidants suggests that mineral-only data may underestimate the oxidative capacity of natural systems with biotic and abiotic As(III) oxidation pathways (*42*).

In Advances in the Environmental Biogeochemistry of Manganese Oxides; Sparks, et al.;
ACS Symposium Series; American Chemical Society: Washington, DC, 2015.

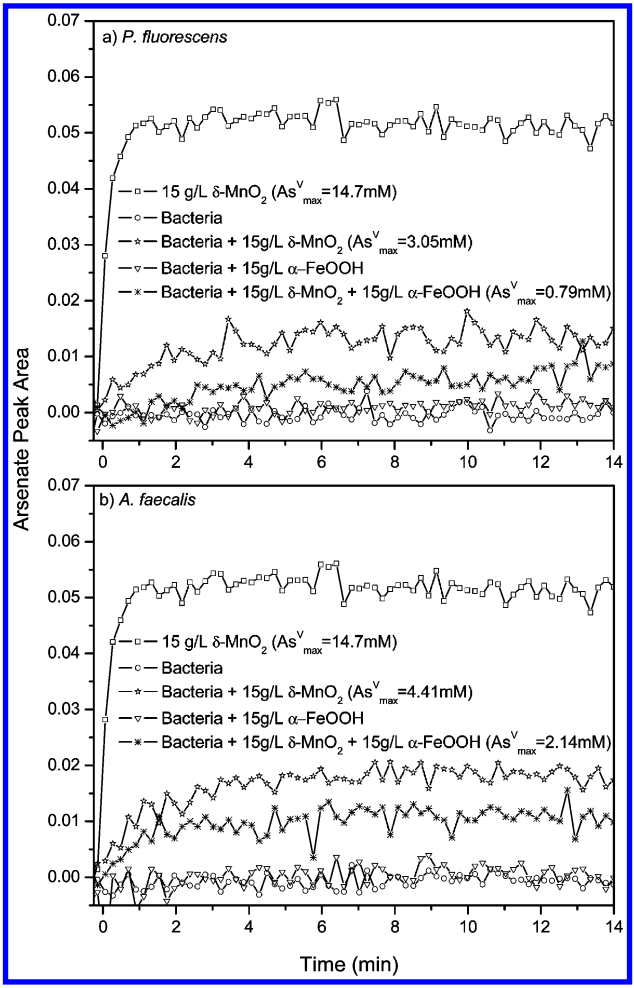

Figure 10. Rapid-scan ATR-FTIR plots of AsV IR peak area as a function of reaction time for 25 mmol kg−1 AsIII (pH 6, 5 mmol kg−1 NaCl) reacted with a) P. fluorescens and b) A. faecalis suspensions (10 times steady state) with and without δ-MnO2 and α-FeOOH. Reproduced with permission from Parikh et al., Environ. Sci. Technol. 44, 3772-377. Copyright (2010) American Chemical Society.

In Advances in the Environmental Biogeochemistry of Manganese Oxides; Sparks, et al.;
ACS Symposium Series; American Chemical Society: Washington, DC, 2015.

Environmental Influences on Cr(III) Oxidation on Mn-Oxides

Chromium predominantly exists in two oxidation states in the environment, Cr^{III} and Cr^{VI} (*50*, *51*). Chromate, chromium(VI), is highly toxic to animals and plants; moreover, it is quite soluble and highly mobile under environmental conditions. The other common Cr oxidation state, chromite (Cr^{III}), is less toxic and generally immobile. Most Cr in the environment is present as Cr^{III}; however, industrial processes and Mn-oxides can oxidize Cr^{III} into Cr^{VI} and release this toxic metal into natural systems (*52*, *53*). The widespread contamination of natural systems with Cr^{VI} necessitates a thorough understanding of the mechanisms of Cr oxidation by Mn-oxides to determine the risk of Cr^{VI} production and develop techniques to reduce its formation.

Mn-oxides are the only naturally occurring mineral capable of oxidizing Cr^{III} (*52*, *53*). While all Mn-oxides are able to oxidize Cr, the extent and rate of Cr^{VI} production is highly dependent on the mineral's surface charge, PZC, surface area, Mn^{II} and Mn^{III} impurities, and the reactive site density of Mn^{IV} (*54*). Most naturally occurring Mn-oxides are poorly crystalline with layered structures. Random stacked birnessite (RSB), acid birnessite (AB), and δ-MnO, are synthesized Mn-oxides which closely resemble those found in the environment. All of these Mn-oxides can rapidly convert a large percentage of Cr^{III}, up to 80%, into Cr^{VI} (*55–57*). Many other Mn-oxides, such as birnessite, manganate, hausmanite, and Mn_2O_3 can also quickly oxidize Cr^{III} (*57*, *58*). Even pyrolusite, which has the highest PZC and is the most crystalline of the Mn-oxides, can oxidize Cr^{III} to Cr^{VI} in small quantities (*53*, *57*).

The oxidative capacity of Mn-oxides can be quantified through the use of batch techniques. Kim *et al.* (*58*) and Weaver & Hochella (*57*) determined this capacity under relatively similar experimental conditions. Weaver & Hochella (*57*) found birnessite had the highest oxidizing ability followed by hausmannite, romanechite, cryptomelane, manganite, pyrolusite, and lithiophorite, in order of decreasing reactivity. Kim *et al.* (*58*) found birnessite to be the most reactive, followed by todorokite, lithiophorite, and finally pyrolusite. The reactivity of Mn-oxides can be closely linked to their degree of crystallinity, which influences surface area (*57–59*). Birnessite has the largest surface area and is the most reactive; however, the relationship between oxidative capacity and surface area is broken by hausmannite, which has a smaller surface area than romanechite and cryptomelane. Excluding hausmannite, surface area is a strong predictor of Cr^{III} oxidation. Kim & Moon's (*59*) study reinforces this trend, showing up to a 20% increase in Cr^{VI} production by a less crystalline birnessite. Biogenic manganese oxides (bioMnOx) follow a similar pattern, where younger, less structured bioMnOx have greater reactivity compared to more aged bioMnOx that contain higher proportions of triclinic birnessite (*60*). The percentage of Cr^{III} oxidation by Mn-oxides is also dependent on the oxidation state of Mn on the mineral surface (*59*), where a higher Mn^{IV} concentration leads to larger amounts of Cr^{III} oxidized. This is due to Cr^{III} supplying two electrons to Mn^{IV} versus only one to Mn^{III} (*58*).

The Cr oxidation reaction proceeds in three phases, first Cr sorbs to the Mn surface, then the Cr exchanges electrons with Mn, and finally the reaction products

In Advances in the Environmental Biogeochemistry of Manganese Oxides; Sparks, et al.;
ACS Symposium Series; American Chemical Society: Washington, DC, 2015.

are desorbed (*52*, *56*, *61*, *62*). The exact kinetics and mechanisms of Mn-oxidation are poorly understood (*63*). An overall equation for the oxidation of Cr(III) is shown in Eq. 9 and a schematic of the multimodal processes is shown in Fig. 11 (*64*).

$$Cr(OH)^{2+} + 1.5MnO_2 \leftrightarrow HCrO_4^- + 1.5Mn^{2+} \quad [9]$$

The pH of the solution can greatly impact Cr oxidation kinetics. As pH rises, the Mn mineral surface becomes more negative, further attracting positively charged Cr^{III}. This increases the electrostatic interaction between the Mn mineral surface and Cr^{III}. Accordingly, more Cr^{III} is sorbed to the Mn surface leading to initially higher rates of Cr^{VI} production (*65*). However, not all of the Cr^{III} is oxidized because Mn^{IV} and Cr^{III} share the same structural environment. Therefore, some of the Cr^{III} can be sorbed to the surface of the manganese and remain un-oxidized. Cr^{III} sorption preferentially occurs at higher pHs, allowing Cr^{III} to be held as an inner-sphere complex on the $Mn(IV)O_2$ surface. This contrasts with Cr^{VI} which is thought to form primarily outer-sphere complexes with Mn-oxide (Fig. 11). Higher pHs ultimately lower the amount of Cr^{III} oxidized which reduces the production of Cr^{VI} (*66*).

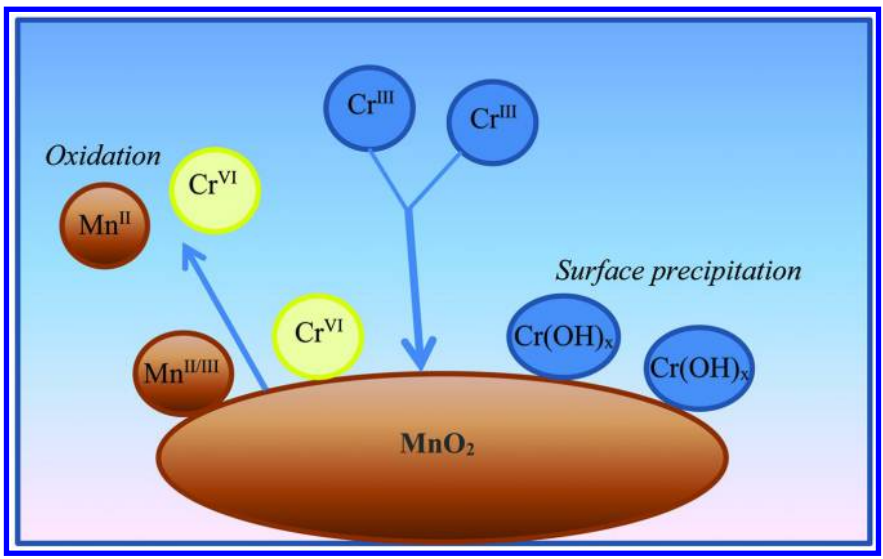

Figure 11. The Cr^{III} in solution interacts with the surface of MnOx. Some of the Cr^{III} is sorbed to the surface of the MnOx, while some is oxidized. Not all of the Cr^{VI} is released back into solution as a portion can sorb on the MnOx surface.

In Advances in the Environmental Biogeochemistry of Manganese Oxides; Sparks, et al.;
ACS Symposium Series; American Chemical Society: Washington, DC, 2015.

Research conducted by Johnson & Xyla (*61*) determined a lower rate of Cr^{III} oxidation by manganite as Cr^{III} concentrations increased. Fendorf and Zasoski also found Cr^{III} oxidation by birnessite was reduced at higher Cr^{III} concentrations (*65*). In both cases, Cr^{III} was below a pH and concentration where it could precipitate in solution alone. Similarly, as the solution pH increases more hydroxide ions are introduced into the reaction, enhancing the formation of Cr hydroxide precipitates on the Mn mineral surface. Fendorf & Zasoski (*65*) determined there was little change in reactivity from pH 2 to 3.5. However, above pH 3.5, the increased availability of hydroxide ions enhanced the formation of Cr hydroxides leading to passivation of the Mn mineral surface (*65*). When the pH was raised above 3.5 Cr^{III} oxidation decreased (*66*). This was confirmed by Feng *et al.* (*67*), who found the amount of Cr^{III} oxidized by birnessite between pH 2 and 3.5 was nearly constant, but oxidation of Cr^{III} was reduced once the pH increased beyond 3.5. Experiments conducted by Landrot *et al.* (*66*) showed greater oxidative capacities at more acidic pHs, even within the pH 2.5 to 3.5 range as can be seen in Fig. 12. The combination of higher pHs and concentrations promote the precipitation of Cr-(oxyhdr)oxide phases. The formation of Cr hydroxides on the Mn mineral surface reduces the availability of reactive sites, which in turn decreases Cr^{III} sorption and oxidation. Chromium hydroxide can precipitate from bulk solution onto the surface of Mn minerals at concentrations below its saturation index (*64*).

Under more neutral pH conditions bioMnOx oxidized more Cr^{III} at higher, rather than lower pHs. At pH 6.2 Cr oxidation by bioMnOx ceased within 10 mins, while at pH 7.2 oxidation continued for 160 mins. The quenching of the reaction at pH 6.2 is due to either the proton promoted dissolution of bioMnOx or the lower activity of bioMnOx towards Mn^{II} oxidation (*60*).

Kinetics and Mechanisms of Cr(III) Oxidation on Mn-Oxides

The identification and quantification of chromium oxidation states using XANES spectroscopy is quite straightforward due to a prominent pre-edge peak at 5993 eV, when Cr is present as Cr^{VI} which is caused by a bound-state 1s to 3d transition. Landrot et al. (*29*) employed the same technique as Ginder-Vogel et al. (*13*) to measure the rapid, initial kinetics of Cr^{III} oxidation on HMO (*29*, *49*, *50*). A complete XANES spectrum was determined in 0.75 sec. Data were collected at pHs of 2.5, 3.0, and 3.5 at Cr^{III} concentrations of 40-100 mM. Chromium^{VI} resulting from the oxidation of Cr^{III} on the HMO surface, displays the prominent pre-edge feature in the XAS spectrum, which is proportional to the amount of Cr^{VI} in the system. Therefore, the height of the pre-edge feature can be measured and compared to a set of Cr^{III}/Cr^{VI} mixtures to determine the amount of Cr^{VI} present over the course of the reaction (*29*, *50*). Figure 13 shows the pre-edge feature increases in intensity with time, indicating the oxidation of Cr^{III} to Cr^{VI}. Chromite oxidation is quite rapid during the first 120 sec of the reaction, when about 35 mM of chromate is produced. The reaction continued to oxidize Cr^{III} to Cr^{VI} for another 30 minutes, before oxidation ceased between 30-60 minutes due to sorption of chromate. Initial reaction rates were determined by quantifying

In Advances in the Environmental Biogeochemistry of Manganese Oxides; Sparks, et al.;
ACS Symposium Series; American Chemical Society: Washington, DC, 2015.

the Cr^{VI} from the height of the pre-edge feature for each experiment, focusing on the reaction from 0-1 minute. Landrot et al. found the rate constants were similar at a given pH and for varying Cr^{III} and HMO concentrations (Table 2) (*29*). Strongly suggesting that the k values are chemical rate constants, as only temperature should impact the magnitude of the k values. Therefore, the use of a method like Q-XAS not only provides valuable information on rapid, initial reaction processes, but also the additional benefit of determining chemical kinetics rate constants. Together these findings provide important insights on reaction mechanisms. Most other techniques cannot significantly reduce or eliminate transport processes. Consequently, the rate parameters that are measured are apparent rate coefficients, and not rate constants. The rapid initial oxidation of Cr(III) by HMO was also confirmed by Dai *et al.* (*68*) who discovered Cr^{VI} levels increased quickly within the first 50 minutes of the reaction and increased slowly before leveling off after 300 minutes, due to the saturation of available surface adsorption sites. Techniques such as Q-XAS and further, more detailed research will unlock the exact kinetics and mechanisms of Cr oxidation by Mn-oxides (*69*).

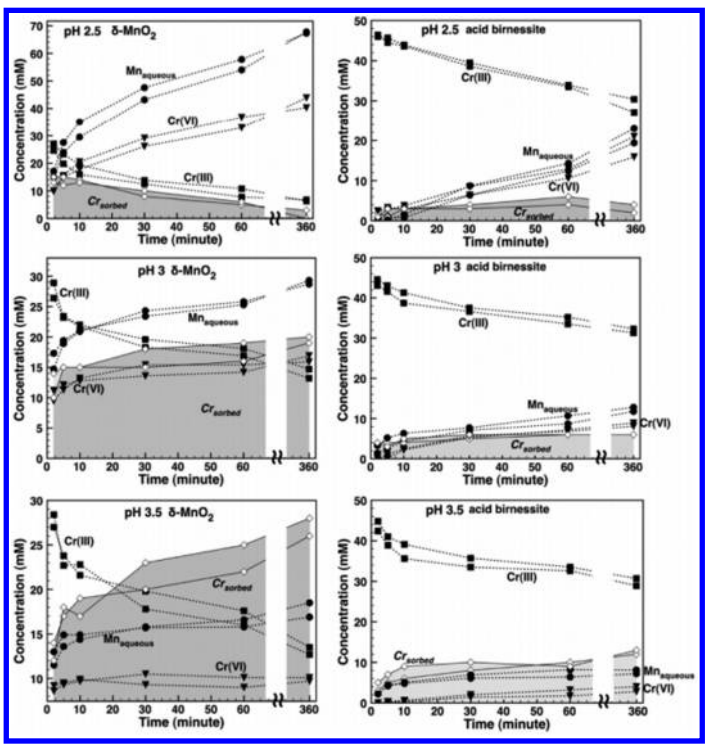

Figure 12. Mn oxides react rapidly with Cr. The reaction is largely complete within the first 20-60 minutes. Lower pHs result in greater oxidation of Cr^{VI}, with less overall surface sorption. Reproduced with permission from Landrot et al., Environ. Sci. Technol. 46, 11594-11600. Copyright (2012) American Chemical Society.

Table 2. Initial Conditions, Measured Initial Rates, and Rate Parameters[a]

		initial rates (mol/L/sec)			k (sec^{-1})		
[Cr(III)] (mM)	[HMO] (g/L)	pH = 2.5	pH = 3	pH = 3.5	pH = 2.5	pH = 3	pH = 3.5
100	20	0.0045/0.0052	0.0045/0.0045	0.0045/0.0047	0.204/0.228	0.277/0.202	0.295/0.364
		(0.00036/0.00071)	*(0.00067/0.00064)*	*(0.0004/0.0006)*			
80	20	0.0035/0.0040	0.0034/0.0035	0.0039/0.0030	0.202/0.220	0.270/0.198	0.353/0.308
		(0.00017/0.00021)	*(0.00031/0.00066)*	*(0.00108/0.00046)*			
60	20	0.0025/0.0029	0.0027/0.0028	0.0022/0.0022	0.197/0.215	0.303/0.208	0.302/0.357
		(0.0002/0.00037)	*(0.0004/0.00017)*	*(0.00043/0.00034)*			
40	20	0.0017/0.0021	0.0015/0.0018	0.0012/0.0012	0.208/0.235	0.266/0.199	0.296/0.363
		(0.00023/0.00003)	*(0.00028/0.00034)*	*(0.00017/0.00017)*			
		Cr partial rate coefficient α					
		1.08/1.01	1.13/1.05	1.43/1.53			
		1.09	**1.09**	**1.48**			
100	20	0.0045/0.0052	0.0045/0.0045	0.0045/0.0047	0.204/0.228	0.277/0.202	0.295/0.364
		(0.00036/0.00071)	*(0.00067/0.00064)*	*(0.0004/0.0006)*			
100	15	0.0035/0.0036	0.0035/0.0036	0.0037/0.0038	0.206/0.207	0.293/0.219	0.291/0.328
		(0.0006/0.0005)	*(0.00046/0.00052)*	*(0.00032/0.00054)*			
100	10	0.002/0.002	0.0023/0.0020	0.0028/0.0029	0.169/0.171	0.287/0.244	0.280/0.311
		(0.00039/0.00039)	*(0.00001/0.00021)*	*(0.0008/0.00059)*			
100	5	0.001/0.0012	0.0010/0.0014	0.0020/0.0022	0.157/0.203	0.257/0.316	0.283/0.346
		(0.00039/0.00001)	*(0.0001/0.0001)*	*(0.00035/0.00031)*			
		Mn partial rate coefficient a					
		0.90/0.98	1.00/1.05	0.58/0.53			
		0.94	**1.02**	**0.55**			
					k (averaged) in sec^{-1}		
					pH = 2.5	*pH = 3*	*pH = 3.5*
					0.192/0.211	0.279/0.227	0.300/0.340
					0.201	**0.242**	**0.322**

[a] The partial rate coefficients α, β at pH 2.5, pH 3, and pH 3.5 shown in this table are averaged values from α and β calculated using eqs 6 and 9 and by combining the initial rates measured at different experimental conditions. The rate constant for each experiment was measured with eq 10. Since all experiments were duplicated, the initial rates and rate parameters are reported with two values separated with "/". The standard error (95% confidence interval) for each initial rate is italicized. Averages of duplicate values are highlighted in bold. Reproduced with permission from Landrot et al. Environ. Sci. Technol. *44*, 143–149. Copyright (2010) American Chemical Society.

In Advances in the Environmental Biogeochemistry of Manganese Oxides; Sparks, et al.;
ACS Symposium Series; American Chemical Society: Washington, DC, 2015.

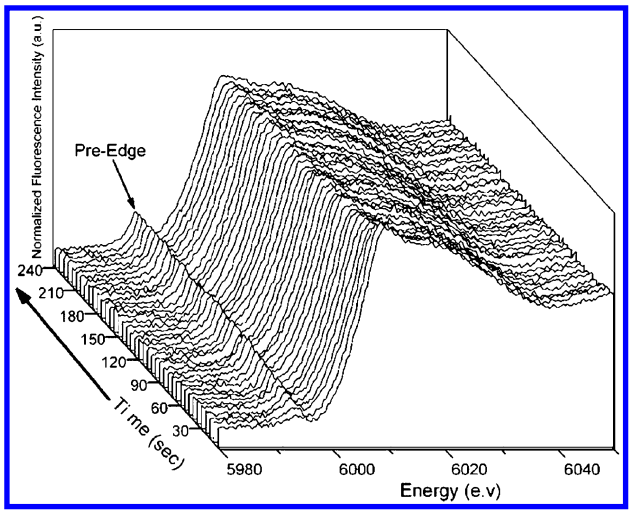

Figure 13. Cr(III) oxidation kinetics using a Q-XAFS technique, at pH 2.5, [Cr(III)] = 100 mM, [HMO] = 20 g/L, and 0−240 s. Each XANES spectrum shown represents 3 s of the reaction (average of four 0.75 s spectra). Reprinted with permission from Landrot et al., Environ. Sci. Technol. 44, 143–149. Copyright (2010) American Chemical Society.

Acknowledgments

The authors gratefully acknowledge the excellent research of former group members, Matthew Ginder-Vogel, Camille Jones, Gautier Landrot, Brandon Lafferty, and Sanjai Parikh, which was reviewed in this chapter.

References

1. Oscarson, D. W.; Huang, P. M.; Defosse, C.; Herbillon, A. The oxidative power of Mn (IV) and Fe (III) oxides with respect to As (III) in terrestrial and aquatic environment. *Nature* **1981**, *291*, 50–51.
2. Shiller, A. M.; Stephens, T. H. Microbial manganese oxidation in the lower Mississippi River: Methods and evidence. *Geomicrobiol. J.* **2005**, *22*, 117–125.
3. Tebo, B. M.; Bargar, J. R.; Clement, B. G.; Dick, G. J.; Murray, K. J.; Parker, D.; Verity, R.; Webb, S. M. Biogenic manganese oxides: Properties and mechanisms of formation. *Annu. Rev. Earth Planet. Sci.* **2004**, *32*, 287–328.
4. Oscarson, D. W.; Huang, P. M.; Hammer, U. T.; Liaw, W. K. Oxidation and sorption of arsenite by manganese dioxide as influenced by surface coatings of iron and aluminum oxides and calcium carbonate. *Water, Air, Soil Pollut.* **1983**, *20*, 233–244.
5. Scott, M. J.; Morgan, J. J. Reactions at oxide surfaces .1. Oxidation of As(III) by synthetic birnessite. *Environ. Sci. Technol.* **1995**, *29*, 1898–1905.

6. Manning, B. A.; Fendorf, S. E.; Bostick, B.; Suarez, D. L. Arsenic(III) oxidation and arsenic(V) adsorption reactions on synthetic birnessite. *Environ. Sci. Technol.* **2002**, *36*, 976–981.
7. Tournassat, C.; Charlet, L.; Bosbach, D.; Manceau, A. Arsenic(III) oxidation by birnessite and precipitation of manganese(II) arsenate. *Environ. Sci. Technol.* **2002**, *36*, 493–500.
8. Chiu, V. Q.; Hering, J. G. Arsenic adsorption and oxidation at manganite surfaces. 1. Method for simultaneous determination of adsorbed and dissolved arsenic species. *Environ. Sci. Technol.* **2000**, *34*, 2029–2034.
9. Petrick, J. S.; Ayala-Fierro, F.; Cullen, W. R.; Carter, D. E.; Aposhian, H. V. Monomethylarsonous acid (MMA(III)) is more toxic than arsenite in Chang human hepatocytes. *Toxicol. Appl. Pharm.* **2000**, *163*, 203–207.
10. Raven, K. P.; Jain, A.; Loeppert, R. H. Arsenite and arsenate adsorption on ferrihydrite: Kinetics, equilibrium, and adsorption envelopes. *Environ. Sci. Technol.* **1998**, *32*, 344–349.
11. Dixit, S.; Hering, J. G. Comparison of arsenic(V) and arsenic(III) sorption onto iron oxide minerals: Implications for arsenic mobility. *Environ. Sci. Technol.* **2003**, *37*, 4182–4189.
12. Moore, J. N.; Walker, J. R.; Hayes, T. H. Reaction scheme for the oxidation of As (III) to As (V) by birnesside. *Clays Clay Miner.* **1990**, *38*, 549–555.
13. Ginder-Vogel, M.; Landrot, G.; Fischel, J. S.; Sparks, D. L. Quantification of rapid environmental redox processes with quick-scanning x-ray absorption spectroscopy (Q-XAS). *Proc. Natl. Acad. Sci. U. S. A.* **2009**, *106*, 16124–16128.
14. Parikh, S. J.; Lafferty, B. J.; Sparks, D. L. An ATR-FTIR spectroscopic approach for measuring rapid kinetics at the mineral/water interface. *J. Colloid Interface Sci.* **2008**, *320*, 177–185.
15. Lafferty, B. J.; Ginder-Vogel, M.; Zhu, M.; Livi, K. J. T.; Sparks, D. L. Arsenite oxidation by a poorly crystalline manganese-oxide. 2. Results from x-ray absorption spectroscopy and x-ray diffraction. *Environ. Sci. Technol.* **2010**, *44*, 8467–8472.
16. Nesbitt, H. W.; Canning, G. W.; Bancroft, G. M. XPS study of reductive dissolution of 7 angstrom-birnessite by H3AsO3, with constraints on reaction mechanism. *Geochim. Cosmochim. Acta* **1998**, *62*, 2097–2110.
17. Tani, Y.; Miyata, N.; Ohashi, M.; Ohnuki, T.; Seyama, H.; Iwahori, K.; Soma, M. Interaction of inorganic arsenic with biogenic manganese oxide produced by a Mn-oxidizing fungus, strain KR21-2. *Environ. Sci. Technol.* **2004**, *38*, 6618–6624.
18. Oscarson, D. W.; Huang, P. M.; Liaw, W. K. Role of manganese in the oxidation of arsenite by freshwater lake sediments. *Clays Clay Miner.* **1981**, *29*, 219–225.
19. Lafferty, B. J.; Ginder-Vogel, M.; Sparks, D. L. Arsenite oxidation by a poorly crystalline manganese-oxide 1. Stirred-flow experiments. *Environ. Sci. Technol.* **2010**, *44*, 8460–8466.
20. Zhu, M. Q.; Paul, K. W.; Kubicki, J. D.; Sparks, D. L. Quantum chemical study of arsenic (III, V) adsorption on Mn-oxides: Implications for arsenic(III) oxidation. *Environ. Sci. Technol.* **2009**, *43*, 6655–6661.

21. Foster, A. L.; Brown, G. E.; Parks, G. A. X-ray absorption fine structure study of As(V) and Se(IV) sorption complexes on hydrous Mn oxides. *Geochim. Cosmochim. Acta* **2003**, *67*, 1937–1953.
22. Peacock, C. L.; Sherman, D. M. Sorption of Ni by birnessite: Equilibrium controls on Ni in seawater. *Chem. Geol.* **2007**, *238*, 94–106.
23. Ramstedt, M.; Shchukarev, A.; Sjoberg, S. Surface properties of manganite (γ-MnOOH). *Geochim. Cosmochim. Acta* **2004**, *68*, A119–A119.
24. Webb, S. M.; Dick, G. J.; Bargar, J. R.; Tebo, B. M. Evidence for the presence of Mn(III) intermediates in the bacterial oxidation of Mn(II). *Proc. Natl. Acad. Sci. U. S. A.* **2005**, *102*, 5558–5563.
25. Perez-Benito, J. F. Reduction of colloidal manganese dioxide by manganese(II). *J. Colloid Interface Sci.* **2002**, *248*, 130–135.
26. Morgan, J. J. Manganese in natural waters and earth's crust: Its availability to organisms. *Met. Ions Biol. Syst.* **2000**, *37*, 1–34.
27. Sparks, D. L. *Kinetics of Soil Chemical Processes*; Academic Press: San Diego, 1989; p xv, 210 pp.
28. Scheidegger, A. M.; Sparks, D. L. A critical assessment of sorption-desorption mechanisms at the soil mineral/water interface. *Soil Sci.* **1996**, *161*, 813–831.
29. Sparks, D. L. *Environmental Soil Chemistry*, 2nd ed.; Academic Press: San Diego, 2002.
30. Landrot, G.; Ginder-Vogel, M.; Sparks, D. L. Kinetics of chromium(III) oxidation by manganese(IV) oxides using quick scanning X-ray absorption fine structure spectroscopy (Q-XAFS). *Environ. Sci. Technol.* **2010**, *44*, 143–149.
31. Siebecker, M.; Li, W.; Khalid, S.; Sparks, D. Real-time QEXAFS spectroscopy measures rapid precipitate formation at the mineral-water interface. *Nat. Commun.* **2014**, *5003*, 1–7.
32. Ginder-Vogel, M.; Stewart, B. D.; Fendorf, S. Kinetic and mechanistic constraints on the oxidation of biogenic uraninite by ferrihydrite. *Environ. Sci. Technol.* **2010**, *44*, 163–169.
33. Sparks, D. L. Advances in the Use of Synchrotron Radiation to Elucidate Environmental Interfacial Reaction Processes and Mechanisms in the Earth's Critical Zone. In *Progress in Soil Science*; Xu, J., Sparks, D. L., Eds.; Springer Science + Business Media: Dordrecht, 2013; pp 93−114.
34. Fendorf, S. E.; Sparks, D. L.; Franz, J. A.; Camaioni, D. M. Electron paramagnetic resonance stopped-flow kinetic study of manganese (II) sorption-desorption on birnessite. *Soil Sci. Soc. Am. J.* **1993**, *57*, 57–62.
35. Dent, A. J. Development of time-resolved XAFS instrumentation for quick EXAFS and energy-dispersive EXAFS measurements on catalyst systems. *Top. Catal.* **2002**, *18*, 27–35.
36. Khalid, S.; Caliebe, W.; Siddons, P.; So, I.; Clay, B.; Lenhard, T.; Hanson, J.; Wang, Q.; Frenkel, A. I.; Marinkovic, N.; Hould, N.; Ginder-Vogel, M.; Landrot, G. L.; Sparks, D. L.; Ganjoo, A. Quick extended x-ray absorption fine structure instrument with millisecond time scale, optimized for in situ applications. *Rev. Sci. Instrum.* **2010**, *81*, 015105.

37. Mitsunobu, S.; Takahashi, Y.; Uruga, T. Observation of chemical reactions at the solid-water interface by quick XAFS combined with a column reactor. *Anal. Chem*. **2006**, *78*, 7040–7043.
38. Ginder-Vogel, M.; Sparks, D. L. The impacts of X-ray absorption spectroscopy on understanding soil processes and reaction mechanisms. In *Developments in Soil Science*; Balwant, S., Markus, G., Eds.; Elsevier: 2010; Vol. 34, pp 1−26.
39. Parikh, S. J.; Chorover, J. ATR-FTIR study of lipopolysaccharides at mineral surfaces. *Colloids Surf., B* **2008**, *62*, 188–198.
40. Lafferty, B. J.; Ginder-Vogel, M.; Sparks, D. L. Arsenite oxidation by a poorly-crystalline manganese oxide. 3. Arsenic and manganese desorption. *Environ. Sci. Technol*. **2011**, *45*, 9218–9223.
41. Parikh, S. J.; Lafferty, B. J.; Meade, T. G.; Sparks, D. L. Evaluating environmental influences on AsIII oxidation kinetics by a poorly crystalline Mn-oxide. *Environ. Sci. Technol*. **2010**, *44*, 3772–3778.
42. Jones, L. C.; Lafferty, B. J.; Sparks, D. L. Additive and competitive effects of bacteria and Mn oxides on arsenite oxidation kinetics. *Environ. Sci. Technol*. **2012**, *46*, 6548–6555.
43. Violante, A.; Pigna, M. Competitive sorption of arsenate and phosphate on different clay minerals and soils. *Soil Sci. Soc. Am. J*. **2002**, *66*, 1788–1796.
44. Luengo, C.; Brigante, M.; Antelo, J.; Avena, M. Kinetics of phosphate adsorption on goethite: Comparing batch adsorption and ATR-IR measurements. *J. Colloid Interface Sci*. **2006**, *300*, 511–518.
45. Roberts, D. R.; Scheidegger, A. M.; Sparks, D. L. Kinetics of mixed Ni-Al precipitate formation on a soil clay fraction. *Environ. Sci. Technol*. **1999**, *33*, 3749–3754.
46. Mihaljevic, M.; Ettler, V.; Sisr, L.; Sebek, O.; Strnad, L.; Vonaskova, V. Effect of low concentrations of phosphate ions on extraction of arsenic from naturally contaminated soil. *Bull. Environ. Contam. Toxicol*. **2009**, *83*, 422–427.
47. Sun, X. H.; Doner, H. E. Adsorption and oxidation of arsenite on goethite. *Soil Sci*. **1998**, *163*, 278–287.
48. Feng, X. J.; Simpson, A. J.; Simpson, M. J. Investigating the role of mineral-bound humic acid in phenanthrene sorption. *Environ. Sci. Technol*. **2006**, *40*, 3260–3266.
49. He, Y. T.; Hering, J. G. Enhancement of arsenic(III) sequestration by manganese oxides in the presence of iron(II). *Water, Air, Soil Pollut*. **2009**, *203*, 359–368.
50. Peterson, M. L.; Brown, G. E., Jr.; Parks, G. A. Direct XAFS evidence for heterogeneous redox reaction at the aqueous chromium/magnetite interface. *Colloids Surf., A* **1996**, *107*, 77–88.
51. Peterson, M. L.; Brown, G. E.; Parks, G. A.; Stein, C. L. Differential redox and sorption of Cr(III/VI) on natural silicate and oxide minerals: EXAFS and XANES results. *Geochim. Cosmochim. Acta* **1997**, *61*, 3399–3412.
52. Sparks, D. L. Kinetics of Soil Chemical Phenomena: Future Directions. In *Future Prospects for Soil Chemistry*; Huang, P. M., Sparks, D. L., Boyd, S. A., Eds.; SSSA: Madison, WI, 1998; Special Publication no. 55, pp 81−101.

53. Fendorf, S. E. Surface reactions of chromium in soils and waters. *Geoderma* **1995**, *67*, 55–71.
54. Gray, M. J.; Malati, M. A. The point of zero charge of manganese dioxides. *J. Electrochem.* **1978**, *89*, 135–140.
55. Fendorf, S. E.; Fendorf, M.; Sparks, D. L. Inhibitory mechanisms of Cr(III) oxidation by δ-MnO2. *J. Colloid Interface Sci.* **1992**, *153*, 37–54.
56. Eary, E.; Rai, D. Kinetics of chromium(III) oxidation to chromium(VI) by reaction with manganese dioxide. *Environ. Sci. Technol.* **1987**, *21*, 1187–193.
57. Manceau, A.; Charlet, L. X-ray adsorption spectroscopy study of the sorption of Cr(III) at the oxide-water interface. I. Molecular mechanism of Cr(III) oxidation on Mn Oxides. *J Colloid Interface Sci.* **1992**, *148*, 425–442.
58. Weaver, R. M.; Hochella, M. F. The reactivity of seven Mn-Oxides with Cr^{3+}_{aq}: a comparative analysis of a complex, environmentally important redox reaction. *Am. Mineral.* **2003**, *88*, 2016–2028.
59. Kim, J. G.; Dixon, J.; Chusui, C. C.; Deng, Y. Oxidation of chromium(III) to (VI) by manganese oxides. *Soil Sci. Soc. Am. J.* **2002**, *66*, 306–316.
60. Tang, Y.; Webb, S. W.; Estes, R. E.; Hansel, M. C. Chromium(III) oxidation by biogenic manganese oxides with varying structural ripening. *Enivron. Sci.: Processes Impacts* **2014**, *16*, 2127–2136.
61. Kim, J. G.; Moon, H. S. Oxidation of chromium (III) to chromium (VI) by a series of synthesized birnessites (δ-MnO2): kinetics and oxidation capacity. *Clay Sci.* **1998**, *10*, 363–374.
62. Johnson, A. C.; Xyla, A. G. The oxidation of chromium(III) to chromium(VI) on the surface of manganite (γ-MnOOH). *Geochim. Cosmochim. Acta* **1991**, *55*, 2861–2866.
63. Banerjee, D.; Nesbitt, H. W. Oxidation of aqueous Cr(III) at birnessite surfaces: constraints on reaction mechanism. *Geochim. Cosmochim. Acta* **1999**, *63*, 1671–1687.
64. Nico, P.; Zasoski, R. Importance of Mn(III) availability on the rate of Cr(III) oxidation on δ-MnO2. *Environ. Sci. Technol.* **2000**, *34*, 3363–3367.
65. Rai, D.; Sass, B.; Moore, D. Chromium(III) hydrolysis constants and solubility of chromium(III) hydroxide. *Inorg. Chem.* **1987**, *26*, 345–349.
66. Fendorf, S. E.; Zasoski, R. J. Chromium(III) oxidation by δ-MnO2 1. Characterization. *Environ. Sci. Technol.* **1992**, *26*, 79–85.
67. Feng, X. H.; Zhai, L. M.; Tan, W. F.; Zhao, W; Liu, F.; He, J. Z. The controlling effect of pH on oxidation of Cr(III) by manganese oxide minerals. *J. Colloid Interface Sci.* **2006**, *298*, 258–266.
68. Dai, R. A.; Liu, J.; Yu, C. Y.; Sun, R.; Lan, Y. Q.; Mao, D. J. A comparative study of oxidation of Cr(III) in aqueous ions, complex ions and insoluble compounds by manganese-bearing mineral (birnessite). *Chemosphere* **2009**, *76*, 536–541.
69. Landrot, G.; Ginder-Vogel, M.; Livi, K.; Fitts, J. P.; Sparks, D. L. Chromium(III) oxidation by three poorly-crystalline manganese(IV) oxides. 1. Chromium(III)-oxidizing capacity. *Environ. Sci. Technol.* **2012**, *46*, 11595–11600.

Chapter 2

Metal Contaminant Oxidation Mediated by Manganese Redox Cycling in Subsurface Environment

Zimeng Wang[1,*] and Daniel E. Giammar[2]

[1]Department of Civil and Environmental Engineering, Stanford University, Stanford, California 94305, United States
[2]Department of Energy, Environmental and Chemical Engineering, Washington University in St. Louis, St. Louis, Missouri 63130, United States
[*]E-mail: wangzm@stanford.edu

Mn oxides can oxidize a variety of metal contaminants in subsurface environments. Fundamental knowledge of the rates, mechanisms, and products of these oxidation reactions is critical to predicting the environmental fate and transport of these metals. This chapter reviews recent advances in characterizing the kinetics and molecular-scale mechanisms of metal oxidation by oxidized forms of Mn. Topics addressed include the dynamics of Mn oxide surface passivation, the mechanisms of solid-solid interactions, the potential importance of soluble Mn(III) species, and the catalytic role of Mn in some linked biotic-abiotic processes that result in metal oxidation. This review highlights the complexity of the coupling of the biogeochemical cycles of Mn and other elements. The Mn species responsible for contaminant metal oxidation goes beyond Mn oxides to also include reactive intermediate species. The chapter identifies future research that is needed to unravel the underlying mechanisms on a process level. Continuing research on metal oxidation by Mn oxides will support improved predictions of metal transport in the environment and aid in decision-making for treatment and remediation.

In Advances in the Environmental Biogeochemistry of Manganese Oxides; Sparks, et al.;
ACS Symposium Series; American Chemical Society: Washington, DC, 2015.

Introduction

Soils have an average manganese composition of 440 mg/kg with a range of 7-9000 mg/kg (*1*). Dissolved manganese concentrations in anoxic groundwater at circumneutral pH are typically in the range of 1–20 μM (0.05-1.0 mg/L). Manganese oxide minerals are ubiquitous in natural environments, and there are more than 30 known Mn(III), Mn(IV), or mixed Mn(III,IV) oxide/hydroxide minerals with various layer or tunnel structures (*2*). Hexagonal phyllomanganates (birnessite-group minerals, MnO_{2-x}, where x depends on the Mn(III) and Mn(II) fraction) are the dominant Mn oxides in natural aquatic systems (*3*).

Mn oxides occur in subsurface environments with redox gradients where soluble Mn(II) encounters dissolved oxygen. The occurrence of Mn oxides in subsurface environments is largely driven by Mn-oxidizing microorganisms (*23*). Phylogenetically diverse microorganisms (bacteria and fungi) that are widespread in nature can oxidize Mn(II) to Mn(III/IV) oxides. Through reactive oxygen species or enzymatic reactions, these microorganisms accelerate Mn(II) oxidation at rates that are orders of magnitude higher than by homogenous oxidation in aqueous solution or by abiotic catalysis on mineral surfaces (*23*, *24*). Even extremely low dissolved oxygen (<1 μM) concentrations can drive rapid Mn(II) oxidation (*25*, *26*). Biogenic manganese oxides are usually poorly crystalline minerals with high average Mn oxidation state (from 3.7 to 4.0) and high specific surface area (*27*). The properties and formation mechanisms of biogenic manganese oxides have been comprehensively reviewed by Tebo et al. (*23*).

The vast literature on the interactions between metals and Mn oxides describes the ways that Mn oxides can exert major geochemical influence as adsorbents and oxidants even if they are only present as minor constituents in the subsurface (*28*). (In this review we will use the term metal to describe metals as well as some metalloids). Their high specific surface areas and structures with highly reactive vacancy sites enable Mn oxides to adsorb metal cations such as Cu^{2+} (*29*), Pb^{2+} (*30*, *31*), Ni^{2+} (*32*) and UO_2^{2+} (*33*) by forming multidentate inner-sphere surface complexes (*34*). The adsorption reactions serve as important sequestration mechanisms for metal contaminants in the subsurface. Mn oxides can oxidize a number of metals from low to high oxidation states (e.g., Cr, U, As, Se, Tc, Np, Pu, Co, Sb) (Table 1). The oxidation of most metals leads to their transformation to more soluble and more weakly adsorbing species; important exceptions to this trend are As and Co. In addition to the concern of contaminant mobilization, oxidative transformation of the metals may also alter their toxicity. The metals in Table 1 represent those whose fate and transport in subsurface environments may be impacted by Mn oxides.

Given that microbial Mn oxidation occurs rapidly even at trace levels of O_2, in the redox transition zone where reduced forms of metal compounds may co-occur with active Mn oxidation, the oxidation of the metals may be catalytically mediated by a sustained cycling of Mn. Mn(II) is regenerated by the redox reaction between the reduced metal compound and Mn oxide (Figure 1). Only small amounts of Mn(II) are needed to maintain the coupled redox process as long as a supply of dissolved O_2 (even as low as 1 μM) is available. Many reduced metal compounds are not readily oxidized by O_2 due to kinetic limitations, for example Cr(III) (*7*) and

In Advances in the Environmental Biogeochemistry of Manganese Oxides; Sparks, et al.;
ACS Symposium Series; American Chemical Society: Washington, DC, 2015.

As(III) (*35*), whereas the presence of an active Mn oxidation process can promote the oxidation of metals due to the high reactivity of Mn oxides that are generated *in situ*.

Table 1. Illustrative oxidation reactions where Mn oxides act as oxidants

Metal(loid)	*Environmental Implications*	*Ref*
As (III to V)	Decrease As mobility by increasing its tendency for sorption and detoxify As(III)	(*4–6*)
Cr (III to VI)	Transform Cr from a benign and poorly soluble form to a mobile and more toxic species	(*7–9*)
U (IV to VI)	Dissolve U from an insoluble phase to highly mobile aqueous species	(*10–12*)
Co (II to III)	Transform to a less soluble phase, alter its bioavailability	(*13*, *14*)
Sb (III to V)	Transform Sb from a poorly soluble phase to a mobile phase. Sb(III) is more toxic than Sb(V)	(*15*, *16*)
Se (IV to VI)	Increase mobility. Adsorption of Se(VI) to minerals is relatively weak.	(*17*, *18*)
Tc (IV to VII)	Dissolve Tc from a less soluble phase to a more mobile aqueous species	(*19*, *20*)
Pu (IV, V to VI)	Dissolve Pu from a less soluble phase to highly mobile aqueous species	(*21*, *22*)

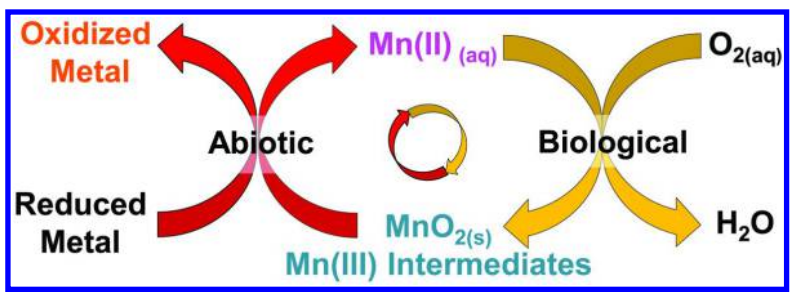

Figure 1. Biogeochemical coupling of Mn redox cycles with another redox sensitive metal in which the Mn serves in a catalytic role to accelerate reduced metal oxidation even at sustained low dissolved oxygen concentrations.

In this review we seek to provide the background needed to discuss several unresolved questions and issues in this field and to identify knowledge gaps that could be filled to yield a more holistic understanding of Mn biogeochemistry. The literature on metal oxidation by Mn oxides is vast, and we do not attempt to give a comprehensive element-by-element review. We review recent progress in characterizing the dynamics of interfacial redox reactions of metals on Mn oxides. An emerging body of literature on soluble Mn(III) species as potential geochemical oxidants is introduced. Combining literature and our recent research on uranium-manganese biogeochemical coupling, we discuss the mechanistic linkage of laboratory derived results on Mn-mediated metal oxidation to field environments.

Oxidation of Metal Contaminants by Mn Oxides

Mn oxides can oxidize a variety of metal contaminants under subsurface relevant conditions (Table 1), and previous reviews have assembled information on these processes (*38*, *39*). The redox couple of Mn(IV)/Mn(II) has such a high redox potential that the thermodynamics for metal oxidation by Mn oxides is almost always favorable (Figure 2). Any trace element whose boundary between oxidation states occurs below the region of dominance of Mn oxides can potentially be oxidized from its lower oxidation state to its higher oxidation state by Mn oxides. This broad range of favorable conditions for metal oxidation by Mn oxides is in contrast to the Fe(III)/Fe(II) couple. Although Fe(III) oxides or hydroxides can act as oxidants (electron acceptor) of metals, their ability to oxidize another metal is often limited by the marginal thermodynamic driving force (see Figure 2 at neutral pH for U and As). For example, thermodynamic calculations and experimental results (*40*, *41*) indicated that only ferrihydrite (not goethite or hematite) could oxidize U(IV) at circumneutral pH. Further the oxidation would cease if Fe(II) accumulates to approach the thermodynamic equilibrium state or if the system lacks dissolved inorganic carbon (a strong U(VI) complexant). In comparison, the thermodynamic favorability of metal oxidation by Mn oxides extends over a much wider range of water chemistry conditions (*11*). Therefore the oxidation rate of metals by Mn oxides is controlled by reaction kinetics and not by the overall energetic driving force. Generally layered Mn-oxide minerals (i.e., phyllomaganates) are more reactive than Mn oxides with tunnel structures (e.g., pyrolusite, romanechite) (*42*, *43*). With respect to the oxidation of metals by Mn oxides there are important questions regarding the passivation of Mn oxide surfaces and the oxidation of poorly soluble metals that we address in the following two sub-sections.

Passivation of Mn Oxides

Many previous experimental studies reported that during the reaction between Mn oxides and the reduced forms of metals, the oxidation initially proceeds rapidly but then is followed by a decrease in the oxidation rate. In those studies,

In Advances in the Environmental Biogeochemistry of Manganese Oxides; Sparks, et al.;
ACS Symposium Series; American Chemical Society: Washington, DC, 2015.

the significant decrease of the oxidation rate (*6*, *44*) could not be explained by the disappearance of the reactant or an approach to thermodynamic equilibrium. In completely mixed batch systems, the time at which a significant decrease in reaction rate occurred ranges from seconds to hours. While earlier reports about Mn oxide surface passivation were mostly based on macroscopic wet chemistry results (*45*, *46*), recent studies employed in-situ spectroscopic techniques with temporal resolution to quantify the molecular scale evolution of metal oxidation process on Mn oxides. Quick-scanning X-ray absorption spectroscopy (Q-XAS) is one of the significant innovations in characterizing the initial kinetics of metal oxidation at solid-water interfaces (*47*, *48*).

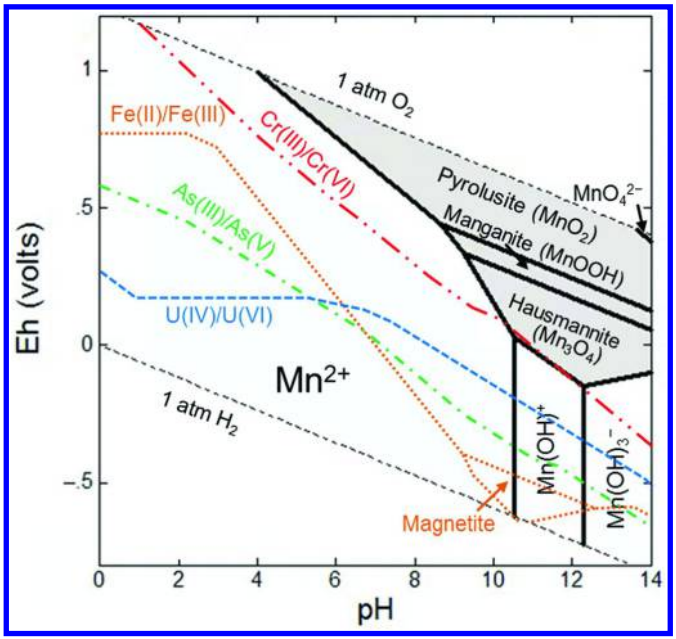

Figure 2. Eh-pH diagram of Mn and different oxidation state boundaries of selected redox sensitive elements. Any redox sensitive elements whose couple appears below the dominance area of Mn oxides can be oxidized from its lower oxidation state to its higher oxidation state by the Mn oxide. The redox couple of Fe(II)/Fe(III) was plotted for a comparison. Note that magnetite ($Fe^{II}(Fe^{III})_2O_4$) may persist in certain Eh and pH domains. The calculations for all the elements (including Mn) were for 10^{-8} M total concentration in pure water, 298.15 K, zero ionic strength and 1 atm. The calculations were conducted using the Act2 program of the Geochemist's Workbench (V8.0) (36). The thermodynamic database used was "thermo" for As, "thermo.com.v8.r6+" for Cr, Fe, and Mn. U specation was calculated using the constants from Guillaumont et al. (37). Suppressed minerals include bixbyite (Mn_2O_3) todorokite ($Mn_7O_{12}{\cdot}3H_2O$), and several minerals with average U oxidation state between +IV and +VI (UO_x, $2<x<3$).

In Advances in the Environmental Biogeochemistry of Manganese Oxides; Sparks, et al.;
ACS Symposium Series; American Chemical Society: Washington, DC, 2015.

The passivation of Mn oxide surfaces is usually believed to be caused by the retention of reaction products, including both the reduced Mn(II) and the oxidized metals (Figure 3, Table 2). In early studies, passivation of the Mn oxide surfaces was attributed to sorption of Mn(II) (*49*). The strong retention of Mn(II) on Mn oxides has been reported in numerous studies (*4*, *6*, *8*, *11*). The passivation of the Mn oxide surface by Mn(II) sorption is not simply a reversible reaction of forming surface complexes that cover the reactive Mn(IV) sites. For example, Mn oxides participating in the oxidation of Cr(III)-organic complexes were passivated by addition of Mn(II) but not of Zn(II); both Zn(II) and Mn(II) can form strong inner sphere surface complexes on Mn oxides (*50*), so the passivating effect was specific to Mn(II) (*51*). More evidence has been reported recently that the layered Mn oxides to which Mn(II) is adsorbed are not static phases, but instead they may undergo a cascade of reactions that gradually lead to Mn(III) and mixed Mn(II, III, IV) phases that include feitknechite (β-MnOOH), hausmannite (Mn_3O_4) and manganite (γ-MnOOH) (*34*, *52*). Although the complete transformation of birnessite to manganite was reported to take days, substantial formation of Mn(III) was observed on a time scale of hours (*34*, *53*), temporally accompanied by the passivation of birnessite reactivity.

The influence of Mn(III) on the reactivity of Mn oxides towards oxidizing metals appears to depend on the exact metal and conditions studied. Weaver and Hochella reported that Mn oxides with more Mn(III) were generally more reactive oxidants for Cr(III) (*42*). The seven different Mn oxide minerals tested in that study varied significantly in degree of crystallinity and overall mineral structure, and the Mn(III) contents originated from the different chemical preparation methods. A recent study by Landrot et al. observed an opposite trend in oxidation rates of aqueous Cr(III) by three birnessite-type Mn oxides with different Mn(III) contents (*44*). Their discussion implied that the conclusions by Weaver and Hochella might have been obscured by the significant differences in the surface charge and crystallinity of the Mn oxides. The passivating effect of increasing Mn(III) contents in Mn oxides has been complicated by apparent contradictions in the literature. Many studies, primarily in literature on As(III) oxidation, proposed that the Mn(III) sites on Mn oxide surfaces are less reactive than Mn(IV) sites (*54*, *57–59*). For example, Lafferty et al. used X-ray absorption spectroscopy (XAS) to characterize the evolution of Mn oxidation states and coordination environments in the As(III) oxidation process, and they found that the Mn(III) was likely formed by comproportionation of sorbed Mn(II) and Mn(IV) in the mineral structure (*54*). The formation of Mn(III) during the reduction of Mn(IV) in the Mn oxide structure was proposed as a passivation mechanism that is beyond the reversible sorption-based passivation induced by Mn(II) (*54*, *55*). Other publications report that the Mn(III) sites on phyllomanganate were critical for the oxidation of Cr(III), sulfide and phenol (*60*, *61*). An inhibitory effect of pyrophosphate, which preferentially binds to Mn(III) sites, on the oxidation rates was observed, and their conclusions were supported by kinetic modeling that incorporated both Mn(III) and Mn(IV) enabled pathways. Nevertheless, given the emerging evidence about the dynamics of Mn(II)-Mn(IV) oxide systems, their interpretation may not be applicable for the passivation process, in which the role of pyrophosphate in the formation of Mn(III) remains unknown.

In Advances in the Environmental Biogeochemistry of Manganese Oxides; Sparks, et al.;
ACS Symposium Series; American Chemical Society: Washington, DC, 2015.

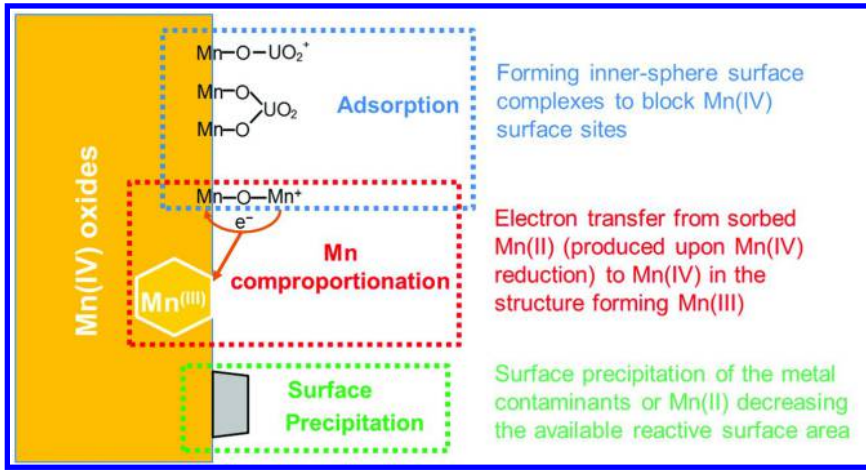

Figure 3. Illustration of possible mechanisms for Mn oxide surface passivation during the oxidation of metals. See details in Table 2 and references therein.

Table 2. Mn oxide passivation mechanisms reported in the literature

Major Passivation Mechanism(s)	*Reaction System*	*Source of Evidences*	*Ref*
Retention of Mn(II) on MnO_2 and subsequent transformation to Mn(III) by comproportionation.	δ-MnO_2 + $As(III)_{aq}$	X-ray absorption spectroscopy, stirred flow experiments	(*6*, *54*, *55*)
Precipitation of Cr(III) hydroxides that coat the MnO_2 surface.	δ-MnO_2 + $Cr(III)_{aq}$	Electron microscopy and diffraction	(*9*, *45*)
Precipitation of Mn carbonate on Mn oxide. The carbonate was accumulated as a microbial metabolite.	Birnessite + As(V) + bacteria + electron donor, in a diffusion limited reactor	X-ray diffraction and modeling	(*56*)
U(VI) adsorption to MnO_2, possibly also due to Mn(II) retention.	δ-MnO_2 + UO_2(s) in stirred flow reactor	Wet chemistry results and XAS	(*11*)

In addition to the passivation induced by Mn(II) produced when a Mn oxide oxidizes a metal, the oxidized metal could also passivate Mn oxide surfaces. The extent of the passivation may depend on the strength of the adsorption. For example, U(VI) forms strong inner-sphere surface complexes on birnessite-type mineral (*62*), and the reactivity of birnessite for oxidizing U(IV) was lower under conditions that favor U(VI) adsorption (e.g., low carbonate concentration) (*11*). Cr(VI) only weakly adsorbed to birnessite-type minerals as an outer-sphere

In Advances in the Environmental Biogeochemistry of Manganese Oxides; Sparks, et al.;
ACS Symposium Series; American Chemical Society: Washington, DC, 2015.

surface complex, which did not passivate the Mn oxide (*63*). In stirred flow experiments on As(III) oxidation by birnessite, the retention of As(V) at steady state was minor, suggesting that As(V) adsorption was not important for Mn oxide passivation (*6*). It may be a common theme that anionic oxidized species do not passivate birnessite-type minerals but cationic species could. Considering the low pH_{pzc} of birnessite-type minerals (usually < pH 2), adsorption of anionic species to highly negatively charged surfaces is expected to be weak.

Another less common but possible passivation mechanism is the precipitation of secondary phases that may block or impede the electron transfer. Mn(II)-arsenate may precipitate upon substantial oxidation of As(III) by Mn oxide (*57*). In environments enriched with carbonate, $MnCO_3$ (rhodochrosite) may also form surface precipitates on Mn oxides, slowing down the rates of oxidation reactions on the surface (*56*). A widely cited study by Fendorf et al. proposed a passivation mechanism due to Cr(III) hydroxide precipitation that was facilitated by the Mn oxide surface even when the bulk solution of Cr(III) was still undersaturated with respect to $Cr(OH)_{3(s)}$ (*9*, *45*). However, a recent study of Cr(III) oxidation by Mn oxides, which reported significant passivation of Mn oxide after 30 min, did not identify any evidence of a Cr surface precipitate, suggesting unknown mechanisms that warrant further study (*63*).

Forms of the Metal Being Oxidized: Aqueous versus Solid

The oxidation of metals on Mn oxides is believed to proceed by adsorption of the reduced metal species on the Mn oxide followed by electron transfer. The process is intuitive for those metals whose reduced forms are in a soluble phase. However, several metals have reduced forms (e.g., Cr(III), U(IV), Tc(IV)) with much lower solubility with respect to their oxides (or hydroxides) than their higher oxidation states (Cr(VI), U(VI), Tc(VI)). In subsurface environments without substantial metal-complexing ligands, solid phases of the reduced metal species may be dominant. Our understanding of redox reactions between insoluble Mn oxides and solid forms of metal contaminants is still emerging.

Only a few studies have investigated the oxidation of solid-state reduced metals by Mn oxides. Using well-mixed batch reactors, Oze et al. reported substantial oxidation and solubilization of Cr(III) in a chromite mineral ($FeCr_2O_4$) by birnessite (*7*), although chromite was traditionally considered as a stable and non-reactive Cr-containing phase. Field evidence supports the oxidation of Cr(III) minerals by Mn (hydr)oxides (*64*, *65*). The importance of the Mn oxide driven oxidation of the insoluble metal-containing minerals depends on the extent of physical contact or proximity of the two different solids. With poorly soluble uraninite (UO_2) and δ-MnO_2 in an abiotic system, our recent study (*11*) used a multichamber reactor with a permeable membrane to explore UO_2 oxidation when direct solid contact with the Mn oxide was eliminated but diffusion of dissolved species across the membrane was possible. The results indicated that physical contact between the two minerals was required for effective oxidation of UO_2 by Mn oxide. A model that consider the dissolution kinetics of $UO_{2(s)}$ and the transport of dissolved U across the membrane suggested that if Mn oxide is not allowed to contact UO_2, then the Mn oxide could only act to take up (and oxidize)

a limited pool of dissolved U(IV) that is mobilized into the bulk solution. Plathe et al. confirmed the lack of Mn oxide-induced UO_2 oxidation in agarose gels where the two different oxides were physically separated in a porous medium with virtually no direct contact (*66*). In completely mixed systems, the region near the contact points between UO_2 and MnO_2 are very likely the predominant location where the redox reactions take place (*11*). Nevertheless, little is known about the intrinsic mechanism governing reactions in the microscopic interface zones. It may be possible that the reactions between UO_2 and MnO_2 are still mediated by transport of aqueous species. These intermediates (U(IV) and/or reactive Mn species) could be in the form of dissolved species or molecular clusters, which might be highly reactive with short life times that would not allow them to be effectively mobilized into the bulk solution.

In subsurface environments, there are several scenarios through which the reduced metal in a low solubility mineral could interact with Mn oxides. Because Mn oxides can be biologically produced from two soluble and mobile reactants, Mn(II) and O_2, the Mn oxides could be directly produced on or in close proximity to a metal-containing mineral (*67*). Depending on the formation mechanisms and aging conditions, the reduced metal minerals may be in the form of mobile nanometer-sized particles (*68*) that could be transported into close proximity of Mn oxides. In the presence of complexing ligands, the solid-solid interaction may be able to circumvent the physical contact barrier through the generation of soluble species of the reduced metal. Organic ligands (such as those with hydroxamate and carboxylate functional groups) are known to mobilize U(IV) and Cr(III) from poorly soluble minerals (e.g., UO_2 and $Cr(OH)_3$) (*69–73*). Experimental studies indicated that Mn oxides are capable of oxidizing the resulting metal complexes (*51*, *74*, *75*). Although it is unlikely that any Mn(IV) will be mobilized into the solution, it is possible that certain ligands could stabilize soluble Mn(III) that may then serve as a mobile oxidant (*76*). This scenario is examined further in the next section.

Because the solid-solid interaction involves multiple processes and is impacted by the physical properties of the particles, it is challenging to develop kinetic models that consider every reaction. Following a more pragmatic approach, studies have modeled the reaction between Mn oxides (as well as iron oxides) and another metal mineral using rate laws with individual solid concentrations as the controlling parameters (e.g., $r = k[MnO_2]^x[UO_2]^y$) (*7*, *10*, *77*, *78*). The apparent kinetic orders (i.e., x and y) were reported to be less than one (*10*, *77*), and they can differ significantly between Mn oxide and the other mineral (*7*). We recently proposed an alternative conceptual model of the kinetics of solid-solid reaction by considering the availability of surface area for the required physical contacts (*76*), which may be used to interpret the fractional kinetic orders observed in previous studies (*7*, *10*, *77*).

Metal Oxidation by Dissolved Mn(III) Complexes

It has long been known that free Mn(III) ions rapidly disproportionate to form Mn(II) and MnO_2, although soluble Mn(III) could be made stable at extremely low

In Advances in the Environmental Biogeochemistry of Manganese Oxides; Sparks, et al.;
ACS Symposium Series; American Chemical Society: Washington, DC, 2015.

pH or through complexation with high affinity ligands (*79*). The environmental occurrence of soluble Mn(III) has only recently been acknowledged. Studies at environmentally relevant conditions suggested that ligand-stabilized Mn(III) species may occur as intermediates of Mn oxidation (*80–82*) or reduction (*83*, *84*) and as ligand-promoted dissolution products of Mn(III)-containing minerals (e.g., MnOOH) (*85–87*). The Mn(III)-complexing ligands, such as pyrophosphate (*88*), siderophores (*86*, *89*), oxalate, and citrate are widely present in natural aquatic environments, particularly in rhizosphere soil environments. Because many of the Mn(III) ligands have biological origins, their presence may also be possible in sites that received organic electron donor addition as part of a bioremediation strategy. More recent evidence of aqueous Mn(III) in suboxic marine environments (*90*, *91*) and estuary sediment porewaters (*91*, *92*) highlighted that Mn(III) can constitute a large fraction of the dissolved Mn pool at oxic/anoxic interfaces. Beyond the oxidation induced by Mn oxides, a holistic understanding of metal contaminant oxidation mediated by Mn redox cycling should include an evaluation of the role of soluble Mn(III) species. Although Mn(III) species have been anticipated as a potential environmental oxidant, their reactivity and kinetic characteristics are not fully appreciated or understood. From the limited number of publications on Mn(III) environmental chemistry, it appears that the reactivity of Mn(III) depends on the exact ligand and the nature of its coordination with the Mn(III). A recent study (*93*) demonstrated that the oxidative decomposition of carbadox ($C_{11}H_{10}N_4O_4$) by MnO_2 could be dramatically accelerated by addition of oxalate, in which the redox reaction between MnO_2 and oxalate produced soluble Mn(III) stabilized by excess oxalate. Soluble Mn(III) was also reported to be able to oxidize Fe(II), sulfide, and Cr(III) (*94–96*). However, other studies have suggested that soluble Mn(III) pyrophosphate complexes could not readily oxidize Cr(III) unless MnO_2 was formed from disproportionation (*14*, *97*, *98*). Therefore, it is important to identify the chemical factors that control the reactivity of soluble Mn(III) complexes.

Our recent study evaluated the kinetics of UO_2 oxidation by soluble Mn(III) complexes stabilized by pyrophosphate and desferrioxamine B (DFOB) (*76*) (Figure 4). The Mn(III)-pyrophosphate complex was a potent oxidant that induced fast UO_2 oxidative dissolution at a rate higher than by a comparable concentration of dissolved O_2. However, the Mn(III)-DFOB complex was not able to oxidize U(IV). The contrasting results suggested the critical effect of Mn(III) coordination environment (e.g., structural hindrance) on its oxidizing potency (Figure 4c and d). Redox potential calculations indicated that the inertness of Mn(III)-DFOB with respect to UO_2 oxidation was not merely due to a lower thermodynamic driving force, but also related to unfavorable kinetic pathways. The hexadentate coordination of Mn(III) by the three hydroxamate groups of the DFOB molecule may limit the ability of the Mn(III) complex to associate with UO_2 surface to enable electron transfer. The reactivity of soluble Mn(III) was higher at lower ratios of pyrophosphate to Mn(III) and lower pH, which is probably related to differences in the ligand-to-metal coordination number and/or protonation states of the Mn(III)-pyrophosphate complexes (Figure 4c).

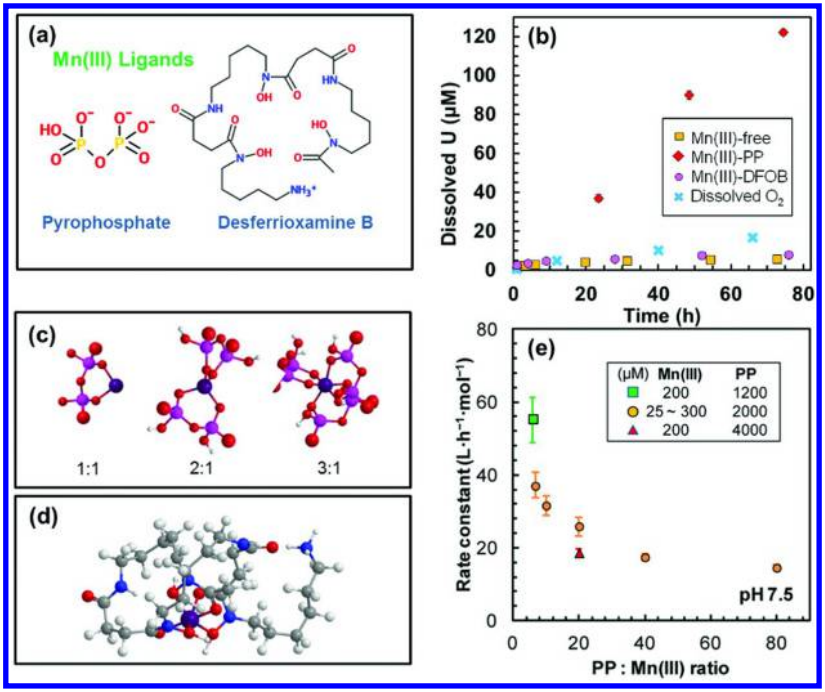

Figure 4. Oxidation of UO_2 by soluble Mn(III) complexes. (a) Structures of pyrophosphate and DFOB as their dominant species at circumneutral pH, (b) Comparison of UO_2 oxidation kinetics for different oxidants at a concentration about 300 μM. (c) Speculated speciation of Mn(III)-pyrophosphate complexes as the pyrophosphate to Mn(III) ratio increases. (d) Molecular structure of Mn(III)-DFOB, (e) Second order rate constants for Mn(III)-UO_2 reaction at different pyrophosphate : Mn(III) ratios. Modified from (76). (Reproduced by permission of American Chemical Society) Panels c and d were prepared with ChemOffice.

Our recent results highlighted the delicate balance that governs the significance of soluble Mn(III) in biogeochemical redox processes. On the one hand, ligands can facilitate the mobilization of Mn(III), which may circumvent the physical contact barrier separating Mn oxides and the reduced metal mineral (*11*). Given the discovery of Mn(III) as a geochemical oxidant, metal oxidation may not necessarily go through the adsorption and subsequent electron transfer on Mn oxide surfaces, but also can happen in aqueous phase or on the surface of the reduced metal mineral. On the other hand, too strong (possibly with steric hindrance) of Mn(III) complexation (e.g., by DFOB) can make the Mn(III) inert with respect to heterogeneous electron transfer. The contrasting behaviors of Mn(III) reactivity are dictated by the different binding strengths of the ligands.

There is still a significant knowledge gap regarding the environmental occurrence, chemical speciation, redox activity and biological roles of aqueous Mn(III) complexes. The stoichiometry and protonation level of Mn(III) complexes with important ligands remain largely speculative. Preliminary understanding of the Mn(III)-pyrophosphate speciation was made possible by capillary electrophoresis (*99*, *100*). The stability of Mn(III) complexes (against disproportionation or dissociation) is also critical to water chemistry and the identity of the ligands (*89*). Solution pH is a very sensitive factor that determines the oxidizing reactivity and stability of Mn(III) complexes. For redox active organic ligands, acidic pH can induce intramolecular electron transfer from the organic ligand to the Mn(III), leading to the oxidation of the organic compound (*81*). In addition to those studied in laboratory, Mn(III) ligands in natural and engineered aquatic environments include a large (and uncharacterized) family of biogenic siderophore compounds and their breakdown products and a variety of phosphonate- and carboxylate-based synthetic chelators that may be introduced as pharmaceuticals, scale inhibitors, and herbicides (*85*, *101*). Luther et al. used a novel kinetic approach to evaluate the overall binding strength of Mn(III) in sediment porewater samples, and found that the natural Mn(III) ligands exhibit a strength that is stronger than pyrophosphate and weaker than DFOB, as reflected by the complex dissociation rates when they were challenged by a high-affinity porphyrin ligand (*102*). With the emerging evidence of its presence in environments with oxic/anoxic interfaces, soluble Mn(III) may be more important than previously thought in the coupling of Mn redox cycling to the oxidation of metal contaminants.

Catalytic Role of Mn Redox Cycling on Metal Oxidation

Our appreciation of a major geochemical influence of Mn even when only present as a minor constituent has been based on the large specific surface area and the reactivity of Mn oxide minerals. In recent years, experimental evidence suggests a catalytic role of Mn redox cycling on metal oxidation that may also contribute to its strong impact on geochemical processes when only present at low concentrations (*14*, *67*, *103–107*). Even at low dissolved oxygen concentrations, oxidation of Mn(II) is thermodynamically favorable and can be catalyzed by ubiquitous Mn-oxidizing microorganisms (*23*) and mineral surfaces (*24*, *108*). Mn(II) oxidation to Mn(III) or Mn(IV) species may provide oxidants that are kinetically more reactive than molecular oxygen. There is evidence that freshly precipitated biogenic MnO_2 may have higher reactivity than aged oxides (*109*), which may also explain why the metal oxidation was faster in the presence of active biological Mn oxidation. Because the Mn is recycled back to Mn oxides, only small amounts of Mn (as low as several μM) are needed to sustain the coupled redox process as long as a supply of dissolved O_2 is maintained (Figure

In Advances in the Environmental Biogeochemistry of Manganese Oxides; Sparks, et al.;
ACS Symposium Series; American Chemical Society: Washington, DC, 2015.

1). For example, Mn oxides are known to be the only mineral that can oxidize Cr(III) to Cr(VI) under circumneutral pH, and the oxidation by O_2 was kinetically limited (*7*). In our work, UO_2 oxidation was much faster when O_2 was present together with a low concentration of Mn(II) and a Mn-oxidizing bacterium compared with O_2 alone (*67*).

While the catalytic effect of Mn cycling on metal oxidation was first observed in the presence of biological Mn oxidation (*14*, *67*, *107*), several recent studies reported the same catalytic effect in abiotic systems. Namgung et al. observed substantial $Cr(OH)_3$ oxidation when Mn(II) was spiked in under oxic condition (*105*). In their study, Mn oxide, identified as hausmannite, accumulated rapidly and was suggested to be the responsible oxidant for Cr(III). We recently reported that at pH 8 under oxic conditions, Mn(II) could accelerate UO_2 oxidation without formation of any particulate Mn species (pragmatically defined as those that could be retained by a 20 nm filter), which confirmed rapid abiotic redox cycling of Mn (*104*).

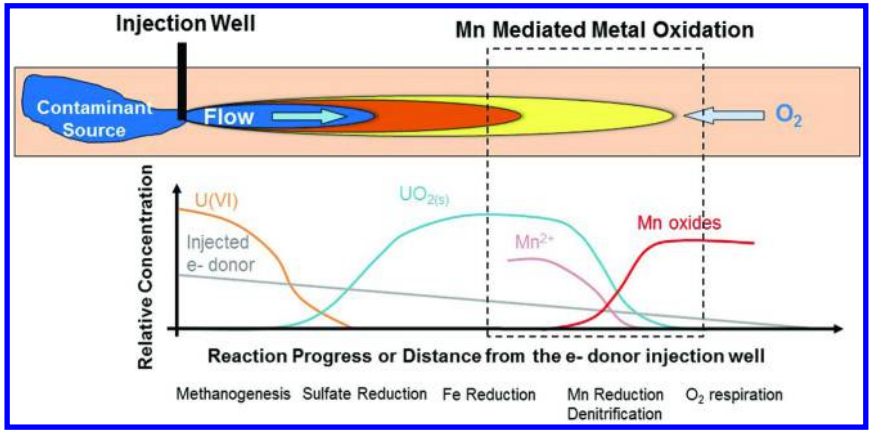

Figure 5. Generic profiles of key redox species in a groundwater plume contaminated with a hypothetical metal (in its oxidized, soluble form) that is being treated by organic electron donor to stimulate microbial activities for in situ remediation. The x-axis represents the evolution of redox condition after the cessation of electron donor injection. For simplicity, the redox sequences of sulfur and iron are not shown. The redox transition zone where Mn-U redox coupling could take place is indicated by the dashed box, where the soluble Mn(II) accumulated upon the reducing condition starts to meet low concentrations of O_2 at the fringes of the more reduced zone. The curves are all for illustrative purposes without quantitative indication.

In Advances in the Environmental Biogeochemistry of Manganese Oxides; Sparks, et al.;
ACS Symposium Series; American Chemical Society: Washington, DC, 2015.

The catalytic mechanism of redox cycling on the oxidation of metal contaminants may be a concern for the long term effectiveness of reductive remediation efforts (Figure 5). Many metal (or metalloid) contaminants (e.g., uranium, chromium, selenium, plutonium and technetium) have orders of magnitude lower solubility in their reduced forms than in their oxidized ones. Delivery of electron donor can facilitate abiotic and biological processes that lead to reductive immobilization of oxidized forms of these contaminants. Once the electron donor supply ceases, insoluble metal species can be reoxidized by various oxidants, including oxygen that reenters the reducing zone (Figure 1). The Mn-mediated metal oxidation processes are expected to occur at redox transition zones, such as at the interfaces of moving or shrinking anoxic groundwater plumes with oxic groundwater at the plume margins. Pinpointing locations where these conditions occur will be crucial to designing optimal remediation strategies for contaminated sites. A pragmatic implication to the design of field remediation strategies is that peripheral and down-field extraction wells and above-ground scrubber systems may need to be implemented to remove Mn(II) for the purposes of protecting the remediated product.

Conclusions

Our understanding of the oxidation of metal contaminants by oxidized Mn species continues to develop as a complex set of biogeochemical processes across multiple scales. The net result of metal oxidation is an excellent example of coupled biological and abiotic processes; Mn oxides are produced in the environment almost entirely by microorganisms, and oxidation of the metal by the Mn oxide proceeds through rapid abiotic reactions. The cycling of Mn between Mn(II) and oxidized forms in this abiotic-biotic process may be one reason that Mn exerts an influence on environmental geochemistry even when Mn is a minor constituent. Rates of metal oxidation by Mn oxides are influenced by both products of the reaction, the oxidized metal species and the Mn(II). The dynamics of Mn(II) interactions with Mn oxides are complex with the transformation of Mn oxides into Mn(III)-containing solids that may be either more or less reactive than the original Mn oxide. Soluble Mn(III) species can also play a significant role in metal oxidation with their recent observation in environmental redox transition zones and laboratory studies of their reaction kinetics with low solubility forms of oxidizable metal contaminants. Important knowledge gaps make Mn-mediated oxidation of metal contaminants a rich area for continuing research. Major knowledge gaps include the occurrence and reactivity of soluble Mn(III) species, the impact of Mn(II)-Mn oxide dynamics on the reactivity of the resulting solids, and the extent to which processes observed in the laboratory may be influencing the behavior of metals at field sites. These knowledge gaps can be filled by research that advances understanding of molecular-scale mechanisms while probing field-scale systems. Ongoing research will benefit from recent developments in interdisciplinary collaborations that integrate microbiological and geochemical expertise and apply the most advanced analytical techniques.

In Advances in the Environmental Biogeochemistry of Manganese Oxides; Sparks, et al.;
ACS Symposium Series; American Chemical Society: Washington, DC, 2015.

Acknowledgments

Our own research on Mn oxides was performed with the support of the U.S. Department of Energy, Office of Science, Subsurface Biogeochemical Research Program under Grant no. DE-SC0005324. We are grateful to Brad Tebo, José Manuel Cerrato, John Bargar, Rizlan Bernier-Latmani, Sung-Woo Lee, and Kelly Plathe for valuable discussions. Comments and suggestions of three anonymous reviewers were helpful for improving an early version of this manuscript.

References

1. Emsley, J. Manganese. In *Nature's building blocks : an A-Z guide to the elements*; Oxford University Press: Oxford, New York, 2003; pp 249−253.
2. Post, J. E. Manganese oxide minerals: Crystal structures and economic and environmental significance. *Proc. Natl. Acad. Sci. U. S. A.* **1999**, *96*, 3447–3454.
3. Villalobos, M.; Bargar, J.; Sposito, G. Trace metal retention on biogenic manganese oxide nanoparticles. *Elements* **2005**, *1*, 223–226.
4. Manning, B. A.; Fendorf, S. E.; Bostick, B.; Suarez, D. L. Arsenic(III) oxidation and arsenic(V) adsorption reactions on synthetic birnessite. *Environ. Sci. Technol.* **2002**, *36*, 976–981.
5. Han, X.; Li, Y. L.; Gu, J. D. Oxidation of As(III) by MnO_2 in the absence and presence of Fe(II) under acidic conditions. *Geochim. Cosmochim. Acta* **2011**, *75*, 368–379.
6. Lafferty, B. J.; Ginder-Vogel, M.; Sparks, D. L. Arsenite oxidation by a poorly crystalline manganese-oxide 1. Stirred-flow experiments. *Environ. Sci. Technol.* **2010**, *44*, 8460–8466.
7. Oze, C.; Bird, D. K.; Fendorf, S. Genesis of hexavalent chromium from natural sources in soil and groundwater. *Proc. Natl. Acad. Sci. U. S. A.* **2007**, *104*, 6544–6549.
8. Eary, L. E.; Rai, D. Kinetics of chromium(III) oxidation to chromium(VI) by reaction with manganese dioxide. *Environ. Sci. Technol.* **1987**, *21*, 1187–1193.
9. Fendorf, S. E.; Zasoski, R. J. Chromium(III) oxidation by δ-MnO_2. 1. Characterization. *Environ. Sci. Technol.* **1992**, *26*, 79–85.
10. Liu, C. X.; Zachara, J. M.; Fredrickson, J. K.; Kennedy, D. W.; Dohnalkova, A. Modeling the inhibition of the bacterial reduction of U(VI) by β-$MnO_{2(s)}$. *Environ. Sci. Technol.* **2002**, *36*, 1452–1459.
11. Wang, Z.; Lee, S.-W.; Kapoor, P.; Tebo, B. M.; Giammar, D. E. Uraninite oxidation and dissolution induced by manganese oxide: A redox reaction between two insoluble minerals. *Geochim. Cosmochim. Acta* **2013**, *100*, 24–40.
12. Fredrickson, J. K.; Zachara, J. M.; Kennedy, D. W.; Liu, C.; Duff, M. C.; Hunter, D. B.; Dohnalkova, A. Influence of Mn oxides on the reduction of uranium(VI) by the metal-reducing bacterium *Shewanella putrefaciens*. *Geochim. Cosmochim. Acta* **2002**, *66*, 3247–3262.

13. Crowther, D. L.; Dillard, J. G.; Murray, J. W. The mechanisms of Co(II) oxidation on synthetic birnessite. *Geochim. Cosmochim. Acta* **1983**, *47*, 1399–1403.
14. Murray, K. J.; Tebo, B. M. Cr(III) is indirectly oxidized by the Mn(II)-oxidizing bacterium *Bacillus* sp strain SG-1. *Environ. Sci. Technol.* **2007**, *41*, 528–533.
15. Belzile, N.; Chen, Y.-W.; Wang, Z. Oxidation of antimony (III) by amorphous iron and manganese oxyhydroxides. *Chem. Geol.* **2001**, *174*, 379–387.
16. Wang, X.; He, M.; Lin, C.; Gao, Y.; Zheng, L. Antimony (III) oxidation and antimony (V) adsorption reactions on synthetic manganite. *Chem. Erde-Geochem.* **2012**, *72*, 41–47.
17. Scott, M. J.; Morgan, J. J. Reactions at oxide surfaces. 2. Oxidation of Se (IV) by synthetic birnessite. *Environ. Sci. Technol.* **1996**, *30*, 1990–1996.
18. Banerjee, D.; Nesbitt, H. W. XPS study of reductive dissolution of birnessite by H_2SeO_3 with constraints on reaction mechanism. *Am. Mineral.* **2000**, *85*, 817–825.
19. Jaisi, D. P.; Dong, H.; Plymale, A. E.; Fredrickson, J. K.; Zachara, J. M.; Heald, S.; Liu, C. Reduction and long-term immobilization of technetium by Fe(II) associated with clay mineral nontronite. *Chem. Geol.* **2009**, *264*, 127–138.
20. Fredrickson, J. K.; Zachara, J. M.; Kennedy, D. W.; Kukkadapu, R. K.; McKinley, J. P.; Heald, S. M.; Liu, C.; Plymale, A. E. Reduction of TcO_4^- by sediment-associated biogenic Fe(II). *Geochim. Cosmochim. Acta* **2004**, *68*, 3171–3187.
21. Tanaka, K.; Suzuki, Y.; Ohnuki, T. Sorption and oxidation of tetravalent plutonium on Mn oxide in the presence of citric acid. *Chem. Lett.* **2009**, *38*, 1032–1033.
22. Morgenstern, A.; Choppin, G. R. Kinetics of the oxidation of Pu(IV) by manganese dioxide. *Radiochim. Acta* **2002**, *90*, 69–74.
23. Tebo, B. M.; Bargar, J. R.; Clement, B. G.; Dick, G. J.; Murray, K. J.; Parker, D.; Verity, R.; Webb, S. M. Biogenic manganese oxides: Properties and mechanisms of formation. *Annu. Rev. Earth Planet. Sci.* **2004**, *32*, 287–328.
24. Morgan, J. J. Kinetics of reaction between O_2 and Mn(II) species in aqueous solutions. *Geochim. Cosmochim. Acta* **2005**, *69*, 35–48.
25. Clement, B. G.; Luther, G. W.; Tebo, B. M. Rapid, oxygen-dependent microbial Mn(II) oxidation kinetics at sub-micromolar oxygen concentrations in the Black Sea suboxic zone. *Geochim. Cosmochim. Acta* **2009**, *73*, 1878–1889.
26. Tebo, B. M. Manganese(II) oxidation in the suboxic zone of the Black-Sea. *Deep-Sea Res.* **1991**, *38*, S883–S905.
27. Villalobos, M.; Toner, B.; Bargar, J.; Sposito, G. Characterization of the manganese oxide produced by *pseudomonas putida* strain MnB1. *Geochim. Cosmochim. Acta* **2003**, *67*, 2649–2662.
28. Borch, T.; Kretzschmar, R.; Kappler, A.; Van Cappellen, P.; Ginder-Vogel, M.; Voegelin, A.; Campbell, K. Biogeochemical redox processes and

their impact on contaminant dynamics. *Environ. Sci. Technol.* **2010**, *44*, 15–23.
29. Sherman, D. M.; Peacock, C. L. Surface complexation of Cu on birnessite (δ-MnO_2): Controls on Cu in the deep ocean. *Geochim. Cosmochim. Acta* **2010**, *74*, 6721–6730.
30. Kwon, K. D.; Refson, K.; Sposito, G. Surface complexation of Pb(II) by hexagonal birnessite nanoparticles. *Geochim. Cosmochim. Acta* **2010**, *74*, 6731–6740.
31. Villalobos, M.; Bargar, J.; Sposito, G. Mechanisms of Pb(II) sorption on a biogenic manganese oxide. *Environ. Sci. Technol.* **2005**, *39*, 569–576.
32. Zhu, M.; Ginder-Vogel, M.; Sparks, D. L. Ni(II) sorption on biogenic Mn-oxides with varying Mn octahedral layer structure. *Environ. Sci. Technol.* **2010**, *44*, 4472–4478.
33. Han, R.; Zou, W.; Wang, Y.; Zhu, L. Removal of uranium(VI) from aqueous solutions by manganese oxide coated zeolite: discussion of adsorption isotherms and pH effect. *J. Environ. Radioact.* **2007**, *93*, 127–143.
34. Elzinga, E. J. Reductive transformation of birnessite by aqueous Mn(II). *Environ. Sci. Technol.* **2011**, *45*, 6366–6372.
35. Han, X.; Li, Y.-L.; Gu, J.-D. Abiotic oxidation of Mn(II) and its effect on the oxidation of As(III) in the presence of nano-hematite. *Ecotoxicology* **2012**, *21*, 1753–1760.
36. Bethke, C. M.; Yeakel, S. *The Geochemist's Workbench, Release 8.0 GWB Essentials Guide*; Hydrogeology Program, University of Illinois: 2010.
37. Guillaumont, R.; Fanghänel, T.; Fuger, J.; Grenthe, I.; Neck, V.; Palmer, D. A.; Rand, M. H., *Update on the Chemical Thermodynamics of Uranium, Neptunium, Plutonium, Americium and Technetium*; Elsevier: Washington, DC, 2003.
38. Hem, J. D. Redox processes at surfaces of manganese oxide and their effects on aqueous metal ions. *Chem. Geol.* **1978**, *21*, 199–218.
39. Gounot, A. M. Microbial oxidation and reduction of manganese: consequences in groundwater and applications. *FEMS Microbiol. Rev.* **1994**, *14*, 339–349.
40. Ginder-Vogel, M.; Criddle, C. S.; Fendorf, S. Thermodynamic constraints on the oxidation of biogenic UO_2 by Fe(III) (hydr)oxides. *Environ. Sci. Technol.* **2006**, *40*, 3544–3550.
41. Du, X.; Boonchayaanant, B.; Wu, W. M.; Fendorf, S.; Bargar, J.; Criddle, C. S. Reduction of uranium(VI) by soluble iron(II) conforms with thermodynamic predictions. *Environ. Sci. Technol.* **2011**, *45*, 4718–4725.
42. Weaver, R. M.; Hochella, M. F. The reactivity of seven Mn-oxides with Cr^{3+} aq: A comparative analysis of a complex, environmentally important redox reaction. *Am. Mineral.* **2003**, *88*, 2016–2027.
43. Oscarson, D. W.; Huang, P. M.; Liaw, W. K.; Hammer, U. T. Kinetics of oxidation of arsenite by various manganese dioxides. *Soil Sci. Soc. Am. J.* **1983**, *47*, 644–648.
44. Landrot, G.; Ginder-Vogel, M.; Livi, K.; Fitts, J. P.; Sparks, D. L. Chromium(III) Oxidation by Three Poorly-Crystalline Manganese(IV)

Oxides. 1. Chromium(III)-Oxidizing Capacity. *Environ. Sci. Technol.* **2012**, *46*, 11594–11600.
45. Fendorf, S. E.; Fendorf, M.; Sparks, D. L.; Gronsky, R. Inhibitory Mechanisms of Cr(III) Oxidation by Delta-MnO_2. *J. Colloid Interface Sci.* **1992**, *153*, 37–54.
46. Oscarson, D.; Huang, P.; Liaw, W. Role of manganese in the oxidation of arsenite by freshwater lake sediments. *Clays Clay Miner.* **1981**, *29*, 219–225.
47. Sparks, D. Advances in coupling of kinetics and molecular scale tools to shed light on soil biogeochemical processes. *Plant Soil* **2014**, *387*, 1–19.
48. Sparks, D., Advances in the Use of Synchrotron Radiation to Elucidate Environmental Interfacial Reaction Processes and Mechanisms in the Earth's Critical Zone. In *Molecular Environmental Soil Science*; Xu, J.; Sparks, D. L., Eds.; Springer: The Netherlands: 2013; pp 93−114.
49. Scott, M. J.; Morgan, J. J. Reactions at oxide surfaces. 1. Oxidation of As(III) by synthetic birnessite. *Environ. Sci. Technol.* **1995**, *29*, 1898–1905.
50. Toner, B.; Manceau, A.; Webb, S. M.; Sposito, G. Zinc sorption to biogenic hexagonal-birnessite particles within a hydrated bacterial biofilm. *Geochim. Cosmochim. Acta* **2006**, *70*, 27–43.
51. Carbonaro, R. F.; Stone, A. T. Oxidation of Cr^{III} aminocarboxylate complexes by hydrous manganese oxide: products and time course behaviour. *Environ. Chem.* **2014**, *12*, 33–51.
52. Lefkowitz, J. P.; Rouff, A. A.; Elzinga, E. J. Influence of pH on the reductive transformation of birnessite by aqueous Mn(II). *Environ. Sci. Technol.* **2013**, *47*, 10364–10371.
53. Lefkowitz, J. P.; Elzinga, E. J. Impacts of aqueous Mn(II) on the sorption of Zn(II) by hexagonal birnessite. *Environ. Sci. Technol.* **2015**, *49*, 4886–4893.
54. Lafferty, B. J.; Ginder-Vogel, M.; Zhu, M. Q.; Livi, K. J. T.; Sparks, D. L. Arsenite oxidation by a poorly crystalline manganese-oxide. 2. Results from X-ray absorption spectroscopy and X-ray diffraction. *Environ. Sci. Technol.* **2010**, *44*, 8467–8472.
55. Lafferty, B. J.; Ginder-Vogel, M.; Sparks, D. L. Arsenite oxidation by a poorly-crystalline manganese oxide. 3. Arsenic and manganese desorption. *Environ. Sci. Technol.* **2011**, *45*, 9218–9223.
56. Ying, S. C.; Kocar, B. D.; Griffis, S. D.; Fendorf, S. Competitive microbially and Mn oxide mediated redox processes controlling arsenic speciation and partitioning. *Environ. Sci. Technol.* **2011**, *45*, 5572–5579.
57. Tournassat, C.; Charlet, L.; Bosbach, D.; Manceau, A. Arsenic(III) oxidation by birnessite and precipitation of manganese(II) arsenate. *Environ. Sci. Technol.* **2002**, *36*, 493–500.
58. Nesbitt, H. W.; Canning, G. W.; Bancroft, G. M. XPS study of reductive dissolution of 7Å-birnessite by H_3AsO_3, with constraints on reaction mechanism. *Geochim. Cosmochim. Acta* **1998**, *62*, 2097–2110.
59. Zhu, M. Q.; Paul, K. W.; Kubicki, J. D.; Sparks, D. L. Quantum chemical study of arsenic (III, V) adsorption on Mn-oxides: Implications for arsenic(III) oxidation. *Environ. Sci. Technol.* **2009**, *43*, 6655–6661.
60. Nico, P. S.; Zasoski, R. J. Importance of Mn(III) availability on the rate of Cr(III) oxidation on δ-MnO_2. *Environ. Sci. Technol.* **2000**, *34*, 3363–3367.

61. Nico, P. S.; Zasoski, R. J. Mn (III) center availability as a rate controlling factor in the oxidation of phenol and sulfide on δ-MnO_2. *Environ. Sci. Technol.* **2001**, *35*, 3338–3343.
62. Wang, Z.; Lee, S.-W.; Catalano, J. G.; Lezama-Pacheco, J. S.; Bargar, J. R.; Tebo, B. M.; Giammar, D. E. Adsorption of uranium(VI) to manganese oxides: X-ray absorption spectroscopy and surface complexation modeling. *Environ. Sci. Technol.* **2013**, *47*, 850–858.
63. Landrot, G.; Ginder-Vogel, M.; Livi, K.; Fitts, J. P.; Sparks, D. L. Chromium(III) Oxidation by Three Poorly Crystalline Manganese(IV) Oxides. 2. Solid Phase Analyses. *Environ. Sci. Technol.* **2012**, *46*, 11601–11609.
64. Chung, J.-B.; Sa, T.-M. Chromium oxidation potential and related soil characteristics in arable upland soils. *Commun. Soil Sci. Plant Anal.* **2001**, *32*, 1719–1733.
65. Ivarsson, M.; Broman, C.; Holm, N. G. Chromite oxidation by manganese oxides in subseafloor basalts and the presence of putative fossilized microorganisms. *Geochem. Trans.* **2011**, *12*, 5.
66. Plathe, K. L.; Lee, S.-W.; Tebo, B. M.; Bargar, J. R.; Bernier-Latmani, R. Impact of microbial Mn oxidation on the remobilization of bioreduced U(IV). *Environ. Sci. Technol.* **2013**, *47*, 3606–3613.
67. Chinni, S.; Anderson, C. R.; Ulrich, K. U.; Giammar, D. E.; Tebo, B. M. Indirect UO_2 oxidation by Mn(II)-oxidizing spores of *Bacillus* sp Strain SG-1 and the effect of U and Mn concentrations. *Environ. Sci. Technol.* **2008**, *42*, 8709–8714.
68. Suzuki, Y.; Kelly, S. D.; Kemner, K. M.; Banfield, J. F. Radionuclide contamination: Nanometre-size products of uranium bioreduction. *Nature* **2002**, *419*, 134–134.
69. Luo, W.; Gu, B. Dissolution and mobilization of uranium in a reduced sediment by natural humic substances under anaerobic conditions. *Environ. Sci. Technol.* **2008**, *43*, 152–156.
70. Luo, W. L.; W., S.; Gu, B. H. Dissolution of uranium-bearing minerals and mobilization of uranium by organic ligands in a biologically reduced sediment. *Environ. Sci. Technol.* **2011**, *45*, 2994–2999.
71. Carbonaro, R. F.; Gray, B. N.; Whitehead, C. F.; Stone, A. T. Carboxylate-containing chelating agent interactions with amorphous chromium hydroxide: adsorption and dissolution. *Geochim. Cosmochim. Acta* **2008**, *72*, 3241–3257.
72. Frazier, S. W.; Kretzschmar, R.; Kraemer, S. M. Bacterial siderophores promote dissolution of UO_2 under reducing conditions. *Environ. Sci. Technol.* **2005**, *39*, 5709–5715.
73. Duckworth, O. W.; Akafia, M. M.; Andrews, M. Y.; Bargar, J. R. Siderophore-promoted dissolution of chromium from hydroxide minerals. *Environ. Sci.: Processes Impacts* **2014**, *16*, 1348–1359.
74. Stewart, B. D.; Girardot, C.; Spycher, N.; Sani, R. K.; Peyton, B. M. Influence of Chelating Agents on Biogenic Uraninite Reoxidation by Fe(III) (Hydr)oxides. *Environ. Sci. Technol.* **2013**, *47*, 364–371.

75. Yang, F.; Guo, J.; Dai, R.; Lan, Y. Oxidation of Cr(III)-citrate/tartrate complexes by δ-MnO2: Production of Cr(VI) and its impact factors. *Geoderma* **2014**, *213*, 10–14.
76. Wang, Z.; Xiong, W.; Tebo, B. M.; Giammar, D. E. Oxidative UO_2 dissolution induced by soluble Mn(III). *Environ. Sci. Technol.* **2014**, *48*, 289–98.
77. Ginder-Vogel, M.; Stewart, B.; Fendorf, S. Kinetic and mechanistic constraints on the oxidation of biogenic uraninite by ferrihydrite. *Environ. Sci. Technol.* **2010**, *44*, 163–169.
78. Spycher, N. F.; Issarangkun, M.; Stewart, B. D.; Sengor, S. S.; Belding, E.; Ginn, T. R.; Peyton, B. M.; Sani, R. K. Biogenic uraninite precipitation and its reoxidation by iron(III) (hydr)oxides: A reaction modeling approach. *Geochim. Cosmochim. Acta* **2011**, *75*, 4426–4440.
79. Johnson, K. S. Manganese redox chemistry revisited. *Science* **2006**, *313*, 1896–1897.
80. Webb, S. M.; Dick, G. J.; Bargar, J. R.; Tebo, B. M. Evidence for the presence of Mn(III) intermediates in the bacterial oxidation of Mn(II). *Proc. Natl. Acad. Sci. U. S. A.* **2005**, *102*, 5558–5563.
81. Duckworth, O. W.; Sposito, G. Siderophore-manganese(III) interactions. I. Air-oxidation of manganese(II) promoted by desferrioxamine B. *Environ. Sci. Technol.* **2005**, *39*, 6037–6044.
82. Butterfield, C. N.; Soldatova, A. V.; Lee, S.-W.; Spiro, T. G.; Tebo, B. M. Mn(II,III) oxidation and MnO_2 mineralization by an expressed bacterial multicopper oxidase. *Proc. Natl. Acad. Sci. U. S. A.* **2013**, *110*, 11731–11735.
83. Ehrlich, H. L. Manganese oxide reduction as a form of anaerobic respiration. *Geomicrobiol. J.* **1987**, *5*, 423–431.
84. Lin, H.; Szeinbaum, N. H.; DiChristina, T. J.; Taillefert, M. Microbial Mn(IV) reduction requires an initial one-electron reductive solubilization step. *Geochim. Cosmochim. Acta* **2012**, *99*, 179–192.
85. Wang, Y.; Stone, A. T. Phosphonate- and carboxylate-based chelating agents that solubilize (hydr)oxide-bound Mn^{III}. *Environ. Sci. Technol.* **2008**, *42*, 4397–4403.
86. Duckworth, O. W.; Sposito, G. Siderophore-manganese(III) interactions II. Manganite dissolution promoted by desferrioxamine B. *Environ. Sci. Technol.* **2005**, *39*, 6045–6051.
87. Peña, J.; Duckworth, O. W.; Bargar, J. R.; Sposito, G. Dissolution of hausmannite (Mn_3O_4) in the presence of the trihydroxamate siderophore desferrioxamine B. *Geochim. Cosmochim. Acta* **2007**, *71*, 5661–5671.
88. Gunary, D. Pyrophosphate in soil; some physico-chemical aspects. *Nature* **1966**, *210*, 1297–1298.
89. Harrington, J. M.; Parker, D. L.; Bargar, J. R.; Jarzecki, A. A.; Tebo, B. M.; Sposito, G.; Duckworth, O. W. Structural dependence of Mn complexation by siderophores: Donor group dependence on complex stability and reactivity. *Geochim. Cosmochim. Acta* **2012**, *88*, 106–119.
90. Trouwborst, R. E.; Clement, B. G.; Tebo, B. M.; Glazer, B. T.; Luther, G. W. Soluble Mn(III) in suboxic zones. *Science* **2006**, *313*, 1955–1957.

91. Madison, A. S.; Tebo, B. M.; Mucci, A.; Sundby, B.; Luther, III, G. W. Abundant porewater Mn(III) is a major component of the sedimentary redox system. *Science* **2013**, *341*, 875–878.
92. Madison, A. S.; Tebo, B. M.; Luther, G. W. Simultaneous determination of soluble manganese(III), manganese(II) and total manganese in natural (pore)waters. *Talanta* **2011**, *84*, 374–381.
93. Chen, W.-R.; Liu, C.; Boyd, S. A.; Teppen, B. J.; Li, H. Reduction of carbadox mediated by reaction of Mn(III) with oxalic acid. *Environ. Sci. Technol.* **2013**, *47*, 1357–1364.
94. Kostka, J. E.; Luther, G. W.; Nealson, K. H. Chemical and biological reduction of Mn(III)-pyrophosphate complexes - Potential importance of dissolved Mn(III) as an environmental oxidant. *Geochim. Cosmochim. Acta* **1995**, *59*, 885–894.
95. Klewicki, J. K.; Morgan, J. J. Kinetic behavior of Mn(III) complexes of pyrophosphate, EDTA, and citrate. *Environ. Sci. Technol.* **1998**, *32*, 2916–2922.
96. Rophael, M. Kinetics of the oxidation of chromium (III) by manganese (III) in sulphuric acid media. *Chem. Scr.* **1982**, *20*, 171–173.
97. Weaver, R. M.; Hochella, Jr, M. F.; Ilton, E. S. Dynamic processes occurring at the Cr^{III}aq-manganite (γ-MnOOH) interface: simultaneous adsorption, microprecipitation, oxidation/reduction, and dissolution. *Geochim. Cosmochim. Acta* **2002**, *66*, 4119–4132.
98. Perez-Benito, J. F.; Arias, C. The pyrophosphate-assisted reduction of chromium(VI) by manganese(II) and its reverse reaction. *New J. Chem.* **2001**, *25*, 1438–1446.
99. Stone, A. T.; Flanders, P. M.; Xia, X. Manganese and iron in water treatment: An atomic orbital view of bonding, speciation, reactivity, and product identity. Presented at The 245th ACS National Meeting, New Orleans, LA, 2013; American Chemical Society.
100. Boland, N. E.; Stone, A. T. Capillary electrophoresis facilitates determination of metal complex stoichiometry by Job's method of continuous variation. *Environ. Chem.* **2013**, *10*, 409–416.
101. Duckworth, O. W.; Bargar, J. R.; Sposito, G. Coupled biogeochemical cycling of iron and manganese as mediated by microbial siderophores. *BioMetals* **2009**, *22*, 605–613.
102. Luther, G. W., III; Madison, A. S.; Mucci, A.; Sundby, B.; Oldham, V. E. A kinetic approach to assess the strengths of ligands bound to soluble Mn(III). *Mar. Chem.* **2015**, *173*, 93–99.
103. Wu, Y.; Deng, B.; Xu, H.; Kornishi, H. Chromium(III) oxidation coupled with microbially mediated Mn(II) oxidation. *Geomicrobiol. J.* **2005**, *22*, 161–170.
104. Wang, Z.; Tebo, B. M.; Giammar, D. E. Effects of Mn(II) on UO_2 dissolution under anoxic and oxic conditions. *Environ. Sci. Technol.* **2014**, *48*, 5546–5554.
105. Namgung, S.; Kwon, M. J.; Qafoku, N. P.; Lee, G. $Cr(OH)_{3(s)}$ oxidation induced by surface catalyzed Mn(II) oxidation. *Environ. Sci. Technol.* **2014**, *48*, 10760–10768.

106. He, J. Z.; Meng, Y. T.; Zheng, Y. M.; Zhang, L. M. Cr(III) oxidation coupled with Mn(II) bacterial oxidation in the environment. *J. Soils Sediments* **2010**, *10*, 767–773.
107. Murray, K. J.; Webb, S. M.; Bargar, J. R.; Tebo, B. M. Indirect oxidation of Co(II) in the presence of the marine Mn(II)-oxidizing bacterium *Bacillus* sp strain SG-1. *Appl. Environ. Microbiol.* **2007**, *73*, 6905–6909.
108. Junta, J.; Hochella, M. F. Manganese(II) oxidation at mineral surfaces - a microscopic and spectroscopic study. *Geochim. Cosmochim. Acta* **1994**, *58*, 4985–4999.
109. Tang, Y.; Webb, S. M.; Estes, E. R.; Hansel, C. M. Chromium (III) oxidation by biogenic manganese oxides with varying structural ripening. *Environ. Sci.: Processes Impacts* **2014**, *16*, 2127–2136.

Chapter 3

Mechanistic Understanding of Metal Sorption by Phyllomanganates through Density Functional Theory

Kideok D. Kwon[1,*] and Garrison Sposito[2]

[1]Department of Geology, Kangwon National University, Chuncheon 200-701, Korea
[2]Geochemistry Department, Earth Sciences Division, Lawrence Berkeley National Laboratory, Berkeley, California 94720, United States
[*]E-mail: kkwon@kangwon.ac.kr

The sorption processes of phyllomanganates (layer type Mn oxides) greatly impact the geochemical cycles of metals in environments ranging from the ocean floor to the land surface. *In situ* spectroscopy has provided valuable insights into the underlying sorption mechanisms on these minerals by identifying molecular-level surface species of trace metals. Accurate determination of metal surface speciation is challenging, however, because of ambiguities often encountered in attempting to interpret the spectra. Adding complexity to these issues, certain experimentally observed trends in metal sorption cannot be explained simply by invoking conventional chemical effects, such as differences in ionic radii or crystal field energies. Geometry optimizations performed using density functional theory, a first-principles approach based in quantum mechanics, can help to resolve these problems by providing highly detailed information about the structure, energetics, and electronic properties of both minerals and metal surface complexes, thus serving as a complementary approach to surface spectroscopy in elucidating sorption mechanisms. This chapter reviews recent applications of density functional theory which illustrate how it accomplishes this goal.

In Advances in the Environmental Biogeochemistry of Manganese Oxides; Sparks, et al.;
ACS Symposium Series; American Chemical Society: Washington, DC, 2015.

Introduction

Surface spectroscopy leads to a mechanistic understanding of metal sorption by phyllomanganates through direct probing of the metal species sorbed by the mineral surface. In this way, two key sorption sites have been identified for metal cations: Mn(IV) vacancies and lateral edge surfaces of the mineral particles (*1–6*). At the vacancy site, the molecular structures of sorbed metal cations are well characterized: a cation either forms a triple-corner-sharing (TCS) surface complex or it enters the vacancy site (INC) as part of the edge-sharing Mn(IV) octahedral sheet (Figure 1). However, transformations between TCS and INC species vary with metal characteristics and sorption conditions, and the transformation mechanisms need to be elucidated. At the lateral edge surfaces, extended X-ray absorption fine structure spectroscopy (EXAFS) studies have indicated formation of double-edge-sharing (DES) or double-corner-sharing (DCS) surface complexes (Figure 2). Metal speciation on edge surface sites, however, poses greater challenges than that on vacancy sites because the structure of lateral edge surfaces is not well characterized experimentally as compared to the Mn(IV) vacancy in the basal plane.

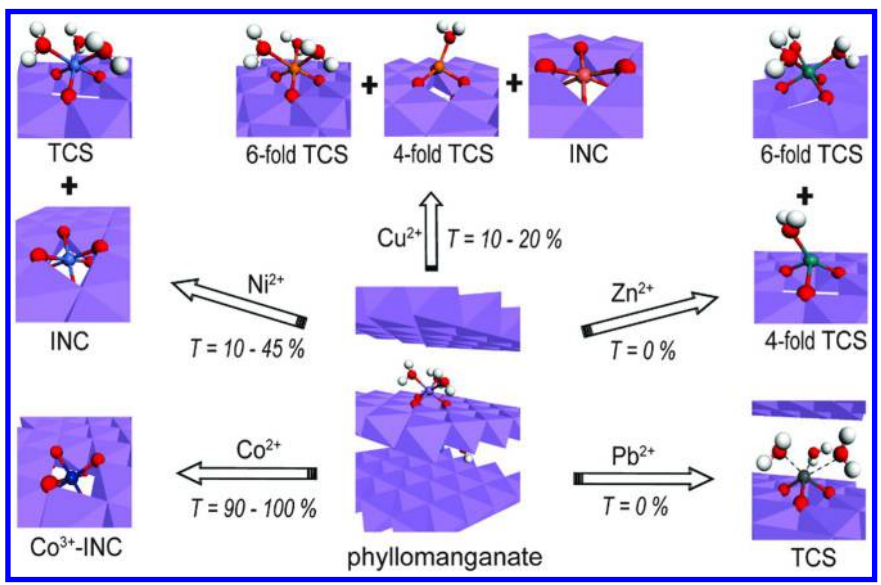

Figure 1. Triple-corner-sharing complex (TCS) and incorporated (INC) metal species at a Mn vacancy. T represents the ratio, INC/(TCS+INC). [modified with permission from reference (29). Copyright 2013 Elsevier]

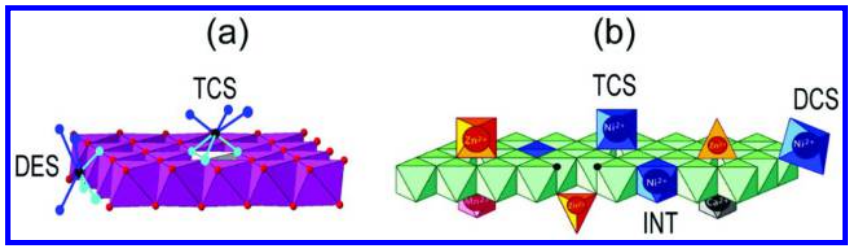

Figure 2. Double-edge-sharing (DES) or double-corner-sharing (DCS) surface complexes occurring at the lateral edges of phyllomanganates for (a) Pb^{2+} and (b) Ni^{2+} as proposed in EXAFS studies. [modified with permission from reference (1, 34) Copyright 2007 Elsevier]

Density functional theory (DFT) can complement spectroscopy as a reliable approach using no adjustable parameters. DFT is an accurate, computationally manageable, first-principles technique that fully characterizes the electronic ground state of a chemical system by iteratively solving the Kohn-Sham equation, an exact quantum-mechanical eigenvalue problem for non-interacting electrons that is equivalent to the Schrödinger equation (*7*). In the Schrödinger equation, strong correlations among electrons and between electrons and nuclei present a formidable computational challenge. In DFT, these correlations are taken into account with an approach based on an equivalent electron gas moving in an external effective potential including an exchange-correlation functional. The exchange correlation energy, which acts as "Nature's glue" to bind atoms and molecules (*8*), is a functional of the electron gas density in DFT. For periodic chemical systems, such as minerals, a plane-wave basis set is typically used to represent wavefunctions along with self-consistent pseudopotentials which replace the strong coulomb interactions between atomic nuclei and core electrons with weak effective interactions (*9*). Extensive discussions of the principles of DFT can be found in (*10*), (*11*), (*12*), and (*13*). This chapter provides a short review of studies on metal sorption by phyllomanganates in which DFT provided quantitative models of structure and bonding to help understand metal partitioning trends and create reference structural models for resolving surface metal speciation.

Chalcophanite Group Minerals

In this section, results are presented for layer-type Mn oxide minerals of the chalcophanite group ($MeMn_3O_7 \cdot 3H_2O$, Me = Mg, Ni, or Zn), in which Me is known to form a TCS surface complex in the interlayer, to demonstrate the degree of details and the accuracy of DFT computational results. Zinc forms tetrahedral or octahedral TCS surface complex, as illustrated in Figure 1; the metal coordination and hydration state can strongly influence the stability of a mineral (*5*, *14*). Changes in the metal coordination and crystal structure of chalcophanite mineral during dehydration process are discussed.

Hydrated Chalcophanites

Chalcophanite ($ZnMn_3O_7 \cdot 3H_2O$) is a hydrous Zn phyllomanganate mineral composed of edge-sharing Mn(IV) octahedral sheets with Zn located in the interlayer above and below a Mn vacancy. Because the coordination structure of Zn at the vacancy (Zn coordinated with three surface O and three O in H_2O molecules) is well characterized (Figure 3), the structure of this mineral is widely used as a reference in EXAFS studies of metal cations sorbed by phyllomanganates. Isostructural Ni- and Mg-end members of chalcophanite group have been also reported: ernienickelite ($NiMn_3O_7 \cdot 3H_2O$) and jianshuiite ($MgMn_3O_7 \cdot 3H_2O$) (*15*, *16*). Table I summarizes the results of DFT geometry optimizations for these minerals performed using the Perdew-Burke-Ernzerhof exchange correlation functional under the generalized gradient approximation (GGA) (*17*) following the method in (*14*). As is well known (*13*), DFT tends to overestimate structural parameters; however, it reproduced experimental results within 0.8 % for the a parameter and 2.5 % for the c parameter. The larger error in the c parameter is also common for optimizations of layer type minerals because the contribution of weak interactions, such as van der Waals interactions, between layers is not negligible and the GGA does not take such weak dispersion forces into account. Overall, DFT predicts that the lattice parameters tend to increase in the order: ernienickelite < jianshuiite < chalcophanite. This trend may be understood simply by comparing the ionic radii of octahedrally-coordinated Ni^{2+}, Mg^{2+}, and Zn^{2+} (0.69, 0.72 and 0.74 Å, respectively). Detailed experimental structural refinements are not available for ernienickelite and jianshuiite. However, DFT predicts that interatomic distances, *d*(Mg–O) and *d*(Mg–Mn), are slightly longer than *d*(Zn–O) and *d*(Zn–Mn), respectively, a trend contrasting with that of the lattice parameters.

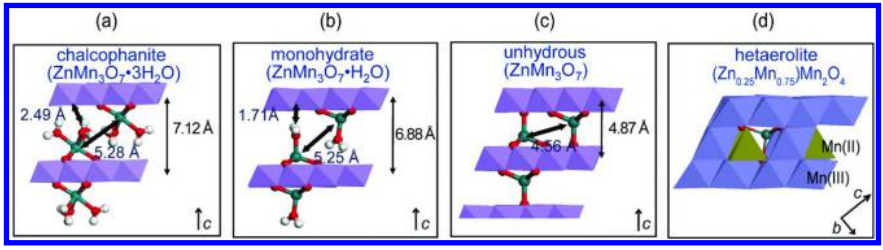

Figure 3. Structures of (a) chalcophanite, (b) its monohydrate, (c) unhydrous Zn-Mn oxide, and (d) Mn(II)-rich hetaerolite.

In Advances in the Environmental Biogeochemistry of Manganese Oxides; Sparks, et al.;
ACS Symposium Series; American Chemical Society: Washington, DC, 2015.

Table I. Geometry-optimized structural parameters (Å) of chalcophanite group minerals ($MeMn_3O_7 \cdot 3H_2O$; Me = Ni, Mg, or Zn).

structural parameters	$NiMn_3O_7 \cdot 3H_2O$		$MgMn_3O_7 \cdot 3H_2O$		$ZnMn_3O_7 \cdot 3H_2O$	
	DFT	*EXP*[a,b]	*DFT*	*EXP*[a,c]	*DFT*	*EXP*[d]
$a = b$	7.567	7.514	7.596	7.54	7.602	7.54
c	21.032	20.517	21.212	20.82	21.349	20.82
d(MeO)	2.00	n.r.	2.09	n.r.	2.07	2.11
d($MeOH_2$)	2.20	n.r.	2.17	n.r.	2.24	2.14
d(MeMn)	3.46	n.r.	3.54	n.r.	3.51	3.49
	3.45	n.r.	3.55	n.r.	3.52	3.50

[a] n.r.: not reported. [b] Ernienickelite (*15*). [c] Jianshuiite (*16*). [d] Chalcophanite (*18*).

Dehydration of Chalcophanites

Time-resolved x-ray diffraction has been applied to examine the dehydration of chalcophanite, which highlights the lability of zinc in accommodating both tetrahedral and octahedral coordination during the accompanying phase transition (*19*). As temperature increases, the crystal undergoes dramatic structural changes. Above 400 K, the chalcophanite interlayer spacing collapses to form the anhydrous Zn phyllomanganate, $ZnMn(IV)_3O_7$. Above 800 K, the anhydrous oxide transforms into Mn-rich hetaerolite, $[Zn_{0.25}Mn(II)_{0.75}]Mn(III)_2O_4$, taking on a spinel structure via reduction of Mn(IV) to Mn(III) and Mn(II).

Geometry optimizations have been performed to obtain the structures of dehydrating chalcophanite, with three, two, one, and zero hydrating water molecules per Zn, as well as Mn-rich hetaerolite (Figure 3). As Zn coordination changed from sixfold to fourfold, the interlayer spacing between Mn(IV) octahedral sheets significantly decreased, from 7.12 to 4.87 Å, consistent with experimental results (*19*). Detailed comparison between sixfold and fourfold Zn can be found in (*14*) for the structural parameters and electronic structure. Figure 3d shows part of the Mn-rich hetaerolite structure with Mn(II) occupying three out of the four tetrahedral sites. Because conventional DFT tends to over-delocalize 3*d* electrons in Mn (*20–22*), the DFT + *U* formalism was used, where $U = 2.5$ eV is the on-site coulomb interaction *U* for the contribution of Mn(II) 3*d* electrons to the total energy, as described in (*23*). Manganese(III) octahedra were significantly distorted in $[Zn_{0.25}Mn(II)_{0.75}]Mn(III)_2O_4$: d(Mn–O) was 1.94 or 2.36 Å, as compared to the experimental values, 1.94 and 2.29 Å. Experimental studies have not reported d(Mn–O) for tetrahedral Mn(II), but tetrahedral d(Zn–O) has been reported (1.99 Å) (*19*); the DFT analysis predicted that d(Mn–O) should be longer than d(Zn–O) (2.07 vs. 2.01 Å, respectively). Mn-rich hetaerolite can be regarded as a solid solution of hetaerolite ($ZnMn_2O_4$) and hausmannite (Mn_3O_4). When the solid solution structure was geometry-optimized as a function of Mn(II)/Zn content for $[Zn_{1-x}Mn(II)_x]Mn_2O_4$ (Figure 4), the results were in good agreement

In Advances in the Environmental Biogeochemistry of Manganese Oxides; Sparks, et al.;
ACS Symposium Series; American Chemical Society: Washington, DC, 2015.

with experiment, having systematic errors of only 1 % and 4 % in the $a = b$ axis and c axis parameters, respectively.

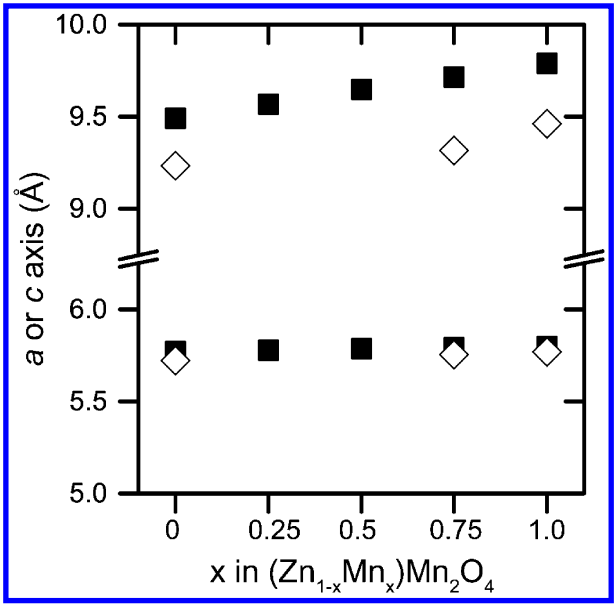

Figure 4. Lattice parameters of $Zn_{1-x}Mn_xMn_2O_4$: hetaerolite (x = 0; $ZnMn_2O_4$), a solid solution ($Zn_{1-x}Mn_xMn_2O_4$ with x = 0.25, 0.5, 0.75), and hausmannite (x = 1; Mn_3O_4). Filled squares = DFT results; open diamonds = experimental results (19, 38, 39).

Metal Sorption Mechanisms

Partitioning at Mn(IV) Vacancies

EXAFS studies have shown that transition metal cations typically bind to Mn(IV) vacancy sites in phyllomanganate minerals, such as birnessite and vernadite, to form interlayer TCS or INC species (Figure 1). Transition metal partitioning between TCS and INC depends strongly on the metal: Zn forms TCS species but does not form INC species (*5*); Co forms exclusively INC species (*2*). On the other hand, solution pH controls the relative ratio between TCS and INC for Ni and Cu: as solution pH increases from 4 to 7 or 8, the INC/(TCS + INC) ratio (= T, Figure 1) increases from 10 to 45 % for Ni (*1*, *6*) and from 0 to 20 % for Cu (*24*). These metal- and pH-specific partitioning trends have led to a proposal to use the ratio T as an indicator of the past precipitation environment of natural Mn oxides (*1*, *25*). Of course, these partitioning trends are useful also in the remediation of contaminated waters using Mn oxides.

In principle, the observed trend of INC species (Co > Ni > Cu > Zn, see Figure 1) may be understood by comparing ionic radii or crystal field stabilization energy

In Advances in the Environmental Biogeochemistry of Manganese Oxides; Sparks, et al.;
ACS Symposium Series; American Chemical Society: Washington, DC, 2015.

(CFSE). A smaller ion can more easily enter a vacancy than a lager ion: $r(Co^{3+})$ = 0.55, $r(Ni^{2+})$ = 0.69, $r(Cu^{2+})$ = 0.73, and $r(Zn^{2+})$ = 0.74 Å (*26*). Inside a vacancy, a metal ion with a greater CFSE would be more stable than an ion with a lower CFSE: CFSE (Co^{3+}) = 481 kJ/mol, CFSE (Ni^{2+}) =122 kJ/mol, CFSE (Cu^{2+}) = 93 kJ/mol, and CFSE (Zn^{2+}) = 0 kJ/mol (*27*, *28*). Although these comparisons are helpful guides, they do not explain the occurrence of Ni-INC and Cu-INC, because both Ni^{2+} and Cu^{2+} ion have a larger radius and smaller CFSE than does the Mn ion in a vacancy [$r(Mn^{4+})$ = 0.53 Å; $r(Mn^{3+})$ = 0.645 Å; CFSE (Mn^{4+}) = 313 kJ/mol; CFSE (Mn^{3+}) = 151 kJ/mol]. A more sophisticated model is thus required to explain how Ni^{2+} and Cu^{2+} can be stabilized inside a vacancy.

Kwon et al. (*29*) examined this question and found that subtle differences in electronic structure determine the molecular-level speciation of metals incorporated in phyllomanganates. When a metal cation enters a vacancy, it exerts stress on the surrounding structure that depends on its size. The DFT study showed that this stress can be relieved by a distortion of the metal-incorporated octahedron to enhance the stability of the metal-incorporated structure. These structural distortions are promoted by partially-occupied 3*d* orbitals, which are stereoactive. For Zn^{2+}, however, the fully-occupied 3*d* orbitals are not stereoactive (*30*, *31*), and the accommodating distortion does not occur. Instead, the stress exerted by the Zn ion inside a vacancy is relieved only by leaving it to form a TCS complex on the vacancy, the only stable location for the metal ion.

The DFT study also suggested that the protonation state of a vacancy impacts the partitioning behavior of Ni and Cu (*29*). When a divalent cation forms a TCS complex on one side of a Mn(IV) vacancy, depending on solution pH, one or two H^+ can bond to surface O on the other side. Calculations of the total potential energy along the metal incorporation pathway across a vacancy site showed that, as the number of H^+ bonded to the vacancy varied (Figure 5), an energy barrier exists between TCS and INC, the size of which decreases when a vacancy loses H^+ (i.e., deprotonation). Population analysis showed that deprotonation of a vacancy increases covalency in the bond between O and the metal cation, thus increasing the relative stability of INC. For Ni, the stability difference between the TCS and INC species is reversed when the vacancy becomes deprotonated. These deprotonation effects on the energy barrier size and metal stability inside a vacancy readily explain the experimental observations of increasing INC species with increasing pH (*1*, *6*, *32*).

Remarkably, regardless of the protonation state, Cu-INC is never more stable than Cu-TCS (Figure 5b). The absence of a stability reversal for Cu is attributed to suppression of Jahn-Teller (JT) distortion inside a vacancy. The JT ratio, the difference between the longest and shortest metal-O distance divided by the average distance, was 22 % when Cu was outside the vacancy, but only 3 % when the metal ion was inside the vacancy. Thus, the stabilization energy obtained by JT distortion is greatly reduced inside a vacancy, leading to INC species always being less stable than TCS. Although most geometry-optimized structural parameters were in good agreement with experiment, there was a significant discrepancy for *d*(Cu–O) in Cu-INC [2.06 Å (*29*) calculated and 1.92 Å experiment (*24*)], suggesting that further investigation of the mechanism of Cu incorporation inside a vacancy is needed.

In Advances in the Environmental Biogeochemistry of Manganese Oxides; Sparks, et al.;
ACS Symposium Series; American Chemical Society: Washington, DC, 2015.

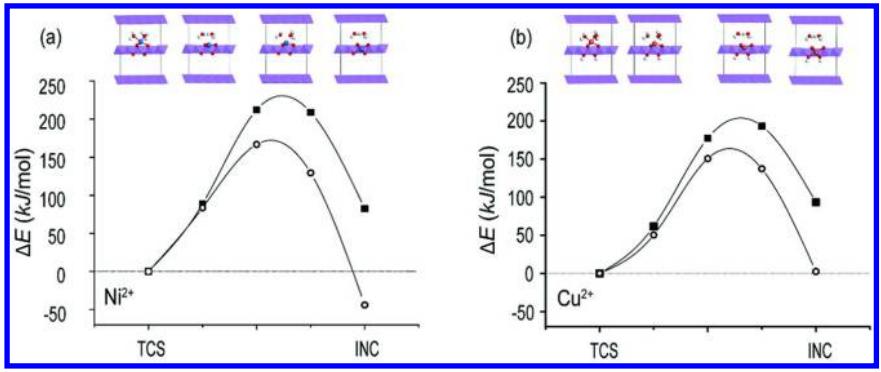

Figure 5. Total energy variation (ΔE) of metal-incorporated Mn oxide along a pathway from TCS to INC species for (a) Ni^{2+} and (b) Cu^{2+} with 2 H (filled squares) or no H (open circles) on the opposite side of the vacancy. Note the absence of a stability reversal for the INC species in the case of Cu. [modified with permission from reference (29). Copyright 2013 Elsevier]

Surface Complexes at Lateral Particle Edges

The lateral edge surfaces of phyllomanganate nanoparticles offer the other major sorption site for metal cations (Figure 2). When the particle size is very small, simple geometric arguments show that the edge surfaces can in fact be the dominant sorption sites (*33*). For Pb^{2+}, DES species was identified to occur (*34*), although DCS species could also occur depending on sorption conditions (*4*, *35*). Based on bond valence considerations, DES species may be a more stable complex because they involve bonds with three surface O of the Mn octahedral sheet, whereas DCS involves bonds with only two surface O. On the other hand, for Ni^{2+} sorption, a DCS species was reported to occur at the lateral edge surfaces (*1*) and a tridentate-edge-sharing surface complex has been reported on the edge surface of triclinic birnessite (*32*, *36*). Thus, the surface complex type occurring at the edge surfaces appears to vary with the metal sorbate and the sorbent Mn oxide.

Density functional theory is useful to examine the lateral edge surface when so little is known experimentally about the edge surface structure itself. A nanodisk particle (diameter of approximately 2 nm) was geometry-optimized using the method described in (*35*) and the predicted structure was compared with the bulk structure of planar MnO_2. Dangling bonds at the lateral edges were fully-coordinated by H_2O or hydroxyl groups to make the overall charge zero. The optimized nanodisk takes on a slightly concave or convex curvature instead of being planar (Figure 6). This curved structure is similar to the recently-proposed spherically or cylindrically bent model for an approximately 4-nm-diameter δ-MnO_2 nanoparticle (*37*). However, the curvature predicted by DFT is not as pronounced as that proposed for the δ-MnO_2 nanoparticle, which possesses Mn vacancies adsorbing hydrated cations. The planar MnO_2 bulk structure showed two distinct O-O distances in its Mn octahedra: one along shared octahedral edges of 2.54 Å and another along unshared edges of 2.90 Å, as would be expected from Pauling's rules (Figure 6). The 2-nm-diameter nanodisk showed large deviations

In Advances in the Environmental Biogeochemistry of Manganese Oxides; Sparks, et al.;
ACS Symposium Series; American Chemical Society: Washington, DC, 2015.

from these two distances. In particular, a broad distribution of distances was found in the range 2.6 - 3.0 Å resulting mainly from highly-distorted Mn octahedra at the lateral edge surfaces. This structural distortion has not been—but should be—taken into account in spectroscopic structural analyses of metals adsorbed on the edge surfaces.

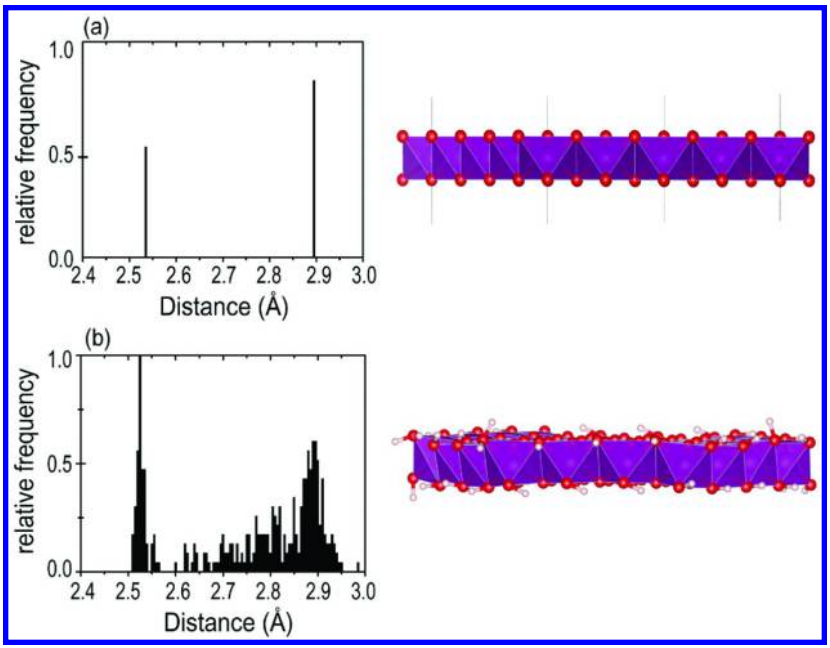

Figure 6. Distribution of O-O distances in Mn octahedra for (a) an infinite MnO_2 octahedral sheet and (b) a nanodisk with diameter ≈ 2.0 nm. The planar MnO_2 sheet structure, visualized using the VESTA software (40), is shown with periodic boundaries in (a); a slightly bent nanodisk is shown in (b).

The structural parameters for metal species sorbed at the edges of the nanodisk (both DCS and DES species) are very similar to those for species sorbed on vacancies (TCS and INC species). The distance between a sorbed metal and nearest-neighbor Mn is a diagnostic structural parameter used in determining the metal speciation. According to DFT computations (Figure 7), d(Pb–Mn_{1st}) for the DCS species was similar to that for the TCS species (3.86 vs. 3.84 Å) (*35*). [This distance is an average value over the results of multiple calculations which varied by ± 0.02 to 0.04 Å.] The signal in EXAFS spectra tends to be greater for vacancy species (sixfold coordination) than for edge species (twofold coordination). If the contribution of TCS species is dominant, the DCS species would be very difficult to resolve, whereas the DES species with d(Pb–Mn_{1st}) = 3.34 Å is readily distinguished from the TCS species in EXAFS spectra. For Ni sorption, d(Ni–Mn_{1st}) in the DCS and TCS species are 3.45 and 3.46 Å, respectively, and the same distances in the DES and INC species are 2.89 and 2.91 Å, respectively

In Advances in the Environmental Biogeochemistry of Manganese Oxides; Sparks, et al.;
ACS Symposium Series; American Chemical Society: Washington, DC, 2015.

(*23*). These strong similarities in the structural parameters lead to ambiguities in spectral identification of edge surface species.

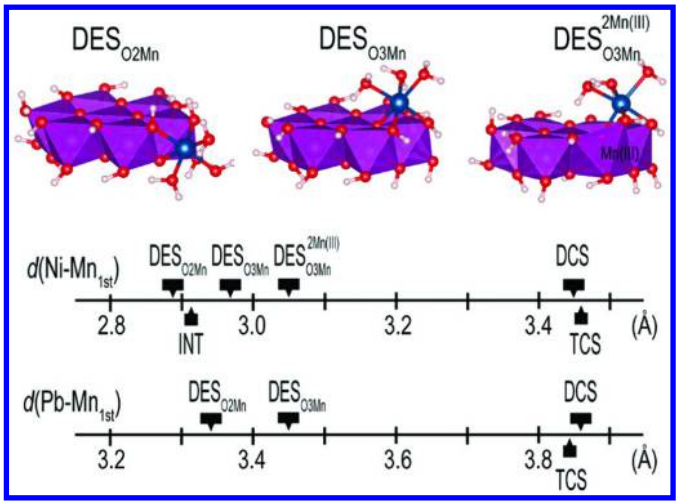

Figure 7. Comparison of diagnostic structural parameters between edge species (DES and DCS) and vacancy species (TCS and INT) for Ni (23) and Pb (35). For notation, see the text.

Geometry optimization can identify new configurations of metal surface complexes that have not been reported by spectroscopic studies. In general, the DES species refers to a configuration in which a metal is bonded to two apical O and one bridging O (Figure 2a and DES_{O2Mn} in Figure 7). But DFT has revealed a different configuration of DES, in which a metal cation sits on the basal plane at a particle edge bonded to triply-coordinated O (DES_{O3Mn} in Figure 7). This species has longer interatomic distances than does DES_{O2Mn}: the diagnostic distance, d(Pb–Mn_{1st}), was 3.45 and 3.34 Å, respectively (*35*). For the case of Ni, d(Ni–Mn_{1st}) was 2.97 and 2.89 Å, respectively (*23*). Due to this longer distance, Ni-DES_{O3Mn} may be more easily distinguished from Ni-INC species (Figure 7).

The presence of Mn(III) at the edge surfaces also influences the structural parameters of metal surface complexes. In particular, d(Ni–Mn_{1st}) in the DES_{O3Mn} species is sensitive to the Mn(III) content. When $Mn(IV)_{1st}$ is replaced by Mn(III), significant Jahn-Teller distortions occur in the octahedra, and d(Ni–Mn_{1st}) in the DES_{O3Mn} species increases from 2.97 to 3.05 Å (*23*). (See $DES^{2Mn(III)}_{O3Mn}$ in Figure 7). Recent EXAFS studies of Ni-sorbed Mn(III)-rich Mn oxides report the occurrence of edge species with d(Ni–Mn_{1st}) ranging from 3.01 to 3.09 Å, which is easily distinguished from distances observed in DES_{O2Mn}, DCS, TCS, or INC species (*23*, *32*, *36*). Thus the DFT geometry optimization indicates that the edge surface species corresponds to DES_{O3Mn}.

Hydration conditions of the metal and protonation states of the lateral edge surfaces may also influence metal surface speciation. In DFT energy minimizations, an initial DCS configuration of unhydrated Pb or Ni is always

In Advances in the Environmental Biogeochemistry of Manganese Oxides; Sparks, et al.;
ACS Symposium Series; American Chemical Society: Washington, DC, 2015.

transformed into a DES configuration to favor binding with three surface O (*35*), but hydration stabilizes the DCS configuration. However, when the apical O of Ni-bonded Mn octahedra are deprotonated, the DCS configuration does not transform to the DES configuration. Instead, Ni remains in the DCS configuration, binding to two apical O without additional coordination from hydrating water molecules.

Spectral ambiguities for metal speciation on phyllomanganates result mainly from lack of ability to probe structural distortion of the Mn octahedral sheet, particularly the edge surface, which produces close similarities in the structural parameters for the vacancy and edge surface species. The spectral analysis is further complicated by oxide surface properties, including Mn(III) content, protonation state, and hydration state. Density functional theory can probe surface structures and disentangle their complicated effects on metal speciation; it offers quantitative structural models for spectral analysis, but also underlying principles to understand variability in metal speciation. A synergistic coupling of surface spectroscopy and DFT computation is thus essential for a mechanistic understanding of metal sorption by phyllomanganates. Compared to metal species determination, less-studied areas are the thermodynamic stability of sorbed metal species and electron transfer reactions occurring at the metal-oxide interface. As computational techniques rapidly advance, DFT is expected to provide useful insights and raise new questions.

Acknowledgments

K.K. was supported by Basic Science Research Program through the National Research Foundation of Korea (NRF) funded by the Ministry of Science, ICT and Future Planning (NRF-2013R1A1A1004657). G.S. was supported by funds allocated in connection with his appointment as Chancellor's Professor, Emeritus, at the University of California, Berkeley. Authors thank Keith Refson for his abiding guidance and many suggestions regarding DFT computations. Part of the computations described here were performed using resources of the National Energy Research Scientific Computing Center, which is supported by the Office of Science of the U.S. Department of Energy under Contract No. DE-AC02-05CH11231.

References

1. Manceau, A.; Lanson, M.; Geoffroy, N. Natural speciation of Ni, Zn, Ba, and As in ferromanganese coatings on quartz using X-ray fluorescence, absorption, and diffraction. *Geochim. Cosmochim. Acta* **2007**, *71*, 95–128.
2. Manceau, A.; Drits, V. A.; Silvester, E.; Bartoli, C.; Lanson, B. Structural mechanism of Co^{2+} oxidation by the phyllomanganate buserite. *Am. Mineral.* **1997**, *82*, 1150–1175.
3. Lanson, B.; Drits, V. A.; Gaillot, A. C.; Silvester, E.; Plancon, A.; Manceau, A. Structure of heavy-metal sorbed birnessite: Part 1. Results from X-ray diffraction. *Am. Mineral.* **2002**, *87*, 1631–1645.

4. Villalobos, M.; Bargar, J.; Sposito, G. Mechanisms of Pb(II) sorption on a biogenic manganese oxide. *Environ. Sci. Technol.* **2005**, *39*, 569–576.
5. Manceau, A.; Lanson, B.; Drits, V. A. Structure of heavy metal sorbed birnessite. Part III: Results from powder and polarized extended X-ray absorption fine structure spectroscopy. *Geochim. Cosmochim. Acta* **2002**, *66*, 2639–2663.
6. Peña, J.; Kwon, K. D.; Refson, K.; Bargar, J. R.; Sposito, G. Mechanisms of nickel sorption by a bacteriogenic birnessite. *Geochim. Cosmochim. Acta* **2010**, *74*, 3076–3089.
7. Kohn, W.; Sham, L. J. Self-consistent equations including exchange and correlation effects. *Phys. Rev.* **1965**, *140*, A1133–A1138.
8. Perdew, J. P.; Ruzsinszky, A. Density functional theory of electronic structure: A short course for mineralogists and geophysicists. In *Reviews in Mineralogy and Geochemistry* Wentzcovitch, R., Stixrude, L., Eds.; The Mineralogical Society of America: Chantilly, VA, U.S.A., 2010; Vol. 71, pp 1−18.
9. Vanderbilt, D. Soft self-consistent pseudopotentials in a generalized eigenvalue formalism. *Phys. Rev. B* **1990**, *41*, 7892–7895.
10. Kohanoff, J. *Electronic Structure Calculations for Solids and Molecules: Theory and Computational Methods*; University Cambridge Press: Cambridge, 2006; p 348.
11. Martin, R. M. *Electronic Structure: Basic Theory and Practical Methods*; Cambridge University Press: Cambridge, 2004; p 624.
12. Payne, M. C.; Teter, M. P.; Allan, D. C.; Arias, T. A.; Joannopoulos, J. D. Iterative minimization techniques for *ab initio* total-energy calculations: molecular-dynamics and conjugate gradients. *Rev. Mod. Phys.* **1992**, *64*, 1045–1097.
13. Sholl, D. S.; Steckel, J. A. *Density Funtional Theory: A practical introduction*; John Wiley & Sons: Hoboken, NJ, U.S.A., 2009; p 238.
14. Kwon, K. D.; Refson, K.; Sposito, G. Zinc surface complexes on birnessite: A density functional theory study. *Geochim. Cosmochim. Acta* **2009**, *73*, 1273–1284.
15. Grice, J. D.; Gartrell, B.; Gault, R. A.; Vanvelthuizen, J. Ernienickelite, $NiMn_3O_7{\bullet}3H_2O$, A new mineral species from the Siberia Complex, Western Australia: Comments on the crystallography of the chalcophanite group. *Can. Mineral.* **1994**, *32*, 333–337.
16. Guiyun, Y.; Shanghua, Z.; Mingkai, Z. Jianshuiite — A new magnesic mineral of chalcophanite group. *Acta Mineral. Sin.* **1992**, *12*, 69–77.
17. Perdew, J. P.; Burke, K.; Ernzerhof, M. Generalized gradient approximation made simple. *Phys. Rev. Lett.* **1996**, *77*, 3865–3868.
18. Post, J. E.; Appleman, D. E. Chalcophanite, $ZnMn_3O_7{\cdot}3H_2O$ - New crystal-structure determinations. *Am. Mineral.* **1988**, *73*, 1401–1404.
19. Post, J. E.; Heaney, P. J. Time-Resolved Synchrotron X-ray Diffraction Study of the Dehydration Behavior of Chalcophanite. *Am. Mineral.* **2014**, *99*, 1956–1961.

20. Dudarev, S. L.; Botton, G. A.; Savrasov, S. Y.; Humphreys, C. J.; Sutton, A. P. Electron-energy-loss spectra and the structural stability of nickel oxide: An LSDA+U study. *Phys. Rev. B* **1998**, *57*, 1505–1509.
21. Cococcioni, M.; de Gironcoli, S. Linear response approach to the calculation of the effective interaction parameters in the LDA+U method. *Phys. Rev. B* **2005**, *71*, 035105.
22. Franchini, C.; Podloucky, R.; Paier, J.; Marsman, M.; Kresse, G. Ground-state properties of multivalent manganese oxides: Density functional and hybrid density functional calculations. *Phys. Rev. B* **2007**, *75*, 195128.
23. Simanova, A. A.; Kwon, K. D.; Bone, S. E.; Bargar, J. R.; Refson, K.; Sposito, G.; Peña, J. Probing the sorption reactivity of the edge surfaces in birnessite nanoparticles using nickel(II). *Geochim. Cosmochim. Acta* **2015**, *164*, 191–204.
24. Sherman, D. M.; Peacock, C. L. Surface complexation of Cu on birnessite (δ-MnO_2): Controls on Cu in the deep ocean. *Geochim. Cosmochim. Acta* **2010**, *74*, 6721–6730.
25. Peacock, C. L. Physiochemical controls on the crystal-chemistry of Ni in birnessite: Genetic implications for ferromanganese precipitates. *Geochim. Cosmochim. Acta* **2009**, *73*, 3568–3578.
26. Shanon, R. D. Revised effective ionic radii and systematic studies of interatomic distances in halides and chalcogenides. *Acta Crystallogr.* **1976**, *A32*, 751–767.
27. Burns, R. G. *Mineralogical Application of Crystal Field Theory*, 2nd ed.; Cambridge University Press: Cambridge, 1993; p 551.
28. Lever, A. B. P. *Inorganic Electronic Spectroscopy*; Elsevier: New York, 1986; p 863.
29. Kwon, K. D.; Refson, K.; Sposito, G. Understanding the trends in transition metal sorption by vacancy sites in birnessite. *Geochim. Cosmochim. Acta* **2013**, *101*, 222–232.
30. Jensen, W. B. The place of zinc, cadmium, and mercury in the periodic table. *J. Chem. Educ.* **2003**, *80*, 952–961.
31. Gerloch, M.; Constable, E. C. *Transition Metal Chemistry: The Valence Shell in d-Block Chemistry*; VCH Publishing: New York, NY, 1994; p 211.
32. Peacock, C. L.; Sherman, D. M. Sorption of Ni by birnessite: Equilibrium controls on Ni in seawater. *Chem. Geol.* **2007**, *238*, 94–106.
33. Villalobos, M. The role of surface edge sites in metal(loid) sorption to pooly-crystalline birnessites. *Advances in the Environmental Biogeochemistry of Manganese Oxides*; ACS Symposium Series 1997; Americal Chemical Society: Washington, DC, 2015; Chapter 4.
34. Takahashi, Y.; Manceau, A.; Geoffroy, N.; Marcus, M. A.; Usui, A. Chemical and structural control of the partitioning of Co, Ce, and Pb in marine ferromanganese oxides. *Geochim. Cosmochim. Acta* **2007**, *71*, 984–1008.
35. Kwon, K. D.; Refson, K.; Sposito, G. Surface complexation of Pb(II) by hexagonal birnessite nanoparticles. *Geochim. Cosmochim. Acta* **2010**, *74*, 6731–6740.

36. Zhu, M.; Ginder-Vogel, M.; Sparks, D. L. Ni(II) sorption on biogenic Mn-oxides with varying Mn octahedral layer structure. *Environ. Sci. Technol.* **2010**, *44*, 4472–4478.
37. Manceau, A.; Marcus, M. A.; Grangeon, S.; Lanson, M.; Lanson, B.; Gaillot, A. C.; Skanthakumar, S.; Soderholm, L. Short-range and long-range order of phyllomanganate nanoparticles determined using high-energy X-ray scattering. *J. Appl. Crystallogr.* **2013**, *46*, 193–209.
38. Baron, V.; Gutzmer, J.; Rundlöf, H.; Tellgren, R. The influence of iron substitution on the magnetic properties of hausmannite, $Mn^{2+}(Fe,Mn)_2{}^{3+}O_4$. *Am. Mineral.* **1998**, *83*, 786–793.
39. Åsbrink, S.; Waśkowska, A.; Gerward, L.; Olsen, J. S.; Talik, E. High-pressure phase transition and properties of spinel $ZnMn_2O_4$. *Phys. Rev. B* **1999**, *60*, 12651.
40. Momma, K.; Izumi, F. VESTA 3 for three-dimensional visualization of crystal, volumetric and morphology data. *J. Appl. Crystallogr.* **2011**, *44*, 1272–1276.

Chapter 4

The Role of Surface Edge Sites in Metal(loid) Sorption to Poorly-Crystalline Birnessites

Mario Villalobos*

Geochemistry Department, Instituto de Geología Universidad Nacional Autónoma de México (UNAM) Ciudad Universitaria, Coyoacán, México 04510, D.F.
***E-mail: mar.villa@stanfordalumni.org**

Birnessite sorption reactivity is typically associated with cation metal sorption at internal vacancy sites, through a highly favorable tridentate configuration. However, poorly-crystalline birnessites are also characterized by their high specific surface areas. This brings into play a considerable number of reactive dangling oxygen bonds present at the edges of their structural sheets, which in most cases surpass those present at vacant sites on basal planes. In this chapter the importance of edge surface reactivity for birnessites will be reviewed in the context of ion adsorption and oxidation. Fundamental birnessite/water interfacial chemistry will be discussed, including bond strength analyses; and chemical and spectroscopic evidence will be presented for oxyanion As(V) adsorption at birnessite edge sites. In the case of heavy metal cation binding, competition between basal plane vacancies and sites at the edges will be presented for Pb(II), Cu(II) and Ni(II). Other potential ions will be discussed.

Introduction

Poorly-crystalline birnessites are structurally disordered layered Mn oxide minerals, comprising randomly arranged stacked sheets of edge-sharing octahedra that contain cation vacancies (Figure 1), and thus show a very high affinity

In Advances in the Environmental Biogeochemistry of Manganese Oxides; Sparks, et al.;
ACS Symposium Series; American Chemical Society: Washington, DC, 2015.

for cation sorption. They are also strong oxidants through electron exchange reactions that take place at their mineral/water interface; and they even show a non-negligible anion adsorption capacity.

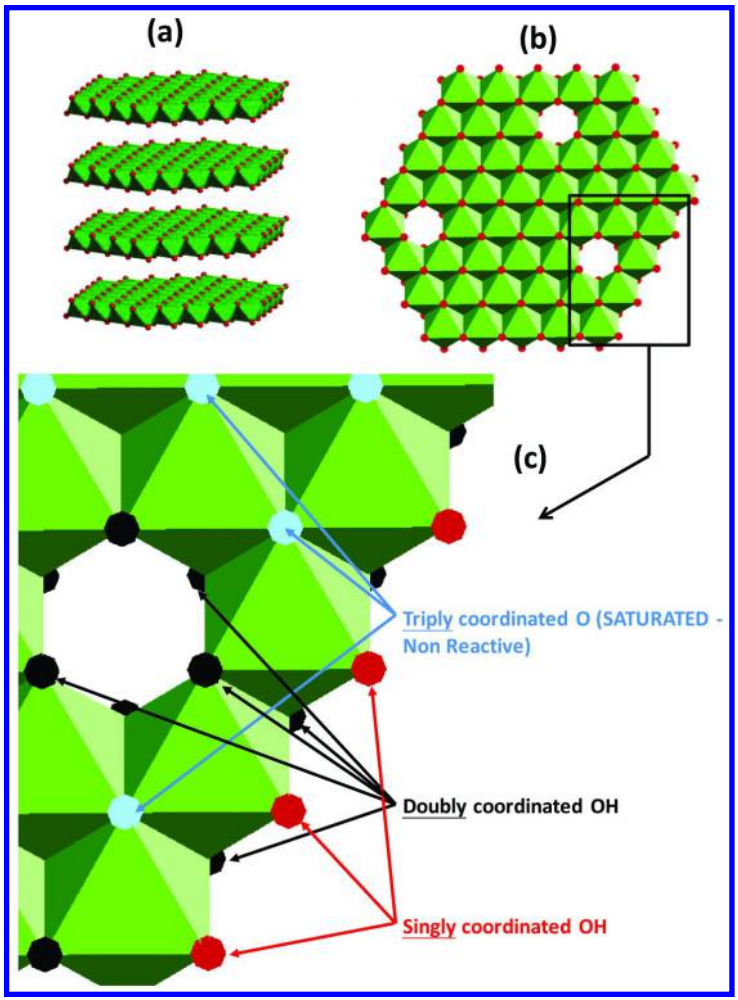

Figure 1. Simplified structure of Mn(IV) birnessites (with the Mn atoms located at the centers of each octahedron), showing ***(a)*** *the sheet configuration of one particle with a four-layer stacking (for ease, no interlayer water molecules, cations, nor vacant sites are depicted, nor is the random stacking of the sheets made evident);* ***(b)*** *the structural details of a component sheet, explicitly depicting the Mn-vacant sites present in poorly-crystalline specimens; and* ***(c)*** *a magnified section of the sheet in (b) identifying the three different oxygen coordinations present, both internally and at the particle edges, and color-coded for ease in their identification (in the digital web-based version).*

In Advances in the Environmental Biogeochemistry of Manganese Oxides; Sparks, et al.;
ACS Symposium Series; American Chemical Society: Washington, DC, 2015.

In the scheme of these different reactions, this chapter presents a review and discussion of the current knowledge on the role that edge sites play on the sorption behavior of birnessites. The surface area contributed by the sheet edges appears to be important, and in some cases may be crucial, for an accurate and complete description of the reactivity of these widespread layered minerals, as will become evident in the developments of the following sections.

Electron transfer reactions for oxidation of vulnerable species appear to occur exclusively on the birnessite particle edges (at least for anionic species), and as such, edge sites constitute the location where reductive dissolution of manganese from the solid birnessite mineral takes place.

Given that the particles of poorly-crystalline birnessites occur in the nanometer size regime, and thus expose high specific surface areas (SSAs), an important contribution of particle edges to the measured SSA is expected with respect to the two outermost basal {001} planes of the particles. Therefore, a high participation of oxygen dangling bonds at particle edge sites is bound to take place as birnessites react towards protons and ions. Two main reactive oxygen sites are present at the edges: those bound to only one Mn atom (singly-coordinated sites), and those bound to two Mn atoms (doubly-coordinated sites) (Figure 1). From a surface complexation perspective, important reactivity differences between the two types of edge sites are thus expected, including their affinities towards proton and electrolyte ions.

A combination of high relative concentrations and high oxygen valence insatisfaction at edge sites is expected to render them highly reactive towards metal(loid) sorption, effectively competing against layer vacancies normally identified in birnessites as the locations for cation binding. Conversely, edge sites are the sole locations expected for anion adsorption on birnessites, since strong anionic electrostatic repulsion will occur at basal plane vacant sites.

In addition, particle edge structural terminations are likely to affect layer vacancy content estimations in small-sized birnessites, when using methods based either on total cation contents (e.g., of electrolyte cations) from wet-chemical sorption data, or on incomplete (< 6) Mn second shell near-neighbors around each Mn center (Figure 1), such as X-ray Absorption Spectroscopy (XAS), which will highly deviate from the theoretical numbers expected in the internal structure. And even methods based on X-ray scattering techniques that don't explicitly consider the under-coordinated Mn atoms at the particle edges may yield vacancy overestimations. This will in turn produce errors in the determinations of specific structural formulas for the different birnessite varieties.

Structural Models for Birnessite Reactivity

The discussion of the structure and reactivity of birnessite particle edges must begin with a description of the internal birnessite structure (i) because the particle edges represent locations where the internal site arrangement is necessarily interrupted, leaving broken (dangling) oxygen bonds from the original structure exposed to the aqueous phase; and (ii) since certain structural similarities will become apparent between reactive internal and external edge sites. In this section

In Advances in the Environmental Biogeochemistry of Manganese Oxides; Sparks, et al.;
ACS Symposium Series; American Chemical Society: Washington, DC, 2015.

a simplified model of the poorly-crystalline birnessite structure is offered, with the goal of introducing the different reactive sites present, and particularly focusing on those expected at the particle surface edges, which will set the baseline for discussing their reactivity in the following sections.

Birnessites are layered structures of pure Mn (IV) (Figure 1a) or mixed Mn(IV)/(III) oxides [sometimes containing variable amounts of Mn(II) [and Mn(III)] at the interlayer space – although Mn(II) may be envisioned as just one more type of the different heavy metal cations that birnessites can sorb]. Their sheets consist of Mn-O octahedral units linked to one another by sharing six of their 12 edges (*1*, *2*). The layer symmetry is believed to be hexagonal or nearly-hexagonal, depending on the Mn(III) content, based on X-ray diffraction data; but more recently, a monoclinic symmetry deviating considerably from hexagonal was proposed using atomic pair distribution function (PDF) analysis from high energy X-ray scattering (*3*).

Layers in birnessite crystals are stacked either in an orderly or a disorderly (i.e., random) fashion, typically for crystalline or poorly-crystalline birnessite structures, respectively. The interlayer space of birnessites is occupied by water molecules and cations (and protons). The centers of the octahedral units of the basal planes in the layers are composed mostly of Mn(IV), although a certain proportion of Mn-vacant sites occur (Figure 1b and c), and in some cases the proportion of these vacancies is decreased through their occupation with Mn(III) (which may also occupy interlayer space above vacancies). In the extreme case of Mn(III) layer substitution, the structure deviates from a hexagonal (or monoclinic) symmetry, to form a triclinic highly crystalline birnessite, through the presence of an orderly arrangement of Mn(III) atoms in the layers, and no vacant sites remaining (*4*).

Reactive oxygen groups in birnessites, responsible for sorption and/or oxidation reactions, may be classified according to either structural or configurational criteria, or to their locations in the birnessite structure:

Type of Mn Atom Coordination

From the standpoint of the number of Mn(IV) atoms to which surface oxygens are coordinated, mainly three different types of reactive oxygen groups may be identified in birnessites (Figure 1c):

1) $Mn\text{-}O^{-1.33}$: Singly coordinated sites,
2) $Mn_2\text{-}O^{-0.67}$: Doubly coordinated sites,
   $Mn_2Mn(III)\text{-}O^{-0.17}$: Triply-coordinated sites (not shown in Figure 1c)

All these sites show incomplete oxygen coordination, the charges shown being the remnant oxygen charges calculated using simple Pauling bond strengths of ⅔ for Mn(IV)-O bonds and ½ for Mn(III)-O bonds. Minor amounts of other groups may occur, for example if a Mn(III) octahedron occurs adjacent to a vacant site or to another Mn(III) octahedron, or at the edges of a layer, but given their relatively minor importance, especially for natural biologically produced birnessites, they will not be discussed here.

In Advances in the Environmental Biogeochemistry of Manganese Oxides; Sparks, et al.;
ACS Symposium Series; American Chemical Society: Washington, DC, 2015.

The negative oxygen charges in all three sites listed above yield a natural tendency towards cation binding (including protons), and their affinity may be expected to decrease in the order listed above. The third one probably binds cations in an outer-sphere configuration; the first two most likely show various degrees of protonation depending on pH, and singly-coordinated sites may even be expected to attain a positive charge upon double protonation at low pH, and thus are identified as the location for anion binding to birnessites.

A more accurate bond-valence analysis suggests that indeed both singly- and doubly-coordinated oxygens are stable in protonated forms: Mn-OH_2 and Mn_2-OH (Table 1), which upon deprotonation as pH is raised would yield sites with net negative proton charges. Notwithstanding, it is likely that singly-coordinated doubly-protonated sites (Mn-OH_2) do attain a certain degree of positive charge, and thus are net anion adsorbents, at least under a certain low pH regime.

Table 1. Bond-Valence Analysis for Reactive Surface Functional Groups on Mn (IV) Birnessites[a].

SURFACE SITES[c]	*Σs_{m-o} at Oxygen (valence units – v.u.)*[b]		
	No H-bonds	*With H-bonds*[d]	*Prediction of occurrence*[e]
Singly-coordinated Oxygens			
Mn-$O^{4/3-}$	0.67	<0.93	Highly Unlikely
Mn-$OH^{1/3-}$	1.35-1.55	<1.81	Plausible
Mn$OH_2^{2/3+}$	**2.04**-2.44		**Highly Plausible**
Doubly-coordinated Oxygens			
Mn_2-$O^{2/3-}$	1.34	<1.60	Plausible
Mn_2-$OH^{1/3+}$	**2.04**-2.23		**Highly Plausible**
Triply-coordinated Oxygens			
Mn_3-O^0	**2.02**		**Highly Plausible**

[a] Non-reported calculations denote obvious bond oversaturation. [b] ***s*** for O-H^- ranges from 0.68 to 0.88 v.u. based on a bond length range from 0.95 to 1.03 Å (*5*). [c] Groups in boldface denote most stable groups. The charge assigned is the result of simple Pauling bond strength calculations. [d] ***s*** for hydrogen bonds ranges from 0.13 to 0.25 v.u. based on a bond length range from 1.65 to 2.50 Å (*5*). [e] Based on the fact that under saturation of oxygen groups (s<2) has low probability of occurrence, and oversaturation has negligible probability since no compounds with oversaturated O bonds are known to exist (*5*).

Triply-coordinated sites to Mn(IV) atoms (Mn_3-O) form the backbone of the layer structures and are considered non-reactive because the oxygen valence in this coordination is completely satisfied (Figure 1c).

In Advances in the Environmental Biogeochemistry of Manganese Oxides; Sparks, et al.;
ACS Symposium Series; American Chemical Society: Washington, DC, 2015.

Basal-Plane *vs.* Layer Edge Reactivity

Reactive sites within the basal planes of the layers (Figure 1c) are comprised of doubly- and triply-coordinated sites listed above. The former occur on Mn vacant sites, and the latter on Mn(III) occupied sites. Therefore, the proton charge they bear is negative, and cation (or proton) adsorption exclusively is expected in the basal plane layers. On the actual octahedral sites the total charge expressed would be for vacant sites evidently -4.0 (=-0.67x6, including both sides of the octahedron), and -1.0 (=-0.17x6), for Mn(III) substituted sites.

At the external edges of the layers, dangling oxygen bonds show singly- and doubly-coordinated sites listed above, in approximately equal proportions (Figure 1c). The small particle sizes and high specific surface areas (SSAs) of poorly-crystalline birnessites, suggest that these reactive sites may encompass an important contribution to the total reactive site concentration of birnessites. Evidently, this will depend on the specific content of vacancies. Figure 2 shows rough estimations of the contributions of basal plane sites *vs.* external edge sites as a function of birnessite particle size in poorly crystalline samples, for two vacancy contents close to recently reported estimates (*2*, *3*): 6% and 15%, normalizing all sites as monovalent sites from a simple Pauling bond strength analysis.

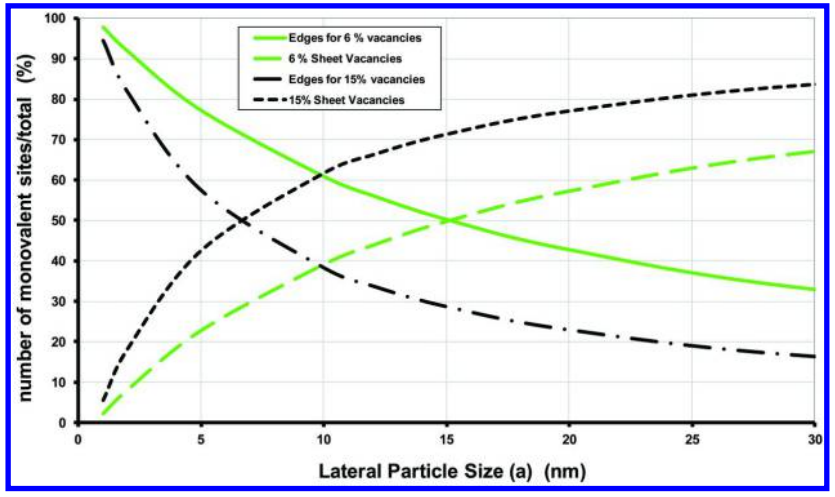

Figure 2. Relationship between lateral particle size of an ideal birnessite sheet and estimates of the relative contributions of reactive edge sites and vacant sites, and two different sheet vacancy contents.

It is evident from Figure 2 that for a 6% vacancy content, edge sites contribute above 33% of the total reactive sites for lateral particle sizes below 30 nm, becoming predominant at particle sizes below 15 nm. If the vacancy content

In Advances in the Environmental Biogeochemistry of Manganese Oxides; Sparks, et al.;
ACS Symposium Series; American Chemical Society: Washington, DC, 2015.

is increased to 15%, obviously these limiting particle sizes also decrease, to 12 nm and 6.5 nm, respectively. This analysis strongly suggests that at the particle sizes determined for poorly-crystalline birnessites, edge sites cannot be ignored vis-à-vis vacant sites.

Nevertheless, a controversial issue that still exists regarding the reactivity of these edge sites is whether they contribute to cation binding in a significant manner; or in other words, whether their affinity towards cations is sufficiently high to render them competitive against the highly stabilizing basal plane layer vacant site configuration. In contrast, edge sites are the only groups considered responsible for anion adsorption, since internal (vacant) sites are highly negatively-charged. Further details and evidences on these issues will be developed in the corresponding sub-sections below.

External (Surface) *vs.* Internal Reactivity

It is a common practice to normalize adsorption data by the specific surface area (SSA) of the solid investigated *in lieu* of normalizing by mass, with the goal of eliminating particle size effects. However, in the case of layered minerals with internal reactivity, such as birnessites, this normalization is misleading because the SSA, measured through experimental BET N_2 gas adsorption, accounts for all external area exposed, i.e., particle edges plus the two external basal planes per particle. The practice of applying this SSA normalization to birnessites is common, and operational reasonings may be invoked. However, there are two reasons why this normalization is incorrect, and should be avoided, or performed with caution, at best: (i) Reactive sites on basal planes occur only at positions where vacancies or isomorphic substitutions take place, i.e., they do not occur across the whole basal plane surface; in contrast, edge sites are all potentially reactive and occur in a highly regular arrangement across the whole particle edge surface of each birnessite sheet (Figure 1). (ii) Reactive sites on basal planes occur partly on the external surface, and partly on internal sites (except for one-sheet particles); in this manner, for layered minerals with more than two layers per particle, these reactive sites will occur predominantly on internal area. Therefore, the SSA of the birnessite will bear no relation to this internal reactivity, because there is no *a priori* relationship between SSA and vacancy content.

Taking the above into account, for adsorption reactions occurring only on one of the location types, e.g., oxyanion adsorption on edges (*cf.* corresponding section below), normalizing adsorption data by SSA will invariably yield underestimated values, arising from an overestimated reactive SSA. Conversely, for sorption reactions taking place on sites at both locations, *e.g.*, proton adsorption, or certain heavy metal ion adsorption such as Pb(II) (*cf.* corresponding section below), the SSA-normalized values are not indicative of the actual sorption mechanism, and may seem disproportionately high, especially at high sorbate loadings, given that considerable binding takes place in the internal layer structure. Additionally, in the latter cases the site density expected for each location is quite different,

In Advances in the Environmental Biogeochemistry of Manganese Oxides; Sparks, et al.;
ACS Symposium Series; American Chemical Society: Washington, DC, 2015.

and may bring about important thermodynamic modeling errors if treated as one single parameter. Therefore, site density values should be treated separately.

One important property of mineral colloidal particles that manifests their external charging behavior is their isoelectric point (IEP), which is measured in electrophoretic experiments from *zeta* (ζ) potential measurements as a function of pH. Away from this IEP the particles adopt a charge that is separable from a certain fraction of their counterions when subjected to attraction by an oppositely-charged electrode, allowing them to travel towards this electrode. The sheer (slipping) plane is located somewhere within the diffuse layer of counterions in the solid/aqueous interface (*6*), in which only external sites are expected to play a role.

Electrophoretic experiments as a function of pH are particularly interesting for minerals with layered structures like birnessites because they may be envisioned to select for external site reactivity exclusively. Internal site charges are counterbalanced by internal (interlayer or in-layer) cations not expected to slip off, because this would entail rupturing the layer arrangement. This means that interfacial proton-charge properties of minerals like birnessites investigated through ζ potential measurements are expected to express only at the outer sections of the structure, and the internal proton charges are likely "invisible" to outside electrode stimuli. This of course is not the case for birnessites consisting of 1-2 layers per particle.

Birnessites have very low IEPs, ranging from pH 1.5 to 2.5 (*7–11*), rendering them highly acidic minerals that, in average, express negatively-charged surface sites at most pH values, brought upon by deprotonation. External sites comprise all particle edge sites, but only external basal-plane sites corresponding to the two outermost layers of the particles (Figure 1a). In this respect, two characteristics will increase edge site reactivity in relation to external basal-plane site reactivity: (i) smaller particles in the lateral (i.e., *a*-*b*) direction, but (iii) larger particles in the *c*-direction because the same two external basal planes will be present regardless of the size, i.e., for an ever growing contribution of particle edges as the number of layers increases.

At pH values above 2-2.5, birnessites have a net negative proton charge. However, this does not necessarily mean that ALL external sites present are negatively-charged, because it is possible that a minor amount of positively-charged sites exist. If positive charges are indeed present, at least within a certain pH interval above 3, this means that they are probably not originating from the doubly-coordinated sites, since they comprise the majority of sites (basal plane sites plus approximately half of the particle edge sites – *cf.* Figure 1c). Therefore, doubly-coordinated sites are expected to be deprotonated and negatively-charged, thus cation adsorbing, but singly coordinated sites may maintain a highly-protonated and thus positively-charged status at pH values above 3. This will become particularly meaningful when discussing anion adsorption capacities of birnessites, in the following section.

In Advances in the Environmental Biogeochemistry of Manganese Oxides; Sparks, et al.;
ACS Symposium Series; American Chemical Society: Washington, DC, 2015.

Evidence of Edge-Site Reactivity

Oxyanion Adsorption and Oxidation

Arsenate Adsorption

Singly-coordinated groups on the external layer edges have been identified by Extended X-ray Absorption Fine Structure (EXAFS) Spectroscopy as the binding sites for oxyanion adsorption on birnessites. This has been demonstrated in detail particularly for arsenate (*11–14*), which binds to two adjacent sites of the birnessite edges to form a double-corner sharing (DCS) or bidentate bridging surface complex (Figure 3). The complex configuration was identified through a distance of 3.15 to 3.22 Å of As(V) to nearly two Mn near neighbor atoms (Table 2). This DCS complex occurs regardless of loading, pH, birnessite type, and presence of pre-sorbed metals(II).

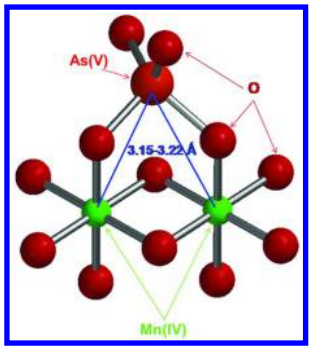

Figure 3. Structure of a double-corner sharing (DCS) or bridging bidentate arsenate complex formed on singly-coordinated sites at the birnessite particle edges. Atoms are not drawn to scale.

Despite the very low pH values of the isoelectric points (IEPs) of birnessites (around 2), (*7–11*), considerable adsorption of As(V) has been measured at up to near-neutral pH values. Figure 4 shows As(V) adsorption isotherms on two Mn(IV) birnessites of different particle sizes, at two different pH values: 3 and 6. The adsorption maxima are evidently higher at pH 3 than at pH 6 because of the negative proton charge increase as pH increases. Despite the high adsorption capacities shown, the initial slopes of the isotherms denote low affinity because of the repulsive electrostatic effect exerted by the net negative proton charge of the birnessites above pH 2.5.

In Advances in the Environmental Biogeochemistry of Manganese Oxides; Sparks, et al.;
ACS Symposium Series; American Chemical Society: Washington, DC, 2015.

Table 2. Results of As K-edge EXAFS for Second Atom (Mn) Near-Neighbors, for Different Birnessites, Under Different Conditions

	Coordination sphere:			*As Mn*		
Birnessite Type[a]	*SSA* (m^2/g)	*Γ* ($\mu mol/m^2$)	*pH*	*N*	*R*(Å)	σ^2(Å)
Acid Birnessite[b]	39	0.18	6.0	1.4	3.17	0.003
δ-MnO_2[b]	114	0.18	6.0	1.7	3.18	0.003
δ-MnO_2 /Zn(II)[b,c]	114	0.18	6.0	1.4	3.18	0.002
δ-MnO_2 /Pb(II)[b,c]	114	0.18	6.0	1.2	3.18	0.002
Acid Birnessite[b]	39	1.60	6.0	1.4	3.17	0.003
Acid Birn. /Pb(II)[b,c]	39	1.60	6.0	1.2	3.18	0.002
Acid Birnessite[b]	39	1.90	6.0	1.5	3.19	0.004
δ-MnO_2[b]	114	2.30	3.0	1.7	3.17	0.003
δ-MnO_2[d]	295	0.05	4.6	1.7	3.16	0.004
δ-MnO_2[d]	295	0.10	5.4	1.9	3.15	0.004
Acid Birnessite[d]	150	0.08	4.7	2.2	3.18	0.004
Acid Birnessite[d]	150	0.57	4.7	2.0	3.16	0.004
Acid Birnessite[e]	32	31.3[f]	6.5	2.0	3.22	0.002

[a] Birnessites are composed purely of Mn(IV) and synthesized by reducing Mn(VII) with hot HCl, or with Mn(II), for acid birnessite or δ-MnO_2, respectively. [b] Data taken from (*11*). [c] The metals(II) added correspond to 10:1 total metal(II):As(V). [d] Data taken from (*13*). [e] Data taken from (*12*). [f] Initial concentration (adsorbed concentration was not reported). One can infer As(V) surface saturation.

The adsorption values shown in Figure 4 are underestimated because SSA normalization includes a portion of the external area originating from the two outermost basal planes of the particles where no As(V) adsorption occurs. Therefore, if the data were corrected by using exclusively the particle edge SSA, which is evidently lower than the total SSA, all adsorption data would be higher. The large differences reported in adsorption between birnessites showcases the problems encountered when normalizing by total SSA, as discussed previously.

Despite this underestimation (the actual calculation cannot be performed because the relative contributions to the total SSA of birnessites are unknown), the maxima reached are quite high and range from 1.70 μmol/m^2 to 3.2 μmol/m^2. These values coincide and even surpass the As(V) adsorption maxima for goethite, of around 2 μmol/m^2 for similar pH values (*15*), i.e., under favorable electrostatic conditions. This comparison underscores the large reactive site density of birnessite that participates in oxyanion adsorption located on its particle edges.

In Advances in the Environmental Biogeochemistry of Manganese Oxides; Sparks, et al.;
ACS Symposium Series; American Chemical Society: Washington, DC, 2015.

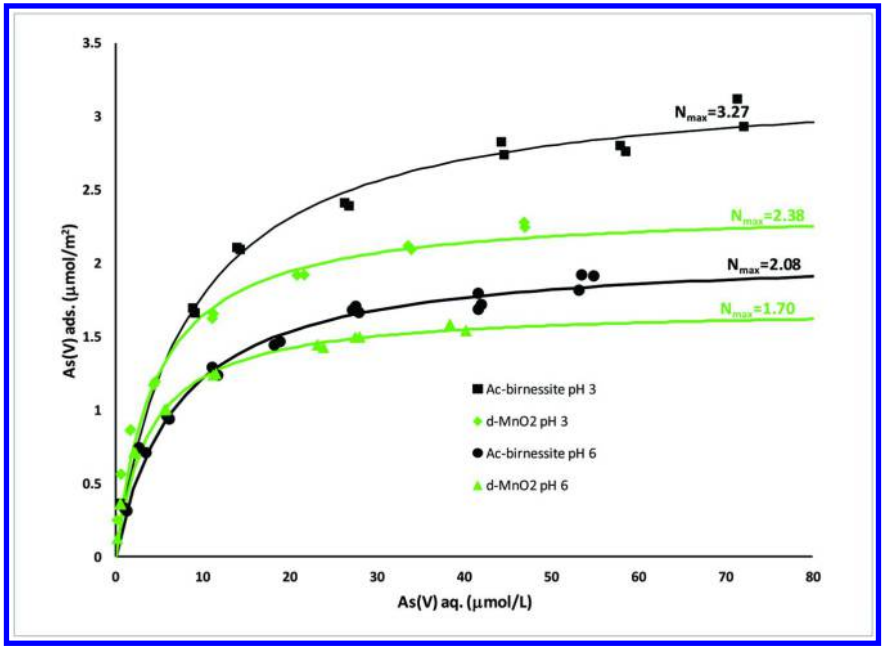

Figure 4. As(V) adsorption isotherms on birnessites at two pH values, and ionic strength of 0.01 M $NaNO_3$ normalized by total surface area. Values above the lines are the adsorption maxima calculated from the corresponding Langmuir isotherm model. (data taken from (11))

This high As(V) anion adsorption capacity on birnessites suggests that singly-coordinated sites at the birnessite particle edges may still be protonated and positively-charged at pH 6. However, the net birnessite charge would still be negative because doubly-coordinated sites would be deprotonated and negatively-charged, and occur in higher net concentrations than singly-coordinated sites (Fig 1c).

The lower maxima shown for δ-MnO_2 as compared to acid birnessite are most likely an artifact, because δ-MnO_2 has a smaller particle stacking layer size (2-3 *vs*. 6 layers) (*2*), which makes for a larger error of using SSA for normalizing, since a larger proportion of the total external surface area in δ-MnO_2 is contributed by the outermost basal planes, which do not bind arsenate.

In Advances in the Environmental Biogeochemistry of Manganese Oxides; Sparks, et al.;
ACS Symposium Series; American Chemical Society: Washington, DC, 2015.

Adsorption or Oxidation of Other Oxyanions

Other oxyanions identified to bind to birnessites are phosphate (*16–18*), selenite, (*13*, *19*), and borate (*20*, *21*). Although, strictly speaking, because of the high pKa value of borate (9.24) (*22*), its adsorption mechanism below pH 9 takes place via the neutral boric acid species, even if the final surface complex is deprotonated. No spectroscopic work has been performed to determine the binding configurations of these oxyanions, but as for arsenate it is presumed that they bind exclusively to the birnessite particle edges, and probably in a similar bidentate bridging fashion (Figure 3).

Phosphate

From wet-chemical adsorption isotherm experiments, phosphate was found to bind to a δ-MnO_2 at seawater pH (=8) with a maximum of 1.79 μmol/m^2 (*16*), which surpasses the value attained for arsenate at pH 6 (Figure 4). Also, a loading of 0.56 μmol/m^2 showed adsorption maxima in a range of pH values from 3 to 5.5. These data support the hypothesis that singly-coordinated sites at the particle edges may be, at least partially, positively charged at near-neutral pH values, despite the overall particle charge being negative. No spectroscopic investigation of the surface phosphate complex configuration on birnessites has been performed.

Selenite

Se(IV) oxyanion ($HSeO_3^-$ – pKa_1=2.62) has also been found to adsorb to poorly-crystalline birnessites, under experimental conditions that minimize its surface oxidation, i.e., short equilibration times (< 24 h) and pH values that are not exceedingly low (pH 5 to 7) (*13*). However, the two EXAFS Se(IV)-Mn shell distances obtained (3.07 Å and 3.49 Å), suggest that binding does not take place on Mn(IV) octahedra, but rather to Mn(III) and/or Mn(II) originally present in the synthesized birnessites structures. As such, the location of these selenite complexes is unclear, and although they are likely found on vacant layer sites, where Mn(II)/(III) atoms bind, it is not possible to rule out participation of Mn(II) atoms adsorbed on particle edge sites (see section below on heavy metal cation adsorption). The same can be said for selenite oxidation by birnessites, under larger equilibration times and lower pH values (*23*).

Borate

Borate [$B(OH)_3$ – pKa_1=9.24] adsorption maxima on poorly crystalline birnessites were found at pH values of 8.5 (*20*, *21*), with adsorbed concentrations normalized by mass close to those shown by goethite. DRIFT spectroscopy showed inner-sphere and outer-sphere trigonal complexes at the birnessite surface, and a probable tetrahedral boron surface complex, which if present is hidden by

In Advances in the Environmental Biogeochemistry of Manganese Oxides; Sparks, et al.;
ACS Symposium Series; American Chemical Society: Washington, DC, 2015.

metal-hydroxide IR bands (*21*). Based on this, surface borate complexes proposed for modeling adsorption data were: a monodentate inner-sphere neutral complex with $BO(OH)_2^-$, a bidentate inner-sphere negative complex with $BO_2(OH)_2^{2-}$, and an outer-sphere complex with neutral $B(OH)_3$ via hydrogen bonds to a birnessite surface group (*21*). Although not discussed in the work, complexes formed with the above anionic borate species have an implicit assumption that their formation occurs through reaction with positively-charged surface sites of birnessite. This again supports the hypothesis that singly-coordinated groups must be positively charged at pH values considerably above the IEPs of birnessites (i.e., pH > 2).

Arsenite Oxidation

Edge sites are also responsible for oxyanion oxidation, such as As(III) to As(V) (*24–26*), although technically at the pH values investigated below 9, As(III) is not an anion [$As(OH)_3$ – pKa_1=9.23] and is not subject to strong electrostatic attractions or repulsions. Therefore, it is possible that basal plane sites participate as well in oxidation of As(III), at least those found externally if access to interlayer space is sterically hindered. Oxidation of As(III) occurs too fast to be able to determine its binding configuration to the birnessite surface previous to being oxidized, but inner-sphere binding is required for the electron transfer reaction to take place.

Heavy Metal Cation Adsorption and Oxidation

Birnessites are excellent heavy metal cation sequesterers, given their net negative proton charge at most environmental pH values. Spectroscopic work has readily identified layer vacancies as the destination sites for these cations, where a strong binding is expected through the stabilizing potential of the three sites involved to form triangular tridentate complexes above the vacancies (Figure 1), and in some cases even fitting into the vacancy space to incorporate the metal into the layer, as may occur for Mn(III), Co(III), Ni(II) (*27*), and possibly Cu(II) (*28*). The role of edge sites in generalized cation adsorption is controversial mainly because it has not been extensively detected by spectroscopic techniques such as EXAFS. However, irrespective of their detection, the oxygen dangling bonds at edges, yielding negative proton surface charges, need to be counterbalanced by cations to ensure overall charge balance of the particles. Therefore, total cation content determined in poorly-crystalline birnessites is bound to yield an important fraction associated to the particle edges, and thus, minimal structural formula determinations for these minerals may highly overestimate interlayer cation contents.

Pb(II) Sorption

The most significant evidence of cation binding to birnessite particle edge sites has arisen from Pb(II) sorption investigations, perhaps because of the

In Advances in the Environmental Biogeochemistry of Manganese Oxides; Sparks, et al.;
ACS Symposium Series; American Chemical Society: Washington, DC, 2015.

particularly high adsorption affinity that birnessites show for Pb(II). Gathered evidence comprises wet-chemical data, EXAFS spectroscopy, and molecular modeling.

Sorption Isotherms Evidence

Pb(II) sorption maxima from isotherms performed on several poorly-crystalline birnessites at pH 5.8 clearly showed that the concentrations surpassed considerably the estimated contents of layer vacant sites, with values of maximum Pb/Mn_{total} in the birnessite structure reaching as high as 0.55 (*29*). A highly linear direct relationship was found between the Pb sorption maxima and the specific surface area (SSA) of the particular birnessite (Figure 5). The value of the intercept (0.0891) of this line corresponds to the portion of the Pb(II) concentration sorbed that is independent of the SSA, which may be attributed to binding above/below the layer vacant sites. This means that 8.91 mole % of the total sorbed Pb(II) in all analyzed birnessites binds above/below layer vacant sites and suggests that all poorly-crystalline birnessites in this analysis have a similar vacancy content.

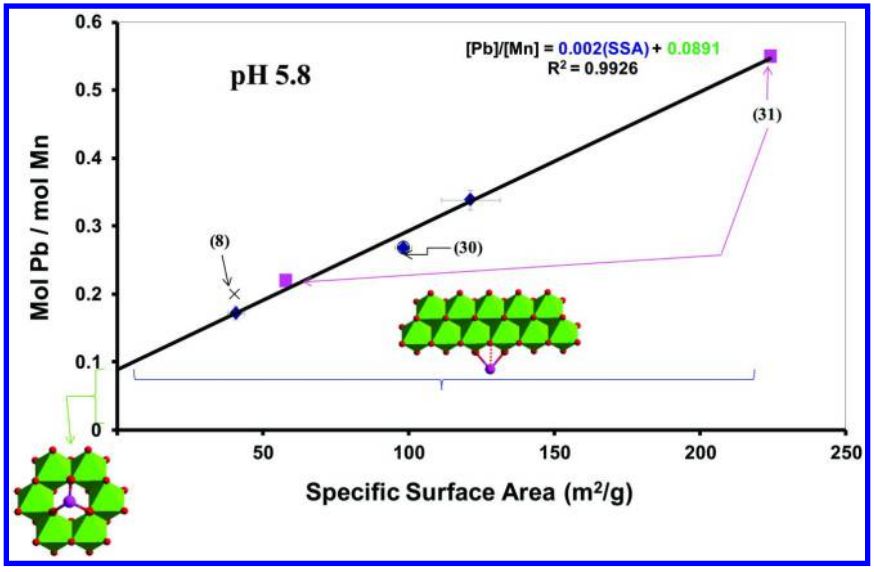

Figure 5. Pb(II) sorption maxima at pH 5.8 on poorly-crystalline birnessites as a function of their specific surface areas (modified from (29)). Data in blue diamonds were taken from (29), other data from (8, 30, 31). The structures shown are the specific structural assignments for Pb(II) binding corresponding to each portion of the linear behavior.

The slope (0.002) of the line in Figure 5 indicates the portion of the Pb(II) sorption behavior that depends on the SSA, i.e., on the particle size, and thus

In Advances in the Environmental Biogeochemistry of Manganese Oxides; Sparks, et al.;
ACS Symposium Series; American Chemical Society: Washington, DC, 2015.

may be assigned to the particle edges. The value may be translated as a 2% increase in Pb/Mn for every 10 m^2/g increase in the SSA of the birnessite. This essentially means that for birnessites with SSA>45 m^2/g, particle edge sites become predominant in the total birnessite Pb(II) sorption.

EXAFS Spectroscopy Evidence

The first attempts to model EXAFS data for Pb(II) sorption on birnessites did not yield detection of this seemingly important fraction of Pb(II) sorbed, because the Pb-Mn distance modeled matched a configuration consistent with occupation over vacancy sites (*8*). In principle it may be suspected that the binding energy of vacant sites is much higher than that on edge sites, so under non-saturated conditions for Pb(II) sorption, its vacancy occupation would be preferred, and therefore dominant in the EXAFS signals. However, even given a theoretical equal Pb(II) occupancy on both regions it is a fact that the number of near-Mn neighbors and a greater structural order would select for considerably stronger EXAFS signals for the vacant-occupied sites (six nearest Mn neighbors), as compared to the edge-occupied sites (two nearest Mn neighbors) (Figure 6). So, EXAFS spectroscopy in effect is considerably more sensitive to the vacancy-occupied Pb(II) complex than to potential edge Pb(II) complexes, and this is true for any cation binding in an inner-sphere mode.

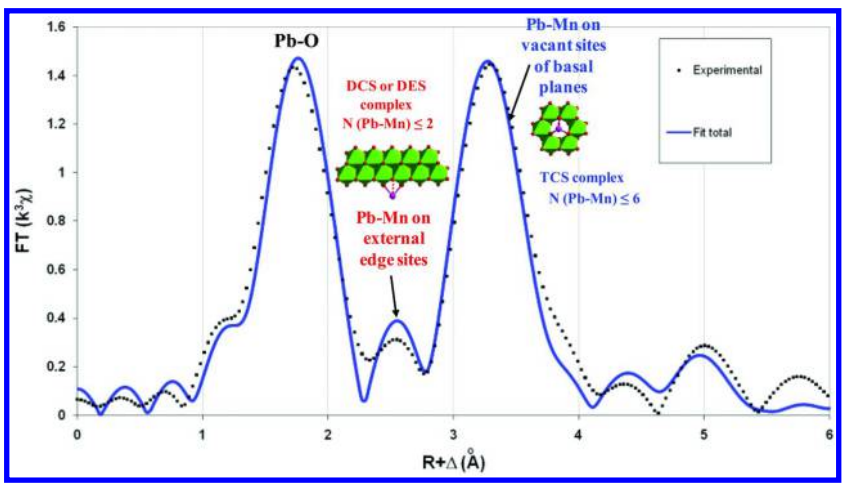

Figure 6. Fourier Transform of Pb L3-edge EXAFS experimental results and simulations of 1 mmol/g Pb on a biogenic layered Mn oxide. pH 5.8, 7-day equilibration. (data taken from (29))

Figure 6 shows an example for Pb(II) sorbed on a 98 m^2/g biogenic birnessite, in which the signal corresponding to the edge binding is clearly significantly weaker, close to the noise level, than the one arising from the vacancy site occupation.

In Advances in the Environmental Biogeochemistry of Manganese Oxides; Sparks, et al.;
ACS Symposium Series; American Chemical Society: Washington, DC, 2015.

The same EXAFS spectra were obtained for a series of birnessite analogs to the biogenic Mn oxide of Figure 6, and conditions ranging from Pb(II) loadings of 0.4 mmol/g to 2 mmol/g, 1 to 7 days equilibrations, and pH 5.8 and 7, in 0.01 M $NaClO_4$ or NaCl (*29*). This similarity in spectra, especially regardless of the Pb(II) loading, suggests that the affinity for Pb(II) binding is similar on both types of sites.

The Pb-Mn distance for the vacancy-occupied triple-corner sharing (TCS) complex was identified as 3.70-3.74 Å (*8*, *29*), and if no other Pb-Mn shell was defined in the modeling, the number of Mn neighbors for this shell obtained was N=3.5, in contrast to the theoretical N=6 (see inset structure in Figure 6). The closer Pb-Mn distance was modeled as an edge-sharing (ES) mononuclear bidentate complex at 3.31 Å (*32*), as a double-corner sharing (DCS) complex at 3.50-3.55 Å (*29*), or as a double-edge sharing (DES) complex at 3.2 Å (*33*) (Figure 7). This latter complex at the particle edges was even found to have a higher affinity than the TCS complex on vacancies when Pb(II) loadings were low (*33*), and involves two singly-coordinated and one doubly-coordinated oxygens. Its contribution at saturated surface Pb(II) conditions was found from EXAFS to range from *ca*. 50% to 75%, in direct close dependence to the SSA of the birnessite, and in agreement with the wet chemistry results (Figure 5) (*29*).

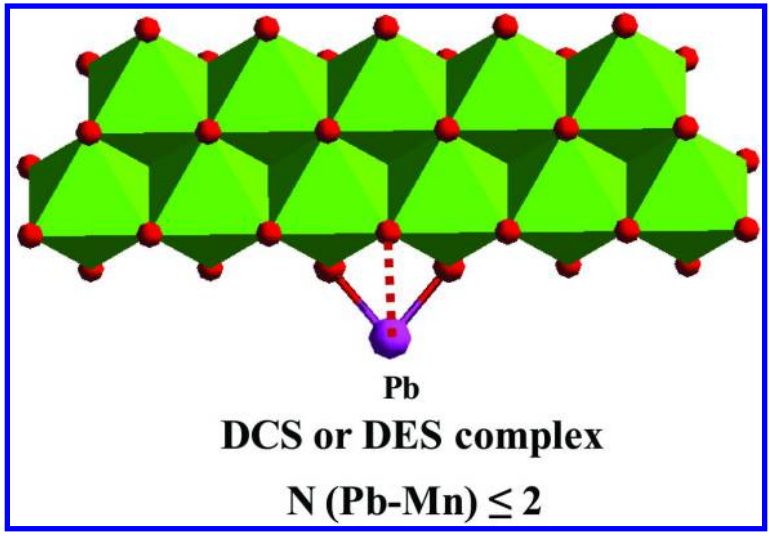

Figure 7. Configuration of the Pb(II), Ni(II), or Cu(II) surface complexes on the particle edges of poorly-crystalline Mn(IV) birnessites, as determined by EXAFS. Effective N may be considerably lower than 2.

Computational Molecular Modeling Evidence

Spin-polarized planewave density functional theory was used to study the Pb(II) complexes formed on birnessite (*34*), in an attempt to distinguish the stabilities between the surface complexes suggested through modeling of

In Advances in the Environmental Biogeochemistry of Manganese Oxides; Sparks, et al.;
ACS Symposium Series; American Chemical Society: Washington, DC, 2015.

experimental Pb-EXAFS data above (*29*, *33*). At the particle edges the relative stabilities of DES and DCS complexes (Figure 7) were evaluated as a function of the protonation status of the oxygen sites involved, as well as the hydration state of the complexes. It was found that the DES complex was more stable, especially under non-protonated conditions or if the singly-coordinated oxygens were protonated, but not if the doubly-coordinated oxygen was protonated. The DCS complex could be stabilized if the local coordination environment was well hydrated, but it would coexist with the DES complex.

Sorption of Ni(II), Cu(II,) and Other Metal(II) Ions

Given the higher affinity that Pb(II) has shown for particle edge sites as compared to layer vacancy sites (*33*), it is rather strange that generalized binding of other metal ions to edge sites on birnessites has not been detected, except marginally for Ni(II), and Cu(II), which also show incorporation into the layer vacancies. This difference in behavior with Pb(II) may involve a much lower affinity of these other metal ions for edge sites.

A tridentate Ni(II) DES complex, was proposed at the edges of triclinic birnessite, which possesses no vacant sites, with an EXAFS Ni-Mn distance of 3.05, 3.09 or 3.49 Å (*35–37*). This complex was not detected in hexagonal H-birnessite or biogenic Mn oxides, which are composed of considerably smaller particles, but do contain layer vacancies. However, it was detected at particle edges of a Mn(III)-rich δ-MnO_2 where two adjacent Mn(III) octahedra occur (*37*). Its configuration is different from the above DES complex in that it "flips" from the sheet edge to the basal plane. In this new DES complex, Ni(II) is bound to two singly-coordinated Mn(III)-bound oxygens at the edge, and to one (outermost) triply-coordinated oxygen on the basal plane (for easy identification see the singly-coordinated oxygens at the top of Figure 7), but the Ni-Mn distances are similar to those for the "edge" DES complex.

A DCS or DES complex of Ni(II) on the particle edges of a Mn(IV)-δ-MnO_2, similar to the complex shown for Pb(II) in Figure 7, has also been detected with a Ni-Mn distance of 3.47-3.49 Å at high nickel loadings (*36–38*). However, this distance is the same as that shown for the TCS Ni(II) complex bound above/below vacancy sites, and thus is difficult to distinguish one from the other spectroscopically. The assignment of the Ni(II) surface complex to the particle edges was based on the low number of Mn near-neighbors obtained in the EXAFS modeling (mostly 3-4) (*36*), and by combining this modeling with DFT geometry optimizations (*37*). An important increase in the proportion of surface edge-bound Ni(II) was attained when the average Mn oxidation state of δ-MnO_2 was considerably decreased to 3.65 by inclusion of a large proportion of Mn(III) in the structure, to form the "flipped" complex described in the previous paragraph. This Mn(III) blocked vacancy sites previously available for Ni(II) binding. In the case of biogenic Mn oxides, detection of the potential Ni(II) complex at the edges of the particles may be further complicated or impeded by the presence of biological or organic cell material on the oxide surfaces (*27*),

In Advances in the Environmental Biogeochemistry of Manganese Oxides; Sparks, et al.;
ACS Symposium Series; American Chemical Society: Washington, DC, 2015.

which at best, if no surface blockage occurred (*39*), would complicate the XAS spectroscopic data interpretations and modeling.

Given that for other heavy metal cations no extensive evidence of binding to the particle edge sites has been reported, the sorption maxima differences between Pb(II) (which binds to both edges and vacancies) and metals like Cu(II), Zn(II), and Cd(II) (which bind mostly only to vacancies) on various different birnessites were used to provide approximate estimates of edge site and vacancy site contents (*40*). For example, a 31.7 m^2/g poorly crystalline Mn(IV) birnessite yielded values between 1.25 and 1.5 mmol/g of vacant sites, and between 0.8 and 1.05 mmol/g of edge sites of equivalent valence. These values were obtained when comparing the sorption maxima for Cu(II), Zn(II), and Cd(II) (1.5, 1.25, and 1.35 mmol/g, respectively), to that for Pb(II))2.3 mmol/g) (*40*). Of course, these are gross estimations, which are also neglecting the fact that protons still pose a competition with cations at the pH of 4.5 in the experiments performed; but at least they allow estimates of the relative proportions of edge/vacant sites.

The large affinity differences for particle edge binding between Pb(II) and the above metal(II) ions has been made evident very recently by investigating Cu(II) and Ni(II) sorption on a δ-MnO_2 of extremely small particle size (254 m^2/g – 2-4 nm lateral sheet size) (*41*), in which edge sites would be expected to occur in considerably larger concentrations than layer vacancies (*cf.* Figure 2). This birnessite showed a disproportionate maximum concentration of Cu(II) sorbed at pH 6 of 0.72 mol Cu/mol Mn, with respect to its vacancy content estimates. Using Cu K-edge EXAFS modeling, the very low numbers of near-neighbor Mn atoms obtained (*ca.* 1-1.5) strongly suggested that Cu(II) was found mostly bound to the particle edges, as opposed to vacancies, and in configurations similar to those of Pb(II), as illustrated in Figure 7; and/or as Cu(II) dimers bound to surface edge sites. In contrast, previous spectroscopic studies on larger-sized birnessites found Cu(II) bound mostly to layer vacancies as a TCS complex, based on much larger numbers (5.4-6) of Mn near-neighbors (*28*, *42*).

A similar finding was obtained for Ni(II) sorbing to the same 254 m^2/g δ-MnO_2, but the Ni(II) adsorption maximum was significantly lower (*ca*. 0.165 Ni/Mn *vs*. 0.72 Cu/Mn) (*37*, *41*). This suggests a much lower binding affinity of birnessite toward Ni(II) than toward Cu(II), and yielded a major part of the Ni(II) still bound to vacancy sites (0.14 *vs*. 0.06 Ni/Mn) (*37*), despite the much larger contents expected of available edge sites as compared to vacancies in this δ-MnO_2 (*cf.* Figure 2).

The Cu(II)-Mn and Ni(II)-Mn distances found for the edge complexes of *ca*. 3.4 Å (*41*) and 3.47 Å (*37*), respectively coincide with the distances of the corresponding TCS complexes at vacancy sites. This similarity in metal(II)-Mn distances between complexes showcases a probable widespread difficulty among metal(II)-birnessite associations in detecting complexes formed at birnessite particle edges by XAS spectroscopy based solely on interatomic distances. Also, the low binding affinity of these divalent metals make it possible for a sizable fraction to be bound as outer-sphere complexes, and therefore difficult to detect by XAS.

Finally, many attempts at quantitatively describing cation sorption data on birnessites, by using Surface Complexation Models have found the need to include

In Advances in the Environmental Biogeochemistry of Manganese Oxides; Sparks, et al.;
ACS Symposium Series; American Chemical Society: Washington, DC, 2015.

at least two types of binding sites, described as low and high energy sites. These may well correspond to the two identified locations of reactive sites at the birnessite structure: particle edge sites, and layer vacant sites.

Cr(III) Oxidation

Cationic aqueous Cr(III) has been found to quantitatively oxidize to the oxyanion Cr(VI) when reacted with poorly-crystalline birnessites in the laboratory at pH values of 2.5 to 3.5 (*9*, *43*), and even at higher pH (*44*, *45*). A small particle-sized birnessite, δ-MnO_2 (272 m^2/g), yielded higher concentrations of Cr(VI) than acid birnessite (84 m^2/g) at equal solid mass concentrations. This inverse dependence on particle size (i.e., direct dependence on SSA) suggests that particle surface edge sites are involved in the oxidation mechanism, since the electron exchange reaction requires Cr(III) to bind to the birnessite structure (*46*). However, it does not preclude the likely participation of layer vacant sites.

Additionally, considerable fractions of the chromate oxyanion produced were found adsorbed to the birnessite surface after reaction, ranging from 26% to 32% of total Cr at pH values of 3 and 3.5, and from 20% to 44% at pH of 2.5, for δ-MnO_2. A lower percentage of 14% Cr(VI) adsorbed was found for acid birnessite (*9*). The adsorbed Cr(VI) was identified by EXAFS as an outer-sphere complex (*43*). These findings are quite meaningful to support the existence of positively charged sites on the particle edges, at pH values above the IEPs of birnessites [pH 1.5 to 2.5] (*7–11*), in which the net charge of the particles would be negative. Outer-sphere complexes of the Cr(VI) oxyanion (pKa_1=0.86) would not be possible if all sites on the birnessite surfaces were negatively charged at pH values above the IEPs. Therefore, this suggest again that singly-coordinated sites are the most likely candidates to bear a positive charge at pH values above the IEPs of birnessites, as was discussed under the oxyanion adsorption section above.

Large fractions of non-reacted Cr(III) were also found adsorbed on the birnessites as inner-sphere complexes, especially on δ-MnO_2, but it was not possible to identify the location of these complexes and to distinguish edge site from layer vacant site binding (*43*).

Implications of Birnessite Edge Site Reactivity

The presence of dangling bonds at birnessite sheet edges of small particle sizes is sufficiently high to yield an important, and sometimes predominant source of reactivity towards ion adsorption, through a variable proton charge behavior. Edge surface area is the sole location for anion binding capacity of birnessites [e.g., of As(V)], because of the likely presence of positive proton charge acquired on singly-coordinated sites. Edges are also the location where oxidation of ionic species takes place [e.g., of As(III)], although participation of basal plane vacant sites cannot be discarded, especially in the case of cation oxidation [e.g., of Cr(III)]. Finally, although interfacial chemistry would certainly point to a non-negligible cation binding capacity at these edge site locations, recent evidence for Cu(II) and Ni(II) binding suggests a much lower affinity of divalent

In Advances in the Environmental Biogeochemistry of Manganese Oxides; Sparks, et al.;
ACS Symposium Series; American Chemical Society: Washington, DC, 2015.

first-row transition metals for birnessite edge sites than to sheet vacancies, in contrast to Pb(II) for which the opposite occurs. Nevertheless, it is clear that doubly-coordinated sites present at edges must be counterbalanced by electrolyte cations most likely in an outer-sphere configuration. Other heavy metal divalent cations may show low enough affinities towards these sites to make them less important (i) in the face of the more energetic tridentate sites on layer vacancies, and (ii) to outcompete electrolyte cation binding on these sites.

In any case, anion and cation edge site reactivity in birnessites makes for an interesting location of interfacial chemistry research, with currently unanswered questions such as: What are the values of affinity constants of Pb(II) and first-row transition metals toward edge sites? and in comparison with those towards vacancy sites? Is there a contribution of outer-sphere complexation on edge sites occurring for the latter metals? Is there a difference between the point of zero net proton charge and the isoelectric point of birnessites? It appears that phosphate sorption to birnessite particle edges can be significant, but it has not been spectroscopically studied. Also, it would be helpful to develop models for the acid-base chemistry of the various reactive (internal and surface) sites in a separate manner, including the values of acidity constants, as well as to generate estimates of surface site densities. These and other questions makes birnessite interfacial edge site reactivity an interesting and exciting future area of research with challenging inquiries, whose answers will yield a more complete picture of the overall reactivity of poorly-crystalline birnessites.

Acknowledgments

I would like to express gratitude to my Ph.D. student Carlos Salazar-Camacho for his help in preparing Figure 3 and for generating the data shown in Figure 4 (*11*). Funding for part of the experimental data shown in this chapter is highly appreciated from the International Foundation for Science (IFS), Stockholm, Sweden, and the Organisation for the Prohibition of Chemical Weapons (OPCW), The Hague, The Netherlands, grant number W/3912-2. Also, generation of part of the data shown in this chapter was funded by the CONACyT through its Basic Sciences branch, grant number 153723. Thanks are also due to two anonymous reviewers who helped improve considerably the presentation of the manuscript, and also to guest editor Xionghan Feng, and to student Pablo Carrera for making me aware during the manuscript review process, of very recent publications showing evidences of Ni(II) and Cu(II) binding at the birnessite edge surface (*37*, *41*), which were incorporated in the manuscript during the revision stage.

References

1. Post, J. E. Manganese oxide minerals: Crystal structures and economic and environmental significance. *Proc. Natl. Acad. Sci. U. S. A.* **1999**, *96*, 3447–3454.

2. Villalobos, M.; Lanson, B.; Manceau, A.; Toner, B.; Sposito, G. Structural model for the biogenic Mn oxide produced by Pseudomonas putida. *Am. Mineral.* **2006**, *91*, 489–502.
3. Zhu, M. Q.; Farrow, C. L.; Post, J. E.; Livi, K. J. T.; Billinge, S. J. L.; Ginder-Vogel, M.; Sparks, D. L. Structural study of biotic and abiotic poorly-crystalline manganese oxides using atomic pair distribution function analysis. *Geochim. Cosmochim. Acta* **2012**, *81*, 39–55.
4. Lanson, B.; Drits, V. A.; Feng, Q.; Manceau, A. Structure of synthetic Na-birnessite: Evidence for a triclinic one-layer unit cell. *Am. Mineral.* **2002**, *87*, 1662–1671.
5. Bargar, J. R.; Towle, S. N.; Brown, G. E.; Parks, G. A. XAFS and bond-valence determination of the structures and compositions of surface functional groups and Pb(II) and Co(II) sorption products on single-crystal alpha-Al2O3. *J. Colloid Interface Sci.* **1997**, *185*, 473–492.
6. Davis, J. A.; Kent, D. B. In *Mineral-Water Interface Geochemistry*; Hochella, M. F., Jr., White, A. F., Ed.; Reviews in Mineralogy, Vol. 23; Mineralogical Society of America: Washington, DC, 1990; pp 177−260.
7. Sposito, G. *The Chemistry of Soils*, 1st ed.; Oxford University Press: Oxford, 1989; p 139.
8. Matocha, C. J.; Elzinga, E. J.; Sparks, D. L. Reactivity of Pb(II) at the Mn(III,IV) (oxyhydr)oxide-water interface. *Environ. Sci. Technol.* **2001**, *35*, 2967–2972.
9. Landrot, G.; Ginder-Vogel, M.; Livi, K.; Fitts, J. P.; Sparks, D. L. Chromium(III) oxidation by three poorly-crystalline manganese(IV) oxides. 1. Chromium(III)-Oxidizing Capacity. *Environ. Sci. Technol.* **2012**, *46*, 11594–11600.
10. Wang, Z. M.; Lee, S. W.; Kapoor, P.; Tebo, B. M.; Giammar, D. E. Uraninite oxidation and dissolution induced by manganese oxide: A redox reaction between two insoluble minerals. *Geochim. Cosmochim. Acta* **2013**, *100*, 24–40.
11. Villalobos, M.; Escobar-Quiroz, I. N.; Salazar-Camacho, C. The influence of particle size and structure on the sorption and oxidation behavior of birnessite: I. Adsorption of As(V) and oxidation of As(III). *Geochim. Cosmochim. Acta* **2014**, *125*, 564–581.
12. Manning, B. A.; Fendorf, S. E.; Bostick, B.; Suarez, D. L. Arsenic(III) oxidation and arsenic(V) adsorption reactions on synthetic birnessite. *Environ. Sci. Technol.* **2002**, *36*, 976–981.
13. Foster, A. L.; Brown, G. E.; Parks, G. A. X-ray absorption fine structure study of As(V) and Se(IV) sorption complexes on hydrous Mn oxides. *Geochim. Cosmochim. Acta* **2003**, *67*, 1937–1953.
14. Deschamps, E.; Ciminelli, V. S. T.; Weidler, P. G.; Ramos, A. Y. Arsenic sorption onto soils enriched in Mn and Fe minerals. *Clays Clay Miner.* **2003**, *51*, 197–204.
15. Antelo, J.; Avena, M.; Fiol, S.; Lopez, R.; Arce, F. Effects of pH and ionic strength on the adsorption of phosphate and arsenate at the goethite-water interface. *J. Colloid Interface Sci.* **2005**, *285*, 476–486.

16. Yao, W. S.; Millero, F. J. Adsorption of phosphate on manganese dioxide in seawater. *Environ. Sci. Technol.* **1996**, *30*, 536–541.
17. Pan, B. C.; Han, F. C.; Nie, G. Z.; Wu, B.; He, K.; Lu, L. New strategy to enhance phosphate removal from water by hydrous manganese oxide. *Environ. Sci. Technol.* **2014**, *48*, 5101–5107.
18. Boujelben, N.; Bouhamed, F.; Elouear, Z.; Bouzid, J.; Feki, M. Removal of phosphorus ions from aqueous solutions using manganese-oxide-coated sand and brick. *Desalin. Water Treat.* **2014**, *52*, 2282–2292.
19. Saeki, K.; Matsumoto, S.; Tatsukawa, R. Selenite adsorption by manganese oxides. *Soil Sci.* **1995**, *160*, 265–272.
20. Tsadilas, C. D.; Dimoyiannis, D.; Samaras, V. Boron sorption by manganese oxide-coated sand. *Commun. Soil Sci. Plant Anal.* **1998**, *29*, 2347–2353.
21. Lemarchand, E.; Schott, J.; Gaillardet, J. How surface complexes impact boron isotope fractionation: Evidence from Fe and Mn oxides sorption experiments. *Earth Planet. Sci. Lett.* **2007**, *260*, 277–296.
22. Langmuir, D., *Aqueous Environmental Geochemistry*; Prentice Hall: Upper Saddle River, NJ, 1997; p 153.
23. Scott, M. J.; Morgan, J. J. Reactions at oxide surfaces. 2. Oxidation of Se(IV) by synthetic birnessite. *Environ. Sci. Technol.* **1996**, *30*, 1990–1996.
24. Tournassat, C.; Charlet, L.; Bosbach, D.; Manceau, A. Arsenic(III) oxidation by birnessite and precipitation of manganese(II) arsenate. *Environ. Sci. Technol.* **2002**, *36*, 493–500.
25. Lafferty, B. J.; Ginder-Vogel, M.; Zhu, M. Q.; Livi, K. J. T.; Sparks, D. L. Arsenite oxidation by a poorly crystalline manganese-oxide. 2. Results from X-ray absorption spectroscopy and X-ray diffraction. *Environ. Sci. Technol.* **2010**, *44*, 8467–8472.
26. Yin, H.; Tan, W. F.; Zheng, L. R.; Cui, H. J.; Qiu, G. H.; Liu, F.; Feng, X. H. Characterization of Ni-rich hexagonal birnessite and its geochemical effects on aqueous Pb2+/Zn2+ and As(III). *Geochim. Cosmochim. Acta* **2012**, *93*, 47–62.
27. Peña, J.; Kwon, K. D.; Refson, K.; Bargar, J. R.; Sposito, G. Mechanisms of nickel sorption by a bacteriogenic birnessite. *Geochim. Cosmochim. Acta* **2010**, *74*, 3076–3089.
28. Sherman, D. M.; Peacock, C. L. Surface complexation of Cu on birnessite (delta-MnO2): Controls on Cu in the deep ocean. *Geochim. Cosmochim. Acta* **2010**, *74*, 6721–6730.
29. Villalobos, M.; Bargar, J.; Sposito, G. Mechanisms of Pb(II) sorption on a biogenic manganese oxide. *Environ. Sci. Technol.* **2005**, *39*, 569–576.
30. McKenzie, R. M. Adsorption of lead and other heavy-metals onoxides of manganese and iron. *Aust. J. Soil Res.* **1980**, *18*, 61–73.
31. Nelson, Y. M.; Lion, L. W.; Ghiorse, W. C.; Shuler, M. L. Production of biogenic Mn oxides by Leprothrix discophora SS-1 in a chemically defined growth medium and evaluation of their Pb adsorption characteristics. *Appl. Environ. Microbiol.* **1999**, *65*, 175–180.
32. Morin, G.; Juillot, F.; Ildefonse, P.; Calas, G.; Samama, J. C.; Chevallier, P.; Brown, G. E. Mineralogy of lead in a soil developed on a Pb-mineralized sandstone (Largentiere, France). *Am. Mineral.* **2001**, *86*, 92–104.

33. Takahashi, Y.; Manceau, A.; Geoffroy, N.; Marcus, M. A.; Usui, A. Chemical and structural control of the partitioning of Co, Ce, and Pb in marine ferromanganese oxides. *Geochim. Cosmochim. Acta* **2007**, *71*, 984–1008.
34. Kwon, K. D.; Refson, K.; Sposito, G. Surface complexation of Pb(II) by hexagonal birnessite nanoparticles. *Geochim. Cosmochim. Acta* **2010**, *74*, 6731–6740.
35. Peacock, C. L.; Sherman, D. M. Sorption of Ni by birnessite: Equilibrium controls on Ni in seawater. *Chem. Geol.* **2007**, *238*, 94–106.
36. Zhu, M. Q.; Ginder-Vogel, M.; Sparks, D. L. Ni(II) sorption on biogenic Mn-oxides with varying Mn octahedral layer structure. *Environ. Sci. Technol.* **2010**, *44*, 4472–4478.
37. Simanova, A. A.; Kwon, K. D.; Bone, S. E.; Bargar, J. R.; Refson, K.; Sposito, G.; Peña, J. Probing the sorption reactivity of the edge surfaces in birnessite nanoparticles using nickel(II). *Geochim. Cosmochim. Acta* **2015**, *164*, 191–204.
38. Manceau, A.; Lanson, M.; Geoffroy, N. Natural speciation of Ni, Zn, Ba, and As in ferromanganese coatings on quartz using X-ray fluorescence, absorption, and diffraction. *Geochim. Cosmochim. Acta* **2007**, *71*, 95–128.
39. Peña, J.; Kwon, K. D.; Refson, K.; Bargar, J. R.; Sposito, G. Role of bacterial biomass in the sorption of Ni by biomass-birnessite assemblages. *Environ. Sci. Technol.* **2011**, *45*, 7338–7344.
40. Wang, Y.; Feng, X. H.; Villalobos, M.; Tan, W. F.; Liu, F. Sorption behavior of heavy metals on birnessite: Relationship with its Mn average oxidation state and implications for types of sorption sites. *Chem. Geol.* **2012**, *292*, 25–34.
41. Peña, J.; Bargar, J. R.; Sposito, G. Copper sorption by the edge surface of synthetic birnessite nanoparticles. *Chem Geol.* **2015**, *396*, 196–207.
42. Manceau, A.; Lanson, B.; Drits, V. A. Structure of heavy metal sorbed birnessite. Part III: Results from powder and polarized extended X-ray absorption fine structure spectroscopy. *Geochim. Cosmochim. Acta* **2002**, *66*, 2639–2663.
43. Landrot, G.; Ginder-Vogel, M.; Livi, K.; Fitts, J. P.; Sparks, D. L. Chromium(III) oxidation by three poorly crystalline manganese(IV) oxides. 2. Solid phase analyses. *Environ. Sci. Technol.* **2012**, *46*, 11601–11609.
44. Feng, X. H.; Zhai, L. M.; Tan, W. F.; Zhao, W.; Liu, F.; He, J. Z. The controlling effect of pH on oxidation of Cr(III) by manganese oxide minerals. *J. Colloid Interface Sci.* **2006**, *298*, 258–266.
45. Dai, R. A.; Liu, J.; Yu, C. Y.; Sun, R.; Lan, Y. Q.; Mao, J. D. A comparative study of oxidation of Cr(III) in aqueous ions, complex ions and insoluble compounds by manganese-bearing mineral (birnessite). *Chemosphere* **2009**, *76*, 536–541.
46. Banerjee, D.; Nesbitt, H. W. Oxidation of aqueous Cr(III) at birnessite surfaces: Constraints on reaction mechanism. *Geochim. Cosmochim. Acta* **1999**, *63*, 1671–1687.

Chapter 5

Reactivity of Natural Mn Oxide Cryptomelane

Anhuai Lu* **and Yan Li**

School of Earth and Space Sciences, Peking University, Beijing 100871, PR China
***E-mail: ahlu@pku.edu.cn**

Cryptomelane is known to be a manganese oxide octahedral molecular sieve for catalysis and oxidation. However, few studies have been focused on natural cryptomelane. This chapter studies the geological output characteristics, mineralogy and environmental properties of natural cryptomelane forming in the supergene oxide zones of Xialei manganese deposit (Guangxi Province, China). Xialei cryptomelane is found to be present as densely packed, nanocrystalline mineral aggregates. Morphology observations under scanning electron microscopy (SEM), as well as the pore size distribution curves determined by N_2 adsorption isotherms give critical information that the Xialei cryptomelane samples are made up of a packing of crystals, most crystals with one or more dimensions in the nanorange. Mesopores are widely found in Xialei cryptomelane and exhibit diverse pore size distributions. Mesopore size distributions have an important impact on the catalytic activities in H_2O_2 decomposition, that the samples with higher average pore diameter show higher H_2O_2 decomposition efficiency. Further, Xialei cryptomelane samples exhibit strong oxidizing properties for phenols degradation. At optimal conditions (cryptomelane concentration of 200 g/L, temperature of 40°C, pH value of 3.0 and reaction time of 3 h), about 90% phenols and 50% COD in phenolic wastewater are removed within 3 h. All of the properties make natural cryptomelane a promising cost-effective environmental material.

In Advances in the Environmental Biogeochemistry of Manganese Oxides; Sparks, et al.;
ACS Symposium Series; American Chemical Society: Washington, DC, 2015.

Introduction

There are more than 30 known manganese oxide/hydroxide minerals distributed in a wide variety of geological settings (*1*). Mn presents in most manganese oxide/hydroxide minerals in three different oxidation states: +2, +3, and +4, giving rise to a range of multi- and mix-valent phases. The basic building block for most manganese oxides atomic structures is the MnO_6 octahedron, which can be assembled by sharing edges and/or corners to form a family of layer and tunnel structures. Typically, the tunnel manganese oxides are constructed of single, double, or triple chains of edge-sharing MnO_6 octahedra, and the chains share corners with each other to produce frameworks with tunnels (*1*).

Cryptomelane ($K_xMn_{8-x}O_{16}$, $0.2<x<1.0$) is a typical tunnel structure manganese oxide belong to hollandite group, and is reported to have monoclinic *I2/m* and tetragonal *I4/m* polymorphs, with cell dimensions of a=9.956 Å, b=2.8705 Å, c=9.706 Å, β=90.95° (*2*) and a=9.866 Å, b=9.866 Å, c=2.872 Å, $\alpha=\beta=\gamma=90°$ (*3*), respectively. It has a well-defined 2×2 tunnel structure and a tunnel size of 0.46 nm×0.46 nm constructed from edge-shared double MnO_6 octahedral chains (Figure 1) (*3–5*). The tunnels are partially filled with K^+ and sometimes water molecules, which balance the charge of mixed Mn^{2+}, Mn^{3+}, and Mn^{4+} (*5–7*). K^+ in the tunnels can be ion-exchanged with other cations with appropriate sizes (Cu^{2+}, Co^{2+}, Ni^{2+}, etc.) (*8*). The special open tunnel structure and variable valence of Mn give cryptomelane unique physicochemical properties as cation-exchange capability, strong oxidation ability and reversible multi-electron redox capacity (*8–10*). Indeed cryptomelane has been recommended as a heterogeneous redox catalyst, chemical sensor, adsorbent and battery material for environmental and industrial use (*8–11*).

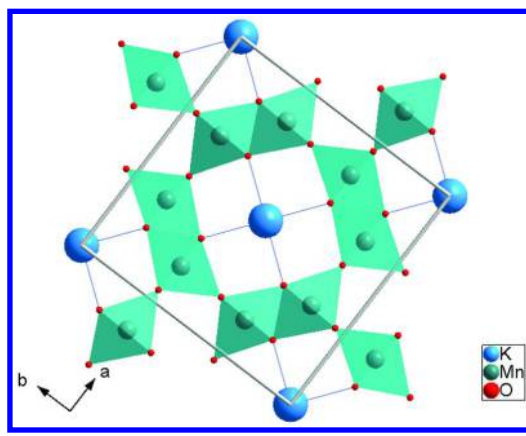

Figure 1. The structure diagram of cryptomelane. (based on datas reported in Reference (3))

In natural environments, cryptomelane is the major manganese oxide in the supergene oxidation zones of Mn-bearing crusts and manganese deposits. The supergene oxidized manganese ore generally occurs as cryptocrystalline

In Advances in the Environmental Biogeochemistry of Manganese Oxides; Sparks, et al.;
ACS Symposium Series; American Chemical Society: Washington, DC, 2015.

aggregates with noticeable conchoidal, botryoidal, reniform and stalactitic textures, which are characteristic assembles of colloidal minerals. Since colloidal minerals are in nano size and with very poor crystalline quality, until the mid-20th century, cryptomelane had been identified by mineralogist and named as a new mineral species. Cryptomelane was first distinguished from psilomelane and named as "true psilomelane" in 1932 (*12*), but was known with few structure and composition information due to the limitation of measurement techniques at that time. Richmond *et al.* characterized the distinct mineral species by X-ray diffraction and chemical analysis, and then nominated the name "cryptomelane" in 1942 (*13*). In 1990s, cryptomelane became the preferred mineral for isotopic dating due to its high content of K and widespread existence in weathered crust (*14–16*). But due to the complex mineralogy and typical occurrence as fine-grained, poorly crystalline aggregates, it is extremely challenging to conduct characterization on natural cryptomelane. Perhaps for this reason, there are relatively few studies concerning on it. Here we do mineralogy characterization on natural cryptomelane with purpose to show it is not only an important Mn metal resource but also highly chemically active in the environmental geochemistry. Natural cryptomelane and its synthetic analogues could be used as cost-effective environmental materials in catalytic, cation-exchange and redox reactions.

Occurrence and Characterization of Natural Cryptomelane

Occurrence

Natural cryptomelane mainly occurs in the supergene oxidation zones of manganese deposits and lateritic weathered profiles (*17–19*), where it is formed by authigenic precipitation (*19*). Meanwhile crytomelane has long been known to originate from a layered (birnessite or vernadite) precursor (*20–22*). Some cryptomelane may occur in weathered ultramafic rocks (*23*), volcanic ash (*24*), marble (*25*), and old weathered shell (*26*). In China, manganese oxide ore is widely distributed at depressed places along the edge of the Jiangnan Old Terrane, the 23° N Zone in the south of China, which is 1500 km in length from east to west and 220 km in width from south to north as well as 50-60 m in depth (*27*). This type of manganese deposit is in favor of the formation of supergene manganese oxide ore due to the humidity climate in South China.

Known as one of the largest manganese deposit in China, Xialei manganese deposit is located in the south of the Youjiang fold belt, south China fold system, Guangxi Province. In this area, weathering of thick manganese carbonate sequences has resulted in massive manganese oxides layers, 10 to 30 m thick in some places. Cryptomelane is the most common manganese mineral in the eastern and central parts of the mining district, which is 9 km in length from east to west and 2.5 km in width from south to north. Xialei cryptomelane commonly occurs in reniform form (Figure 2a). While in the cracks and pores of manganese ore, cryptomelane may develop in veined form (Figure 2b), and is leaden with strong metallic luster on the fresh surface, hard and brittle. The orebody in this type is very rich in Mn oxides as cryptomelane, psilomelane, pyrolusite and nsutite, and with very rare fraction of gangue minerals. The samples used for this

In Advances in the Environmental Biogeochemistry of Manganese Oxides; Sparks, et al.;
ACS Symposium Series; American Chemical Society: Washington, DC, 2015.

study are collected from the central part of the mining district NC1 (reniform), and the eastern part of the mining district NC2 (veined).

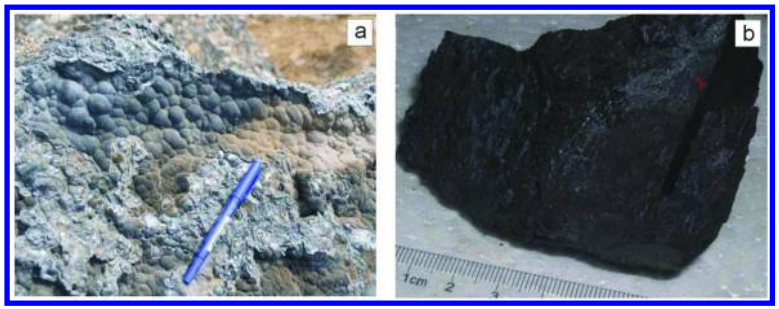

Figure 2. Xialei cryptomelane ore (a) in reniform form; (b) in veined form.

Characterization of Natural Cryptomelane

Under optical microscope, Xialei cryptomelane samples show concentric circular, enterolithic, pisolitic and veined micostructures (Figure 3). The morphologies of natural cryptomelane are more complicated under scanning electron microscope (SEM). Figure 4 shows a great variety of morphologies as minute, but densely packed and ill-defined crystals (Figure 4a, e), acicular and blade-like crystals (Figure 4b, c), wavy, fibrous crystals (Figure 4d, f). Importantly, all of the images show crystal dimensions and features fell down into the nano-range.

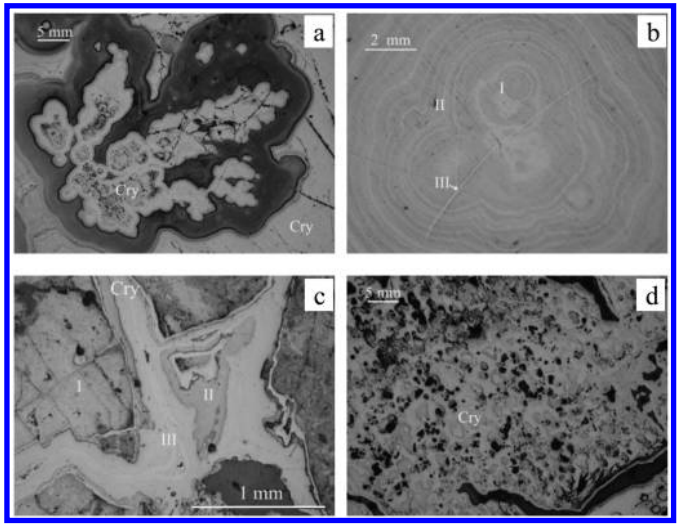

Figure 3. Optical microscope images of cryptomelane showing (a) veined structure; (b) concentric circular structure; (c) enterolithic structure; (d) pisolitic structure. I, II, III represent three periods of mineralization; Cry is the abbreviation of cryptomelane.

In Advances in the Environmental Biogeochemistry of Manganese Oxides; Sparks, et al.;
ACS Symposium Series; American Chemical Society: Washington, DC, 2015.

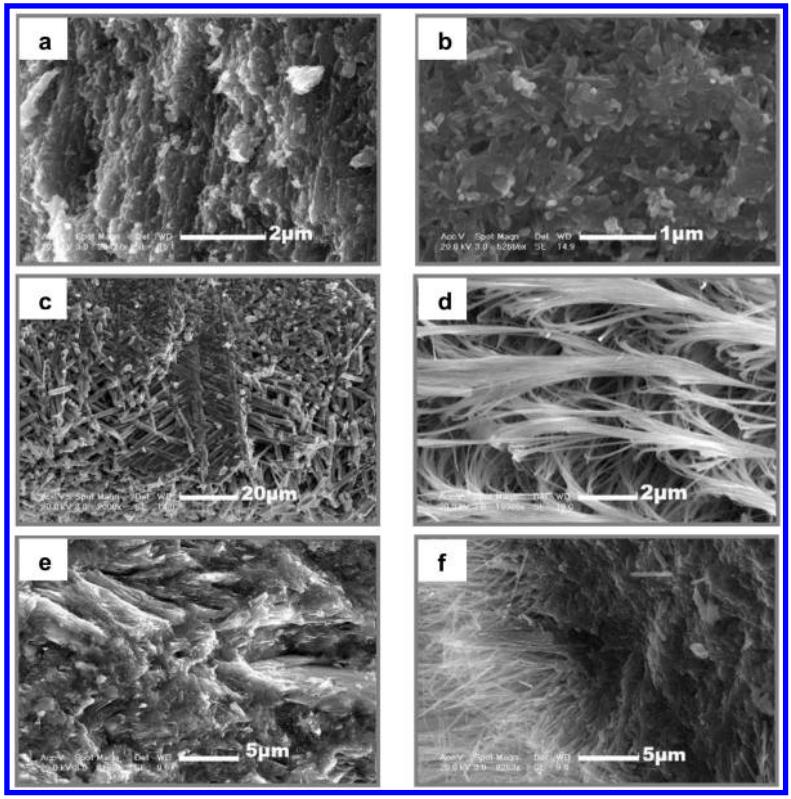

Figure 4. Scanning electron microscope images of cryptomelane in samples NC1 (a-d) and NC2 (e, f). See text for descriptions and explanations.

The XRD patterns of NC1 and NC2 (Figure 5) show characteristic peaks of cryptomelane (JCPDS: 34-0168). While several impurity peaks of nsutite and quartz appeared in XRD pattern of NC2.

The chemical compositions of several randomly selected cryptomelane particles are characterized by electron microprobe analyses (EMPA) and listed in Table 1. In veined samples, the MnO_2 content is over 90%, K_2O about 3%. While in reniform samples, the MnO_2 content is about 90%, K_2O more than 3%. Most samples contain Al_2O_3, SiO_2 and Fe_2O_3, and part of samples contain trace elements of Ni, Ba, Sr and Mg. The corresponding chemical formulas of natural cryptomelane particles are calculated as shown in Table 2.

In Advances in the Environmental Biogeochemistry of Manganese Oxides; Sparks, et al.;
ACS Symposium Series; American Chemical Society: Washington, DC, 2015.

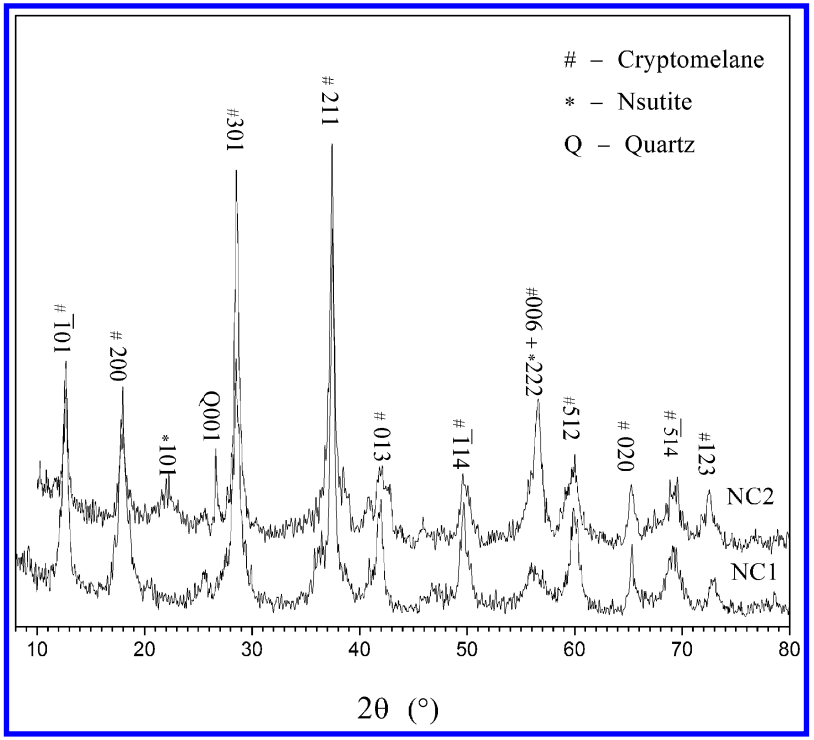

Figure 5. XRD patterns of natural cryptomelane.

Lattice fringes paralleled to the crystal direction under high-resolution transmission electron microscope (TEM). Generally, the lattice fringes of ($\bar{1}$01) plane have a spacing of about 0.7 nm (Figure 6a). While, those with bigger spacing (about 0.9 nm) were also observed (Figure 6b), possibly due to the intergrowth of tunnels with different sizes. Lattice defects are easily found in natural cryptomelane samples (Figure 6c), which are probably caused by cation-exchange. In general, the ($\bar{1}$01) planes are homogeneous and continuous (Figure 6a, b). Also, there are some lattice bending and lattice distortion (Figure 6b, c). Lattice defects often develop in the transition zone of two different planes. For instance, in the transition zone boundary of ($\bar{1}$01) planes and (301) planes, where the lattice fringes of ($\bar{1}$01) planes (d=0.7 nm) are broader than those of (301) planes (d=0.3 nm), lattice fringes bend, narrow down and even disappear (Figure 6c).

In Advances in the Environmental Biogeochemistry of Manganese Oxides; Sparks, et al.;
ACS Symposium Series; American Chemical Society: Washington, DC, 2015.

Publication Date (Web): November 17, 2015 | doi: 10.1021/bk-2015-1197.ch005

Table 1. Electron microprobe analyses of cryptomelane in Xialei Manganese Deposit (wt%) [a]

Sample	*MnO_2*	*K_2O*	*Na_2O*	*CaO*	*BaO*	*SrO*	*Fe_2O_3*	*Al_2O_3*	*SiO_2*	*MgO*	*NiO*	*Total*
NC1-1	90.58	3.9	0.04	0.14	0.00	0.05	0.11	3.98	0.39	0.00	0.00	99.19
NC1-2	90.59	3.84	0.04	0.16	0.00	0.04	0.00	3.84	0.37	0.00	0.00	98.88
NC1-3	93.17	4.37	0.07	0.10	0.00	0.00	0.13	2.17	0.29	0.00	0.00	100.3
NC1-4	89.59	3.89	0.10	0.26	0.10	0.02	0.09	4.33	0.45	0.00	0.00	98.83
NC2-1	96.02	2.72	0.11	0.15	0.00	0.00	0.11	0.02	0.05	0.02	0.01	99.21
NC2-2	97.72	2.79	0.17	0.22	0.00	0.00	0.04	0.09	0.06	0.00	0.04	101.13
NC2-3	97.71	2.88	0.17	0.17	0.00	0.00	0.18	0.03	0.05	0.00	0.03	101.22
NC2-4	94.18	2.96	0.20	0.15	2.00	0.00	0.07	1.46	0.12	0.05	0.21	101.40
NC2-5	94.9	2.52	0.13	0.18	1.81	0.00	0.25	0.50	0.09	0.06	0.15	100.59

[a] NC1-1, 2, 3, 4 represent four different mineral particles randomly selected from sample NC1; NC2-1, 2, 3, 4, 5 represent five different mineral particles randomly selected from sample NC2.

Table 2. Chemical Formula of Xialei Cryptomelane

Sample	*Chemical Formula*
NC1-1	$(K_{0.59}Ca_{0.02}Na_{0.01})_{0.62}(Mn_{7.37}Al_{0.55}Si_{0.05}Fe_{0.01})_{7.98}O_{16}$
NC1-2	$(K_{0.58}Ca_{0.02}Na_{0.01})_{0.61}(Mn_{7.4}Al_{0.53}Si_{0.04})_{7.97}O_{16}$
NC1-3	$(K_{0.65}Na_{0.02}Ca_{0.01})_{0.68}(Mn_{7.56}Al_{0.3}Si_{0.03}Fe_{0.01})_{7.9}O_{16}$
NC1-4	$(K_{0.59}Ca_{0.03}Na_{0.02})_{0.64}(Mn_{7.32}Al_{0.60}Si_{0.05}Fe_{0.01})_{7.98}O_{16}$
NC2-1	$(K_{0.41}Na_{0.03}Ca_{0.02})_{0.46}(Mn_{7.86}Si_{0.01})_{7.87}O_{16}$
NC2-2	$(K_{0.41}Na_{0.04}Ca_{0.03})_{0.48}(Mn_{7.85}Al_{0.01}Si_{0.01})_{7.87}O_{16}$
NC2-3	$(K_{0.43}Na_{0.04}Ca_{0.02})_{0.49}(Mn_{7.85}Fe_{0.02}Si_{0.01})_{7.88}O_{16}$
NC2-4	$(K_{0.44}Ba_{0.09}Na_{0.05}Ca_{0.02})_{0.6}(Mn_{7.64}Al_{0.2}Ni_{0.02}Fe_{0.01}Si_{0.01}Mg_{0.01})_{7.89}O_{16}$
NC2-5	$(K_{0.38}Ba_{0.08}Na_{0.03}Ca_{0.02})_{0.51}(Mn_{7.75}Al_{0.07}Fe_{0.02}Si_{0.01}Mg_{0.01}Ni_{0.01})_{7.85}O_{16}$

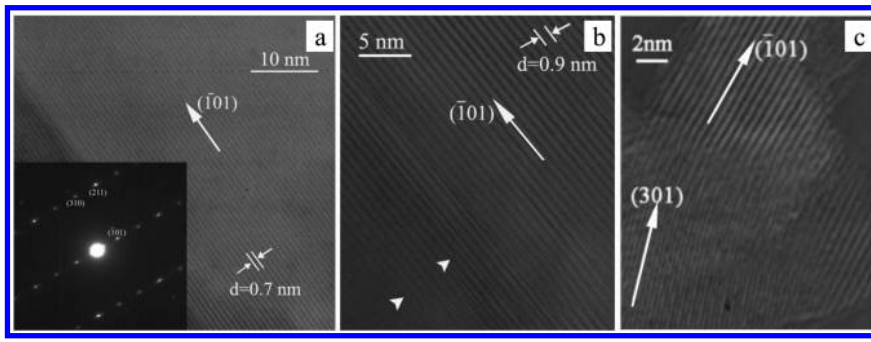

Figure 6. HRTEM images of cryptomelane showing (a) lattice fringes with the d-spacing of 0.7 nm, corresponding to ($\bar{1}$01) plane (inset is the result of selected area electron diffraction); (b) lattice fringes with the d-spacing of 0.9 nm, lattice defects are indicated by arrows; (c) the transition zone of ($\bar{1}$01) and (301) plane.

Nanoporosity and Catalyst Reactivity of Natural Cryptomelane

Porosity and Surface Area

NC1 and NC2 samples are ground to 96-117 μm (labeled NC1-1 and NC2-1) and 57-76 μm (labeled NC1-2 and NC2-2) for porosity and surface area analysis. The N_2 adsorption isotherms (77K) for these cryptomelane samples exhibit characteristics of typical type IV isotherms according to the International Union of Pure and Applied Chemistry (IUPAC) classification (*28*, *29*) (Figure 7). It is well known that this type of capillary condensation, with its characteristic adsorption isotherm hysteresis loop, occurs in materials with mesopores (*30*). Also, all of cryptomelane samples show type H3 hysteresis loops (Figure 7), meaning that the adsorption branch of the hysteresis loop does not achieve ultimate adsorbing capacity even at high relative pressure.

In Advances in the Environmental Biogeochemistry of Manganese Oxides; Sparks, et al.;
ACS Symposium Series; American Chemical Society: Washington, DC, 2015.

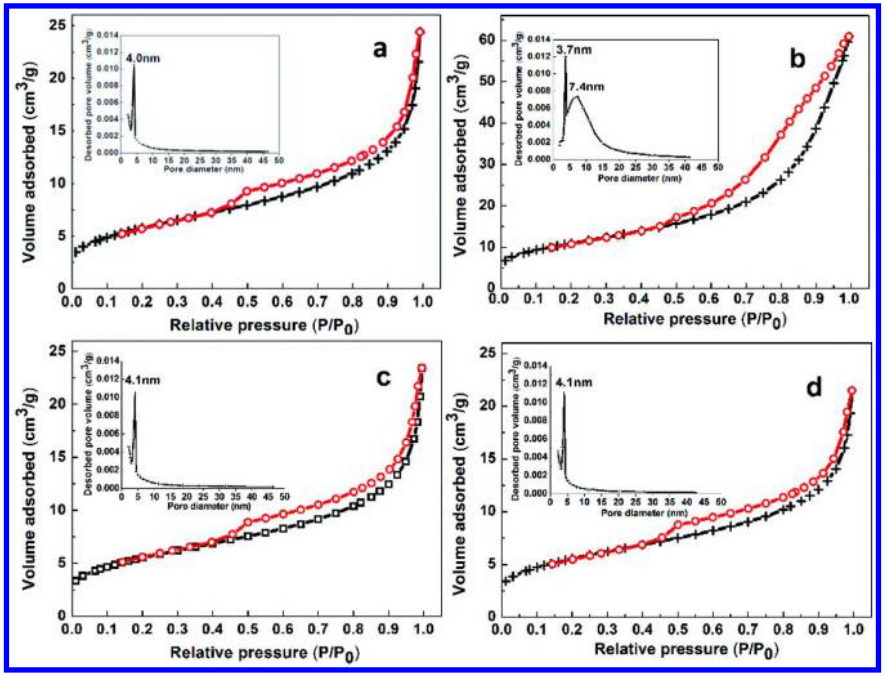

Figure 7. Isotherms of N2 adsorption/desorption and pore size distribution using the BJH method of (a) NC1-1; (b) NC1-2; (c) NC2-1; (d) NC2-2.

Desorption isotherms are used to calculate mesopore size distribution by Barrett-Joyner-Halenda (BJH) method (*31*). Figure 7 also shows the pore volume distribution as a function of pore diameter for each of the four samples. The position of peaks in the pore volume distribution curves and BET surface areas for all four samples are listed in Table 3. The shape of the pore size distribution curves give critical information about the nature of these mineral samples which are made up of a packing of cryptomelane crystals, most crystals with one or more dimensions in the nanorange. The curves for samples NC2-1, NC2-2, and NC1-1 suggest an increasing proportion of pores with diameters below 15 nm in size, with a large proportion around 4 nm in size. Some pores down to 10 nm can be directly seen in high resolution SEM images (e.g. Figure 4b). For sample NC1-2, which is sample NC1-1 ground to a smaller size (from an average of just over 100 μm to just over 60 μm), the curve suggests an increasing proportion of pores with diameters below about 40 nm with a peak distribution around 7 nm. The grinding process has apparently altered the pore size distribution in sample NC1, but this has not occurred in sample NC2. Although the NC1 and NC2 samples visually look a bit different by eye in the field and in the SEM (Figure 4), the reason for this difference in the pore distribution curves for sample NC1 after more intense grinding is not known. It is unlikely, however, that grinding has caused the mesopores at 4 nm size in these samples because this peak is not modified in sample NC2, and only slightly modified in NC1, after the additional grinding in going from the courser to finer samples.

Table 3. BET surface and porosity of cryptomelane

Sample	*NC1-1*	*NC1-2*	*NC2-1*	*NC2-2*
Grain sizes (μm)	96-117	57-76	96-117	57-76
Pore size distribution peak (nm)	4.0	3.7, 7.4	4.1	4.1
Average Pore Diameter [a] (nm)	7.2	9.5	7.3	6.6
BET surface area (m2/g)	21.3	39.5	20.0	19.3

[a] Calculated by Brunauer-Emmett-Teller (BET) method.

Overall, and importantly, the fact that nitrogen can be adsorbed and desorbed freely within and between cryptomelane crystals with dimensions that range down into the nanometer regime suggests that simple reactants of environmental interest can access the surfaces of nanominerals in a densely packed sample.

Catalyst Activity of Cryptomelane under the Influence of Mesopores

The catalytic decomposition of hydrogen peroxide is one of the most useful methods to analyze the activity of solid catalysts (*32–35*). Experiments to measure the catalytic decomposition of hydrogen peroxide are performed as described by Zhou (*36*). 10 mg of cryptomelane powder is loaded into a wedge-shaped plastic container, and then the container is carefully floated on the 1 M H_2O_2 solution at 273 K. When the magnetic stirrer is turned on, the wedge-shaped plastic container overturned, and the cryptomelane powder in it reacts with the H_2O_2 solution. The increase in gas volume due to oxygen released from the H_2O_2 decomposition pushes the water in an adjoining U-shaped glass tube into a graduated flask. Water level in the graduated flask is measured as a function of time. We do these experiments in triplicate for each sample and calculate the average times for various displacement volumes. The variation of the concentration of hydrogen peroxide with reaction time is shown in Figure 8a. It is known that the catalytic decomposition of H_2O_2 by manganese dioxide is a first-order reaction at pH 3-8 (*32*), and the pH changes from approximately 5.6 to 7 during the course of our experiments. So, the decomposition rates are determined by the following equation (*37*):

$$kt = \ln V_\infty - \ln(V_\infty - V_t)$$

Where V_∞ and V_t are the volumes of O_2 when all the H_2O_2 is decomposed and at time t, respectively. k is the rate constant. Figure 8b shows the decomposition rates of NC1-1, NC2-1 and NC2-2 are similar, but that NC1-2 has a higher reaction rate, and as a result, a much higher catalytic activity than the other three samples. For all samples, an expected log-linear fits with initial part of time, but the experimental data seem to deviate with going-on reaction. This deviation is likely due to the invalid approximate expression where (H^+) is much higher than dissociation constant of $HO_2\cdot$ radical in the adsorbed state when pH value slightly changes during the reaction. The mesoporous of these cryptomelane samples,

In Advances in the Environmental Biogeochemistry of Manganese Oxides; Sparks, et al.;
ACS Symposium Series; American Chemical Society: Washington, DC, 2015.

where the reacting solution comes into contact with internal surfaces, as well as the generation of oxygen gas bubbles within these passageways, may also complicate the overall reaction rate as a function of time.

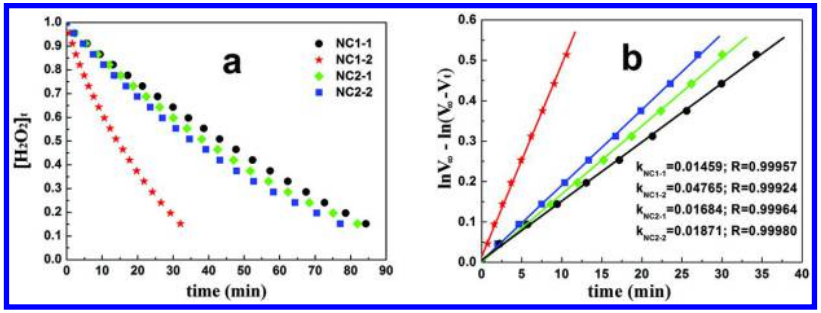

Figure 8. (a) The proportion of hydrogen peroxide remaining, relative to the starting amount, at different times of reaction. (b) First order reaction kinetics plot of kt (=lnV_∞ -ln(V_∞ - V_t)) vs. t. The rate constant k of initial reacting section is equal to the slope of the data. The associated errors with rate constants of four samples are in the scale of 10^{-4}. Each point stands for an average experimental data point.

Our experiments show that natural, densely packed, nanoaggregates can display highly efficient catalytic activity with reactants in aqueous solutions. With the exception of sample NC1-2, the mesopore networks in our cryptomelane specimens collected at two different sites, and showing two different specimen textures, have very similar mesopore distributions, and have very similar catalytic activities. For sample NC1-2 only, the nature of the sample is such that the extra grinding modified a portion of the mesopore network by opening it up, and extended specific surface area, allowing for an even greater catalytic efficiency. In all cases, the reactants are clearly accessing the surfaces of the constituent nanocrystalline minerals, even though one of the resulting products generated on the reactive surfaces is nominally a gas. In addition, even though the change in the behavior and reactivity of these cryptomelane surfaces as a function of crystal size and shape in the nanorange is not specifically known, as is the case for only a very few similar geologically relevant systems to date (*38*, *39*), it is very likely that cryptomelane's nanoscale behavior is significantly modified relative to bulk behavior, and that the catalytic properties are enhanced in the nanoscale.

Oxidation of Phenols by Cryptomelane

Previous studies have shown that manganese oxides could oxidize phenolic compounds including phenol and substituted phenols (*40–42*). In our study, natural cryptomelane samples (NC2) with the manganese oxidation state (AOS) of 3.56 is used for reaction with phenolic wastewater.

Two kinds of phenolic wastewater are collected from coal gas plant and gasification plant, respectively. The concentration of total phenols is measured

In Advances in the Environmental Biogeochemistry of Manganese Oxides; Sparks, et al.;
ACS Symposium Series; American Chemical Society: Washington, DC, 2015.

by bromide method commonly used in factories for water quality determination (EPA 320.1). An excessive bromide agent would react with the existing phenols and then iodometric method (EPA 345.1) is used to measure excessive bromide agent to help calculate the total phenols (*43*). COD_{Cr} is measured by fast digestion spectrophotometric method (HJ/T 399-2007) using Model HATO CTL-12 COD rapid determination instrument.

It has been established that pH has a considerable influence on the performance of phenol removal by manganese oxides (*40*). The effect of pH on phenols removal rate is shown in Figure 9. It is obvious that the efficiency of phenol removal increases evidently in more acidic aqueous suspensions. After 3 h' reaction, the removal efficiency was above 60% at pH 1-5, and at pH 1 the removal efficiency reached almost 100%. Solution pH determines the protonation reactions and formation of surface complexes between phenols and manganese oxide (*40*). Moreover, pH is of great importance in changing the thermodynamic redox potentials of manganese oxides and phenols (*44*). At lower pH, cryptomelane has higher redox potential and is easier to take phenols degradation.

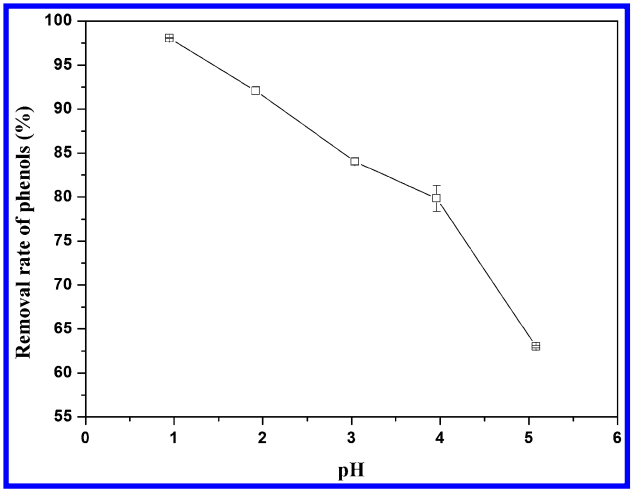

Figure 9. The effect of pH on removal of phenols with original phenols of 4592 mg/L, cryptomelane concentration of 200 g/L, liquid temperature of 20 °C and reaction time of 3h.

Figure 10 displays phenols removal as a function of liquid temperature at 15, 20, 30 and 40°C, respectively. It is found that high temperature is in favor of phenols removal. The removal rate of total phenols reaches 96.2% at 40°C and 69.8% at 15°C. Temperature may influence mineral surface chemistry properties such as intrinsic acidity constant and surface charge (*45*, *46*). Some studies indicate that the pH_{PZC} of metal oxides/hydroxides generally decreases with

In Advances in the Environmental Biogeochemistry of Manganese Oxides; Sparks, et al.;
ACS Symposium Series; American Chemical Society: Washington, DC, 2015.

temperature increases (*45*). Even a slight temperature change could also have a strong influence on the stability of surface complex (*46*). However, there are no available data on the effect of temperature on the surface charge and pH_{PZC} of manganese oxides so far. The role of temperature on phenol removal behavior by manganese oxide is uncertain, which is based on surface complexion reactions. More comprehensive study would be done on the variations in surface charge as a function of temperature.

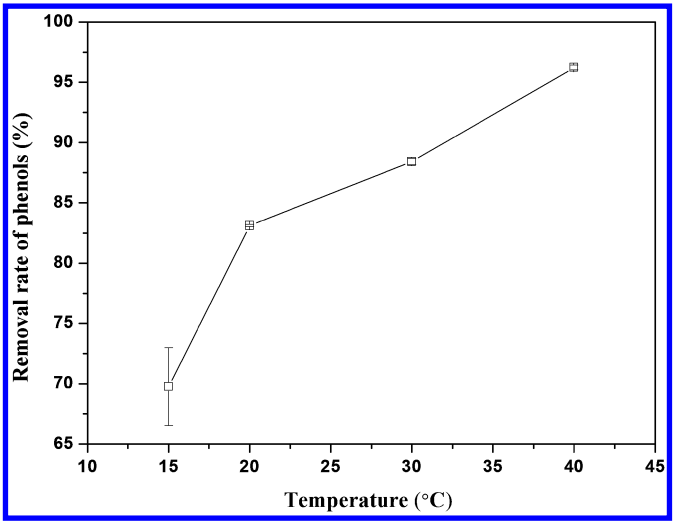

Figure 10. The effect of liquid temperature on the removal of phenols with original phenols of 4592 mg/L, cryptomelane concentration of 200 g/L, pH value of 2.0 and reaction time of 2 h.

Based on above experiments, we choose the optimal experimental conditions (cryptomelane concentration of 200 g/L, temperature of 40°C, pH value of 3.0 and reaction time of 3 h) and conduct the reaction with five kinds of phenolic wastewater. The degradation efficiency of total phenols, COD_{Cr} are illustrated in Table 4. Removal rates of total phenols reach 84.6%-97.4% after suspension reaction. In the process, protons are consumed and Mn^{2+} is leaching in the solution with oxidation of phenols. Take phenol for example: $\equiv Mn^{(IV)}\text{-}O+C_6H_5OH+H^+ \rightarrow Mn^{2+}+C_6H_4O_2+H_2O$ (*40*). After removal of Mn ions in solutions by alkali precipitation method, COD_{Cr} removal rates reach close to and even higher than 50%. If air bubbles are introduced into precipitation process of dissolved Mn(II), it can be collected in the form of manganese oxide and recycling used. Since the concentrations of organic compounds have been considerably reduced, the remaining compounds with relatively low concentrations facilitate further biological treatment. Thus, this method will be designed as a feasible pretreatment process for industrial wastewater.

In Advances in the Environmental Biogeochemistry of Manganese Oxides; Sparks, et al.;
ACS Symposium Series; American Chemical Society: Washington, DC, 2015.

Table 4. Indexes of original and treated phenolic wastewater by natural cryptomelane NC2

Water quality index	*Wastewater from coal gas plant*		*Wastewater from plastic auxiliary plant*	*Wastewater from gasification plant*	
	Before extraction	*After extraction*		*Before extraction*	*After extraction*
Total phenols before treatment (mg/L)	4592	1040	5376	4440	1180
Total phenols after treatment (mg/L)	320	160	140	148	147
CODcr before treatment (mg/L)	6604	2036	18473	3275	2975
Removal rate of total phenols (%)	93.0	84.6	97.4	96.7	87.5
Removal rate of CODcr(%)	49.3	57.4	63.1	70.8	48.3

Remarks on the Reactivity of Nanomineral Aggregates

Mn oxides are highly chemically active in soils, rocks and natural waters. Specifically, we have found that the manganese oxide cryptomelane ($K_xMn_{8-x}O_{16}$ where x ranges from 0.2 to 1.0) with densely packed, nanoaggregates can display highly efficient catalytic activity in aqueous solutions. Under SEM, the cryptomelane nanoaggregates are observed as assembled with nanocrystals in nanofibre, nanoneedle and nanorod form and with the diameter ranging from 10 to 80 nm. It is well-known that naturally occurring nanominerals provide unimaginably large surface areas for Earth-influencing interfacial reactions and exchange of electrons, elements, and energy. In the broadest context, this exchange provides an important pathway by which the hydrosphere, atmosphere, and solid Earth communicate with one another. However, it is often thought that such nanomineral aggregates will not show unusual properties associated with well dispersed nanominerals. That is, these aggregates might be assumed to predominately exhibit the properties of bulk minerals rather than their constituent nanocrystals. Moreover, it may be unlikely for natural conditions to ever promote the dispersion of these aggregates, and if for some reason the nanocrystals are dispersed, to preserve them in a nanoscale dispersion.

Previous studies suggest that meso-porosity and permeability, defined as pores and channels in the dimensional range of 2 to 50 nm, can exist in natural nanocrystalline aggregates (*38*, *47–49*), perhaps allowing reactive contributions from the surfaces of nanominerals in aggregates. The present study directly

In Advances in the Environmental Biogeochemistry of Manganese Oxides; Sparks, et al.;
ACS Symposium Series; American Chemical Society: Washington, DC, 2015.

demonstrated this phenomenon for a manganese oxide cryptomelane that all of natural samples have slit-shaped mesopores. The mesopores give aggregates exceptionally small scale porosity and permeability and provide an abundance of reactive sites on internal nanomineral surfaces, driving the hydrogen peroxide breakdown reaction ($H_2O_2 \rightarrow H_2O+1/2O_2$) at a rapid rate. Importantly, we have also demonstrated that natural cryptomelane aggregates with different mesopore size distributions show different rates of H_2O_2 decomposition reaction.

Nanomineral aggregates of Mn oxides are widespread near and on the Earth's surface, which most likely play an important role, yet to date still a largely undetermined one, in the cycling of Earth materials, in environmental behavior, and in remediation efforts (*39*, *48*). Geoscientists, as well as environmental and materials scientists, will play an important role in developing a much better understanding of the nano-effect in natural nanoscaled minerals. Finally, such mineral aggregates, including what we have seen with cryptomelane in this study, have great potential for use as ion-exchange, heavy metal immobilization, organic oxidation and catalytic materials.

Acknowledgments

Funding for part of the experimental data shown in this chapter is highly appreciated from the National Basic Research Program of China (973 Program) (Grant No. 2014CB846001) and the National Natural Science Foundation of China (Grant No. 41230103 & 41272003 & 49972017).

References

1. Post, J. E. Manganese oxide minerals: Crystal structures and economic and environmental significance. *Proc. Natl. Acad. Sci. U. S. A*. **1999**, *96*, 3447–3454.
2. Post, J. E.; Von Dreele, R. B.; Buseck, P. R. Symmetry and cation displacements in hollandites: structure refinements of hollandite, cryptomelane and priderite. *Acta Crystallogr., Sect. B* **1982**, *38* (4), 1056–1065.
3. Vicat, J.; Fanchon, E.; Strobel, P.; Qui, D. T. The structure of $K_{1.33}Mn_8O_{16}$ and cation ordering in hollandite-type structures. *Acta Crystallogr., Sect. B* **1986**, *42*, 162–167.
4. Pasero, M. A short outline of the tunnel oxides. *Rev. Mineral. Geochem.* **2005**, *57*, 291–305.
5. Feng, Q.; Kanoh, H.; Ooi, K. Manganese oxide porous crystals. *J. Mater. Chem.* **1999**, *9*, 319–333.
6. Post, J. E.; Burnham, C. W. Modeling tunnel-cation displacements in hollandites using structure-energy calculations. *Am. Mineral.* **1986**, *71*, 1178–1185.
7. Feng, Q.; Kanoh, H.; Miyai, Y.; Ooi, K. Alkali metal ions insertion/extraction reactions with hollandite-type manganese oxide in the aqueous phase. *Chem. Mater.* **1995**, *7*, 148–153.

8. Malinger, K. A.; Ding, Y. S.; Sithambaram, S.; Espinal, S.; Gomez, S. L.; Suib, S. L. Microwave frequency effects on synthesis of cryptomelane-type manganese oxide and catalytic activity of cryptomelane precursor. *J. Catal.* **2006**, *239*, 290–298.
9. Makwana, V. D.; Son, Y. C.; Howell, A. R.; Suib, S. L. The role of lattice oxygen in selective benzyl alcohol oxidation using OMS-2 catalyst: A kinetic and isotope-labeling study. *J. Catal.* **2002**, *210*, 46–52.
10. Thackeray, M. M. Manganese oxides for lithium batteries. *Prog. Solid State Chem.* **1997**, *25*, 1–71.
11. Suib, S. L. A review of open framework structures. *Annu. Rev. Mater. Sci.* **1996**, *26*, 135–151.
12. Ramsdell, L. S. An X-ray study of psilomelane and wad. *Am. Mineral.* **1932**, *17*, 143–149.
13. Richmond, W. E.; Fleischer, M. Cryptomelane, A new name for the commonest of the "psilomelane" minerals. *Am. Mineral.* **1942**, *27*, 607–613.
14. Hautmann, S.; Lippolt, H. J. $^{40}Ar/^{39}Ar$ dating of central European K–Mn oxides—a chronological framework of supergene alteration processes during the Neogene. *Chem. Geol.* **2000**, *170*, 37–80.
15. Vasconcelos, P. M. K-Ar and $^{40}Ar/^{39}Ar$ geochronology of weathering processes. *Annu. Rev. Earth Planet. Sci.* **1999**, *27*, 183–229.
16. Ruffet, G.; Innocent, C.; Michard, A.; Feraud, G.; Beauvais, A.; Nahon, D.; Hamelin, B. A geochronological $^{40}Ar/^{39}Ar$ and $^{87}Rb/^{81}Sr$ study of K-Mn oxides from the weathering sequence of Azul, Brazil. *Geochim. Cosmochim. Acta* **1996**, *60*, 2219–2232.
17. Parc, S.; Nahon, D.; Tardy, Y.; Vieillard, P. Estimated solubility products and fields of stability for cryptomelane, nsutite, birnessite, and lithiophorite based on natural lateritic weathering sequences. *Am. Mineral.* **1989**, *74*, 466–475.
18. Ostwald, J. Genesis and paragenesis of the tetravalent manganese oxides of the Australian continent. *Econ. Geol.* **1992**, *87*, 1237–1252.
19. Vasconcelos, P. M.; Renne, P. R.; Brimhall, G. H.; Becker, T. A. Direct dating of weathering phenomena by $^{40}Ar/^{39}Ar$ and K-Ar analysis of supergene K-Mn oxides. *Geochim. Cosmochim. Acta* **1994**, *58*, 1635–1665.
20. Taylor, R. M.; McKenzie, R. M.; Norrish, K. The mineralogy and chemistry of manganese in some Australian soils. *Aust. J. Soil Res.* **1964**, *2*, 235–248.
21. Ross, S. J.; Franzmeier, D. P.; Roth, C. B. Mineralogy and chemistry of manganese oxides in some Indiana soils. *Soil Sci. Soc. Am. J.* **1976**, *40*, 137–143.
22. Glasby, G. P.; Hodgson, G. W. The distribution of organic pigments in marine manganese nodules from the Northwest Indian Ocean. *Geochim. Cosmochim. Acta* **1971**, *35*, 845–851.
23. Llorca, S.; Monchoux, P. Supergene cobalt minerals from New Caledonia. *Can. Mineral.* **1991**, *29*, 149–161.
24. Carlos, B. A.; Chipera, S. J.; Bish, D. L.; Craven, S. J. Fracture-lining manganese oxide minerals in silicic tuff, Yucca Mountain, Nevada, USA. *Chem. Geol.* **1993**, *107*, 47–69.

25. Nimfopoulos, M. K.; Pattrick, R. A. D. Mineralogical and textural evolution of the economic manganese mineralisation in western Rhodope massif, N. Greece. *Mineral. Mag.* **1991**, *55*, 423–434.
26. Li, J. C.; Vasconcelos, P. M.; Zhang, J. Behavior of argon gas release from manganese oxide minerals as revealed by $^{40}Ar/^{39}Ar$ laser incremental heating analysis. *Chinese Sci. Bull.* **2002**, *47*, 1502–1511.
27. Lu, A.; Gao, X.; Qin, S.; Wang, C. Cryptomelane ($K_xMn_{8-x}O_{16}$): Natural active octahedral molecular sieve (OMS-2). *Chinese Sci. Bull.* **2003**, *48*, 920–923.
28. Kijima, N.; Yasuda, H.; Sato, T.; Yoshimura, Y. Preparation and characterization of open tunnel oxide α-MnO_2 precipitated by ozone oxidation. *J. Solid State Chem.* **2001**, *159*, 94–102.
29. López, T.; Ortiz, E.; Alvarez, M.; Manjarrez, J.; Montes, M.; Navarro, P.; Odriozola, J. A. Catalytic nanomedicine: Functionalisation of nanostructured cryptomelane. *Mater. Chem. Phys.* **2010**, *120*, 518–525.
30. Fan, C.; Lu, A.; Li, Y.; Wang, C. Synthesis, characterization, and catalytic activity of cryptomelane nanomaterials produced with industrial manganese sulfate. *J. Colloid Interface Sci.* **2008**, *327*, 393–402.
31. Barrett, E. P.; Joyner, L. G.; Halenda, P. P. The determination of pore volume and area distributions in porous substances. I. Computations from nitrogen isotherms. *J. Am. Chem. Soc.* **1951**, *73*, 373–380.
32. Kanungo, S. B.; Parida, K. M.; Sant, B. R. Studies on MnO_2-III. The kinetics and the mechanism for the catalytic decomposition of H 2 O 2 over different crystalline modifications of MnO_2. *Electrochim. Acta* **1981**, *26*, 1157–1167.
33. Hasan, M. A.; Zaki, M. I.; Pasupulety, L.; Kumari, K. Promotion of the hydrogen peroxide decomposition activity of manganese oxide catalysts. *Appl. Catal. A: General* **1999**, *181*, 171–179.
34. Mochida, I.; Takeshita, K. Transition metal ions on molecular sieves. II. Catalytic activities of transition metal ions on molecular sieves for the decomposition of hydrogen peroxide. *J. Phys. Chem.* **1974**, *78*, 1653–1657.
35. Ahuja, L. D.; Rajeshwer, D.; Nagpal, K. C. Physicochemical properties and catalytic behavior of manganese oxides. *J. Colloid Interface Sci.* **1987**, *119*, 481–490.
36. Zhou, H.; Shen, Y. F; Wang, J. Y.; Chen, X.; O'Young, C. L.; Suib, S. L. Studies of decomposition of H_2O_2 over manganese oxide octahedral molecular sieve materials. *J. Catal.* **1998**, *196*, 321–328.
37. Campbell, I. M.; Nudelman, C. *Reaction Kinetics*; Blackie: Glasgow, 1980; pp 1−12.
38. Hochella, M. F. Nanoscience and technology: the next revolution in the Earth sciences. *Earth Planet. Sci. Lett.* **2002**, *203*, 593–605.
39. Hochella, M. F.; Kasama, T.; Putnis, A.; Putnis, C. V.; Moore, J. N. Environmentally important, poorly crystalline Fe/Mn hydrous oxides: Ferrihydrite and a possibly new vernadite-like mineral from the Clark Fork River Superfund Complex. *Am. Mineral.* **2005**, *90*, 718–724.
40. Stone, A. T. Reductive dissolution of manganese (III/IV) oxides by substituted phenols. *Environ. Sci. Technol.* **1987**, *21*, 979–988.

41. Abecassis-Wolfovich, M.; Jothiramalingam, R.; Landau, M. V.; Herskowitz, M.; Viswanathan, B.; Varadarajan, T. K. Cerium incorporated ordered manganese oxide OMS-2 materials: Improved catalysts for wet oxidation of phenol compounds. *Appl. Catal. B: Environ.* **2005**, *59*, 91–98.
42. Ulrich, H. J.; Stone, A. T. The oxidation of chlorophenols adsorbed to manganese oxide surfaces. *Environ. Sci. Technol.* **1989**, *23*, 421–428.
43. Yang, C.; Qian, Y.; Zhang, L.; Feng, J. Solvent extraction process development and on-site trial-plant for phenol removal from industrial coal-gasification wastewater. *Chem. Eng. J.* **2006**, *117*, 179.
44. Ukrainczyk, L.; McBride, M. B. Oxidation of phenol in acidic aqueous suspensions of manganese oxides. *Clays Clay Miner.* **1992**, *40*, 157–166.
45. Alvarez-Merino, M. A.; Fontecha-Camara, M. A.; Lopez-Ramon, M. V.; Moreno-Castilla, C. Temperature dependence of the point of zero charge of oxidized and non-oxidized activated carbons. *Carbon* **2008**, *46*, 778–787.
46. Halter, W. E. Surface acidity constants of α-Al_2O_3 between 25 and 70°C. *Geochim. Cosmochim. Acta* **1999**, *63*, 3077–3085.
47. Hochella, M. F.; Banfield, J. F. Chemical weathering of silicates in nature; a microscopic perspective with theoretical considerations. *Rev. Mineral. Geochem.* **1995**, *31*, 353–406.
48. Banfield, J. F., Navrotsky, A., Eds. *Nanoparticles and the Environment*; Reviews in Mineralogy & Geochemistry; Mineralogical Society of America: 2001; Vol. 44.
49. Hochella, M. F.; Lower, S. K.; Maurice, P. A.; Penn, R. L.; Sahai, N.; Sparks, D. L.; Twining, B. S. Nanominerals, mineral nanoparticles, and earth systems. *Science* **2008**, *319*, 1631–1635.

Chapter 6

Transformation from Phyllomanganates to Todorokite under Various Conditions: A Review of Implication for Formation Pathway of Natural Todorokite

Xionghan Feng,[1,*] Huaiyan Zhao,[1] Fan Liu,[1] Haojie Cui,[1,2] Wenfeng Tan,[1] and Wei Li[3]

[1]Key Laboratory of Arable Land Conservation (Middle and Lower Reaches of Yangtse River), Ministry of Agriculture, College of Resources and Environment, Huazhong Agricultural University, Wuhan 430070, China
[2]Institute of Urban Environment, Chinese Academy of Sciences, Xiamen 361021, China
[3]Key Laboratory of Surficial Geochemistry, Ministry of Education, School of Earth Sciences and Engineering, Nanjing University, Nanjing 210093, China
[*]E-mail: fxh73@mail.hzau.edu.cn

Todorokite, a family of tunnel-structured Mn oxides with a 3 × 3 array of edge-shared MnO_6 octahedra, is commonly associated with ferromanganese oxides in the marine and terrestrial geological settings. Natural todorokite is thought to form from phyllomanganates, such as birnessite, buserite and vernadite. The synthesis of todorokite has also gained much interest due to its unique MnO_6 octahedral molecular sieve (OMS) structure and physicochemical properties, providing many potential applications, such as adsorbents, catalysts and rechargeable battery materials. In this chapter, a review is presented of the transformation from phyllomanganates to todorokite under various conditions to highlight the factors governing todorokite formation and the underlying mechanisms. The three key factors were found to be (i) stable 10-Å phyllomanganate with an appropriate amount and type of interlayer cations, (ii) an appropriate number of Mn(III) in the phyllomanganate and (iii) a relatively high temperature conditions. On this basis, the possible pathway of natural todorokite formation is

In Advances in the Environmental Biogeochemistry of Manganese Oxides; Sparks, et al.;
ACS Symposium Series; American Chemical Society: Washington, DC, 2015.

proposed as: biogenic or abiotic phyllomanganate → stable 10-Å phyllomanganate with appropriate interlayer cations and structural Mn(III) → todorokite. These results advance our fundamental knowledge on both todorokite formation mechanisms in nature and OMS synthesis design in application.

Introduction

Todorokite is a naturally occurring manganese (Mn) oxide found in terrestrial Mn ore deposits, weathering products of manganese-bearing rocks, and marine Mn nodules (*1*, *2*). The MnO_6 octahedra of todorokite share edges within chains and corners between chains to form a 3 × 3 tunnel framework. Inside the tunnels are incorporated water molecules and foreign metal cations, such as Ca^{2+}, Mg^{2+}, Ba^{2+}, Na^{+}, K^{+} (*2–4*). Synthetic todorokite is predominantly prepared with Mg^{2+} in the tunnels (*5–8*), although other divalent cations of a similar size are also used (*9*, *10*). The Mn in these minerals is mixed-valent, with average oxidation states ranging from 3.4 to 3.8 (*5–9*, *11*). Due to its superior characteristics in ion exchange, specific surface area, thermal stability and molecule-sized tunnels (*6*), todorokite has many potential industrial applications such as molecular sieves, lithium-manganese-oxide cathode materials, heterogeneous catalysts and sensors (*6*, *7*, *11–14*), and it also plays an important role in cleaning up natural water and controlling the concentration of heavy metals in soil solution (*15–18*).

Todorokite was first found in the Todoroki mine (Japan) in 1934, but the natural samples with high purity and crystallinity are rare, indicating the necessity of creating its synthetic counterpart for its structure, properties and origin studies (*3*, *5*, *6*, *19–23*). Todorokite was first synthesized by Golden et al. (*5*) through autoclave treatment of Mg^{2+}-exchanged birnessite, which is known as Mg-buserite (Figure 1 Reaction process diagram). Birnessite, a 0.7 nm manganate, has layer structure by stacking MnO_6 sheets along the *c* axis with a basal plane spacing of ~0.7 nm due to the presence of monolayer water molecules between the layers (*24–26*). When hydrated in the suspension or Mg^{2+}-exchanged with an expanded basel plane spacing of 1.0 nm due to bilayer water molecules in the interlayers, the as formed birnessite is called "buserite", a 1 nm manganate, structurally related to "birnessite" (*15*, *27*, *28*). Other hydrated inorganic divalent cations, such as Ni^{2+}, Co^{2+} and Cu^{2+}, have been used successfully as templates for the synthesis of todorokites with different physical and chemical properties (*6*, *9*, *10*, *29*). An nm-sized todorokite with a higher BET surface area and improved catalytic performance was synthesized from a phyllomanganate precursor prepared using a sol-gel process by Liu et al. (*16*). A microwave-assisted hydrothermal method was also used to synthesize the todorokite with properties superior to those of conventionally synthesized todorokite, such as greater stability, crystallinity and catalytic activity (*30*, *31*). However, in these studies, high temperature and pressure were exclusively required in the autoclave hydrothermal treatment, leading to low productivity and difficulties in monitoring and controlling the reaction. Feng et al. (*21*, *32*) first synthesized todorokite in an open container at atmospheric pressure by reflux treatment (at 100 °C) of Mg-buserite, and

In Advances in the Environmental Biogeochemistry of Manganese Oxides; Sparks, et al.;
ACS Symposium Series; American Chemical Society: Washington, DC, 2015.

found the structure and characteristics of the product were similar to those of hydrothermally synthesized samples. The formation of todorokite is greatly accelerated under mild reflux conditions, enabling the simulation of formation processes for naturally occurring todorokite (*14*, *18*, *21*, *33–37*).

Although pure todorokite can be obtained by chemical methods, todorokite is often found associated with Mn oxides of microbial origin in ocean nodules, soils and sediments, and the pathways and mechanisms of todorokite formation from biogenic Mn oxides in nature still remain unknown (*15*, *17*, *38–41*). In the presence of high concentration of U(VI), poorly ordered tunnel structured biogenic Mn oxide, similar to todorokite, was formed by *Bacillus* sp. strain SG-1 (*42*). In addition, a todorokite-like tunnel structural MnO_X formed by the fungus *Acremonium* sp. Strain KR21-2 was also reported (*43*). These microbe mediated MnO_X materials may not be yielded from the direct oxidation of Mn^{2+}, but possibly as the products of secondary mineralization, because Mn(IV)-oxides resembling δ-MnO_2, a turbostratic variety of birnessite, were the exclusive primary oxidation products by the same microbial species (*44*, *45*). The association of biogenic Mn oxide with todorokite, or bio-related origin of todorokite, was observed in many natural environments (*17*, *39*, *41*, *46*). Feng et al. (*36*) also synthesized a nanoscale, todorokite-like phase from biogenic Mn oxide produced by the freshwater bacterium *Pseudomonas putida* strain GB-1 at atmospheric pressure through reflux treatment. Based on these reports, a simple bio-related formation pathway of natural todorokite can be expressed as: biogenic Mn oxide → 10-Å phyllomanganate → todorokite. To our knowledge, this is the first report about the experimental evidence of the transformation of biogenic Mn oxide to a todorokite-like phase.

In this chapter, the transformation from phyllomanganates (*i.e.* abiotic (synthesized) birnessite, biogenic Mn oxide) to todorokite under various reaction conditions (hydrothermal or reflux treatment) will be reviewed. A flow diagram for summary of the transformation of phyllomanganates into todorokite in the previous studies is shown in Figure 1.

Synthesis of Todorokite under Hydrothermal Conditions

Todorokite is one of the major manganese minerals in many marine manganese concretions and hydrothermal deposits (*15*), whose composition, shape and properties are influenced by the temperature and pressure of hydrothermal condition. Thus todorokite can be adopted as genetic indicators for manganese concretions, ores and sediments, as well as a geothermometer in the search of ancient and modern hydrothermal vents (*47*). Mellin and Lei (*47*) reported that the structural stability of hydrothermal todorokite increases with increasing temperature of the hydrothermal fluids, but shows little pressure dependence. Under hydrothermal conditions, todorokite was synthesized by Golden et al. (*5*) through autoclave treatment of Mg^{2+} exchanged birnessite (Mg-buserite) at 155 °C for 8 h, but manganite appeared with the reaction time prolonged for 24 h. Shen and co-workers obtained thermally stable todorokite by autoclave treatment of Mg-buserite from 150 to 180 °C for more than 2 d (*6*). All these reports indicate

In Advances in the Environmental Biogeochemistry of Manganese Oxides; Sparks, et al.;
ACS Symposium Series; American Chemical Society: Washington, DC, 2015.

that temperature, pressure and reaction time may be the major influential factors in todorokite formation. The following experiments were conducted to explore the effects of these factors on the todorokite formation under hydrothermal conditions in terms of kinetics and mineralogical characteristics (*48*). Understanding of the roles of those influential factors in todorokite formation can shed light on the mechanisms of todorokite formation and facilitate todorokite synthesis and application in practice.

To quickly determine the produced mineral phases, oriented glass slides mounted with samples were prepared and heat-treated for the X-ray diffraction (XRD) analyses. Although both Mg(or $M^{2+/3+}$)-buserite and todorokite are stable 1-nm manganates at the room temperature, todorokite has a higher thermal stability compared to Mg(or $M^{2+/3+}$)-buserite. Mg (or $M^{2+/3+}$)-buserite can be transformed into the 0.7-nm manganate by heating or dehydrating at a certain temperature, for instance 140 °C, but todorokite maintains stable under this condition. Thus the oriented slides mounted with intermediate reaction product samples were heated for 12 h at 140 °C before XRD measurement, and the 1 nm peak in the XRD pattern can be assigned to the diagnostic characteristics of todorokite (*21*, *32*) and used to determine the degree of buserite transformation to todorokite. All of the oriented XRD patterns in figures for the intermediate or final products in the todorokite formation experiments throughout the chapter were collected using the oriented slides mounted with samples and heat treated for 12 h at 140 °C.

Todorokite was synthesized by exchanging birnessite, prepared by oxidation of $Mn(OH)_2$ in alkaline media, with Mg^{2+} and an autoclave hydrothermally treatment. Figure 2a shows the powder XRD pattern of the synthesized todorokite. The characteristic diffraction peaks at 0.958, 0.716, 0.478, 0.446, 0.319, 0.245, 0.241, 0.236, 0.222, 0.216, 0.198, 0.192, 0.174, 0.169, 0.153 and 0.142 nm of todorokite are consistent with those of natural todorokite (JCPDS 38-475) (*48*). From the TEM images, synthesized todorokite particles consisted of fibers extending from a central plate (Figure 3a) and the electron diffraction pattern of the plate presented pseudo hexagonal symmetry resulting from the fibers running in three directions (Figure 3b). The trilling pattern of the twinned crystals is typical of todorokite. The morphology and growth characteristics of the synthesized todorokite agree very well with those of naturally occurring todorokite (*3*, *17*, *39*, *48*, *49*).

Hydrothermally process can provide a relatively higher temperature and pressure in the autoclave. The effects of various temperatures and pressures on todorokite formation were investigated. At the same temperature, the pressure of the system increased with an increment of the autoclave filling ratio, *i.e.*, the ratio of mineral suspension volume to autoclave volume (*48*). The XRD patterns of todorokites synthesized at 160 °C for 4 h with the 60% and 90% filling ratios are shown in Figure 2b. The todorokites synthesized at different pressures exhibited similar XRD patterns, indicating that pressure had a relatively small impact on the synthesis of todorokite. In addition, Feng et al. also synthesized todorokite successfully at the ambient pressure (*21*), which further confirmed that the pressure is not a governing factor for todorokite formation.

Publication Date (Web): November 17, 2015 | doi: 10.1021/bk-2015-1197.ch006

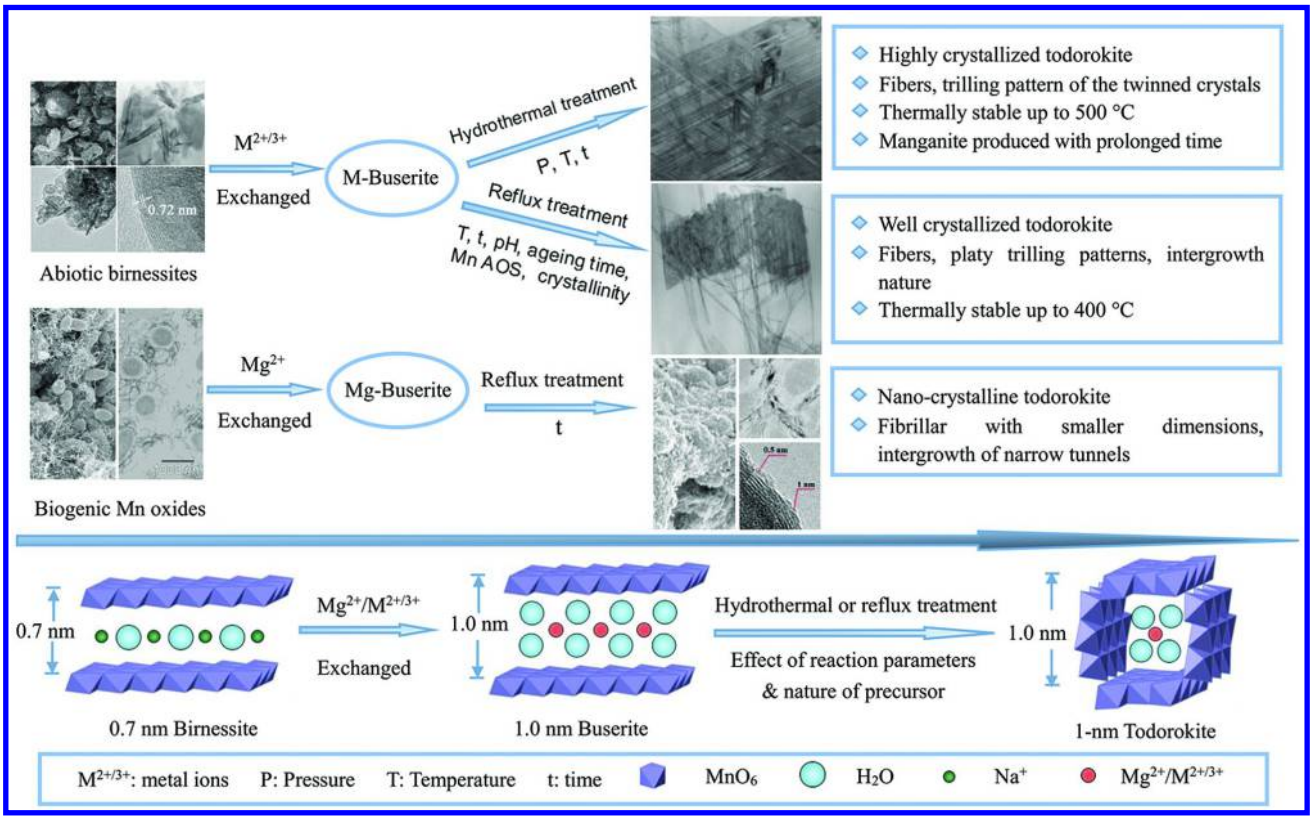

Figure 1. Flow diagram for the transformation of phyllomanganates into todorokite in the previous studies (6, 14, 21, 23, 32–36, 48, 56).

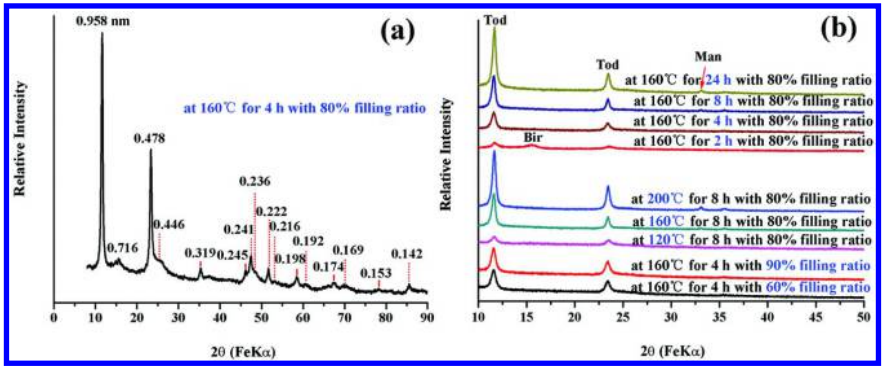

Figure 2. Powder (a) and oriented XRD (b) patterns of todorokites synthesized at different conditions (Tod: todorokite; Bir: birnessite; Man: manganite). Adapted with permission from ref. (48). Copyright (2005) Earth Science.

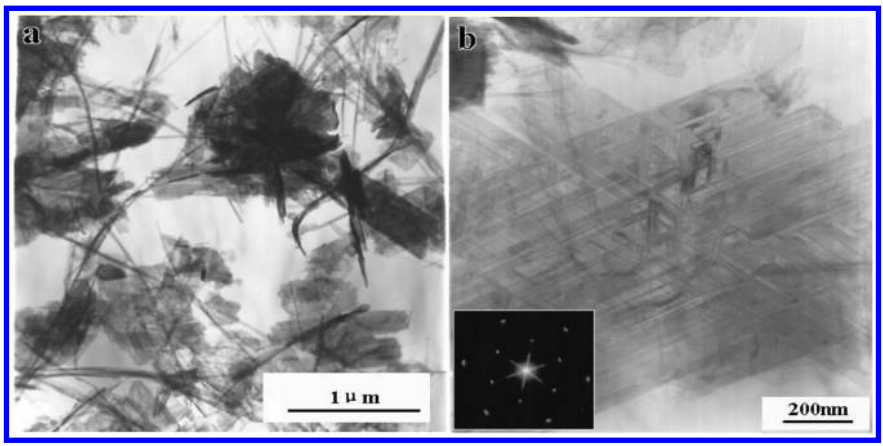

Figure 3. TEM images of the todorokite synthesized for 4 hours at 160 °C: (a) morphology image; (b) high multiple TEM images of the trilling crystal and ED pattern in the direction of [001]. Reproduced with permission from ref. (48). Copyright (2005) Earth Science.

Figure 2b shows the XRD patterns of the products synthesized at 120, 160, and 200 °C for 8 h with the 80% filling ratio. The diffraction reflections in the XRD pattern of the product synthesized at 120 °C can be all ascribed to todorokite, while the reflection of manganite (γ-MnOOH, JCPDS 8-0099) appeared apart from those of todorokite at 160 °C and 200 °C. This suggests that increasing hydrothermal temperature accelerates the transformation rate of Mg-buserite to todorokite, whereas at a higher temperature todorokite converts into manganite. Thus the transformation of birnessite to todorokite is probably an endothermic process due to bond dissociation during the transformation of layer manganese oxides into tunnel manganates (*16*). The effect of an extended treatment time is

similar to that of an increased in hydrothermal temperature, as indicated by the XRD patterns of the products synthesized at 160 °C with the 80% filling ratio for different time periods (Figure 2b).

The typical process of birnessite transformation into todorokite under hydrothermal conditions can be simply denoted as follows (*48*).

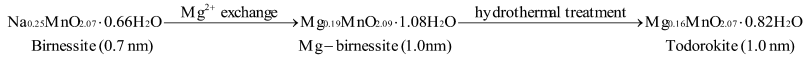

Synthesis of Todorokite at Atmospheric Pressure

The aforementioned results indicate that reaction pressure has little impact on synthesis of todorokite, so a refluxing process in an open container at atmospheric pressure has been developed to prepare todorokites by a simple two-step procedure (*21*). First, the birnessite prepared by oxidation of $Mn(OH)_2$ with O_2 in alkaline media was exchanged with Mg^{2+} in $MgCl_2$ solution for 12 h to produce Mg-buserite, followed by separating, washing and dispersing the Mg-buserite in H_2O or $MgCl_2$ solution, and heating the Mg-buserite suspension to reflux under stirring for up to 24 h.

Characterization of Todorokite Synthesized at Atmospheric Pressure by a Refluxing Process

The diffraction reflections in the powder XRD pattern of the todorokite synthesized at atmospheric pressure matched well with those of the naturally formed todorokites (Figure 4a, JCPDS 13-164 and JCPDS 38-475) and the hydrothermally synthesized samples (Figure 2a). The broad diffraction peaks at 0.48 and 0.24 nm suggested that the crystal size of the synthetic todorokite was small and significant quantities of tunnels larger than 3 × 3 were probably present in the todorokite (*24*). The size of the synthesized todorokite crystallite was calculated to be 23 nm, from half peak width of 0.962 nm diffraction peak. The todorokite crystal grew along the *b* axis, running parallel to the tunnel direction (*9*, *24*).

The morphology of the synthesized todorokite was dominated by fibers with various lengths, which extend from a platy fiber-matted matrix (Figure 4b). The electron diffraction (ED) pattern of the matrix showed a pseudo hexagonal symmetry. From the lattice image of todorokite across the fiber direction (inset of Figure 4a), tunnels of 3 MnO_6 octahedral chain widths (1 nm) were predominant. Tunnels with a different width were also observed: a 4, 3 chains arranged sequence on the upper side changed to a 2, 5 sequence on the lower side. Such morphological and intergrowth properties, typical characteristics of the natural todorokite samples, can be used to distinguish todorokite from other manganese oxides and may account for the streaking of ED pattern and broadening of XRD peaks (*3–5*, *24*, *49*).

In Advances in the Environmental Biogeochemistry of Manganese Oxides; Sparks, et al.;
ACS Symposium Series; American Chemical Society: Washington, DC, 2015.

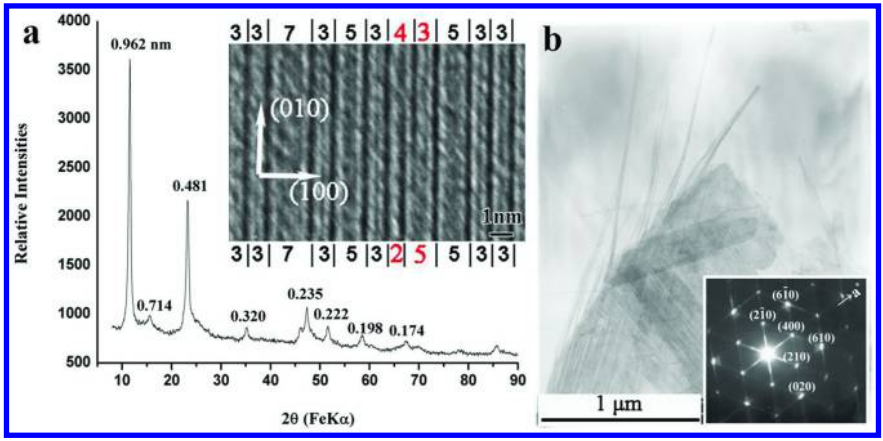

Figure 4. Powder XRD diffraction pattern of todorokite (a); TEM image and selected area of electron diffraction of todorokite (b); (001) plane HRTEM images of individual fibers (the inset of Figure (a)). Adapted with permission from ref. (21, 32). Copyright (2004) American Chemical Society and Copyright (2004) Science China Press.

The Raman spectrum of synthesized todorokite exhibited one dominant band at around 644 cm^{-1} and two weak bands at 296 and 359 cm^{-1} (Figure 5a), which was different from those of birnessite (*21*, *50*). The adsorbed band around 764 cm^{-1} in the IR spectrum of todorokite (Figure 5b), which was assigned to the characteristic adsorbent of manganese oxides with tunnel structure, can distinguish todorokite from birnessite (*9*, *18*, *51*). However, the IR and Raman spectra of synthesized todorokite were in agreement with those of the natural samples and the todorokite synthesized hydrothermally by Golden et al. (*5*, *9*, *21*, *27*). This demonstrated that the todorokite synthesized by a refluxing process was similar to the others in short-ranged structure. Similar to natural todorokite, synthesized samples maintained a todorokite structure below 400 °C (*20*, *52*). Weight loss below 405 °C was probably due to the loss of water physically adsorbed on the surface and bound in the tunnels, and the weight loss in the two steps (405-580 °C, 580-700 °C) could be attributed to the destruction and collapse of tunnel structure, respectively (*10*, *52*).

The effects of synthesis parameters, such as reaction temperature and pH, nature of the precursor birnessite, and exchanged ions in the interlayer of birnessite on the transformation of birnessite into todorokite were explored in the following experiments.

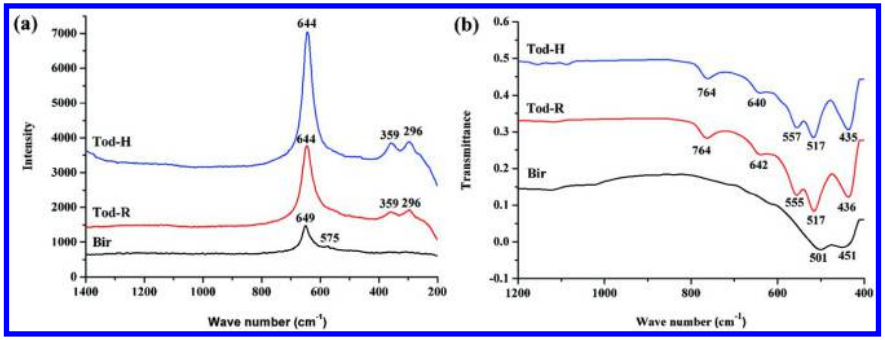

Figure 5. (a) Raman and (b) IR spectra of birnessite (Bir) and todorokite synthesized via reflux treatment at atmospheric pressure (Tod-R) or hydrothermally treatment (Tod-H). Data of todorokite samples were taken from ref. (21) with permission. Copyright (2004) American Chemical Society

Effect of Reaction Temperature on Todorokite Formation

To explore the effect of reaction temperature, transformation experiments of buserite to todorokite were carried out at temperatures of 100, 90 and 40 °C. At a refluxed temperature of 100 °C, XRD patterns of the intermediate products indicated that the complete conversion of Mg-buserite to todorokite took 2 h (Figure 6a), while at a heating temperature of 90 °C, the complete conversion took as long as 48 h (Figure 6a). When the temperature was reduced to 40 °C, the transformation dramatically slowed down and the intensity of characteristic peaks of todorokite became similar to that of birnessite after 8 d of reaction, indicating that around half of the Mg-buserite was converted to todorokite at this time interval (Figure 6a). After that, the XRD peak intensity ratio of todorokite to birnessite remained almost unchanged even with the reaction time prolonged up to 35 d. These results suggest that the transformation from Mg-buserite to todorokite takes more time at a lower reaction temperature, and Mg-buserite could not be transformed completely into todorokite at a relatively low temperature of 40 °C (*33*). When reaction temperature decreased below 100 °C, the conversion of buserite to todorokite decelerated both in terms of kinetics (conversion rate) and thermodynamics (conversion ratio), suggesting an endothermic transformation process.

In Advances in the Environmental Biogeochemistry of Manganese Oxides; Sparks, et al.;
ACS Symposium Series; American Chemical Society: Washington, DC, 2015.

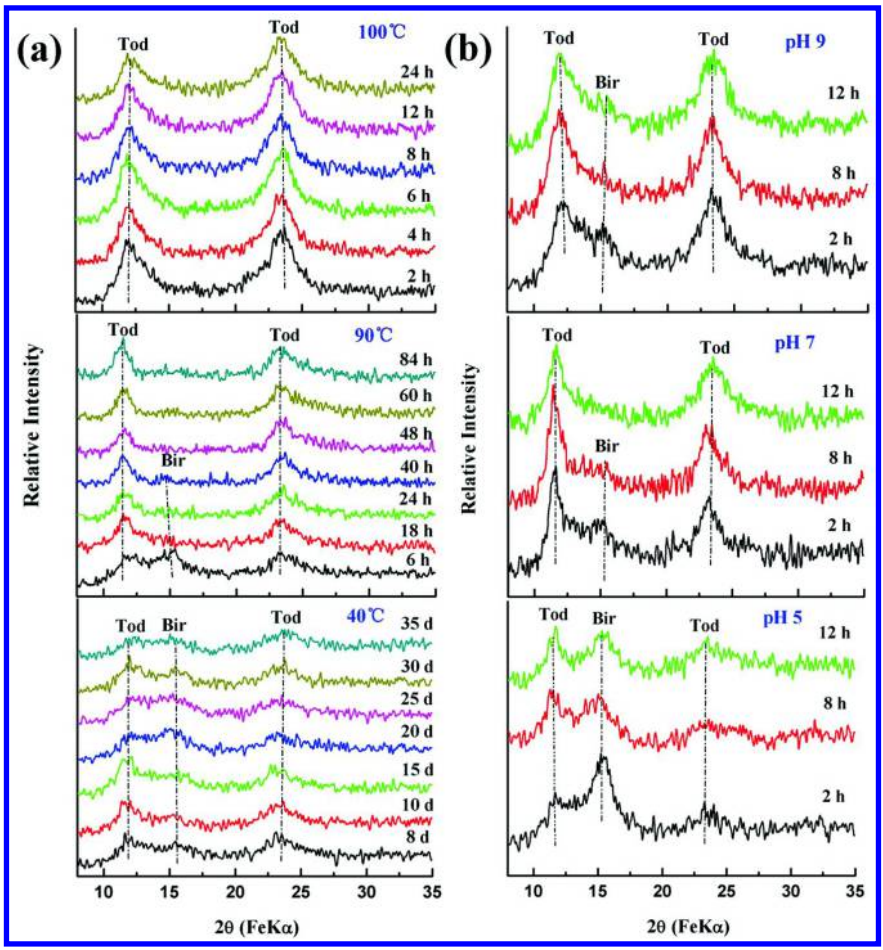

Figure 6. Oriented XRD patterns of the heat-treated (140 °C) intermediates when Na-buserites were exchanged with Mg^{2+} and reflux treatment at different temperatures (pH 7) (a) and different pH values (at 100 °C) (b). Adapted with permission from ref. (33). Copyright (2006) The Clay Minerals Society.

Effect of pH on Todorokite Formation

At a relatively wide pH range of 5-9, todorokite can be obtained from Mg-buserite (*33*), but the rate of todorokite formation in a neutral or alkaline medium is higher than that in an acidic medium (Figure 6b). When Mg-buserite was treated in a slightly acidic medium, the interlayer Mg^{2+} of the Mg-buserite could be extracted by H^+ in the solution (*22*). Moreover, some of the remaining Mn^{3+}_{layer} cations could migrate from the layer into the interlayer and disproportion to form Mn^{4+}_{layer} and Mn^{2+}_{aq}. The Mn^{2+}_{aq} could be adsorbed above or below vacant sites at pH 5 (*53*, *54*). The decreased amount of Mg^{2+} and Mn^{3+}_{layer} may impede the transformation of buserite into todorokite. On the other hand, todorokite can form in a weak alkaline medium, but no todorokite has been found in acid soils so far, probably due to lack

In Advances in the Environmental Biogeochemistry of Manganese Oxides; Sparks, et al.;
ACS Symposium Series; American Chemical Society: Washington, DC, 2015.

of base ions such as Ca^{2+} and Mg^{2+} in acid soils because of strong eluviations (*55*). These divalent cations, possessing larger hydrated ion radii and higher hydration energies, can readily expand the 0.7 nm basal plane spacing of birnessite to the 1.0 nm of buserite (*9*). The interlayer space of stable 10-Å phyllomanganate just matches the T (3 × 3) tunnel size of todorokite (*4*). In addition, todorokite is not stable in acidic conditions (*55*), leading to no occurrence of todorokite in those environments. Therefore, the pH values in the media may be critical to the transformation of birnessite to todorokite in the geological settings.

Effect of Ageing Treatment of Na-Buserites on Todorokite Formation

Before natural todorokite formation, the precursor birnessite or buserite may be subject to ageing for a period of time, which could impact their structural characteristics and transformation to todorokite. The common synthetic precursor for the transformation is a triclinic birnessite with a basal plane spacing of ~0.7 nm. With ageing treatment for different durations, the basal reflections of birnessite shifted slightly to larger values and the 20*l* and 11*l* reflections broadened or disappeared (Figure 7a, (*56*)). This suggested that ageing treatment can alter, to a certain extent, the substructural characteristics of birnessite, such as stacking order or symmetric type of MnO_6 octahedral layer, because the 20*l* and 11*l* reflections are the most sensitive to structural parameters of layered manganese oxides (*54*, *57*). Moreover, the occurrence of $Mn^{2+/3+}$ ions in the interlayer region may lead to the rearrangement of the Na^+ ions with ageing treatment, resulting in a slight shift in the basal reflection. After Na-buserites with different ageing durations were exchanged with Mg^{2+} and heated at 80 °C for 12 h, more todorokite was produced with increasing ageing duration (Figure 7b). At an ageing time of 12 months, most of the Na-buserite was converted into todorokite. In contrast, only small amount of the pristine Na-buserite, without ageing treatment, underwent the transformation under the reflux condition. The results indicate that the ageing of the precursor does alter its structural characteristics and enhance the transformation to todorokite at the ambient pressure.

Na-buserite contains very little octahedral vacancy in MnO_6 layers and the ordered distribution of Mn^{3+}-rich rows parallel to [010] is separated in the [100] direction by two Mn^{4+} rows (*6*, *15*, *54*). In the course of ageing, some Mn^{3+} in the MnO_6 layers may be subjected to slow thermodynamically favorable disproportionation reaction in the following sequence: $Mn^{3+}_{layer} + Mn^{3+}_{layer} \rightarrow Mn^{4+}_{layer} + Mn^{2+}_{layer} \rightarrow Mn^{4+}_{layer}$ + vacancy + Mn^{2+}_{aq}. The released aqueous Mn^{2+} could migrate back into the interlayers and/or be further oxidized by free oxygen in the solution. Thus ageing treatment of Na-buserite would produce more octahedral vacancies and corner-sharing Mn(III) octahedra, which may promote the transfer and rearrangement of manganese to construct a tunnel structure during the transformation to todorokite. This may explain the significant increase in the transformation rate from Mg-buserite into todorokite after ageing of the precursor Na-buserite. These results suggest that using aged phyllomanganates as the precursors is a more proper and efficient method to simulate the origination of natural todorokite in the surface environments.

In Advances in the Environmental Biogeochemistry of Manganese Oxides; Sparks, et al.;
ACS Symposium Series; American Chemical Society: Washington, DC, 2015.

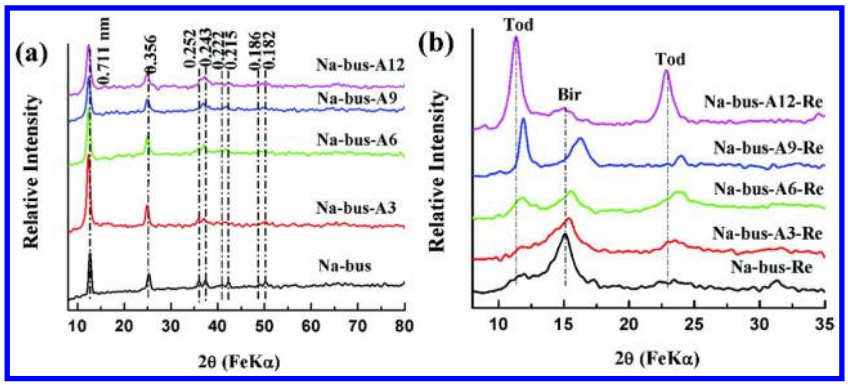

Figure 7. Powder XRD patterns of freeze-dried Na-buserites after different ageing durations (a) and oriented XRD patterns of their products after exchange with Mg^{2+} and reflux treatment at 80 °C for 12 h (b). (Re-reflux). Adapted with permission from ref. (56). Copyright (2010) Springer.

Effect of Crystallinity of Na-Buserites on Todorokite Formation

Na-buserite samples with different crystallinities were synthesized at temperatures of 5 and 25°C to elucidate the effect of crystallinity of the precursors on their transformation to todorokite. The crystallinity of Na-buserite prepared at 25 °C was much higher than that prepared at 5 °C (*33*). When using the poorly crystalline Na-buserite as the precursor, the complete transformation from Na-buserite to todorokite only took 48 h (Figure 8a), while the full transformation of the highly crystalline Na-buserite into todorokite required about 7 d under the same conditions (Figure 8b). This suggested that the poorly crystalline birnessite is more easily transformed into todorokite than the highly crystalline one. When using poorly crystalline birnessite as the precursor, both dissolution and structural rearrangement of the birnessite could facilitate the formation of todorokite phase via either a dissolution-recrystallization process (*18*) or a topotactic transformation mechanism (*36*). Natural birnessite typically occurs as poorly crystalline nano-sized particles, which may facilitate its conversion to todorokite and other Mn oxides.

Effect of Average Manganese Oxidation States (Mn AOS) of Na-Buserites on Todorokite Formation

The buserites with different Mn AOS values were prepared by controlling the MnO_4^-/Mn^{2+} ratio in concentrated NaOH or KOH solution (*14*). Either $KMnO_4$ or $NaMnO_4$ were used as the permanganate. Table 1 lists the synthesis conditions and compositions of the products. The Mn AOS increased with increasing MnO_4^-/Mn^{2+} ratio. The XRD patterns of products formed after reflux

treatment showed that the intensities of diagnostic diffraction reflections of todorokite at 0.96 and 0.48 nm became stronger and those of birnessite became weaker when the MnO_4^-/Mn^{2+} ratio in (Na, K)-buserite samples decreased from 0.55 to 0.33 (Figure 9). It suggested that more buserite was converted into todorokite for the precursors with a lower Mn AOS. The effect of Mn AOS on the transformation of the Na-buserites into todorokite was similar to that for the (Na, K)-buserite samples, except that the 0.55-Na-Bus sample was not transformed into todorokite. However, none of the K-buserite samples could be transformed into todorokite. Therefore, transformation of birnessite to todorokite at atmospheric pressure is impeded with an increase in the Mn AOS values of (Na, K)/(Na)-buserites and inhibited by interlayer K^+ in K-buserites. In buserite, the Mn(IV) is dominating, the amount of Mn(III) is about 25.7 %, and the amount of Mn(II) is small (about 4.7 %) (*58*). Thus buserite with a low Mn AOS is due to the increase of Mn(III) content. From the results, it can be deduced that in the process of birnessite transformation into todorokite, Mn(III) moves from the layers of birnessite (buserite) to the interlayer to build the tunnel structure via linkage between adjacent MnO_6 octahedral layers. The elongation and weakening of Mn(III)-O bond in the octahedral layer due to the Jahn-Teller effect will lead to the occurrence of the kink-like fold of the layer (*17*), from which the tunnel walls can be easily constructed. Thus, Mn(III) in birnessites plays a crucial role in the transformation of birnessite into todorokite as well as the construction of tunnel structures (*36*, *59*). Such a role was also confirmed by the Mn(III) removal experiments (*34*). When Na-buserite was treated with pyrophosphate solutions at pH 7, Mn(III) migrated into solution from MnO_6 layers because of chelation with pyrophosphate. The Mn(III) removal treatment remarkably inhibits the transformation of birnessite into todorokite.

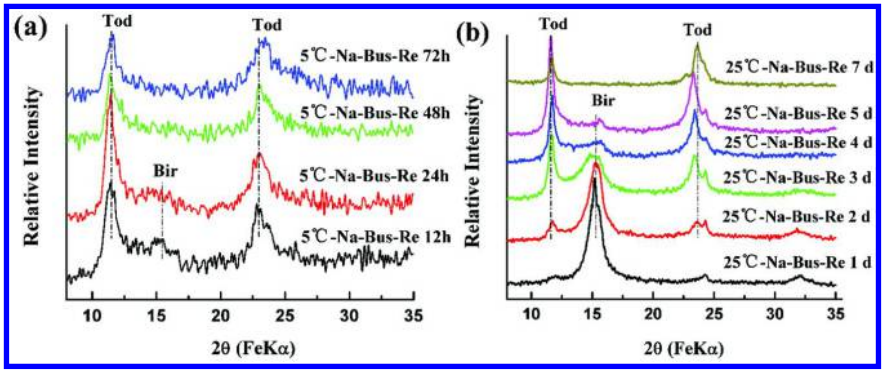

Figure 8. Oriented XRD patterns of the heat-treated (140 °C) intermediates when Na-buserites of different crystallinities as precursors were exchanged with Mg^{2+} and reflux treatment at 80 °C: (a) Na-buserite synthesized at 5 °C; (b) Na-buserite synthesized at 25 °C. (pH 7). Adapted with permission from ref. (33). Copyright (2006) The Clay Minerals Society.

Publication Date (Web): November 17, 2015 | doi: 10.1021/bk-2015-1197.ch006

Table 1. Reaction conditions for preparing the buserite products, and elemental compositions of the synthesized buserite samples and average manganese oxidation states (AOS). Adapted with permission from ref. (*14*). Copyright (2009) The Clay Minerals Society.

Reaction condition	*Ratio of MnO_4^-/Mn^{2+}*	*Sample*	*Na mmol/g*	*K mmol/g*	*Mn mmol/g*	*AOS*
$KMnO_4$+NaOH+$MnCl_2$	0.33	0.33-Na(K)-Bus	3.06	0.13	8.47	3.51
$KMnO_4$+NaOH+$MnCl_2$	0.45	0.45-Na(K)-Bus	3.25	0.16	8.32	3.63
$KMnO_4$+NaOH+$MnCl_2$	0.55	0.55-Na(K)-Bus	3.05	0.31	7.83	3.76
$NaMnO_4$+NaOH+$MnCl_2$	0.33	0.33-Na-Bus	3.09		8.67	3.53
$NaMnO_4$+NaOH+$MnCl_2$	0.45	0.45-Na-Bus	2.99		8.03	3.80
$NaMnO_4$+NaOH+$MnCl_2$	0.55	0.55-Na-Bus	3.12		7.91	3.87
$KMnO_4$+KOH+$MnCl_2$	0.33	0.33-K-Bus		0.61	10.23	3.50
$KMnO_4$+KOH+$MnCl_2$	0.45	0.45-K-Bus		1.11	9.93	3.61
$KMnO_4$+KOH+$MnCl_2$	0.55	0.55-K-Bus		0.90	9.11	3.89

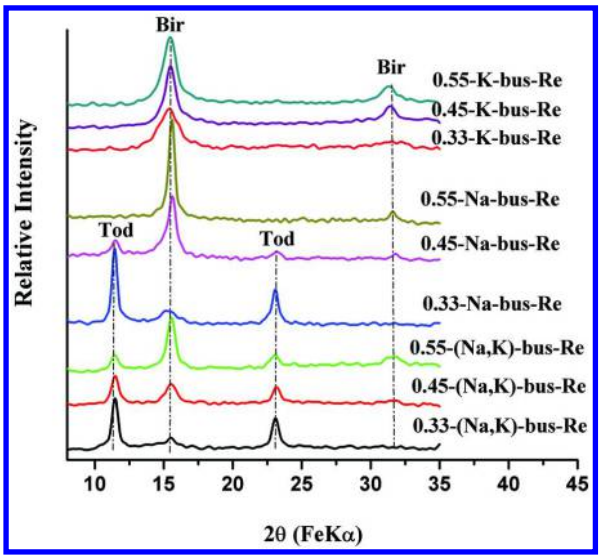

Figure 9. Oriented XRD patterns of Na-buserites exchanged with Mg^{2+} and refluxed at 100 °C for 24 h. Adapted with permission from ref. (14). Copyright (2009) The Clay Minerals Society.

Effect of Type and Amount of Ions Exchanged with Na-Buserites on Todorokite Formation

Na^+, Co^{2+}, and $Co(NH_3)_6^{3+}$ exchanged birnessites are assigned to buserite samples with a 1.0 nm *d* spacing of (001) basal plane (*22*). Li^+ exchanged birnessite retains the interlayer structure of birnessite with a diffraction reflection at 0.72 nm. The basal *d* spacing of La-buserite is 1.13 nm, larger than that of the normal buserite (<1.0 nm), which may result from triple layer water molecules between adjacent MnO_6 octahedral sheets of La-buserite (Figure 10a, (*60*)). After reflux treatment for 24 h, the Li-, Na-, and Co-buserite samples retain the layered structure with their basal *d* spacings maintaining or collapsed to 0.7 nm, while Mg-, Ni-, $Co(NH_3)_6$-, and La-buserite samples, with their basal *d* spacings remaining stable at ~1.0 nm, were transformed into todorokites under the same conditions (Figure 10b). However, todorokites were reported to form after hydrothermal treatment of Li-, Na-, Co-, and Cu-buserites subjected to a double-aging process (*60*). So the effects of various template cations on the transformation from layered to tunneled structure vary when Me-buserite samples are treated under different conditions.

The position and quantity of cations among the interlayers of buserite as well as the strength of bond between them and MnO_6 octahedral layers mainly depend on the physicochemical properties of exchanged cations. There are three possible sites for the exchanged cations to occupy in the layered structure, *i.e.* A, R and M sites, standing for free interlayer sites, vacancy sites and layer sites, respectively (Figure 11, (*61*)). Mn^{2+} generally occupies R site, while Na^+ and Li^+ are mainly

located in A site (*23*). The hydration energies of Li^+ and Na^+ are very low (520 kJ mol^{-1} and 406 kJ mol^{-1}), indicating that the Li- and Na-buserites can easily lose H_2O molecules in the interlayer, impeding the formation of stable buserite with a 1.0 nm basal d spacing similar to that of todorokite. Therefore, it is difficult for monovalent ion exchanged buserite samples, such as Li- or Na-buserite, to convert to 1.0 nm tunnel structure phases by the mild refluxing process. The radius of divalent Mg^{2+} (0.066 nm) is less than that of Mn^{2+} (0.080 nm), and without d electronic orbits, Mg^{2+} can hardly form coordination bonding and replace Mn^{2+} located in R site. In addition, hydrated Mg^{2+} ions in Mg-buserite are stable (hydration energy is 1921 kJ mol^{-1}) and bound with MnO_6 octahedral layers through weak force, such as electrostatic and van der Walls force. Thus the interlayer structure of Mg-buserite can be readily adjusted and converted to todorokite with a tunnel structure after reflux treatment.

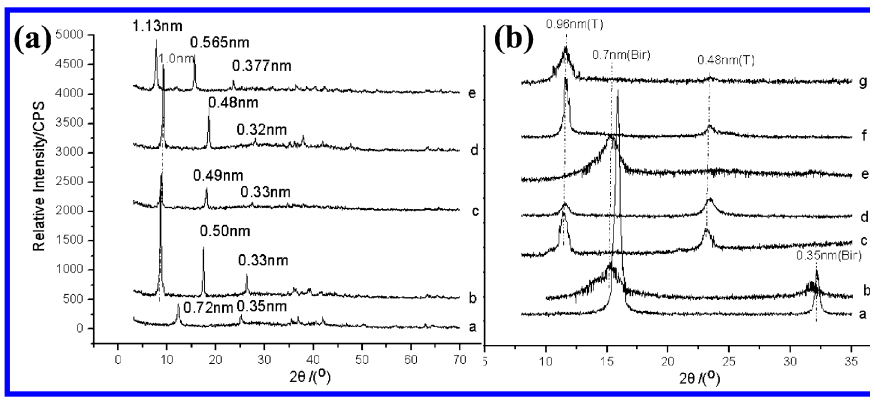

Figure 10. (a) Powder XRD patterns of Na-buserites exchanged with different ions: a, Li^+; b, Na^+; c, Co^{2+}; d, $Co(NH_3)_6^{3+}$; e, La^{3+}; (b) Oriented XRD patterns of different Me-buserites (Me-bus) after reflux treatment for 24 h: a, Li-bus; b, Na-bus; c, Mg-bus; d, Ni-bus; e, Co-bus; f ,$Co(NH_3)_6$-bus; g, La-bus (the products were heated at 140 °C for 10 h, T-todorokite; Bir-birnessite). Reproduced with permission from ref. (23). Copyright (2005) Science China Press.

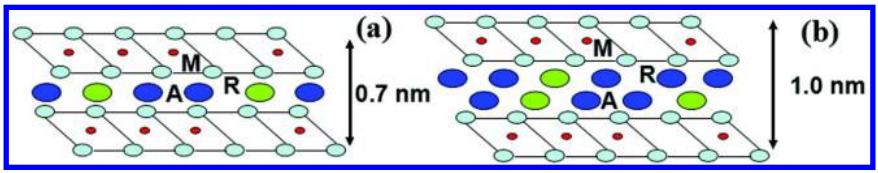

Figure 11. Schemes for structures of birnessite (a) and buserite (b). Adapted with permission from ref. (61). Copyright (1998) Acta Oceanologica Sinica.

The other divalent ions of trace metals, such as Ni^{2+}, Co^{2+}, and Cu^{2+} possess a radius close to that of Mn^{2+} and higher crystal field stabilization energy (CFSE) than Mn^{2+} in an octahedral crystal field, indicating that they can easily replace Mn^{2+} ions in R site (*62*). The occupancies of smaller Cu^{2+}, Ni^{2+} and Co^{2+} ions in R site lead to higher CFSE and shorter coordination distances in bonding with $O^{2-}_{3+x}(OH^-)_{3-x}$ of adjacent Mn(IV, III)O_6 octahedra. Compared to Ni^{2+} ion, the Cu^{2+} and Co^{2+} ions exhibit a closer radius to that of Mn^{2+}, lower CFSE and asymmetrical electron configuration (*47*). Therefore, Cu^{2+} and Co^{2+} ions could be bound more tightly than Ni^{2+} ion in R site with low symmetric $O^{2-}_{3+x}(OH^-)_{3-x}$ coordination. The stability of their coordination in R site can also be reflected by the order of their exchange capacities with Na-buserite: $Cu^{2+} > Co^{2+} > Ni^{2+} > Mg^{2+}$ (*10*, *47*, *63*). Lower exchange capacities imply the weaker bonding between interlayer cations and MnO_6 octahedral layer of buserite, which is expected to promote the tunnel wall construction in R site and todorokite formation.

The Cu-buserites were produced by different concentrations of $CuCl_2$ ion-exchanged with Na-buserite at an uncontrolled pH (*35*). With the concentration of Cu^{2+} increased from 0 to 6 mmol, the basal d-spacing of Cu-buserites decreased gradually from 1.020 nm to 0.956 nm (Figure 12a). After 24 h reflux treatment of Cu-buserites, the intensity of diffraction peaks of todorokite increased gradually with an increment of the amount of Cu^{2+} from 0.5 to 3 mmol (Figure 12b), indicating that Cu^{2+} addition promoted the formation of todorokites. However, at a Cu^{2+} concentration above 4 mmol, the intensity of diffraction peaks of todorokite weakened or even disappeared, indicating the interruption of the todorokites formation under a higher concentration of Cu^{2+}.

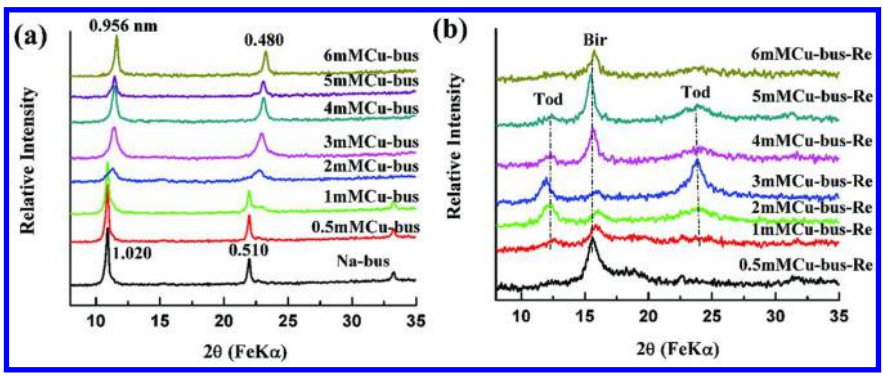

Figure 12. Powder XRD patterns of buserites exchanged with different concentrations of Cu^{2+} (a) and oriented XRD patterns of their products after reflux treatment for 24 h (b). Adapted with permission from ref. (35). Copyright (2009) Elsevier.

When ion-exchange with Na-buserite was performed at a low concentration of Cu^{2+} (0.5–3 mmol), no vacancy was formed and little Mn^{3+} migrated into the interlayer because of the high solution pH and the exchange of Cu^{2+} mainly with interlayer Na^+ of Na-buserite. In this case, the hydrated species of interlayer Cu^{2+}

In Advances in the Environmental Biogeochemistry of Manganese Oxides; Sparks, et al.;
ACS Symposium Series; American Chemical Society: Washington, DC, 2015.

was dominant, which was favorable to the todorokite formation (Figure 12b). With the increase of Cu^{2+} (4–6 mmol) and the concomitant decrease in solution pH during the ion exchange reaction, more Mn^{3+} migrated from MnO_6 layers into the interlayer and disproportionated into Mn^{2+} and Mn^{4+}. The Cu^{2+} was bound to the unsaturated O of three MnO_6 octahedra adjacent to the octahedral vacancy by a Cu–O bond and three interlayer H_2O molecules and the tight Cu–O bond was unfavorable to the formation of todorokite. As a result, the transformation from Na-buserite to todorokite was inhibited with increasing Cu^{2+} concentration (4–6 mmol) (Figure 12b), showing a sharp contrast to the result of a low concentration of Cu^{2+} (0.5–3 mmol).

Todorokite was successfully obtained by hydrothermal treatment of divalent Mg^{2+}, Zn^{2+}, Ni^{2+}, Co^{2+}, and Cu^{2+} exchanged Na-buserite samples, which were synthesized by oxidation of $Mn(OH)_2$ with either O_2 or $Mg(MnO_4)_2$ in alkaline media (*6*, *9*). The formation rate of todorokite was accelerated under hydrothermal conditions at a relatively high temperature and pressure with respect to reflux treatment. The bonds between interlayer divalent cations and MnO_6 layers can be broken more easily under hydrothermal conditions, which facilitates the transformation of phyllomanganates into tectomanganates after the tunnel wall construction between interlayers. The effects of different divalent cations on todorokite formation are not apparent under hydrothermal conditions, but their effects on the transformation of phyllomanganates into tectomanganates can be evident under a mild Earth surface condition or reflux condition. In this scenario, the Me-buserite can be readily transformed into todorokite when the divalent cations bond weakly with MnO_6 octahedral layers, otherwise the layered structure would remain stable and could not be converted into todorokite. This may explain why todorokite formed in the earth surface environment is commonly associated with alkaline earth cations, such as Ca^{2+}, Mg^{2+}, and Ba^{2+} rather than trace metals.

Formation of Todorokite from Biogenic Mn Oxides

Natural todorokite is widely considered to form from layer structured Mn oxides with a hexagonal symmetry, such as vernadite (δ-MnO_2), which are generally of biogenic origin. However, this geochemical process has rarely been documented in the environment or demonstrated in the laboratory (*17*, *18*), except when using precursor phases with a triclinic symmetry as precursors. The formation of a nanoscale, todorokite-like phase from biogenic Mn oxides produced by the freshwater bacterium *Pseudomonas putida* strain GB-1 was reported by Feng et al. (*36*). At long- and short-range structural scales, biogenic Mn oxides were transformed to a todorokite-like phase at atmospheric pressure through refluxing.

Production of Biogenic Mn Oxides and Their Transformation into Todorokite

Biogenic Mn oxides were produced by cultures of *Pseudomonas putida* strain GB-1 (*36*). The Mg^{2+}-exchanged biogenic Mn oxide (hereafter BMO-Mg) was

In Advances in the Environmental Biogeochemistry of Manganese Oxides; Sparks, et al.;
ACS Symposium Series; American Chemical Society: Washington, DC, 2015.

heated to reflux for different time periods. Diffraction patterns of BMO and BMO-Mg exhibit two broad peaks at 0.246 and 0.142 nm resulting from the reflections of the *ab*-layer plane (*28*, *64*, *65*) of the biogenic Mn oxides (Figure 13a). Diffraction patterns of the refluxed products have broad peaks centered at 0.477, 0.248, 0.154, 0.146 and 0.142 nm, all of which can be attributed to the monoclinic todorokite structure (JCPDS 38-475).

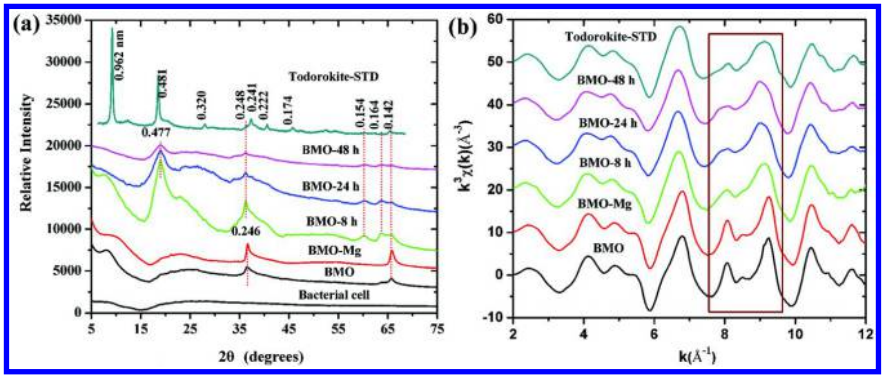

Figure 13. (a) Synchrotron X-ray diffraction patterns and (b) Mn K-edge k^3-weighted EXAFS of the bacterial cell and the intermediate products after Mg^{2+} exchange and reflux treatment for different time periods and the synthesized todorokite standard. Adapted with permission from ref. (36). Copyright (2010) Elsevier.

The *k* space EXAFS spectrum for BMO (Figure 13b) is consistent with those reported for the biogenic Mn oxides produced by other model Mn oxidizing bacteria, such as *P. putida* strain MnB1 (*28*, *65*), *L. discophora* SP6 (*64*, *66*) and *Bacillus sp.* strain SG-1 (*42*, *67*, *68*). The region of the EXAFS spectrum from 7.5 to 9.5 $Å^{-1}$ varies the most between tunnel and layer manganate structures (*42*, *69*, *70*). After the reflux treatment, instead of distinct peaks, two steadily rising slopes gradually appear between 7.5 and 9.5 $Å^{-1}$ (Figure 13b), indicative of the formation of a tunnel structure manganate during refluxing (*17*, *18*, *42*, *67*). Mn EXAFS spectra of the refluxed products are most similar to T(3 × 3) tunnel structure manganate (*i.e.*, todorokite) rather than cryptomelane (T(2 × 2)), pyrolusite (T(1 × 1)) or psilomelane (T(2 × 3)) (*36*, *69*).

In the SEM image (Figure 14a), the biogenic oxide is closely associated with oval shaped cells and stringy, rope-like membrane bound EPS desiccated during sample preparation (*71*). The TEM images show that biogenic oxide particles are scattered around the periphery of the cells and have a morphology of fibrillar thin planes with dimensions of ~10 nm wide by ~100 nm long (Figure 14b and c). This morphology is also similar to that of biogenic Mn oxides derived from *Leptothrix discophora* SP6 (*64*) or *Pseudomonas putida* strain MnB1 (*28*). The fibrillar morphology of biogenic Mn oxide particles remained unchanged after 48 h of reflux treatment (Figure 14d and e), and the particles become less scattered and smaller in dimension probably due to partial reductive dissolution

In Advances in the Environmental Biogeochemistry of Manganese Oxides; Sparks, et al.;
ACS Symposium Series; American Chemical Society: Washington, DC, 2015.

by residual biological substances. Therefore, after reflux treatment, the product almost retains the features of the precursor biogenic Mn oxide in morphology and crystallization, implying a topotactic transformation process for todorokite formation from phyllomanganate precursors (*5*, *17*, *21*). The ~1 nm lattice fringes with a common tunnel width of three MnO_6 octahedra of todorokite along the *a** direction (*1*, *15*, *52*) can be observed in the HR-TEM image of an individual as-prepared Mn oxide fiber after 48 h of reflux (Figure 14f). Additionally, ~0.5 nm lattice fringes, a narrow tunnel with one MnO_6 octahedron width, can be also observed nearby along the consistent direction, indicative of their intergrowth relationship with the former ~1 nm lattice fringes. The feature of intergrowth with a different tunnel width is very common for natural and synthetic todorokite samples (*3*, *5*, *17*, *21*, *49*).

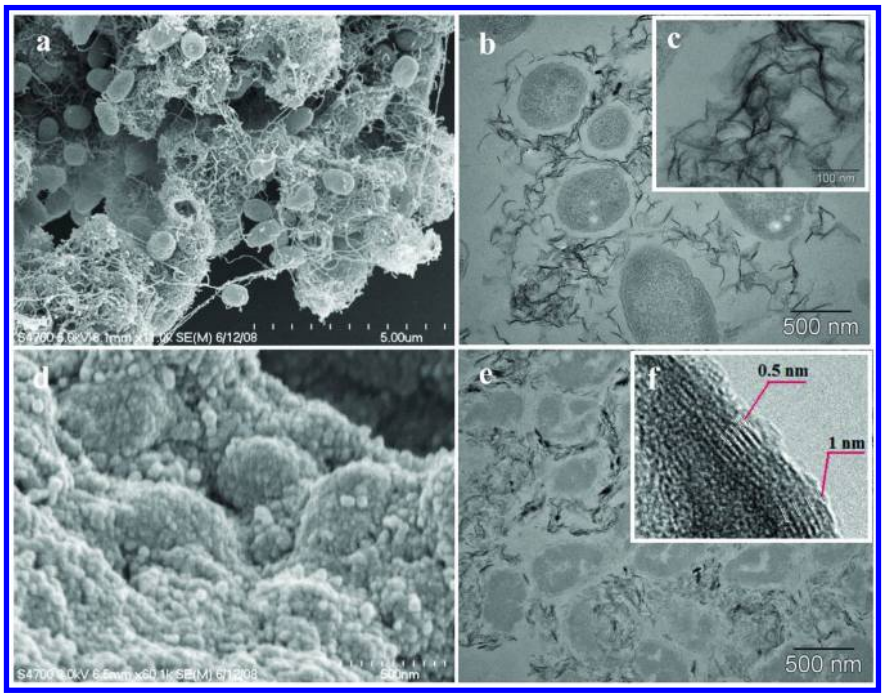

Figure 14. Electron micrographs of the biogenic Mn oxide produced by Pseudomonas putida GB-1 (a-c) and the product (d-f) after Mg^{2+} exchange and reflux treatment for 48 h. (f) was adapted with permission from ref. (36). Copyright (2010) Elsevier.

Factors Governing the Formation of Todorokite and the Pathway of Todorokite Formation in the Environment

Based on data from laboratory and field observations, todorokite does not form directly via precipitation or bio-oxidation processes (*5*, *6*, *17*, *18*, *21*, *39*, *41*); instead, it is likely a product from the transformation of a 1.0 nm phyllomanganate

In Advances in the Environmental Biogeochemistry of Manganese Oxides; Sparks, et al.;
ACS Symposium Series; American Chemical Society: Washington, DC, 2015.

precursor (*17*). Stable 10-Å phyllomanganate is a major prerequisite for todorokite formation because its interlayer space matches the T(3 × 3) tunnel size (*4*). Thus interlayer divalent cations with a high enthalpy of hydration, such as Mg^{2+}, Cu^{2+}, Ni^{2+}, and Ca^{2+}, are essential to a stable 10-Å phyllomanganate (*36*). In addition, weak bonding between the divalent metal ions, such as Mg^{2+} and Ca^{2+}, and MnO_6 layers of buserite is conducive to the adjustment of interlayer structure and the construction of tunnel walls, facilitating todorokite formation, especially under the mild reflux condition. Therefore, buserite samples are enriched with the strong bonding divalent trace metal ions, such as Cu^{2+}, Ni^{2+} and Co^{2+}, as the interlayer cations are less likely to be transformed into todorokite in the surface environment or during the diagenesis processes.

The Mn(III) also plays a key role in the transformation of buserite to todorokite via reflux treatment, and the transformation from Na-buserite to todorokite decreased gradually with decreasing Mn(III) content (*34*, *35*). Mn(III) moves from the layers of birnessite (buserite) to the interlayer, resulting in structural rearrangement to construct the "walls" of the tunnels. Recently, a four-stage process was proposed for the transformation of c-disordered birnessite to todorokite under reflux conditions at atmospheric pressure (*18*). The initial stage involves the formation of todorokite tunnel walls via kinking the layer enriched with the distorted Mn(III) octahedra due to Jahn-Teller effect. It was also reported that the redox conditions not only influenced the Mn(III) content in the phyllomanganate, but also the tunnel size of natural todorokite along *a** direction (*47*, *72*). Some Mn(III) might be produced by re-oxidation of Mn(II) originating from the partial reductive dissolution of biogenic Mn oxide, which facilitates todorokite formation during reflux of Mg exchanged biogenic oxide (*36*). In addition, a recent study on solid state transformation of phyllomanganate into cryptomelane (a tectomanganate with 2 × 2 tunnel size) shows that cryptomelane-like tunnel structure fragments start to form when the number of interlayer Mn(III) migrating from layers during ageing reaches the maximum value of ~1/3 per layer octahedron (*59*). Therefore, structural Mn(III) in the phyllomanganate is another factor governing the formation of tunnel structure, both in todorokite and cryptomelane.

Furthermore, the kinetics of todorokite transformation from phyllomanganate can be accelerated with increasing reaction temperature (Figure 15a and b). At a reflux temperature of 100 °C, Mg^{2+}-buserite completely converts to todorokite within 8 h (*21*, *33*), but the similar conversion at 90 °C and 80 °C takes 48 h and 120 h, respectively. At 160 °C under hydrothermal condition, only 4 h is required to complete the conversion (*48*). These results indicate that the temperature required for todorokite formation is negatively correlated with time. We assume that the temperature T_{Ea} just meets the requirement of the activation energy of todorokite formation. When temperature is higher than T_{Ea}, todorokite can theoretically form with longer time in the surface environment (Figure 15a). At relatively low temperatures, the rate of todorokite formation decreases sharply (*33*), which may explain why todorokite tends to occur prevalently in ocean hydrothermal deposits, while in diagenetic deposits and hydrogenetic-type deposits, 1 nm phyllomanagnates and 0.7 nm varieties (birnessite or vernadite) typically prevail, respectively (*17*).

In Advances in the Environmental Biogeochemistry of Manganese Oxides; Sparks, et al.;
ACS Symposium Series; American Chemical Society: Washington, DC, 2015.

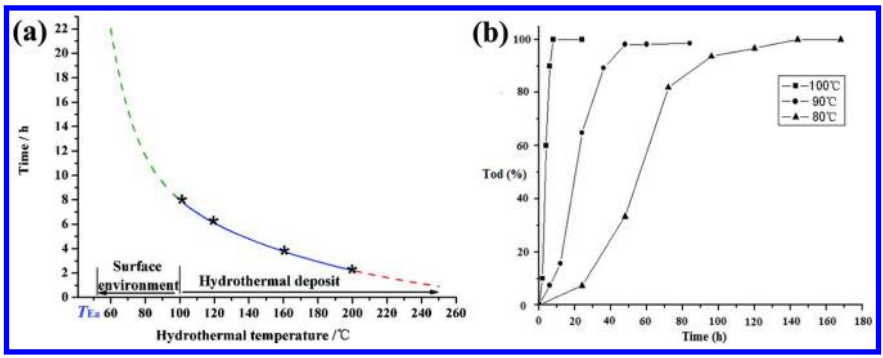

Figure 15. Schemes for the formation condition of todorokite (a) and relationship between ratio of todorokite conversion and refluxing time at different temperatures (b). (a) was adapted with permission from ref. (48). Copyright (2005) Earth Science. (b) was reproduced with permission from ref. (23). Copyright (2005) Science China Press.

Regarding to the crystallographic evolution during todorokite formation, different crystal growth processes were reported. Burns and Burns (*46*) proposed a simple two-step dissolution-recrystallization process for natural todorokite formation in ocean nodules. Initially, cryptocrystalline Mn oxide precipitated at the surface of detrital matter is partially reduced by the surrounding organic substances to release Mn^{2+}, which is then absorbed by the Mn oxide and transformed into todorokite. Bodeï et al. (*17*) suggested the step of semi-ordered 10-Å phyllomanganate formation before the conversion. A new four-stage process was recently proposed for the transformation of birnessite to todorokite (*18*), *i.e.* beginning with todorokite nucleation, followed by todorokite primary particle formation via crystal growth from solution, then the self-assembly and oriented growth of todorokite primary particles to form crystalline todorokite laths, and finally traditional crystal ripening to further improve crystallinity. This four-stage crystal growth process is well supported by the morphological evolution of our synthetic todorokite samples with triclinic birnessites as the precursors either under hydrothermal conditions or under reflux conditions (Figure 3 and 4). However, the original morphologies of fibrillar thin planes remained unchanged after the transformation of biogenic oxide into nano-crystalline todorokite (Figure 14e), which could be attributed to a topotactic transformation process due to the presence of tightly bound cell and biological materials with biogenic oxide inhibiting the aforementioned four crystal growth processes. As a corollary, the topotactic transformation from birnessite to todorokite in the local domains occurs prior to the todorokite nucleation during the todorokite formation from abiotic birnessite samples.

Taken together, the three key factors governing todorokite formation are stable 10-Å phyllomanganate with an appropriate amount and type of interlayer cations, an appropriate number of Mn(III) in the phyllomanganate, and a relatively high temperature condition. In combination with these factors, the possible formation pathway of natural todorokite can be expressed as: biogenic or abiotic

phyllomanganate → stable 10-Å phyllomanganate with appropriate interlayer cations and structural Mn(III) → todorokite. These results provide clues for the usual occurrence of todorokite in marine hydrothermal Mn deposits (*17*, *41*, *73–76*), marine diagenetic Mn concretions (*74*, *75*, *77*), and ferromanganese aggregates in soils or sediments enriched with Ca (*1*, *69*, *78–81*).

Conclusion

The phase transformation from phyllomanganates to todorokite is influenced not only by several reaction parameters, such as temperature, pH and reaction time, but also by the layer structure, crystallinity, amount and type of interlayer cations and Mn AOS of phyllomanganate precursors. The structural Mn(III) in phyllomanganate plays a significant role in tunnel wall construction during todorokite formation. Di or trivalent cations weakly bound with MnO_6 layers, such as Mg^{2+}, Ca^{2+}, and La^{3+} in the stable 10-Å phyllomanganate precursor favor todorokite formation with respect to strongly bonding ones, such as Cu^{2+}, Ni^{2+} and Co^{2+}. Mg-buserite cannot be completely converted into todorokite at a temperature lower than 40 °C, while the conversion rate and crystallinity of todorokite increase with raising temperature. The pressure has little effect on todorokite formation. The rate of conversion and crystallinity of todorokite prepared at pH 5-9 is in the order: neutral ≈ alkaline > acidic. The poorly crystalline Na-buserite is more easily transformed into todorokite than the highly crystalline one.

Acknowledgments

The authors acknowledge the National Natural Science Foundation of China (Grant Nos. 41471194 & 41171197), and the Strategic Priority Research Program of the Chinese Academy of Sciences (No. XDB15020402) for financial support of this research. We are grateful to The Clay Minerals Society, publisher of *Clays and Clay Minerals* for the kind permission of reproduction of the table and figures from [Cui et al., (2009, Table 1 and Figure 4) (2006, Figure 1, Figure 4, Figure 6)].

References

1. Turner, S.; Buseck, P. R. Todorokites: a new family of naturally occurring manganese oxides. *Science* **1981**, *212*, 1024–1027.
2. Ostwald, J. Some observations on the chemical composition of todorokite. *Miner. Mag.* **1986**, *50*, 336–40.
3. Turner, S.; Siegel, M. D.; Buseck, P. R. Structure features of tordorokite intergrowths in manganese nodules. *Nature* **1982**, *296*, 841–842.
4. Post, J. E.; Bish, D. L. Rietveld refinement of the todorokite structure. *Am. Mineral.* **1988**, *73*, 861–869.
5. Golden, D. C.; Chen, C. C.; Dixon, J. B. Synthesis of todorokite. *Science* **1986**, *231*, 717–719.

6. Shen, Y. F.; Zerger, R. P.; DeGuzman, R. N.; Suib, S. L.; McCurdy, L.; Potter, D. I.; O'Young, C. L. Manganese oxide octahedral molecular sieves: preparation, characterization and application. *Science* **1993**, *260*, 511–515.
7. Vileno, E.; Ma, Y.; Zhou, H.; Suib, S. L. Facile synthesis of synthetic todorokite (OMS-1), co-precipitation reactions in the presence of a microwave field. *Microporous Mesoporous Mater.* **1998**, *20*, 3–15.
8. Feng, Q.; Yanaqisawa, K.; Yamasaki, N. Transformation of manganese oxides from layered structures to tunnel structures. *Chem. Commun.* **1996**, *14*, 1607–1608.
9. Golden, D. C.; Chen, C. C.; Dixon, J. B. Transformation of birnessite to buserite, todorokite, and manganite under mild hydrothermal treatment. *Clays Clay Miner.* **1987**, *35*, 271–280.
10. Shen, Y. F.; Suib, S. L.; O'Young, C. L. Effects of inorganic cation templates on octahedral molecular sieves of manganese oxide. *J. Am. Chem. Soc.* **1994**, *116*, 11020–11029.
11. Ching, S.; Krukowska, K. S.; Suib, S. L. A new synthetic route to todorokite-type manganese oxides. *Inorg. Chim. Acta* **1999**, *294*, 123–132.
12. Feng, Q.; Kanoh, H.; Ooi, K. Manganese oxide porous crystals. *J. Mater. Chem.* **1999**, *9*, 319–333.
13. Suib, S. L. Current Opinion in Solid State and Materials Science. *Chem. Mater.* **1998**, *3*, 63–70.
14. Cui, H. J.; Qiu, G. H.; Feng, X. H.; Tan, W. F.; Liu, F. Birnessites with different average manganese oxidation states were synthesized, characterized, and transformed to todorokite at atmospheric pressure. *Clays Clay Miner.* **2009**, *57*, 715–724.
15. Post, J. E. Manganese oxide minerals: crystal structures and economic and environmental significance. *Proc. Natl. Acad. Sci. U. S. A.* **1999**, *96*, 3447–3454.
16. Liu, J.; Cai, J.; Son, Y. C.; Gao, Q.; Suib, S. L.; Aindow, M. Magnesium manganese oxide nanoribbons: Synthesis, characterization, and catalytic application. *J. Phys. Chem. B* **2002**, *106*, 9761–9768.
17. Bodeï, S.; Manceau, A.; Geoffroy, N.; Baronnet, A.; Buatier, M. Formation of todorokite from vernadite in Ni-rich hemipelagic sediments. *Geochim. Cosmochim. Acta* **2007**, *71*, 5698–5716.
18. Atkins, A. L.; Shaw, S.; Peacock, C. L. Nucleation and growth of todorokite from birnessite: Implications for trace-metal cycling in marine sediments. *Geochim. Cosmochim. Acta* **2014**, *144*, 109–125.
19. Naoaki, K.; Shinichi, K.; Hiroiki, S.; Nobuko, K. Preparation of todorokite-type manganese-based oxide and its application as lithium and magnesium rechargeable battery cathode. *J. Power Source* **2001**, *97*, 515–517.
20. Post, J. E.; Heaney, P. J.; Hanson, J. Synchrotron X-ray diffraction study of the structure and dehydration behavior of todorokite. *Am. Mineral.* **2003**, *88*, 142–150.
21. Feng, X. H.; Tan, W. F.; Liu, F.; Wang, J. B.; Ruan, H. D. Synthesis of todorokite at atmospheric pressure. *Chem. Mater.* **2004a**, *16*, 4330–4336.

22. Liu, Z. H.; Kang, L.; Ooi, K.; Yoji, M.; Feng, Q. Studies on the formation of todorokite-type manganese oxide with different crystalline birnessites by Mg^{2+}-templating reaction. *J. Colloid Interface Sci.* **2005**, *285*, 239–246.
23. Cui, H. J.; Feng, X. H.; Liu, F.; Tan, W. F.; He, J. Z. Factors governing formation of todorokite at atmospheric pressure. *Sci. China Ser. D* **2005**, *48*, 1678–1689.
24. Post, J. E. Crystal structures of manganese oxide minerals. In *Biomineralization, Processes of Iron and Manganese*; Skinner, H. C. W., Fitzpatrick, R. W., Eds.; Cremlingen-Destedt: CATENA Verlag, 1992; pp 51−73
25. Yang, D. S.; Wang, M. K. Syntheses and characterization of well crystallized birnessite. *Chem. Mater.* **2001**, *13*, 2589–2594.
26. Lanson, B.; Drits, V. A.; Feng, Q.; Manceau, A. Crystal structure determination of synthetic Na-rich birnessite: Evidence for a triclinic one-layer cell. *Am. Mineral.* **2002a**, *87*, 1662–1671.
27. Potter, R. M.; Rossman, G. R. The tetravalent manganese oxides: identification, hydration, and structural relationships by infrared spectroscopy. *Am. Mineral.* **1979**, *64*, 1199–1218.
28. Villalobos, M.; Toner, B.; Bargar, J.; Sposito, G. Characterization of the manganese oxide produced by Pseudomonas putida strain MnB1. *Geochim. Cosmochim. Acta* **2003**, *67*, 2649–2662.
29. Fuertes, A.; Da Costa-Serra, J. F.; Chica, A. New catalysts based on Ni-Birnessite and Ni-Todrokite for the efficient production of hydrogen by bioethanol steam reforming. *Energy Procedia* **2012**, *29*, 181–191.
30. Vileno, E.; Zhou, H.; Zhang, Q.; Suib, S. L.; Corbin, D. R.; Koch, T. A. Synthetic todorokite produced by microwave heating: An active oxidation catalyst. *J. Catal.* **1999**, *187*, 285–297.
31. Malinger, K. A.; Laubernds, K.; Son, Y. C.; Suib, S. L. Effects of microwave processing on chemical, physical and catalytic properties of todorokite-type manganese oxide. *Chem. Mater.* **2004**, *16*, 4296–4303.
32. Feng, X. H.; Liu, F.; Tan, W. F.; Liu, X. W.; Hu, H. Q. Synthesis of todorokite by refluxing process and its primary characteristics. *Sci. China Ser. D* **2004b**, *47*, 760–768.
33. Cui, H. J.; Feng, X. H.; He, J. Z.; Tan, W. F.; Liu, F. Effects of reaction conditions on the formation of todorokite at atmospheric pressure. *Clays Clay Miner.* **2006**, *54*, 605–615.
34. Cui, H. J.; Liu, X. W.; Tan, W. F.; Feng, X. H.; Liu, F.; Ruan, H. D. Influence of Mn(III) availability on the phase transformation from layered buserite to tunnel-structured todorokite. *Clays Clay Miner.* **2008**, *56*, 397–403.
35. Cui, H. J.; Feng, X. H.; Tan, W. F.; He, J. Z; Hu, R. G.; Liu, F. Synthesis of todorokite-type manganese oxide from Cu-buserite by controlling the pH at atmospheric pressure. *Microporous Mesoporous Mater.* **2009**, *117*, 41–47.
36. Feng, X. H.; Zhu, M. Q.; Ginder-Vogel, M.; Ni, C. Y.; Parikh, S. J.; Sparks, D. L. Formation of nano-crystalline todorokite from biogenic Mn oxides. *Geochim. Cosmochim. Acta* **2010**, *74*, 3232–3245.

37. Ren, Q. T.; Ma, J. H.; Li, W. X.; Ma, Z. S.; Liu, Y. Synthesis of cerium-doped todorokite by refluxing process at atmospheric pressure. *Adv. Mater. Res.* **2013**, *807-809*, 609–612.
38. Burns, V. M.; Burns, R. G. Authigenic todorokite and phillipsite inside deep-sea manganese nodules. *Am. Mineral.* **1978**, *63*, 827–831.
39. Siegel, M. D.; Turner, S. Crystalline todorokite associated with biogenic debris in manganese nodules. *Science* **1983**, *219*, 172–174.
40. Mandernack, K. W.; Post, J.; Tebo, B. M. Manganese mineral formation by bacterial spores of the marine Bacillus, strain SG-1: Evidence for the direct oxidation of Mn(II) to Mn(IV). *Geochim. Cosmochim. Acta* **1995**, *59*, 4393–4408.
41. Buatier, M. D.; Guillaume, D.; Wheat, C. G.; Hervé, L.; Adatte, T. Mineralogical characterization and genesis of hydrothermal Mn oxides from the flank of the Juan the Fuca Ridge. *Am. Mineral.* **2004**, *89*, 1807–1815.
42. Webb, S. M.; Fuller, C. C.; Tebo, B. M.; Bargar, J. R. Determination of uranyl incorporation into biogenic manganese oxides using X-ray absorption spectroscopy and scattering. *Environ. Sci. Technol.* **2006**, *40*, 771–777.
43. Saratovsky, I.; Gurr, S. J.; Hayward, M. A. The structure of manganese oxide formed by the fungus *Acremonium* sp.strain KR21-2. *Geochim. Cosmochim. Acta* **2009**, *73*, 3291–3300.
44. Bargar, J. R.; Fuller, C. C.; Marcus, M. A.; Brearley, A. J.; De la Rosa, M. P.; Webb, S. M.; Caldwell, W. A. Structural characterization of terrestrial microbial Mn oxides from Pinal Creek, AZ. *Geochim. Cosmochim. Acta* **2009**, *73*, 889–910.
45. Miyata, N.; Tani, Y.; Maruo, K.; Tsuno, H.; Sakata, M.; Iwahori, K. Manganese(IV) oxide production by *Acremonium* sp. strain KR21-2 and extracellular Mn(II) oxidase activity. *Appl. Environ. Microbiol.* **2006**, *72*, 6467–6473.
46. Burns, V. M.; Burns, R. G. Post-depositional metal enrichment processes inside manganese nodules from the north equatorial Pacific. *Earth Planet. Sci. Lett.* **1978b**, *39*, 341–348.
47. Mellin, T. A.; Lei, G. B. Stabilization of 10 Å-manganates by interlayer cations and hydrothermal treatment: Implications for the mineralogy of marine manganese concretions. *Mar. Geol.* **1993**, *115*, 67–83.
48. Feng, X. H.; Tan, W. F.; Liu, F.; Xu, Y. S.; Wang, Y. J. Hydrothermal synthesis of todorokite and its influencing factors. *Earth Science* **2005**, *30*, 347–352.
49. Chukhrov, F. V.; Gorshkov, A. I.; Sivtsov, A. V.; Beresovskaya, V. V. New data on natural todorokites. *Nature* **1979**, *278*, 631–632.
50. Julien, C. M.; Massot, M.; Poinsignon, C. Lattice vibrations of manganese oxides part I. periodic structures. *Spectrochim. Acta A* **2004**, *60*, 689–700.
51. Kang, L. P.; Zhang, M. M.; Liu, Z. H.; Ooi, K. IR spectra of manganese oxides with either layered or tunnel structures. *Spectrochim. Acta A* **2007**, *67*, 864–869.
52. Post, J. E.; Bish, D. L. Rietveld refinement of the coronadite structure. *Am. Mineral.* **1989**, *74*, 913–917.

53. Silvester, E.; Manceau, A.; Drits, V. A. The structure of synthetic monoclinic Na-rich birnessite and hexagonal birnessite. Part 2. Results from chemical studies and EXAFS spectroscopy. *Am. Mineral.* **1997**, *82*, 962–978.
54. Lanson, B.; Drits, V. A.; Silvester, E.; Manceau, A. Structure of H-exchanged hexagonal birnessite and its mechanism of formation from Na-rich monoclinic buserite at low pH. *Am. Mineral.* **2000**, *85*, 826–838.
55. Tan, W. F.; Liu, F.; Li, Y. H.; He, J. Z.; Li, X. Y. Mineralogy of manganese in iron-manganese nodules of several main soils in China. *Pedosphere* **2000**, *10*, 265–274.
56. Cui, H. J.; Liu, F.; Feng, X. H.; Tan, W. F.; Wang, M. K. Aging promotes todorokite formation from layered manganese oxide at near-surface conditions. *J. Soils Sediments* **2010**, *10*, 1540–1547.
57. Lanson, B.; Drits, V. A.; Gaillot, A.; Silvester, E.; Plancon, A.; Manceau, A. Structure of heavy-metal sorbed birnessite: Part 1. Results from X-ray diffraction. *Am. Mineral.* **2002b**, *87*, 1631–1645.
58. Yin, H.; Liu, Y.; Koopal, L. K.; Feng, X. H.; Chu, S. Q.; Zhu, M. Q.; Liu, F. High Co-doping promotes the transformation of birnessite layer symmetry from orthogonal to hexagonal. *Chem. Geol.* **2015**, *410*, 12–20.
59. Grangeon, S.; Lanson, B.; Lanson, S. Solid-state transformation of nanocrystalline phyllomanganate into tectomanganate: influence of initial layer and interlayer structure. *Acta Crystallogr., Sect. B: Struct. Sci* **2014**, *70*, 828–838.
60. Luo, J.; Zhang, Q.; Huang, A.; Giraldo, O.; Suib, S. L. Double-aging method for preparation of stabilized Na-buserite and transformations to todorokites incorporated with various metals. *Inorg. Chem.* **1999**, *38*, 6106–6113.
61. Qian, J. C. Study on structural stability of 1 nm manganates. *Acta Oceanol. Sin.* **1998**, *20*, 56–63.
62. Manceau, A.; Lanson, B.; Drits, V. A. Structure of heavy metal sorbed birnessite. Part III: Results from powder and polarized extended X-ray absorption fine structure spectroscopy. *Geochim. Cosmochim. Acta* **2002**, *66*, 2639–2663.
63. Qian, J. C.; Mellin, T. A. Study on exchange ability of metal ions in 1nm manganates. *Acta Oceanol. Sin.* **1996**, *18*, 56–62.
64. Saratovsky, I.; Wightman, P. G.; Pastén, P. A.; Gaillard, J. F.; Poeppelmeier, K. R. Manganese oxides: Parallels between abiotic and biotic structures. *J. Am. Chem. Soc.* **2006**, *128*, 11188–11198.
65. Villalobos, M.; Lanson, B.; Manceau, A.; Toner, B.; Sposito, G. Structural model for the biogenic Mn oxide produced by *Pseudomonas putida*. *Am. Mineral.* **2006**, *91*, 489–502.
66. Kim, H. S.; Pasten, P. A.; Gaillard, J. F.; Stair, P. C. Nanocrystalline todorokite-like manganese oxide produced by bacterial catalysis. *J. Am. Chem. Soc.* **2003**, *125*, 14284–14285.
67. Webb, S. M.; Tebo, B. M.; Bargar, J. R. Structural characterization of biogenic manganese oxides produced in seawater by the marine *Bacillus sp*. strain SG-1. *Am. Mineral.* **2005a**, *90*, 1342–1357.

68. Webb, S. M.; Tebo, B. M.; Bargar, J. R. Structure influence of sodium and calcium ions on the biogenic manganese oxides produced by the marine *Bacillus sp*. strain SG-1. *Geomicrobiol. J.* **2005**, *22*, 181–193.
69. McKeown, D.; Post, J. E. Characterization of manganese oxide mineralogy in rock varnish and dendrites using X-ray absorption spectroscopy. *Am. Mineral.* **2001**, *86*, 701–713.
70. Manceau, A.; Tommaseo, C.; Rihs, S.; Geoffroy, N.; Chateigner, D.; Schlegel, M.; Tisserand, D.; Marcus, M. A.; Tamura, N.; Chen, Z. S. Natural speciation of Mn, Ni, and Zn at a micrometer scale in clayey paddy soil using X-ray fluorescence, absorption, and diffraction. *Geochim. Cosmochim. Acta* **2005**, *69*, 4007–4034.
71. Toner, B.; Fakra, S.; Villalobos, M.; Warwick, T.; Sposito, G. Spatially resolved characterization of biogenic manganese oxide production within a bacterial biofilm. *Appl. Environ. Microbiol.* **2005**, *71*, 1300–1310.
72. Lei, G. B. Crystal structures and metal uptake capacity of 10 angstrom-manganates: an overview. *Mar. Geol.* **1996**, *133*, 103–112.
73. Usui, A.; Mellin, T. A.; Nohara, M.; Yuasa, M. Structural stability of marine 10 Å manganates from the Ogasawara (Bonin) Arc: Implication for low-temperature hydrothermal activity. *Mar. Geol.* **1989**, *86*, 41–56.
74. Usui, A.; Bau, M.; Toshitsugu, Y. Manganese microchimneys buried in the Central Pacific pelagic sediments: evidence of intraplate water circulation? *Mar. Geol.* **1997**, *141*, 269–285.
75. Takahashi, Y.; Manceau, A.; Geoffroy, N.; Marcus, M. A.; Usui, A. Chemical and structural control of the partitioning of Co, Ce, and Pb in marine ferromanganese oxides. *Geochim. Cosmochim. Acta* **2007**, *71*, 984–1008.
76. Dubinin, A. V.; Uspenskaya, T. Y.; Gavrilenko, G. M.; Rashidov, V. A. Geochemistry and genesis of Fe–Mn mineralization in island arcs in the west Pacific Ocean. *Geochem. Int.* **2008**, *46*, 1206–1227.
77. Yoshikawa, K. The relationship between manganese minerals and metallic elements in deep-sea manganese nodules. *Mar. Geol.* **1991**, *101*, 267–286.
78. Taylor, R. M.; McKenzie, R. M.; Norrish, K. The mineralogy and chemistry of manganese in some Australian soils. *Aust. J. Soil Res.* **1964**, *2*, 235–248.
79. McKenzie, R. M. Manganese oxides and hydroxides. In *Minerals in Soil Environments*, 2nd ed.; SSSA Book Series No. 1; Dixon, J. B., Weed, S. B., Eds.; Soil Science Society of America: 1989; pp 439−465.
80. Bilinski, H.; Giovanoli, R.; Usui, A.; Hanzel, D. Characterization of Mn oxides in cemented streambed crusts from Pinal Creek, Arizona, U.S.A., and in hot-spring deposits from Yuno-Taki Falls, Hokkaido, Japan. *Am. Mineral.* **2002**, *87*, 580–591.
81. Tan, W. F.; Liu, F.; Li, Y. H.; Hu, H. Q.; Huang, Q. Y. Elemental composition and geochemical characteristics of iron–manganese nodules in main soils of China. *Pedosphere* **2006**, *16*, 72–81.

Chapter 7

Manganese-Oxide Solids as Water-Oxidation Electrocatalysts: The Effect of Intercalating Cations

Lizhi Tao, Troy A. Stich, Hugues Jaccard, R. David Britt, and William H. Casey*

Department of Chemistry, University of California, One Shield Avenue, Davis, California 95616, United States
***E-mail: whcasey@ucdavis.edu**

A set of birnessite-type manganese oxides with both monovalent alkaline cations (Li^+, Na^+, K^+, Rb^+ or Cs^+) and divalent alkaline- earth cations (Ca^{2+} or Mg^{2+}) has been synthesized using electrolytic deposition methods. X-ray diffraction gives typical birnessite-type patterns, with diffraction peaks at 2θ = ~12.01° and 24.7° assigned to (001) and (002) planes. Electron paramagnetic resonance spectra suggest differences in the stability of Mn(III) species in manganese-oxide layer, which is more stable in birnessite samples with divalent cations than samples with monovalent cations. The activity of samples for an anodic O_2-evolution reaction is considerably affected by electrostatic potential and Lewis acidity of the monovalent cation, following the sequence of $Li^+ > Na^+ > K^+ > Rb^+ > Cs^+$. While for samples with intercalating divalent alkaline-earth cations, there was slightly lower activity for O_2 evolution, which may be correlated to different stability of Mn(III) species in the birnessite layers. In addition, we observed much higher O_2-evolution activity at an overpotential of ca. 220 – 230 mV if the samples were heat-treated between 300 – 500 °C once they were electrolytically deposited as $LiMnO_x$ films. Clearly dry heating causes changes in both the crystalline structure and electronic structure of manganese-oxide layers, as indicated by associated changes in water-oxidation activity.

In Advances in the Environmental Biogeochemistry of Manganese Oxides; Sparks, et al.;
ACS Symposium Series; American Chemical Society: Washington, DC, 2015.

1. Introduction

Sunlight is a carbon-neutral energy source that daily provides ~10^4 times the current energy needs of the human population (*1*). Nature traps light energy as chemical energy via photosynthesis—a process of rearranging chemical bonds of water molecule to form O_2 and NADPH (a reduced form of nicotinamide adenine dinucleotide phosphate, a means of storing H_2 reducing equivalents) (*2*, *3*). The key four-electron step occurs in the Oxygen-Evolving-Complex (OEC) in Photosystem-II (PSII), a transmembrane cofactor-protein complex embedded in the thylakoid membrane of plants and cyanobacteria (*4–7*). Human efforts to mimic this reaction have so far fallen short, in part because the synthetic catalysts often suffer oxidative damage during water oxidation, much as the protein in PSII becomes photodamaged.

Parallel efforts are now focusing on simple inorganic materials that regenerate themselves during the water electrolysis. Several researchers have attempted to utilize solar energy to generate electron-hole pairs in a semi-conductor that then power a catalyst. In a typical strategy, electrons are transferred to catalysts doped onto a cathode to form H_2, which is collected and stored, and the holes are transferred to catalysts on an anode to produce O_2, which is usually released. This electrolysis process is referred to as "water-splitting" in subsequent discussion (*8–13*), which focuses on the energetically expensive, four-electron oxidation step of making O_2 from H_2O.

One of the biggest challenges for an artificial solar fuel is to develop an efficient catalyst for water oxidation from metals that are abundant in the Earth. To date, the most efficient catalysts for O_2 evolving are IrO_2 and RuO_2 exhibiting high turnover frequencies (TOF), which have been investigated extensively (*14–25*). However, the high cost of mining these materials could limit the wide use of these noble metals as catalysts in making solar fuels. Therefore, it is essential and necessary to develop affordable and comparable efficient catalysts for O_2 evolution reaction from Earth-abundant materials like iron or manganese.

Manganese (Mn), the 10th most abundant element on the earth crust, is a key element in environment and global redox cyclying processes, which enable it to serve as a plentiful cheap and clean natural resource (*26*). Actually, manganese has been selected by Nature as the catalyst for O_2 evolution, the OEC, which is a μ-oxo-bridged tetrameric manganese cluster Mn_4CaO_5 found in nearly all photosynthetic organisms (*27–30*). The OEC catalyzes water oxidation with low overpotential (η: ~160 mV) in near-neutral pH environment (pH 6.5) (*31–33*). Inspired by the OEC, many manganese complexes and particles have been synthesized and investigated as catalysts for water oxidation (*34–60*). In general, there are two approaches used to assess the redox suitability of these catalysts. One is an electrochemical procedure whereby catalysts are doped onto the anode electrode to measure the overpotential (η) needed for O_2 evolution (the lower η, the more valuable the catalyst becomes because the cost of generating oxygen decreases) (*34–40*). The second approach does not use a solid electrode. Instead, O_2 production from water is coupled to solute chemical oxidants, such as $(NH_4)_2Ce(NO_3)_6$ or $Na_2S_2O_8$, which serve as electron acceptors for homogeneous catalysts in solution or with a suspension of solid catalyst particles (*48–60*). Shown in Table 1 is a summary of

In Advances in the Environmental Biogeochemistry of Manganese Oxides; Sparks, et al.;
ACS Symposium Series; American Chemical Society: Washington, DC, 2015.

Najafpour et al.'s work focusing on the second reaction geometry and employing varying types of manganese-oxide nanoparticles as catalysts for water oxidation reaction (*50–58*, *61*).

Birnessite-type manganese-oxide minerals have a layered structure consisting of edge-sharing octahedral MnO_6, with water molecules and various cations occupying the interlayer spaces (*26*, *62*). This open structure provides a high contact surface for the various reactive species if it serves as a catalyst (*63–66*). and has a well-known ion-exchange capacity (*67*). Varying the intercalating cation with different radii and positive charges could result in different interlayer distance (d_{001}) values and different concentrations of Mn(III) in manganese-oxide layer. These are thought to affect the activity for O_2 evolution from water oxidation reaction.

In the present work, a set of birnessite-type manganese oxide solids with both monovalent alkaline and divalent alkaline-earth cations ($MMnO_x$, M = Li^+, Na^+, K^+, Rb^+, Cs^+, Mg^{2+} or Ca^{2+}) are synthesized via electrolytic-deposition method. The structure and electronic properties are characterized by X-ray diffraction (XRD) and electron paramagnetic resonance (EPR) spectroscopy. The activity of these samples for the anodic water-oxidation reaction was then established via linear-sweep voltammetry (LSV) in neutral Tris-buffered solution with pH = 7.8. Our goal is to establish a set of correlations between structure and the overpotential η needed for O_2 evolution.

2. Experimental Procedures

2.1. Electrodeposition of Manganese Oxide Film

Birnessite-type manganese oxide was prepared via electrodeposition on fluorine-doped tin-oxide-coated glass (FTO; Hartford Glass Co. Inc., Hartford City, IN, USA), which has been described in the literature (*36*). Before electrodeposition, the FTO electrode (1 × 2 cm) was ultrasonically washed with soapy water, acetone, isopropanol alcohol and purified water (18 MΩ resistance). Electrodeposition was achieved using a Princeton Applied Research (Oak Ridge, TN, USA) Model 263 A potentiostat/galvanostat and PowerStep package software in a three-electrode system, in which Ag/AgCl (in saturated NaCl solution, 0.194 V vs NHE) was the reference electrode, FTO was employed as the working electrode with exactly 1 cm^2 immersing in electrolyte and nickel foam was used as the counter electrode.

Manganese-oxide solids with intercalating cations of Li^+, Na^+, K^+, Rb^+, Cs^+, Mg^{2+} or Ca^{2+} were prepared by potentiostatic electrodeposition (on the submerged half FTO plates with area = 1 × 1 cm) at an initial potential of 0.8 V for 300 s (in order to improve the oxide-FTO interface by forming an interfacial film ca. < 2 nm (*36*)) and then holding the potential at 1.0 V vs Ag/AgCl (in saturated NaCl solution) in a bath containing electrolyte of 2 mM $MnSO_4$ and 0.05 M LiCl, NaCl, KCl, RbCl, CsCl, $MgCl_2$ or $CaCl_2$, correspondingly, to obtain a stable current 0.8 mA/cm^2. The thickness of the film was assessed by the total deposited charge (ca. 144 mC/cm^2) on the FTO plate, corresponding to ~161 nm thickness of deposited film (*36*). The final created brown film of manganese oxide was stored in the

In Advances in the Environmental Biogeochemistry of Manganese Oxides; Sparks, et al.;
ACS Symposium Series; American Chemical Society: Washington, DC, 2015.

corresponding electrolyte for later catalytic testing. We denote these samples as **M**MnO_x (**M** = Li^+, Na^+, K^+, Rb^+, Cs^+, Mg^{2+} or Ca^{2+}). To make heat-treated $LiMnO_x$ samples, the FTO electrode (area = 1×2 cm) that had been electrolytically coated with $LiMnO_x$ film (area = 1×1 cm) was placed on the surface of a hot plate for 2 hours exposured in air, with the temperature set as 200, 300 or 500 °C.

2.2. XRD Characterization

Powder X-ray diffraction (XRD) patterns of manganese-oxide samples ($LiMnO_x$, $NaMnO_x$ and $CaMnO_x$) were recorded on a Bruker D8 Advance X-ray diffractometer with a Ni-filtered Cu $K\alpha$ (λ = 0.15406 nm) radiation source at 40 kV and 40 mA. Scans were made in the range of 5° – 80° at a rate of 0.04 deg s^{-1}.

2.3. EPR Characterization

The samples ($LiMnO_x$, $NaMnO_x$, $CsMnO_x$, $CaMnO_x$ and $MgMnO_x$) for EPR characterization were prepared using the same electrodeposition procedure as above, except on a larger FTO electrode (area = 10 × 12 cm). The prepared film was washed at least six times using purified water in order to wash away any free Mn^{2+} ion on the surface of electrode that remained from the electrolyte solution. The washed film was then air-dried at room temperature and scraped from the electrode surface using a razor blade, yielding ~7 mg of dark brown powder. This separated powder was loaded into a Q-band EPR tube (Vitrocom CV2024 ID = 2.0mm OD = 2.4mm L = 100mm), flame-sealed immediately and stored at room temperature.

X-band continuous wave (CW)-EPR spectra were recorded using a Bruker (Billerica, MA) Biospin EleXsys E500 spectrometer with a super-high Q resonator (ER4122SHQE). Cryogenic temperatures (30 and 70 K) were achieved and controlled by an Oxford Instrument ESR900 liquid-helium cryostat in conjunction with an Oxford Instrument ITC503 temperature and gas-flow controller. All CW-EPR data were acquired under non-saturating conditions, with an excitation microwave frequency = 9.39 GHz, microwave power = 0.6325 mW, modulation amplitude = 8 G, and modulation frequency = 100 kHz.

2.4. Electrolysis

Electrolysis for the water-oxidation reaction was conducted at 23 °C in an airtight glass reactor with a three-electrode system. An FTO electrode (area = 1 × 2 cm) that had been coated with the manganese-oxide film (area = 1 × 1 cm) was placed in the middle of the reactor to serve as a working electrode, with nickel foam as the counter electrode and Ag/AgCl (saturated with NaCl) as a reference electrode. The distance between the reference electrode and working electrode was no more than 2 mm in order to reduce the solution resistance (*iR*). The electrolytes were 0.5 M **M**Cl (**M** = Li, Na, K, Rb, Cs, Mg or Ca) all in a Tris-buffered solution (pH = 7.8). Electrolysis was started after bubbling argon gas through each solution for at least 1 h before measurement in order to displace any atmospheric O_2 from the system.

In Advances in the Environmental Biogeochemistry of Manganese Oxides; Sparks, et al.;
ACS Symposium Series; American Chemical Society: Washington, DC, 2015.

Publication Date (Web): November 17, 2015 | doi: 10.1021/bk-2015-1197.ch007

Table 1. Properties of water-oxidation catalysts from selected studies.

Catalysts	BET Surface area ($m^2 \cdot g^{-1}$)	Particle Size	Valence of Mn Species	TOF (mmol O_2·mol $Mn^{-1} \cdot s^{-1}$)	TOF (TOF (per surfacearea of 1 mol MnO_x × number of Mn ions in one mole oxide) × 10^6)	Reference
$CaMn_2O_4 \cdot 4H_2O$	303	5 – 50 μm	Mn(IV)/20% Mn(II)	0.325	74	[50]
$CaMn_2O_4 \cdot H_2O$	205			0.540	23	
$CaMn_2O_4$	2.62			0.024	Trace	
α-Mn_2O_3	16.6			0.027	21	
$CaMn_2O_4 \cdot H_2O$ (Concentrated KOH used)	-	< 50 nm	-	2.0	-	[51]
A soluble homogenous form of Mn Oxide colloid ($KMnO_4$ + $Na_2S_2O_3$)	-	-	-	5.28	-	[52]
$CaMn_3O_6$	2.53	Nanorod	3.33	0.046	182	[53]
$CaMn_4O_8$	2.66	520nm× 65 nm	3.5	0.035	136	
$CaMnO_3$	2.54	100 – 150 nm	IV	0.012	37	[54]
$CaMn_3O_8$	3.47	~ 600 nm	IV	0.016	33	
MnZnOx	-	~ 200 nm	-	1.1	-	[55]
MnAlOx				1.1		
5.64 wt% MnO_x/Zeolites	129	-	-	2.62	-	[56]
α-Mn_2O_3 +amorphous MnO_2	33.49	~ 100 nm	III/IV	0.15	-	[57]
Hollandite	-	1μm×5μm×50μm		0.068	-	[58]
Hausmannite				0.012		
PSII(OEC)	-	0.5nm×0.25nm×0.25nm	III/IV	25000	-	[61]

Current (*j*) vs Potential (U) curves were obtained from linear-sweep voltammetry (LSV) recorded from 0 to 2.0 V vs Ag/AgCl (in saturate NaCl solution) at 1 mV/s with regular stirring (without *iR* compensation). The amount of O_2 evolved was monitored independently and simultaneously via the current and by using a fluorescence-based oxygen sensor (NeoFox Phase Measurement System with a FOXY-T1000-TS-NEO probe, Ocean Optics, Dunedin, FL, USA), which was placed in front of the working electrode.

3. Results and Discussion

3.1. Manganese-Oxide Film

Figure 1 shows typical X-ray diffraction patterns of manganese oxide after electrolytic deposition in the presence of Li^+, Na^+, or Ca^{2+}. Diffraction peaks are evident at $2\theta = 11.84°\sim12.01°$, and 24.7° and assigned to characteristic (001) and (002) planes of a typical birnessite-type layer-by-layer structure, with (100) plane diffraction at $2\theta = 36.5°$ (*36*, *68*). These XRD results are consistent with previous work by Jaramillo et al. (*36*), and the resulting materials consist of birnessite-type manganese oxides, with layers of edging-sharing octahedral MnO_6 and with counterions and water molecules occupying the interlayer space. According to Sposito et al. (*69*), synthetic birnessites tend to have triclinic defects resulting from the substitution of Mn(IV) with Mn(III), which generate negative charges in the layer that must be compensated by the counterions. Therefore, cations with different radii and charges could result in different interlayer distance d_{001} values and could stabilize different concentrations of Mn(III) in the manganese-oxide layers by presenting varying average oxidation state of manganese. As shown in Table 2, the interlayer distance d_{001} values of 7.46 Å, 7.36 Å and 7.46 Å determined in this study for $LiMnO_x$, $NaMnO_x$ and $CaMnO_x$, respectively, are broadly similar to previously reported values obtained for $LiMnO_x$, $KMnO_x$, $RbMnO_x$, and $CsMnO_x$ of 7.2 Å, 7.2 Å, 7.3 Å and 7.5 Å, respectively (*70*). The d_{001} value increases predictably with the radius of interlayer cation (*60*, *70*). However, in our samples, d_{001} for $LiMnO_x$ is slightly larger than that found for the $NaMnO_x$ sample, which could be due to the fact that the $LiMnO_x$ is not as well-crystallized as the other materials shown in Figure 1.

Cations also affect the average oxidation states of manganese in the layer. In general, one expects the concentration of Mn(III) to vary with the equivalents of counterion charge in the interlayer. Matsui et al. (*71*) reported the average oxidation state of manganese in similar materials by measuring the ratio of Na^+ to manganese in the solid using ICP analysis, since the concentration of Na^+ should be equal to that of Mn(III) in the layer. In their samples, the ratio of Mn(III) to Mn(IV) was 0.28:0.72 (*71*) calculating the average oxidation state of manganese to be 3.72. X-ray photoelectron spectroscopy has also been employed to determine the average oxidation state of manganese and shown to fall into the range of 3.6 – 3.7 for birnessite-type manganese oxides similar to those we produced electrolytically (*72*).

In Advances in the Environmental Biogeochemistry of Manganese Oxides; Sparks, et al.;
ACS Symposium Series; American Chemical Society: Washington, DC, 2015.

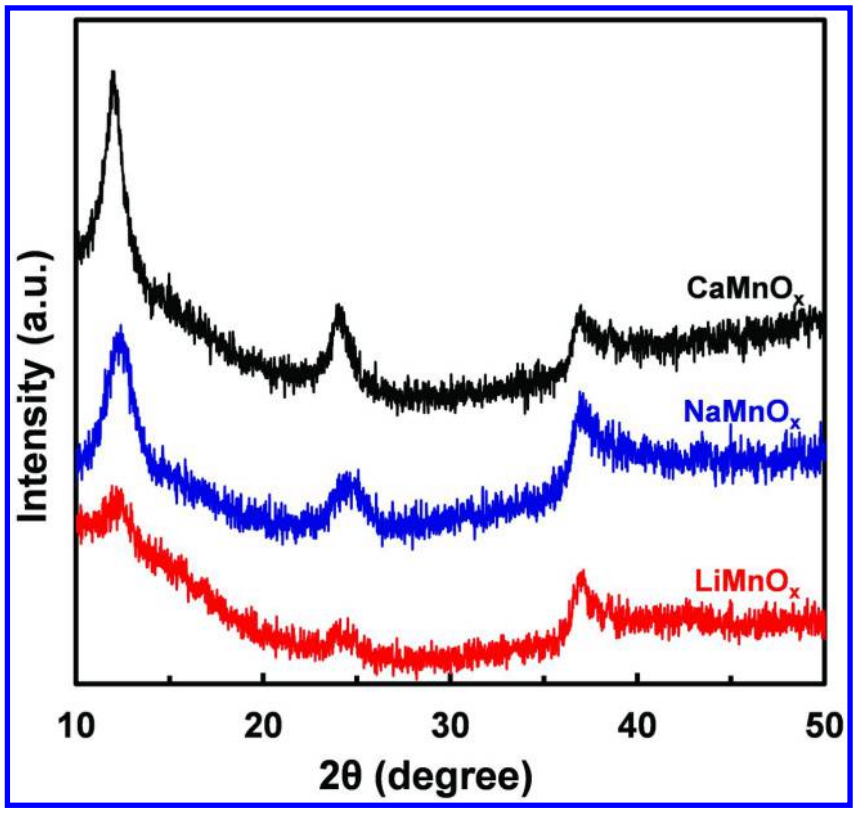

Figure 1. Powder X-ray Diffraction patterns of manganese oxides ($LiMnO_x$, $NaMnO_x$ and $CaMnO_x$) prepared by electrolytic-deposition.

For our materials, CW-EPR spectroscopy was employed to characterize the electronic structure of manganese species in the layer. Figure 2 presents X-band CW-EPR spectra of manganese oxide films with divalent alkaline-earth cations (Ca^{2+} or Mg^{2+}) and monovalent alkaline cation (Li^+, Na^+ or Cs^+) in the interlayer. The spectra were collected at 70 K and 30 K. Samples with interlayer divalent cations exhibit markedly different spectra than samples with monovalent cations, indicating that substitution of these cations is coupled directly to the electronic structure of manganese in the metal-oxide layers, as was expected.

For both Ca- and Mg-bearing samples, broad EPR signals are observed at 70 K with a peak-to-peak spectral width ($\Delta B_{p\text{-}p}$) of ca. 4620 G. However, no obvious signals are detected in spectra acquired at 30 K. This temperature dependence to the signals is consistent with previous EPR studies on manganese oxides that contained Ca^{2+} (*73*, *74*). The interpretation is that significant exchange coupling between Mn(III) and Mn(IV) occurs in the manganese-oxide layers of $CaMnO_x$ and $MgMnO_x$ at 70 K. At much lower temperatures, the spins are S = 1/2 Mn(III,IV) dimeric units are antiferromagnetically coupled with other nearby mixed-valent dimers with the extent of coupling dependent upon the separation distance of Mn(III) (ca. < 2.8 Å) (*73*).

Table 2. $d_{(001)}$ and overpotential needed for oxygen evolution for manganese oxides with different intercalating cations.

Cation	*Radius (Å)*	*$d_{(001)}$ (Å) in this work*	*$d_{(001)}$ (Å) in reference*	*Overpotential (mV) in pH = 7.8*
Li^+	0.60	7.46	7.2, (*70*)	430±75
Na^+	0.95	7.36	7.2, (*70*)	550±75
K^+	1.33	-	7.2, (*70*)	680±75
Rb^+	1.48	-	7.3, (*70*)	740±75
Cs^+	1.69	-	7.5, (*70*)	770±75
Mg^{2+}	0.65	-	7.2, (*60*)	630±75
Ca^{2+}	0.99	7.46	7.1, (*60*)	740±75

Samples that were prepared with monovalent cations ($LiMnO_x$, $NaMnO_x$ and $CsMnO_x$), exhibited EPR spectra with a narrower signal centered at $g = 2.0$ with $\Delta B_{p\text{-}p}$ ca. 560 G. We attribute this signal to $S = 5/2$ Mn^{2+}-containing-species. Although, no ^{55}Mn hyperfine splitting is apparent, the 560 G spectral width is consistent with the 88-95 G magnitude for ^{55}Mn hyperfine typically observed for Mn^{2+} species (*74*). This assignment to a Mn^{2+} species is also consistent with the observed temperature dependence: intensity for the narrow signal decreases as the temperature is increased from 30 K to 70 K (Figure 2). The Mn^{2+} could have originated as an adsorbate metal from the electrolyte solution, but more likely originated as the product of disproportionation of unstable Mn(III) in the manganese-oxide layers. The central observation, however, is that Mn(III) species are more evident in the manganese-oxide material when the interlayer cation is divalent (Ca^{2+} or Mg^{2+}), which could resulting in higher concentration of Mn(III) species.

3.2. O_2 Evolution

Sets of manganese oxides were employed as electrocatalysts for the water-oxidation reaction in Tris-buffered solutions (pH = 7.8) with the current-potential (*j-U*) curves shown in Figure 3. These measurements were collected via LSV at 1 mV/s scanning rate without *iR* compensation. It should be mentioned that by using a small FTO electrode (area = 1 × 2 cm), the measured uncompensated resistance was ~12.5 Ω, with *iR* corresponding to <12.5 mV. The resulting uncompensated current was no more than 1 mA, which will not affect our comparison.

In Advances in the Environmental Biogeochemistry of Manganese Oxides; Sparks, et al.;
ACS Symposium Series; American Chemical Society: Washington, DC, 2015.

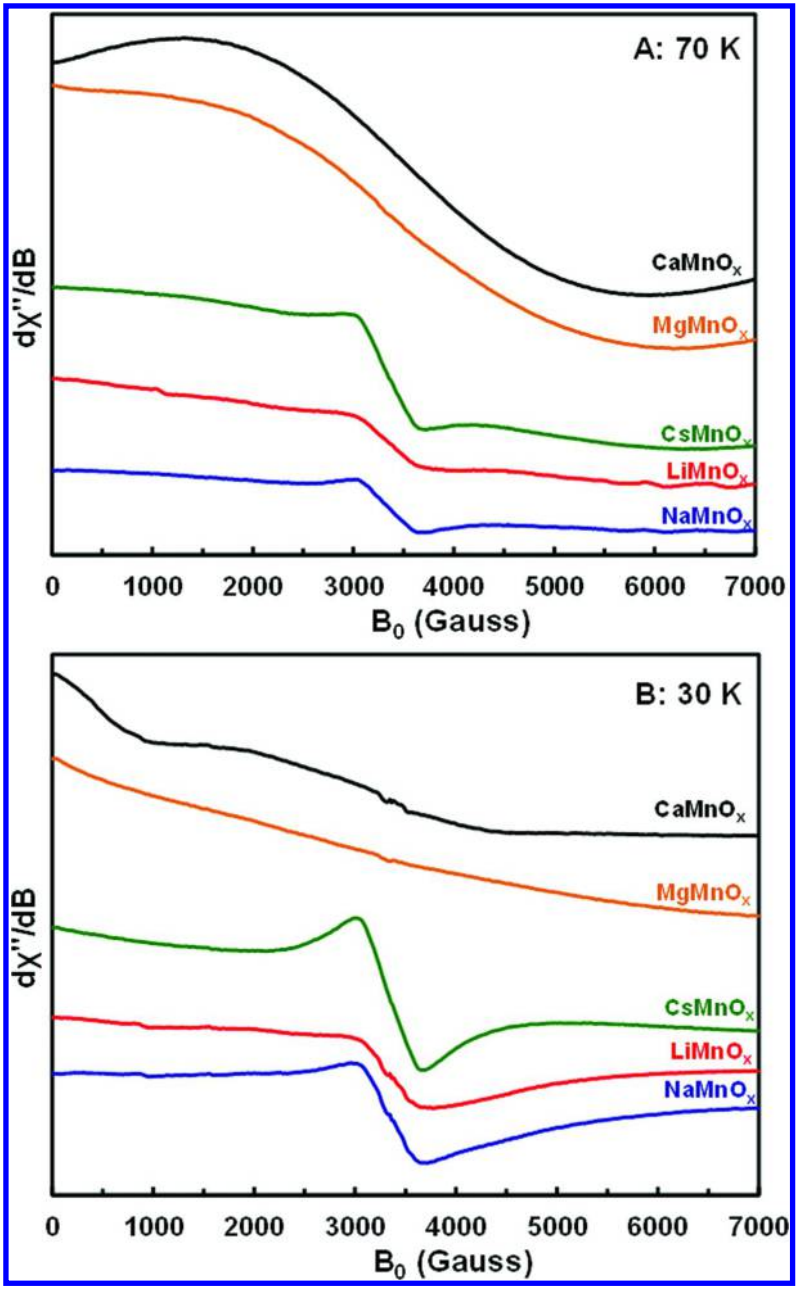

Figure 2. X-band CW-EPR spectra of manganese oxide with both divalent alkaline-earth cation (Ca^{2+} or Mg^{2+}) and monovalent alkaline cation (Li^+, Na^+ or Cs^+) at 70 K (A) and 30 K (B). The samples were analyzed with parameters of power 0.6325 mW (no saturation), microwave frequency: 9.39 GHz, conversion time: 40 ms, modulation amplitude: 8 G, modulation frequency: 100 kHz.

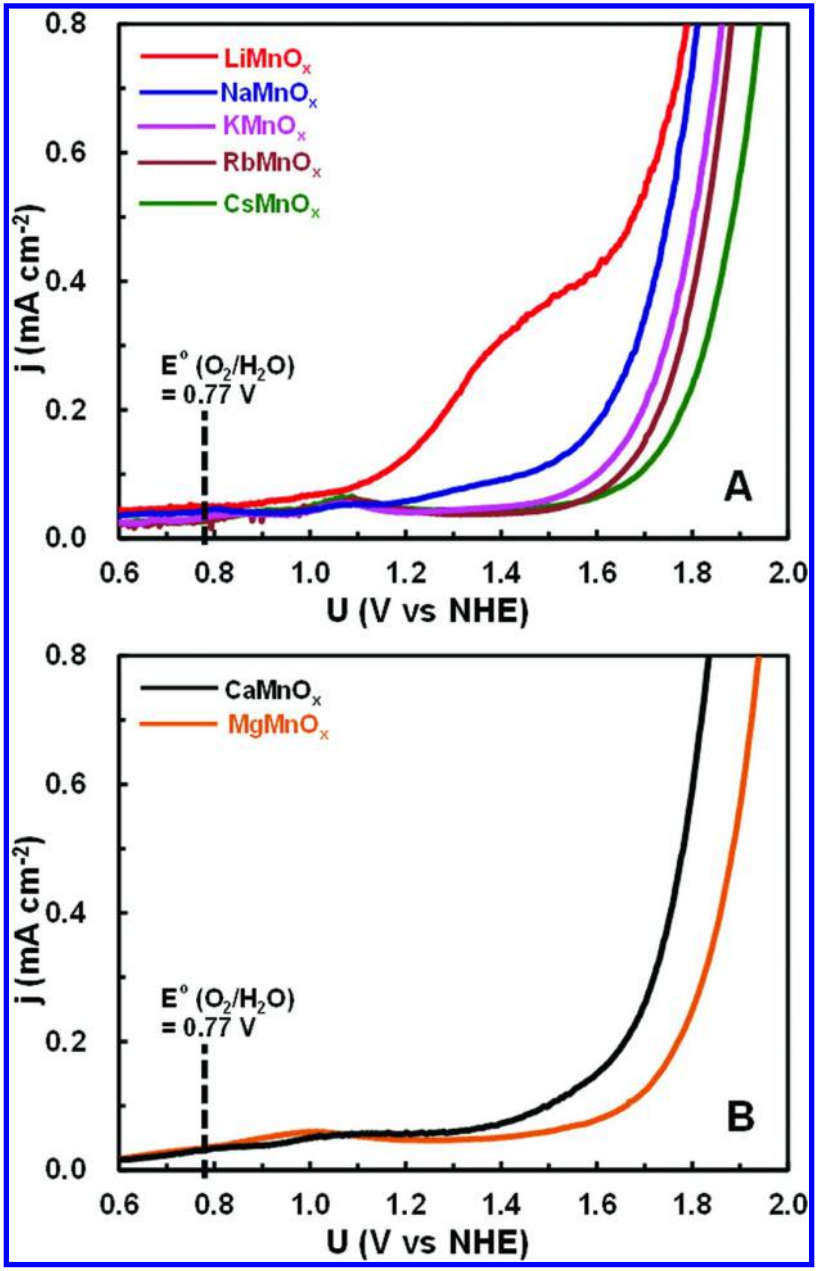

Figure 3. Current density (j: mA cm^{-2}) of manganese oxides with monovalent alkaline cations (A) and divalent alkaline-earth cations (B) in the corresponding 0.5 M MCl (M = Li, Na K, Rb, Cs, Mg or Ca) tris-buffer solution (pH = 7.8) during the positive potential linear sweep at scanning rate of 1 mV/s. $E^o(O_2/H_2O)$ reflects to the standard potential for O_2 evolution.

In Advances in the Environmental Biogeochemistry of Manganese Oxides; Sparks, et al.;
ACS Symposium Series; American Chemical Society: Washington, DC, 2015.

For manganese-oxide solids with Li^+, Na^+, K^+, Rb^+ or Cs^+ as the interlayer cation, the onset potentials for O_2 evolution are: 1.20 V, 1.32 V, 1.45 V, 1.51 V and 1.54 V (vs NHE), respectively (Figure 3A), with uncertainties within ±0.02 V. These values corresponds to an overpotential (η) of ca. 430 mV, 550 mV, 680 mV, 740 mV, and 770 mV (with uncertainties within ±20 mV), respectively, since the standard potential for O_2 evolution at this pH condition is 0.77 V. These overpotentials are comparable to those reported by other researchers for pH-neutral solutions and similar conditions (*39*). This trend of increasing overpotential with increasing cation size parallels the increase in the electrostatic potential value, as shown in Figure 4. We can only speculate about the cause of this trend of oxidation catalysis with intercalating cation, since the stability Mn(III) species in the layer revealed from EPR (Figure 2) is similar. The difference of intercalating monovalent alkaline cations in radius, electrostatic potential as well as Lewis acidity could contribute to this trend.

Manganese-oxide solids with alkaline-earth cations (Mg^{2+} or Ca^{2+}) exhibit higher overpotentials (ca. 630 and 740 mV ±20 mV, respectively; Figure 3B) than the lighter alkali metals, Li^+ and Na^+, that have similar affects on the spacing of layers. The interlayer distance, d_{001}, for $CaMnO_x$ is same to that of $LiMnO_x$ and Lewis acidity of both Ca^{2+} and Mg^{2+} is higher than Li^+. If Lewis acidity alone was important, one would expect that the electrochemical behavior of electrocatalysts with these alkaline-earth cations to be comparable to that of samples with Li^+ and Na^+.

In this case, the lower activity must reflect differences in electronic structures of Mn species in the oxide layer (Figure 2). Mn(III) species in manganese oxide layers with alkaline-earth cations (Ca^{2+} or Mg^{2+}) are more stable than samples with alkaline cations (Li^+, Na^+ or Cs^+). We speculate that the divalent cations may affect the localization of layer charge in the MnO_2 solids, enabling the metal-oxide layers to sustain large amounts of Mn(III). However, the stability of Mn(III) species as revealed by EPR could be different from that of the "*in-situ*" working catalyst in contact with the electrolyte, which greatly complicates comparison.

Above all, for our set of as-deposited birnessite-type manganese oxides with both monovalent alkaline (Li^+, Na^+, K^+, Rb^+ or Cs^+) and divalent alkaline-earth cations (Mg^{2+} or Ca^{2+}), the catalytic activity for electronic water oxidation reaction follows the sequence: $Li^+ > Na^+ > Ca^{2+} > K^+ > Mg^{2+} \sim Rb^+ > Cs^+$, which was similar to the activity reported by Dau et al. in water oxidation reaction system using $(NH_4)_2Ce(NO_3)_6$ as electron acceptor and synthetic birnessite-type manganese oxides as catalysts (*60*). Besides, for Ca^{2+}-depleted PSII enzyme that was then reactivated with Ca^{2+}, Sr^{2+}, Mg^{2+} or Na^+, the activity for water oxidation followed a similar trends of $Ca^{2+} > Sr^{2+} \sim Mg^{2+} > Na^+$ (*75*, *76*).

In addition, the effect of post heat-treatment of the as-deposited $LiMnO_x$ film on the activity of O_2 evolution reaction was investigated; results are shown in Figure 5. The potential needed for O_2 evolution is 1.20 V, 1.10 V, 1.00 V and 0.99 V (vs NHE, with uncertainties within ±0.01 V) respectively, for samples before heat treatment, and for those heated to 200, 300, and 500 °C for 2 h, respectively. These values for the onset of O_2 production from water correspond to an overpotentials of ca. 430 mV, 330 mV, 230 mV and 220 mV, indicating that heat treatment dramatically affects O_2 evolution. Such heat treatment,

of course, would dramatically change the surface/structure of birnessite-type manganese-oxide films and characterization of these changes is underway.

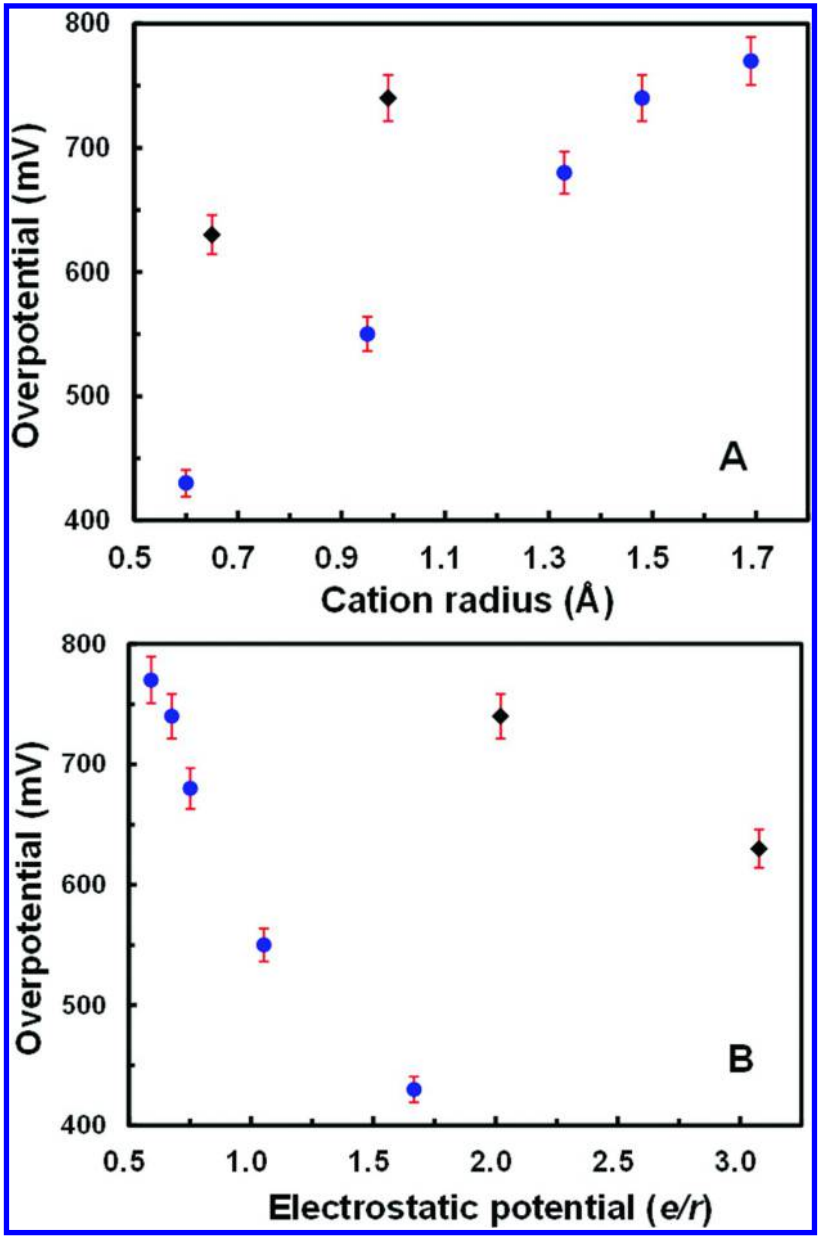

Figure 4. Correlations between overpotential needed for O_2 evolution and radius (A) and electrostatic potential of cation (B). The blue circles are monovalent alkaline cations and the black diamonds are divalent alkaline-earth cations.

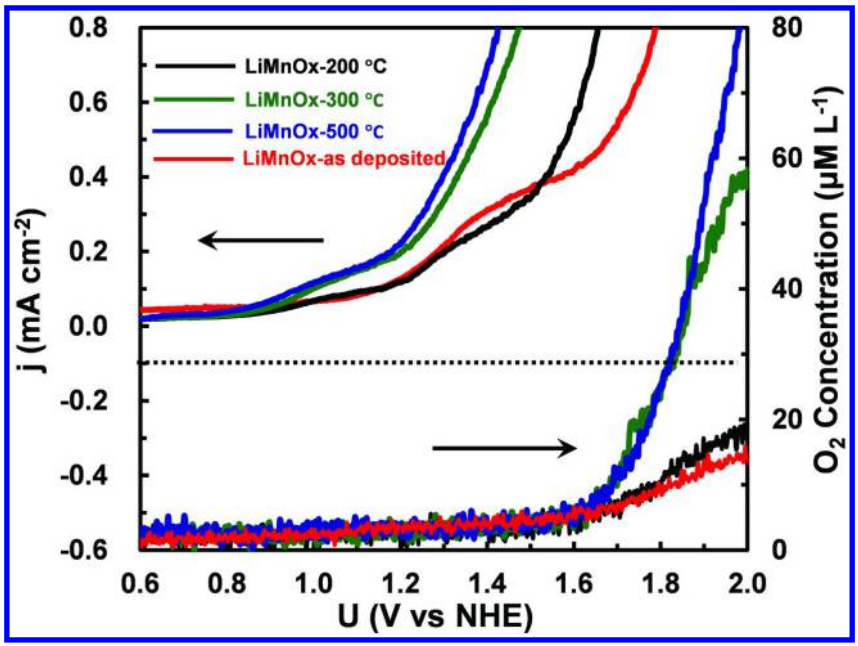

Figure 5. Current density (j: mA cm^{-2}) and evolved O_2 concentration for as-deposited $LiMnO_x$ film, and samples with post heat-treated at 200, 300, and 500 °C for 2 h. Positive potential linear sweep at 1 mV/s is in 0.5 M LiCl tris-buffer solution (pH = 7.8)

The evolution of O_2 as detected from fluorescence measurements matches the electrochemistry. Heat-treated samples evolve O_2 to an enhanced degree relative to as-deposited samples and samples heat-treated at low temperatures (200 °C). It should also be mentioned that there is an experimental delay of ca. 400 mV before the O_2 sensor can detect evolved O_2, which defines response time for the sensor in solution.

In summary, as for birnessite-type manganese oxide with intercalating monovalent alkaline cation (Li^+, Na^+, K^+, Rb^+ or Cs^+), the onset potential for anodic O_2-evolution reaction is lowest for LiMnOx and follows the trend: $Li^+ < Na^+ < K^+ < Rb^+ < Cs^+$ and divalent alkaline-earth cations (Mg^{2+} or Ca^{2+}) appear to affect the manganese-oxide layer more than monovalent cations. Heat-treatment of $LiMnO_x$ film also yields dramatically lower onset potential, with η as low as 220 mV ±10 mV.

4. Conclusions

Birnessite-type manganese oxides can serve as electrocatalysts for water oxidation, with catalytic activities that depend on the intercalating cation. EPR spectra of birnessite samples with divalent cations (Ca^{2+} or Mg^{2+}) and monovalent cations (Li^+, Na^+ or Cs^+) suggest that Mn(III) species are more stable in divalent-cation-substituted samples. By far, the smallest overpotential needed

In Advances in the Environmental Biogeochemistry of Manganese Oxides; Sparks, et al.;
ACS Symposium Series; American Chemical Society: Washington, DC, 2015.

to enable water oxidation was found for heat-treated of as-deposited $LiMnO_x$, suggesting possible changes in both physical and electronic structure.

Acknowledgments

This work was supported by the National Science Foundation via EAR1231322. The authors thank Prof. Leone Spiccia for advice.

References

1. Lewis, N. S.; Nocera, D. G. Powering the planet: chemical challenges in solar energy utilization. *Proc. Natl. Acad. Sci. U.S.A.* **2006**, *103*, 15729–15735.
2. Nelson, N.; Ben-Shem, A. The complex architecture of oxygenic photosynthesis. *Nat. Rev. Mol. Cell Biol.* **2004**, *5*, 971–982.
3. Barber, J. Biological solar energy. *Philos. Trans. R. Soc. London, Ser. A* **2007**, *365*, 1007–1023.
4. Lubitz, W.; Reijerse, E. J.; Messinger, J. Solar water-splitting into H_2 and O_2: design principles of Photosystem II and hydrogenases. *Energy Environ. Sci.* **2008**, *1*, 15–31.
5. McEvoy, J. P.; Brudvig, G. W. Water-splitting chemistry of Photosystem II. *Chem. Rev.* **2006**, *106*, 4455–4483.
6. Yano, J.; Kern, J.; Sauer, K.; Latimer, M. J.; Pushkar, Y.; Biesiadka, J.; Loll, B.; Saenger, W.; Messinger, J.; Zouni, A.; Yachandra, V. K. Where water is oxidized to dioxygen: structure of the photosynthetic Mn_4Ca cluster. *Science* **2006**, *314*, 821–825.
7. Dau, H.; Zaharieva, I.; Haumann, M. Recent developments in research on water oxidation by Photosystem II. *Curr. Opin. Chem. Biol.* **2012**, *16*, 3–10.
8. Kirch, M; Lehn, J.-M.; Sauvage, J.-P. Hydrogen generation by visible light irradiation of aqueous solutions of metal complexes. An approach to the photochemical conversion and storage of solar energy. *Helv. Chim. Acta* **1979**, *62*, 1345–1384.
9. Armaroli, N.; Balzani, V. The future of energy supply: challenges and opportunities. *Angew. Chem., Int. Ed.* **2007**, *46*, 52–66.
10. Balzani, V.; Credi, A.; Venturi, M. Photochemical conversion of solar energy. *ChemSusChem* **2008**, *1*, 26–58.
11. Magnuson, A.; Anderlund, M.; Johansson, O.; Lindblad, P.; Lomoth, R.; Polivka, T.; Ott, S.; Stensjo, K.; Styring, S.; Sundstrom, V.; Hammarstrom, L. Biomimetic and microbial approaches to solar fuel generation. *Acc. Chem. Res.* **2009**, *42*, 1899–1909.
12. Maeda, K.; Domen, K. Photocatalytic water splitting: recent progress and future challenges. *J. Phys. Chem. Lett.* **2010**, *1*, 2655–2661.
13. Bard, A. J.; Fox, M. A. Artificial photosynthesis: solar splitting of water to hydrogen and oxygen. *Acc. Chem. Res.* **1995**, *28*, 141–145.
14. Zhao, Y.; Hernandez-Pagan, E. A.; Vargas-Barbosa, N. M.; Dysart, J. L.; Mallouk, T. E. A high yield synthesis of ligand-free iridium oxide

nanoparticles with high electrocatalytic activity. *J. Phys. Chem. Lett.* **2011**, *2*, 402–406.
15. Morris, N. D.; Suzuki, M.; Mallouk, T. E. Kinetics of electron transfer and oxygen evolution in the reaction of $[Ru(bpy)_3]^{3+}$ with colloidal iridium oxide. *J. Phys. Chem. A* **2004**, *108*, 9115–9119.
16. Lodi, G.; Sivieri, E.; De Battisti, A.; Trasatti, S. Ruthenium dioxide-based film electrodes. *J. Appl. Electrochem.* **1978**, *8*, 135–143.
17. Nakagawa, T.; Beasley, C. A.; Murray, R. W. Efficient eelectro-oxidation of water near its reversible potential by a mesoporous IrO_x nanoparticle film. *J. Phys. Chem. C* **2009**, *113*, 12958–12961.
18. Yagi, M.; Tomita, E.; Sakita, S.; Kuwabara, T.; Nagai, K. Self-assembly of active IrO_2 colloid catalyst on an ITO electrode for efficient electrochemical water oxidation. *J. Phys. Chem. B* **2005**, *109*, 21489–21491.
19. Mills, A.; Russell, T. Comparative study of new and established heterogeneous oxygen catalysts. *J. Chem. Soc., Faraday Trans.* **1991**, *87*, 1245–1250.
20. Harriman, A.; Pickering, I. J.; Thomas, J. M.; Christensen, P. A. Metal oxides as heterogeneous catalysts for oxygen evolution under photochemical conditions. *J. Chem. Soc., Faraday Trans.* **1988**, *84*, 2795–2806.
21. Han, H.; Frei, H. In situ spectroscopy of water oxidation at Ir oxide nanocluster driven by visible TiOCr charge-transfer chromophore in mesoporous silica. *J. Phys. Chem. C* **2008**, *112*, 16156–16159.
22. Nakamura, R.; Frei, H. Visible light-driven water oxidation by Ir oxide clusters coupled to single Cr centers in mesoporous silica. *J. Am. Chem. Soc.* **2006**, *128*, 10668–10669.
23. Howells, A. R.; Sankarraj, A.; Shannon, C. A diruthenium-substituted polyoxometalate as an electrocatalyst for oxygen generation. *J. Am. Chem. Soc.* **2004**, *126*, 12258–12259.
24. Satorel, A.; Carraro, M.; Scorrano, G.; Zorzi, R. D.; Geremia, S.; McDaniel, N. D.; Bernhard, S.; Bonchio, M. Polyoxometalate embedding of a tetraruthenium(IV)-oxo-core by template-directed metalation of $[\gamma\text{-}SiW_{10}O_{36}]^{8-}$: a totally inorganic oxygen-evolving catalyst. *J. Am. Chem. Soc.* **2008**, *130*, 5006–5007.
25. Geletii, Y. V.; Huang, Z.; Hou, Y.; Musaev, D. G.; Lian, T.; Hill, C. L. Homogeneous light-driven water oxidation catalyzed by a tetraruthenium complex with all inorganic ligands. *J. Am. Chem. Soc.* **2009**, *131*, 7522–7523.
26. Post, J. E. Manganese oxide minerals: crystal structures and economic and environmental significance. *Proc. Natl. Acad. Sci. U.S.A.* **1999**, *96*, 3447–3454.
27. Siegbahn, P. E. M. Structures and energetics for O_2 formation in Photosystem II. *Acc. Chem. Res.* **2009**, *42*, 1871–1880.
28. Armstrong, F. A. Why did Nature choose manganese to make oxygen? *Philos. Trans. R. Soc. London, Ser. B* **2008**, *363*, 1263–1270.
29. Tributsch, H. The challenge of non-linear and co-operative mechanisms for electrocatalysis. *Electrochim. Acta* **1994**, *39*, 1495–1502.

30. Tributsch, H. On the significance of the simultaneity of electron transfer and cooperation in electrochemistry. *J. Electroanal. Chem.* **1992**, *331*, 783–800.
31. Vass, I.; Styring, S. pH-dependent charge equilibria between tyrosine-D and the S states in Photosystem II. Estimation of relative midpoint redox potentials. *Biochemistry* **1991**, *30*, 830–839.
32. Geijer, P.; Morvaridi, F.; Styring, S. The S_3 state of the oxygen-evolving complex in Photosystem II is converted to the $S_2Y_Z^{\bullet}$ state at alkaline pH. *Biochemistry* **2001**, *40*, 10881–10891.
33. Metz, J. G.; Nixon, P. J.; Rogner, M.; Brudvig, G. W.; Diner, B. A. Directed alteration of the D1 polypeptide of Photosystem II: evidence that tyrosine-161 is the redox component, Z, connecting the oxygen-evolving complex to the primary electron donor, P680. *Biochemistry* **1989**, *28*, 6960–6969.
34. Morita, M.; Iwakura, C.; Tamura, H. The anodic characteristics of massive manganese oxide electrode. *Electrochim. Acta* **1979**, *24*, 357–362.
35. Gorlin, Y.; Jaramillo, T. F. A bifunctional nonprecious metal catalyst for oxygen reduction and water oxidation. *J. Am. Chem. Soc.* **2010**, *132*, 13612–13614.
36. Pinaud, B. A.; Chen, Z.; Abram, D. N.; Jaramillo, T. F. Thin films of sodium birnessite-type MnO_2: optical properties, electronic band structure, and solar photoelectrochemistry. *J. Phys. Chem. C* **2011**, *115*, 11830–11838.
37. El-Deab, M. S.; Awad, M. I.; Mohammad, A. M.; Ohsaka, T. Enhanced water electrolysis: Electrocatalytic generation of oxygen gas at manganese oxide nanorods modified electrodes. *Electrochim. Commun.* **2007**, *9*, 2082–2087.
38. Brimblecombe, R.; Bond, A. M.; Dismukes, G. C.; Swiegers, G. F.; Spiccia, L. Electrochemical investigation of Mn_4O_4-cubane water-oxidizing clusters. *Phys. Chem. Chem. Phys.* **2009**, *11*, 6441–6449.
39. Takashima, T.; Hashimoto, K.; Nakamura, R. Mechanisms of pH-dependent activity for water oxidation to molecular oxygen by MnO_2 electrocatalysts. *J. Am. Chem. Soc.* **2012**, *134*, 1519–1527.
40. Hocking, R. K.; Brimblecombe, R.; Chang, L.-Y.; Singh, A.; Cheah, M. H.; Glover, C.; Casey, W. H.; Spiccia, L. Water-oxidation catalysis by manganese in a geochemical-like cycle. *Nat. Chem.* **2011**, *3*, 461–466.
41. Yagi, M.; Narita, K. Catalytic O_2 evolution from water induced by adsorption of $[(OH_2)(Terpy)Mn(\mu\text{-}O)_2Mn(Terpy)(OH_2)]^{3+}$ complex onto clay compounds. *J. Am. Chem. Soc.* **2004**, *126*, 8084–8085.
42. Narita, K.; Kuwabara, T.; Sone, K.; Shimizu, K.; Yagi, M. Characterization and activity analysis of catalytic water oxidation induced by hybridization of $[(OH_2)(terpy)Mn(\mu\text{-}O)_2Mn(terpy)(OH_2)]^{3+}$and clay compounds. *J. Phys. Chem. B* **2006**, *110*, 23107–23114.
43. Robinson, D. M.; Go, Y. B.; Greenblatt, M.; Dismukes, G. C. Water oxidation by λ-MnO_2: catalysis by the cubical Mn_4O_4 subcluster obtained by delithiation of spinel $LiMn_2O_4$. *J. Am. Chem. Soc.* **2010**, *132*, 11467–11469.
44. Brimblecombe, R.; Swiegers, G. F.; Dismukes, G. C.; Spiccia, L. Sustained water oxidation photocatalysis by a bioinspired manganese cluster. *Angew. Chem., Int. Ed.* **2008**, *47*, 7335–7338.
45. Limburg, J.; Vrettos, J. S.; Liable-Sands, L. M.; Rheingold, A. L.; Crabtree, R. H.; Brudvig, G. W. A functional model for O-O bond formation

by the O_2-evolving complex in Photosystem II. *Science* **1999**, *283*, 1524–1527.
46. Naruta, Y.; Sasayama, M.; Sasaki, T. Oxygen evolution by oxidation of water with manganese porphyrin dimers. *Angew. Chem., Int. Ed.* **1994**, *33*, 1839–1841.
47. Gao, Y.; Akermark, T.; Liu, J.; Sun, L.; Akermark, B. Nucleophilic attack of hydroxide on a Mn^V oxo complex: A model of the O−O bond formation in the oxygen evolving complex of Photosystem II. *J. Am. Chem. Soc.* **2009**, *131*, 8726–8727.
48. Jiao, F.; Frei, H. Nanostructured manganese oxide clusters supported on mesoporous silica as efficient oxygen-evolving catalysts. *Chem. Commun.* **2010**, *46*, 2920–2922.
49. Boppana, V. B. R.; Jiao, F. Nanostructured MnO_2: an efficient and robust water oxidation catalyst. *Chem. Commun.* **2011**, *47*, 8973–8975.
50. Najafpour, M. M.; Ehrenberg, T.; Wiechen, M.; Kurz, P. Calcium manganese(III) oxides ($CaMn_2O_4{\cdot}xH_2O$) as biomimetic oxygen-evolving catalysts. *Angew. Chem., Int. Ed.* **2010**, *49*, 2233–2237.
51. Najafpour, M. M.; Nayeri, S.; Pashaei, B. Nano-size amorphous calcium–manganese oxide as an efficient and biomimetic water oxidizing catalyst for artificial photosynthesis: back to manganese. *Dalton Trans.* **2011**, *40*, 9374–9378.
52. Najafpour, M. M. A soluble form of nano-sized colloidal manganese(IV) oxide as an efficientcatalyst for water oxidation. *Dalton Trans.* **2011**, *40*, 3805–3807.
53. Najafpour, M. M. Mixed-valence manganese calcium oxides as efficient catalysts for water oxidation. *Dalton Trans.* **2011**, *40*, 3793–3795.
54. Najafpour, M. M.; Pashaei, B.; Nayeri, S. Calcium manganese(IV) oxides: biomimetic and efficient catalysts for water oxidation. *Dalton Trans.* **2012**, *41*, 4799–4805.
55. Najafpour, M. M.; Pashaei, B.; Nayeri, S. Nano-sized layered aluminium or zinc–manganese oxides as efficient water oxidizing catalysts. *Dalton Trans.* **2012**, *41*, 7134–7140.
56. Najafpour, M. M.; Pashaei, B. Nanoscale manganese oxide within Faujasite zeolite as an efficient and biomimetic water oxidizing catalyst. *Dalton Trans.* **2012**, *41*, 10156–10160.
57. Najafpour, M. M.; Amini, M.; Nayeri, S.; Bagherzadeh, M. A very simple method to synthesize nano-sized manganese oxide: an efficient catalyst for water oxidation and epoxidation of olefins. *Dalton Trans.* **2012**, *41*, 11026–11031.
58. Najafpour, M. M. Hollandite as a functional and structural model for the biological water oxidizing complex: manganese-calcium oxide minerals as a possible evolutionary origin for the $CaMn_4$ cluster of the biological water oxidizing complex. *Geomicrobiol. J.* **2011**, *28*, 714–718.
59. Najafpour, M. M. Self-assembled layered hybrid $[Ru(bpy)_3]^{2+}$/ manganese(III,IV) oxide: a new and efficient strategy for water oxidation. *Chem. Commun.* **2011**, *47*, 11724–11726.

60. Wiechen, M.; Zaharieva, I; Dau, H; Kurz, P. Layered manganese oxides for water-oxidation: alkaline earth cations influence catalytic activity in a Photosystem II-like fashion. *Chem. Sci.* **2012**, *3*, 2330–2339.
61. Tommos, C.; Babcock, G. T. Proton and hydrogen currents in photosynthetic water oxidation. *Biochim. Biophys. Acta* **2000**, *1458*, 199–219.
62. Francesco Femi Marafattoa, F. F.; Straderb, M. L.; Gonzalez-Holgueraa, J.; Schwartzbergc, A.; Gilbertd, B.; Peñaa, J. Rate and mechanism of the photoreduction of birnessite (MnO_2) nanosheets. *Proc. Natl. Acad. Sci. U.S.A.* **2015**, *112*, 4600–4605.
63. Feng, X. H.; Zhai, L. M.; Tan, W. F.; Liu, F.; He, J. Z. Adsorption and redox reactions of heavy metals on synthesized Mn oxide minerals. *Environ. Pollut.* **2007**, *147*, 366–373.
64. Scott, M. J.; Morgan, J. J. Reactions at oxide surfaces. 2. oxidation of Se(IV) by synthetic birnessite. *Environ. Sci. Technol.* **1996**, *30*, 1990–1996.
65. Manceau, A.; Charlet, L. X-ray absorption spectroscopic study of the sorption of Cr(III) at the oxide-water interface: I. molecular mechanism of Cr(III) oxidation on Mn oxides. *J. Colloid Interface Sci.* **1992**, *148*, 425–442.
66. Huang, P. M., Kinetics of redox reactions on manganese oxides and its impact on environmental quality. *Rates of Soil Chemical Processes*; SSSA Spec; Sparks, D. L., Suarez, D. L., Eds.; Soil Science Society of America: Madison, WI, 1991; *Vol.* 27, pp 191–230.
67. Armstrong, A. R.; Bruce, P. G. Synthesis of layered $LiMnO_2$ as an electrode for rechargeable lithium batteries. *Nature* **1996**, *381*, 499–500.
68. Nakayama, M.; Kanaya, T.; Lee, J. W.; Popov, B. N. Electrochemical synthesis of birnessite-type layered manganese oxides for rechargeable lithium batteries. *J. Power Sources* **2008**, *179*, 361–366.
69. Kwon, K. D.; Refson, K.; Sposito, G. On the role of Mn(IV) vacancies in the photoreductive dissolution of hexagonal birnesite. *Geochim. Cosmochim. Acta* **2009**, *73*, 4142–4150.
70. Nakayama, M. Cathodic synthesis of birnessite-type layered manganese oxides for electrocapacitive catalysis. *J. Electrochem. Soc.* **2012**, *159*, A1176–A1182.
71. Matsui, H.; Ju, J.; Odaira, T.; Toyota, N. Two-dimensionally confined water in between MnO_2 layers of Na-birnessite. *J. Phys. Soc. Jpn.* **2009**, *78*, 074801.
72. Nakayama, M.; Fukuda, M.; Konishi, S.; Tonosaki, T. Effect of reaction parameters on the electrochemical formation of multilayer films composed of manganese oxides and tetraalkylammonium ions. *J. Mater. Res.* **2006**, *21*, 3152–3160.
73. Glaunsinger, W. S.; Horowitz, H. S.; Longo, J. M.; Chang, A. Magnetic properties of the mixed-valence compounds $CaMn_3O_6$ and $CaMn_4O_8$. *J. Solid State Chem.* **1980**, *35*, 187–191.
74. Kakazey, M.; Ivanova, N.; Sokolsky, G.; Gonzalez-Rodriguez, J. G. Electron paramagnetic resonance of MnO_2 powders. *Electrochem. Solid State Lett.* **2001**, *4*, J1–J4.

75. Ghanotakis, D. F.; Babcock, G. T.; Yocum, C. F. Calcium reconstitutes high rates of oxygen evolution in polypeptide depleted Photosystem II preparations. *FEBS Lett.* **1984**, *167*, 127–130.
76. Ono, T.-A.; Inoue, Y. Discrete extraction of the Ca atom functional for O_2 evolution in higher plant Photosystem II by a simple low pH treatment. *FEBS Lett.* **1988**, *227*, 147–152.

In Advances in the Environmental Biogeochemistry of Manganese Oxides; Sparks, et al.;
ACS Symposium Series; American Chemical Society: Washington, DC, 2015.

Chapter 8

In Situ Immobilization of Arsenic in Water and Soil Using Polysaccharide Stabilized Iron Manganese Binary Oxide Nanoparticles

Byungryul An, Wenbo Xie, and Dongye Zhao*

Environmental Engineering Program, Department of Civil Engineering, Auburn University, Auburn, Alabama 36849
***E-mail: zhaodon@auburn.edu**

Stabilized Fe-Mn binary oxide nanoparticles were synthesized and tested for removal and in-situ immobilization of arsenic, As(III) and As(V), in simulated groundwater and soil. A water soluble starch or carboxymethyl cellulose (CMC) was used as a stabilizer to prevent the particles from aggregation and facilitate in situ delivery of the particles into contaminated soil. Both bare and stabilized Fe-Mn nanoparticles showed rapid sorption kinetics and high capacity. The maximum Langmuir capacity was determined to be 338 mg-As/g-Fe for As(III) and 272 for As(V) at pH 5.5. The highest sorption capacity was observed over the pH range of 5–8 for As(III), while acidic pH favored the uptake of As(V). Column breakthrough tests demonstrated that CMC-stabilized nanoparticles were deliverable in a model sandy soil. Column breakthrough tests coupled with filtration modeling indicated that the delivered nanoparticles will remain virtually immobile in soil under typical groundwater conditions, serving as a fixed sink for the contaminants. When the pre-contaminated soil was treated with CMC-stabilized Fe–Mn at an Fe-to-As molar ratio of 6.5–39, the water-leachable As(III) was reduced by 91-96%, and the TCLP-based leachability was reduced by 94-98%. Column elution tests showed that when an As(III)-laden soil was amended with 22 pore volumes of the nanoparticles suspension, nearly all water-soluble As(III) was transferred to the nanoparticle phase, and eventually immobilized as the

In Advances in the Environmental Biogeochemistry of Manganese Oxides; Sparks, et al.;
ACS Symposium Series; American Chemical Society: Washington, DC, 2015.

particles were immobilized in soil. The technology holds the potential to fill a major technology gap and substantially cut down the cost in remediation of arsenic-contaminated soil and groundwater.

Introduction

Iron-based particles have been widely tested for water treatment and environmental remediation as effective absorbents for decades (*1*–*5*). A number of studies have shown that iron (hydr)oxides can effectively adsorb oxyanions which are also wide-spread contaminants, arsenite, arsenate, selenate, and phosphate (*3*, *6*, *7*). However, the effectiveness of these adsorbents is often dependent of the oxidation state or speciation of the contaminants. For example, amorphous iron hydroxide, goethite, and magnetite can offer high adsorption capacities towards arsenate, As(V), but much less removal for arsenite, As(III) (*8*, *9*). Manganese oxide has been known to be an effective oxidizing agents for As(III) (*10*, *11*). Typically, manganese oxide can convert As(III) to As(V), but it offers only limited adsorption capacity (*12*), e.g., the removal capacity of As(III) was 13.5 mg/g for manganese dioxide (*13*) and 7.5 mg/g for synthesized birnessite (*11*).

Both iron and manganese oxides are low-cost and environmentally friendly materials, existing ubiquitously in the natural environment, and when combined, they can form various composite oxide minerals (*14*). Zhang et al. (*15*, *16*) reported that synthesized binary Fe-Mn binary oxides can enhance the As(III) removal. FTIR and XPS results showed that the imbedded manganese dioxide played an important role in the enhanced As(III) removal by partial oxidation of As(III) to As(V).

However, the conventionally synthesized nanoparticles rapidly aggregate into the micrometer to millimeter particles, which not only reduce the sorption capacity but render the particles undeliverable into contaminated soil or sediment. To overcome this technical obstacle and facilitate soil delivery of the nanoparticles, An and Zhao (*17*) synthesized a new class of polysaccharide stabilized Fe-Mn binary oxide nanoparticles using starch and carboxymethyl cellulose (CMC) as a stabilizer. The stabilized nanoparticles are not only soil-deliverable but offer high adsorption capacities for both As(III) and As(V), and thus, are promising for in situ immobilization of arsenic in soil and groundwater.

Arsenic contamination of soil and groundwater has been one of the most challenging environmental issues due to the high toxicity of As, the huge population effected and the tremendous treatment cost. Arsenic in groundwater can be from natural sources (i.e., weathering of As minerals and geothermal discharge) and from industrial/agricultural inputs (i.e., uses of arsenical pesticides and from coal fly ash) (*18*). In 2006, the World Health Organization (WHO) reported some regions experiencing serious As contamination of drinking water, including the Bengal Delta in Bangladesh and India, the Red River Delta in Vietnam, South America (i.e., Chile and Argentina), the western United States and many other areas (*3*). To mitigate the human exposure, the U.S. EPA tightened the

In Advances in the Environmental Biogeochemistry of Manganese Oxides; Sparks, et al.;
ACS Symposium Series; American Chemical Society: Washington, DC, 2015.

As rule and lowered the maximum contaminant level (MCL) for As in drinking water from its previous 50 μg/L to 10 μg/L effective in 2006. This value also coincided with the limit set by WHO.

Arsenic exists in the environment as organic forms such as roxarsone, nitarsone, arsanilic acid, carbarsone etc., and inorganic forms including two oxidation states, As(III) and As(V). In general, inorganic As is more mobile and toxic than organic As, and As(III) is more mobile and toxic than As(V) (*19*, *20*). Under typical groundwater reducing environment, As(III) is often the more prevalent species than As(V). The background soil concentration of arsenic is typically below 15 mg/kg, but can exceed 2000 mg/kg in some contaminated areas (*21*). In the subsurface, As can be a long-term contaminant to groundwater and affected surface water.

The goal of this chapter is to overview the feasibility of using the starch- or CMC-stabilized Fe–Mn oxide nanoparticles (denoted as Fe–Mn) for in situ immobilization or removal of both As(III) and As(V) in contaminated soils. Special attention is placed to: 1) preparation starch- or CMC-stabilized Fe–Mn nanoparticles, 2) the effectiveness of the stabilized nanoparticles for As(III) and As(V) removal from water, 3) soil deliverability of the stabilized Fe–Mn nanoparticles, and 4) effectiveness of the stabilized Fe–Mn nanoparticles for in situ immobilizing As(III) in a contaminated soil.

Preparation of Stabilized Fe-Mn Nanoparticles

Nanoparticles are formed through clustering (i.e., nucleation and crystallization) of atoms or nuclei. Due to the high specific surface area, high surface energy, and possible reactivity, nanoparticles are unstable both chemically and physically. Chemically, the particles tend to react to lower the surface chemical potential; and physically, they tend to aggregate or dissolve to minimize the surface free energy. In the absence of a stabilizer, such surface reaction or aggregation processes are usually thermodynamically favorable.

A stabilizer refers to a chemical that can be adsorbed to the surfaces of the nanoparticles and can prevent the aggregation through the steric and/or electrostatic stabilization mechanisms. The proper uses of a stabilizer during the particle preparation can facilitate the particle growth and control the particle size and possibly the morphology. By preventing the particle aggregation, a proper particle stabilization strategy can facilitate synthesis of soil-deliverable nanoparticles that can be used for in situ remediation uses.

A number of studies have shown the advantages of stabilized nanoparticles in both physical and chemical properties. For example, Yean et al. (*22*) reported that oleic acid stabilized magnetite nanoparticles offered an arsenic sorption capacity 4.6 times higher than a commercial magnetite powder. He et al. (*23*) reported that CMC stabilized Fe-Pd nanoparticles degraded trichloroethene (TCE) 17 times faster than the non-stabilized counterparts, and the stabilized nanoparticles were deliverable in a loamy-sand soil. Gong et al. (*24*) and Xiong et al. (*25*) reported that stabilized FeS nanoparticles can effectively immobilize mercury in situ in contaminated soils or sediments.

In Advances in the Environmental Biogeochemistry of Manganese Oxides; Sparks, et al.;
ACS Symposium Series; American Chemical Society: Washington, DC, 2015.

For environmental applications, a stabilizer must satisfy some critical features, including 1) it must not cause any environmental harm, 2) it should not alter the soil physical and chemical properties, and 4) it should be cost-effective. Starch and CMC are low-cost, biocompatible and 'green' polysaccharides. Both have been widely employed as stabilizers for various nanoparticles, such as zero-valent iron (*26*), FeS (*27*), magnetite (*28*) and iron phosphate (*29*). Starch stabilizes nanoparticles via the steric stabilization mechanism, whereas CMC works through both steric and the electrostatic stabilization mechanisms due to the negative charges (pKa = 4.3) (*23*).

An and Zhao synthesized a new class of stabilized Fe-Mn nanoparticles in the presence of starch or CMC as a stabilizer (Figure 1). First, prepare a 1 wt.% stock solution of starch or a 1 wt.% CMC stock solution (proper heating is needed to dissolve starch in water). Then, take a desired volume (from 0 to 28 mL) of the starch or CMC solution and dilute with DI water to 120 mL, and mix for 10 min. Prepare an $FeSO_4 \cdot 7H_2O$ solution of 13.9 g/L and another solution of 2.65 g/L of $KMnO_4$ in DI water, and then add 10 mL of the $FeSO_4 \cdot 7H_2O$ solution into 120 mL of a stabilizer solution and mix for 15 min under N_2 purging. The redox reaction is then initiated by adding 10 mL of the $KMnO_4$ solution into the mixture of iron sulfate and one of the stabilizers under vigorous magnetic stirring. Immediately increase the pH of the mixture to ~7.5 using 4 M NaOH, and shake the mixture on a platform shaker at 200 rpm for 1 h. Fe–Mn nanoparticles are then obtained as either on-stabilized aggregates or fully stabilized suspension depending on the concentration and type of the stabilizers present. The Fe–Mn particles are then tested or analyzed within 1 h of preparation. Based on the chemical cost calculation, the preparation of the starch-stabilized nanoparticles is about 6.6 $/lb-Fe-Mn.

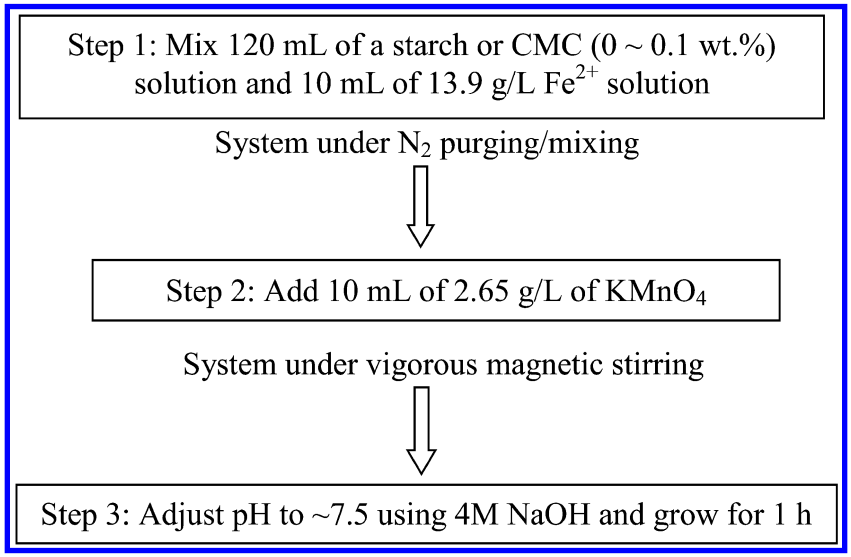

Figure 1. Procedures for synthesizing starch- or CMC-stabilized Fe-Mn nanoparticles.

In Advances in the Environmental Biogeochemistry of Manganese Oxides; Sparks, et al.;
ACS Symposium Series; American Chemical Society: Washington, DC, 2015.

XRD analysis revealed that the resulting Fe-Mn particles are largely amorphous, which agrees with the report by Zhang et al. (*15*), who prepared non-stabilized Fe-Mn oxides. The hydrodynamic diameter was determined by the dynamic light scattering (DLS) to be 348 ± 46 (mean ± standard deviation) nm and 247 ± 9 nm for the CMC-and starch- stabilized Fe–Mn nanoparticles, respectively. TEM images (Figure 2) showed a mean diameter of 38±9 (±standard deviation) nm for CMC-stabilized nanoparticles, and 47±11 nm for starch-stabilized nanoparticles. While the bare particles were poly-dispersed aggregates with a mean diameter of 78±16 nm, with large aggregates of >250 nm (*30*).

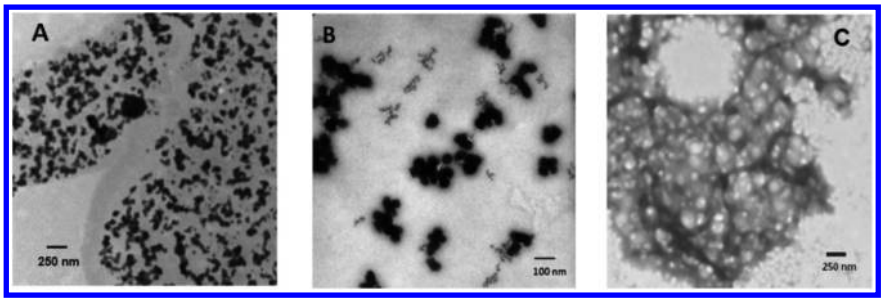

Figure 2. TEM images of Fe-Mn binary oxide nanoparticles prepared at 0.1 g/L as Fe with: (A) no stabilizer, (B) 0.10 wt.% CMC, and (C) 0.10 wt.% starch. Adapted with permission from ref. (30). Copyright (2015) Elsevier.

The use of a stabilizer can greatly impact the surface charge and zeta potential of the nanoparticles. For bare Fe-Mn particles, the ζ potential varied from +2 mV at pH 5.7 to -45 mV at pH 8.9, with the pH of the point of zero charge (pH_{PZC}) being estimated at ~6. However, the surface potential was altered remarkably in the presence of stabilizers. For starch-stabilized Fe-Mn, the ζ value was nearly zero over the pH range of 3.3–7.2, and it was only changed to −10 mV when pH was extended to 10.5. In contrast, for CMC-stabilized Fe-Mn, the ζ value was substantially lowered to below −50 mV throughout the pH range (<−65 mV at pH >5), confirming that the stabilization of the nanoparticles is attributed to the electrosteric repulsion induced by the attachment of negatively charged CMC (pKa = 4.3).

Immobilization of As(III) in Water and Soil Using Stabilized Fe-Mn Nanoparticles

Sorption of As(III) in Water

An and Zhao observed that both stabilized and non-stabilized Fe-Mn particles displayed high sorption capacities for As(III) removal from water (*17*). At an

In Advances in the Environmental Biogeochemistry of Manganese Oxides; Sparks, et al.;
ACS Symposium Series; American Chemical Society: Washington, DC, 2015.

Fe–Mn dosage of 0.20 g/L as Fe and at an initial As(III) concentration of 100 mg/L, the As(III) removal rate reached 69%, 75%, and 77%, respectively, for CMC-stabilized, bare, and starch-stabilized Fe-Mn. The stabilized particles offered a faster sorption rate (< 1 h) than the bare particles (> 4 h). An and Zhao also studied detailed kinetic modeling (*17*). However, the particle stabilization didn't enhance the sorption capacity proportional to gain in the specific surface area. In fact, the stabilizers on the particle surface may inhibit arsenic uptake both thermodynamically (due to reduced sorption sites and site accessibility) and kinetically (due to increased mass transfer resistance). Additionally, the highly negative surface potential induced by CMC rendered an unfavorable sorption condition for CMC-stabilized Fe-Mn nanoparticles to take up As(V) or As(III) species, though CMC-stabilized particles are smaller and more deliverable in soil.

Figure 3 shows the sorption isotherms of As(III) and As(V) by CMC-stabilized Fe-Mn nanoparticles. The classical Langmuir model well fits the experimental data, which is in accord with the monolayer surface complexation mechanism. At pH 5.5, the maximum sorption capacity for As(III) and As(V) was observed at 338 mg/g and 272 mg/g, respectively, which is much greater than those reported for other adsorbents, such as 135 mg-As(III)/g for magnetite (*22*) and 55 mg-As(III)/g for Ce–Ti powder (*31*). The great As(III) sorption capacity enhancement was contributed to: 1) the oxidizing power of manganese dioxide, which converts part of As(III) to more adsorbable As(V), and 2) the presence of MnO_2 opens up more accessible surface sorption sites for arsenic. The oxidative sorption process for As(III) removal can be described by the following stoichiometry (*32*):

$$2MnO_2 + H_3AsO_3 = 2MnOOH^* + H_3AsO_4 \quad (1)$$

$$2MnOOH^* + H_3AsO_3 + 4H^+ = 2Mn^{2+} + H_3AsO_4 + 3H_2O \quad (2)$$

$$MnO_2 + H_3AsO_3 + 2H^+ = Mn^{2+} + H_3AsO_4 + H_2O \quad (3)$$

where $MnOOH^*$ represents Mn(III) intermediate reaction product. Upon the sorption equilibrium, the concentration of soluble manganese was measured to be 9 to 13 mg/L for the case of As(III) and 0.046–0.72 mg/L for As(V). The measured soluble manganese accounted for 14.5–21.0 wt.% of the total Mn in the particles for the case of As(III), confirming participation of MnO_2 in the reaction. This result was also confirmed by the FTIR analysis by Zhang et al. (*32*). Manning et al. (*11*) and Scott and Morgan (*10*) reported that about 70, 90, 95, and ~100% As(III) was oxidized to As(V) by synthesized birnessite at a Mn:As molar ratio of 6.2, 44.5, 15, and 29, respectively, within 10 h.

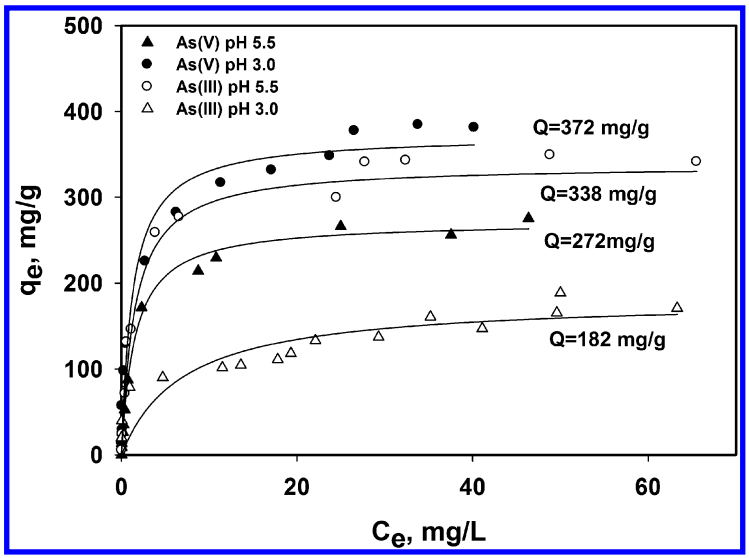

Figure 3. As(III) and As(V) sorption isotherms for CMC-stabilized Fe–Mn nanoparticles at pH 3.0 and 5.5. (Symbols: observed data; lines: Langmuir model fits.) Initial arsenic = 5–140 mg/L, Fe–Mn = 0.27 g/L as Fe–Mn, CMC in Na form = 0.16 wt.%. Adapted with permission from ref. (17). Copyright (2012) Elsevier.

Immobilization of As in Soil

Batch As Immobilization Tests

An and Zhao (*17*) demonstrated the effectiveness of stabilized Fe–Mn nanoparticles for As(III) immobilization in a sandy soil in batch tests at various dosages of nanoparticles. Figure 4a shows the releases of arsenic from the As-laden soil in the absence and the presence of the nanoparticles. Approximately 3800 μg/L of As was leached into the aqueous solution when the As-laden soil was mixed with the simulated ground water (SGW) prepared following the method by Lien and Wilkin (*33*), while the leaching of As was reduced by 91% and 84% by CMC- and starch-stabilized Fe-Mn, respectively, at an Fe:As molar ratio of 6.5; and by more than 95% when the dosage of the nanoparticles was increased to Fe:As = 39. Evidently, the stabilized nanoparticles were able to immobilize the soluble As(III) into the solid phase. It is noteworthy that CMC-stabilized Fe-Mn outperformed starch-stablized Fe-Mn, while Figure 3 showed a greater Langmuir capacity for the latter based on the aqueous-phase adsorption data. The observed greater effectiveness of CMC-stabilized Fe-Mn for soil treatment can be attributed to the smaller particle size and the more negative surfaces of CMC-stabilized Fe-Mn. The negative surfaces prevent the particles from interacting with soil and soil components, resulting less fouling; and the smaller size allows the particles to access to more arsenic sites. The soil samples in the batch tests were subjectd to the toxicity characteristic leaching procedure (TCLP).

In Advances in the Environmental Biogeochemistry of Manganese Oxides; Sparks, et al.;
ACS Symposium Series; American Chemical Society: Washington, DC, 2015.

Figure 4b shows the TCLP leachable As concentration reached 3000 µg/L for the water amended soil, while less than 180 and 300 µg/L for the soil samples treated by CMC- and starch-stabilized Fe–Mn, respectively, i.e., the TCLP leachability of As was reduced by 94–98% with CMC-stabilized Fe–Mn, and by 90–99% with starch-stabilized Fe–Mn. FTIR analysis indicated that the high arsenic affinity of the nanoparticles is attributed to the inner sphere complexation between arsenate and Fe of the nanoparticles (*28*).

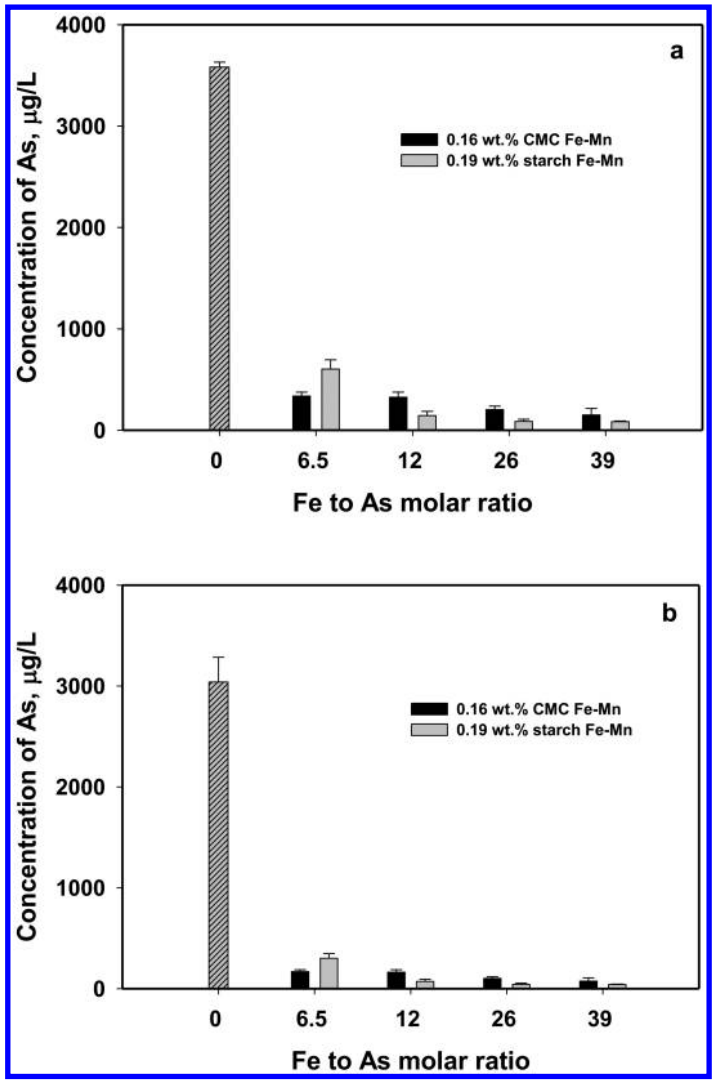

Figure 4. (a) Arsenic concentration in the aqueous phase when an As(III)-laden soil was amended with water or various doses of CMC- or starch-stabilized Fe–Mn nanoparticles for 4 days; (b) Arsenic concentration in the TCLP fluid when the soil samples in (a) were subjected to TCLP tests. Adapted with permission from ref. (17). Copyright (2012) Elsevier.

For *in situ* immobilization applications, the nanoparticles must be deliverable in contaminated soils. Figure 5 shows the breakthrough curves of CMC-stabilized Fe-Mn nanoparticles in a sandy soil bed. Compared to the tracer (Br^-), the nanoparticles displayed a similar starting breakthrough at 1 PV (pore volume) and a steady full breakthrough at 4 PVs, after which ~10% of the particles were consistently retained in the soil bed due to the filtration effect. Similar breakthrough profiles were also reported by Gong et al. (*24*) who studied the transport of CMC-stabilized FeS nanoparticles through a sediment and field soil and observed nearly 20% of nanoparticles were retained. According to the classical filtration theory, the deposition of the particles on the media are attributed to the Brownian diffusing, interception, and/or gravitational sedimentation (*34*, *35*).

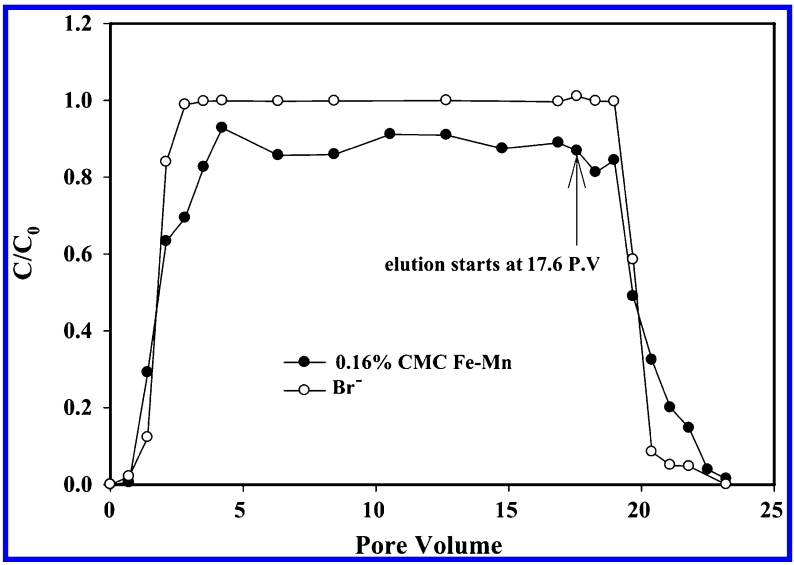

Figure 5. Breakthrough curves and subsequent elution histories of a tracer (Br–) and CMC stabilized Fe–Mn nanoparticles through a sandy soil. Experimental conditions: EBCT: 35.6 min, SLV: 3.8 ×10⁻⁵ m/s, influent pH 7 ± 0.1, Fe–Mn = 0.27 g/L, CMC = 0.16 wt.%. (Arrow indicates the point where elution was started). Adapted with permission from ref. (17). Copyright (2012) Elsevier.

Figure 5 also indicates that the subsequent elution was unable to remobilize or elute the nanoparticles that were previously retained in the soil bed.

The transport and deposition of nanoparticles in porous media were strongly affected by the flow velocity. He et al. (*34*) studied breakthrough behaviors of CMC-stabilized ZVI (zero-valent iron) nanoparticles under the pore flow velocity ranging from 0.0176 to 0.0706 cm/s. Based on the particle breakthrough curves and the filtration modeling, they obtained the maximum travel distance (MTD)

In Advances in the Environmental Biogeochemistry of Manganese Oxides; Sparks, et al.;
ACS Symposium Series; American Chemical Society: Washington, DC, 2015.

of the nanoparticles as a function of the pore velocity (Figure 6). Evidently, the effective area or particle travel distance can be manipulated by controlling the injection velocity, i.e. injection pressure. Figure 6 also reveals that under typical groundwater flow conditions, the delivered nanoparticles will remain in a very confined domain.

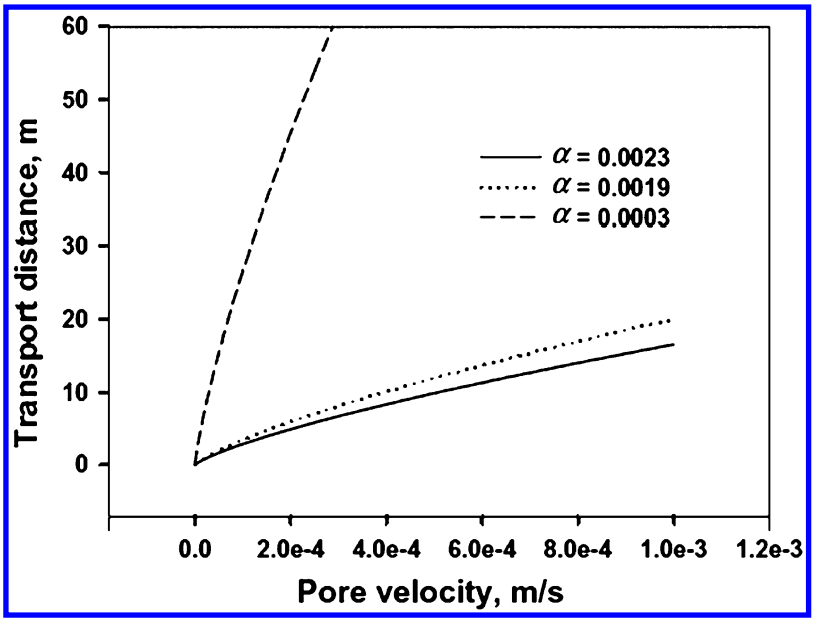

Figure 6. Relationship between the maximum travel distance of CMC-stabilized ZVI nanoparticles and interstitial liquid velocity in a fixed bed sand column. Adapted with permission from ref. (34). Copyright (2009) Elsevier.

In Situ Immobilization of As in Soil Using CMC-Stabilized Fe-Mn Nanoparticles

Figure 7 shows the As(III) immobilization effectiveness in the arsenite-laden sandy soil by CMC-stabilized Fe–Mn nanoparticles through fixed-bed column tests. When the soil bed was treated with SGW, the arsenic elution curve displayed an immediate peaking followed by a gradual tailing, and ~17% of arsenic loaded in the soil was eluted. In contrast, when the nanoparticle suspension was passed through the same soil, a similar elution profile of arsenic was observed, with ~15% of arsenic being eluted. However, ~94% of the eluted As was associated with the nanoparticles, with only 6% being soluble As. In addition, when the water-treated and nanoparticle-amended soil samples were subjected to the TCLP tests, the arsenic leachability for the nanoparticles-amended soil was more than 78% less.

The results indicate that the nanoparticles treatment transferred most of the water-soluble As onto the nanoparticles. As discussed earlier, because the nanoparticles are to be retained in the soil matrix under natural groundwater flow conditions (Figure 6), the associated arsenic will be immobilized along with the

particles. Consequently, the delivered nanoparticles will serve as an immobile sink for immobilization of water-leachable arsenite.

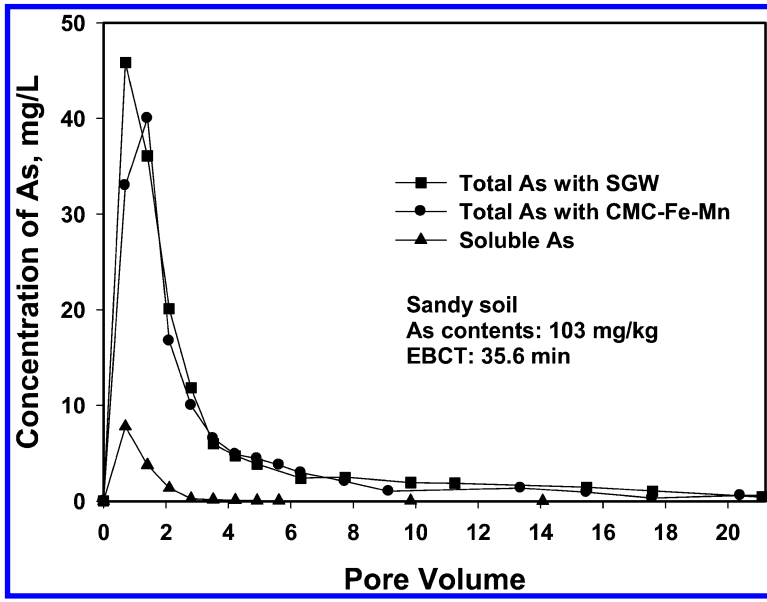

Figure 7. Arsenic elution profiles using simulated groundwater or CMC-stabilized Fe–Mn nanoparticle suspensions (soluble As refers to As concentration after nanoparticles are removed from the effluent samples). Adapted with permission from ref. (17). Copyright (2012) Elsevier.

Conclusions

A new class of CMC- and starch-stabilized Fe-Mn nanoparticles were synthesized and tested for removal or immobilization of As(III) and As(V) in simulated groundwater and soil. The addition of MnO_2 in the iron oxide phase enhanced the adsorption capacity for As(III) by partial oxidation of As(III) to As(V) and by opening up more surface sites for direct sorption of As(III) and As(V). Compared to traditional aggregated particles, the largely amorphous Fe-Mn nanoparticles offer some unique properties, such as much smaller particle size, larger specific surface area, much improved soil deliverability, and strong affinity for As. Consequently, the stabilized nanoparticles hold the promise to facilitate in situ As immobilization in contaminated soil and groundwater. The nanoparticles are transportable under moderate external pressure, but remain in a confined domain once delivered in soil and when the external pressure is released. The nanoparticle treatment converts most (>95%) of the water soluble arsenic onto the nanoparticles, and arsenic is co-immobilized as the nanoparticles are retained by the soil matrix. For a given soil, the effective travel distance of the nanoparticles is a function of pore water flow velocity, and thus, can be manipulated by tuning the injection pressure. The nanoparticle amendment can also greatly (by >78%) lower the TCLP leachability of arsenic in soil. Therefore,

In Advances in the Environmental Biogeochemistry of Manganese Oxides; Sparks, et al.;
ACS Symposium Series; American Chemical Society: Washington, DC, 2015.

the particles may also be used for converting hazardous wastes into non-hazardous materials. Compared to conventional remediation technologies, this in situ remediation technique offers some unprecedented advantages, including: 1) it can be directly used in contaminated source zones where conventional technologies cannot reach, 2) it is less disruptive to the local environment, 3) it requires much less overall remediation time, and 4) it is likely much more cost-effective.

References

1. Kanel, S. R.; Greneche, J.-M.; Choi, H. Arsenic(V) removal from groundwater using nano scale zero-valent iron as a colloidal reactive barrier material. *Environ. Sci. Technol.* **2006**, *40*, 2045–2050.
2. Liang, L.; Yang, W.; Guan, X.; Li, J.; Xu, Z.; Wu, J.; Huang, Y.; Zhang, X. Kinetics and mechanisms of pH-dependent selenite removal by zero valent iron. *Water Res.* **2013**, *47*, 5846–5855.
3. Liang, Q.; Zhao, D.; Qian, T.; Freeland, K.; Feng, Y. Effects of stabilizers and water chemistry on arsenate sorption by polysaccharide-stabilized magnetite nanoparticles. *Ind. Eng. Chem. Res.* **2012**, *51*, 2407–2418.
4. Martínez, M.; Giménez, J.; de Pablo, J.; Rovira, M.; Duro, L. Sorption of selenium(IV) and selenium(VI) onto magnetite. *Appl. Surf. Sci.* **2006**, *252*, 3767–3773.
5. Raven, K. P.; Jain, A.; Loeppert, R. H. Arsenite and Arsenate Adsorption on Ferrihydrite : Kinetics , Equilibrium , and Adsorption Envelopes. *Environ. Sci. Technol.* **1998**, *32*, 344–349.
6. Zeng, L.; Li, X.; Liu, J. Adsorptive removal of phosphate from aqueous solutions using iron oxide tailings. *Water Res.* **2004**, *38*, 1318–1326.
7. Rovira, M.; Giménez, J.; Martínez, M.; Martínez-Lladó, X.; de Pablo, J.; Martí, V.; Duro, L. Sorption of selenium(IV) and selenium(VI) onto natural iron oxides: goethite and hematite. *J. Hazard. Mater.* **2008**, *150*, 279–284.
8. Dixit, S.; Hering, J. G. Comparison of arsenic(V) and arsenic(III) sorption onto iron oxide minerals: implications for arsenic mobility. *Environ. Sci. Technol.* **2003**, *37*, 4182–4189.
9. Mamindy-Pajany, Y.; Hurel, C.; Marmier, N.; Roméo, M. Arsenic (V) adsorption from aqueous solution onto goethite, hematite, magnetite and zero-valent iron: Effects of pH, concentration and reversibility. *Desalination* **2011**, *281*, 93–99.
10. Scott, M. J.; Morgan, J. J. Reactions at Oxide Surfaces. 1. Oxidation of As(III) by Synthetic Birnessite. *Environ. Sci. Technol.* **1995**, *29*, 1898–1905.
11. Manning, B. A.; Fendorf, S. E.; Bostick, B.; Suarez, D. L. Arsenic(III) oxidation and arsenic(V) adsorption reactions on synthetic birnessite. *Environ. Sci. Technol.* **2002**, *36*, 976–981.
12. Lenoble, V.; Laclautre, C.; Serpaud, B.; Deluchat, V.; Bollinger, J.-C. As(V) retention and As(III) simultaneous oxidation and removal on a MnO2-loaded polystyrene resin. *Sci. Total Environ.* **2004**, *326*, 197–207.

13. Bissen, M.; Frimmel, F. H. Arsenic— a Review. Part II: Oxidation of Arsenic and its Removal in Water Treatment. *Acta Hydrochim. Hydrobiol.* **2003**, *31*, 97–107.
14. Liu, Y.-T.; Hesterberg, D. Phosphate bonding on noncrystalline Al/Fe-hydroxide coprecipitates. *Environ. Sci. Technol.* **2011**, *45*, 6283–6289.
15. Zhang, G.; Qu, J.; Liu, H.; Liu, R.; Wu, R. Preparation and evaluation of a novel Fe-Mn binary oxide adsorbent for effective arsenite removal. *Water Res.* **2007**, *41*, 1921–1928.
16. Zhang, G.; Liu, H.; Liu, R.; Qu, J. Adsorption behavior and mechanism of arsenate at Fe-Mn binary oxide/water interface. *J. Hazard. Mater.* **2009**, *168*, 820–825.
17. An, B.; Zhao, D. Immobilization of As(III) in soil and groundwater using a new class of polysaccharide stabilized Fe-Mn oxide nanoparticles. *J. Hazard. Mater.* **2012**, *211-212*, 332–341.
18. Arai, Y.; Sparks, D. L.; Davis, J. a. Effects of dissolved carbonate on arsenate adsorption and surface speciation at the hematite--water interface. *Environ. Sci. Technol.* **2004**, *38*, 817–824.
19. Chang, F.; Qu, J.; Liu, H.; Liu, R.; Zhao, X. Fe-Mn binary oxide incorporated into diatomite as an adsorbent for arsenite removal: preparation and evaluation. *J. Colloid Interface Sci.* **2009**, *338*, 353–358.
20. Guo, H.; Stüben, D.; Berner, Z. Adsorption of arsenic(III) and arsenic(V) from groundwater using natural siderite as the adsorbent. *J. Colloid Interface Sci.* **2007**, *315*, 47–53.
21. Chen, Z.; Kim, K.-W.; Zhu, Y.-G.; McLaren, R.; Liu, F.; He, J.-Z. Adsorption (AsIII,V) and oxidation (AsIII) of arsenic by pedogenic Fe–Mn nodules. *Geoderma* **2006**, *136*, 566–572.
22. Yean, S.; Cong, L. Effect of magnetite particle size on adsorption and desorption of arsenite and arsenate. *J. Mater. Res.* **2005**, 3255–3264.
23. He, F.; Zhao, D.; Liu, J.; Roberts, C. B. Stabilization of Fe-Pd nanoparticles with sodium carboxymethyl cellulose for enhanced transport and dechlorination of trichloroethylene in soil and groundwater. *Ind. Eng. Chem. Res.* **2007**, *46*, 29–34.
24. Gong, Y.; Liu, Y.; Xiong, Z.; Kaback, D.; Zhao, D. Immobilization of mercury in field soil and sediment using carboxymethyl cellulose stabilized iron sulfide nanoparticles. *Nanotechnology* **2012**, *23*, 294007.
25. Xiong, Z.; He, F.; Zhao, D.; Barnett, M. O. Immobilization of mercury in sediment using stabilized iron sulfide nanoparticles. *Water Res.* **2009**, *43*, 5171–5179.
26. He, F.; Zhao, D. Manipulating the size and dispersibility of zerovalent iron nanoparticles by use of carboxymethyl cellulose stabilizers. *Environ. Sci. Technol.* **2007**, *41*, 6216–6221.
27. Gong, Y.; Liu, Y.; Xiong, Z.; Zhao, D. Immobilization of mercury by carboxymethyl cellulose stabilized iron sulfide nanoparticles: reaction mechanisms and effects of stabilizer and water chemistry. *Environ. Sci. Technol.* **2014**, *48*, 3986–3994.

28. An, B.; Liang, Q.; Zhao, D. Removal of arsenic(V) from spent ion exchange brine using a new class of starch-bridged magnetite nanoparticles. *Water Res.* **2011**, *45*, 1961–1972.
29. Liu, R.; Zhao, D. In situ immobilization of Cu(II) in soils using a new class of iron phosphate nanoparticles. *Chemosphere* **2007**, *68*, 1867–1876.
30. Xie, W.; Liang, Q.; Qian, T.; Zhao, D. Immobilization of selenite in soil and groundwater using stabilized Fe-Mn binary oxide nanoparticles. *Water Res.* **2015**, *70*, 485–494.
31. Li, Z.; Deng, S.; Yu, G.; Huang, J.; Lim, V. C. As(V) and As(III) removal from water by a Ce–Ti oxide adsorbent: Behavior and mechanism. *Chem. Eng. J.* **2010**, *161*, 106–113.
32. Zhang, G.; Qu, J.; Liu, H.; Liu, R.; Li, G. Removal mechanism of As(III) by a novel Fe-Mn binary oxide adsorbent: oxidation and sorption. *Environ. Sci. Technol.* **2007**, *41*, 4613–4619.
33. Lien, H.-L.; Wilkin, R. T. High-level arsenite removal from groundwater by zero-valent iron. *Chemosphere* **2005**, *59*, 377–386.
34. He, F.; Zhang, M.; Qian, T.; Zhao, D. Transport of carboxymethyl cellulose stabilized iron nanoparticles in porous media: column experiments and modeling. *J. Colloid Interface Sci.* **2009**, *334*, 96–102.
35. Kretzschmar, R.; Borkovec, M.; Grolimund, D.; Elimelech, M. Mobile Subsurface Colloids and Their Role in Contaminant Transport. *Adv. Agron.* **1999**, *66*, 121–193.

Chapter 9

Synthesis of a Biotemplated Lithium Ion-Sieve Derived from Fungally Formed Birnessite

Keiko Sasaki*,[1] and Qianqian Yu[1,2]

[1]Department of Earth Resources Engineering, Kyushu University, 744 Motooka, Fukuoka 819-0395, Japan
[2]Advanced Science Research Center, Japan Atomic Energy Agency, Tokai, Ibaraki 319-1195, Japan
***E-mail: keikos@mine.kyushu-u.ac.jp**

Biogenic birnessite is a stable form of manganese oxide found in nature that originates from microbial oxidation. Its unique structural properties provide potential for materials scientists to fabricate new functionalized materials. This study used a manganese-oxidizing fungus, *Paraconiothyrium* sp. WL-2, as a bio-oxidizer and biotemplate to prepare a lithium ion-sieve in the shape of a microtube through a solid-state transformation by calcination. The effect of calcination temperature was studied in terms of chemical composition, structure, and morphology. The results showed that the calcination temperature affects not only the weight fraction but also the crystallinity of the lithium manganese oxide spinel, which significantly influences the adsorption capacity of lithium ions.

Introduction

Latest Trends in Lithium Recovery

Lithium (Li) is one of the most important elements in modern industry owing to its wide use in advanced batteries (e.g., metal–air batteries) and supercapacitors. The primary Li sources are enriched brine lakes and seawater. Because of rising demand, recovery of Li from these sources has attracted increasing attention (*1–4*).

As a hole-type ion-sieve material, spinel-type lithium manganese oxides (LMOs) show excellent topotactic Li^+ insertion and extraction properties (*1*).

In Advances in the Environmental Biogeochemistry of Manganese Oxides; Sparks, et al.;
ACS Symposium Series; American Chemical Society: Washington, DC, 2015.

Therefore, these materials can be used as Li^+ ion-sieves for the recovery of Li from primary sources. LMO possesses a cubic structure with space group *Fd3m*. Oxygen (O) atoms occupy the 32*e* sites to form a cubic-close-packed array, manganese (Mn) atoms occupy the octahedral 16*d* sites, and Li atoms occupy the tetrahedral 8*a* sites (Figure 1) (*2*). In the reaction of $LiMn_2O_4$ with H^+, Mn(III) disproportionates as follows:

$$4(Li)[Mn^{(III)}, Mn^{(IV)}]O_4 + 8\ H^+ = 3(\square)[Mn^{(IV)}{}_2]O_4 + 4\ Li^+ + 2\ Mn^{2+} + 4\ H_2O \quad (1)$$

where ( ), [ ], and □ indicate the 8*a* tetrahedral sites, 16*d* octahedral sites, and vacant sites, respectively (*2*). Adsorption of Li^+ occurs through ion exchange with H^+ and the redox reaction involving the oxidation of Mn(III) to Mn(IV). However, the former contributes to a far greater extent than the latter. The specific structure provides a three-dimensional interstitial space for Li^+ transport. The insertion and/or extraction of lithium ions proceeded topotactically (*3*). An insertion of lithium results in an increase in the lattice parameter, and an extraction of lithium results in decreased lattice parameter. Thus, LMOs could be applied as Li-ion batteries and sieves. The stoichiometric spinel phase can be expressed by the chemical formula $Li_{1+x}Mn_{2-x}O_4$ ($0 \leq x \leq 0.33$), in which x is the number of Mn atoms in the octahedral 16*d* sites replacing Li^+ ions. The lattice constant of the stoichiometric spinel and the Li^+ insertion/extraction capacity are affected by the Li/Mn ratio (*3*).

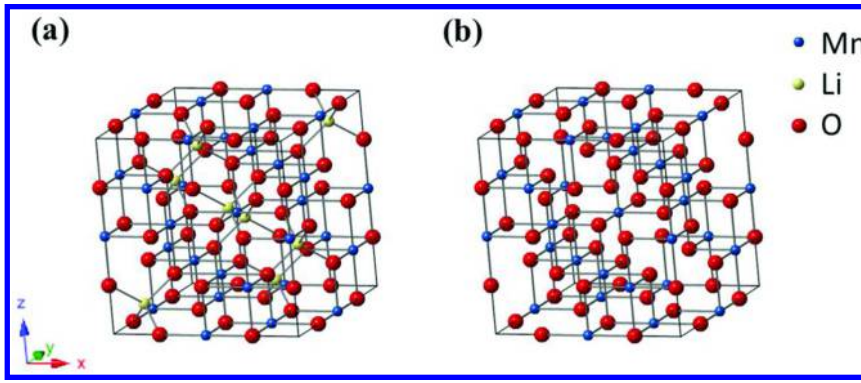

Figure 1. Structure model of (a) spinel lithium manganese oxide (LMO) and (b) lithium ion-sieve (HMO).

Spinel-type Li ion-sieves (HMOs) can be prepared with a two-step method. In the first step, LMO is prepared using Li^+ as the template ions. In the second step, Li^+ is extracted topotactically from the tunnel to obtain HMO. The LMO preparation process can be generally classified into three types: solid state reaction (*4*), wet processing (*5*), and the sol–gel method (*12*). Recent research on

the synthesis of HMOs and the Li^+ sorption capacity is summarized in Table 1. The selection of the Mn oxide precursor and the Li/Mn molar ratio are important factors. In the calcination process the crystal phase of Mn oxide precursor governs the changes in Mn valency, degree of shrinkage, and structural changes. The ratio of Li/Mn influences the numbers of atomic holes in the spinel which is the final product. Most HMOs are in powder form (*5*, *7*, *8*, *12*), which limits their industrial application. However, conventional methods for the assembly of HMO particles, such as granulation and membranization, significantly decrease the sorption capacity of Li^+ because the binding materials, such as polyvinyl chloride, and polysulfone, envelop the particles (*9*, *10*). Therefore, the assembly of nanomaterials to obtain highly ordered microscale architectures is of great significance to fabricate high-efficiency Li^+ adsorbents (*11*).

Biogenic Birnessite: A New Functional Bionanomaterial

In bio-mineralization processes, microorganisms show tremendous control over the orientation of the structural crystal phase through biosorption followed by redox reactions (*13–17*). Understanding of bio-mineralization systems provides great potential for materials scientists to fabricate new composites. Microorganisms are attractive biotemplates because of their unique microstructures, uniform size, availability of functional surfaces, high reproducibility, and low cost (*18*). Biominerals are generally hierarchically organized, nano-particulate, and have poor crystallinity—factors that might seem disadvantageous for lithium recovery, if it is directly tried to use. However, there have been no reports on the use of biogenic Mn oxides for the synthesis of the adsorbents to recover Li^+ ions after modification.

The Mn-oxidizing fungus *Paraconiothyrium* sp. WL-2 used here, which was isolated from a constructed wetland in Kaminokuni, Hokkaido, Japan (*19*), shows high tolerance as well as the ability to oxidize more than 380 mg L^{-1} Mn(II). During incubation in a Mn(II)-containing medium, biogenic birnessite was formed in close proximity to the fungal hyphae. Compared with abiotic birnessites, the biogenic birnessite shows poor crystallinity with a turbostratic structure (*20*). In this chapter, we will discuss the preparation of Li ion-sieves using *Paraconiothyrium* sp. WL-2 as a biotemplate and bio-oxidant.

A New Role of Mn-Oxidizing Fungi as Biotemplates

Paraconiothyrium sp. WL-2 was incubated in a medium containing 0.6 g L^{-1} $MgSO_4 \cdot 7H_2O$, 0.07 g L^{-1} $CaCl_2 \cdot 2H_2O$, 0.05 g L^{-1} peptone, 0.05 g L^{-1} yeast extract, and 4.35 g L^{-1} PIPES at pH 6.5 ± 0.1. The incubation medium had an initial Mn(II) concentration of 0.2–3 mmol L^{-1}. Changes in the Mn(II) concentration in the solution were monitored and the solid products were collected after 72 h incubation for scanning electron microscopy (SEM) observation.

In Advances in the Environmental Biogeochemistry of Manganese Oxides; Sparks, et al.;
ACS Symposium Series; American Chemical Society: Washington, DC, 2015.

Publication Date (Web): November 17, 2015 | doi: 10.1021/bk-2015-1197.ch009

Table 1. Summary of synthesized lithium ion sieve in different methods

Method	*Chemical formula*	*BET (m^2/g)*	*Q^a (mmol/kg)*	*Remarks*	*References*
Mn_2O_3 + LiOH Hydrothermally treated, Calcined at 410°C	$H_{1.6}Mn_{1.6}O_4$	n.d. [b]	3880 (at pH 5.35, 50°C)	aggregated powders	(*5*)
Li/Mn = 5 Oxidation of Mn^{2+} by H_2O_2 followed by heating at 120°C for 24 hrs, and then calcined at 400°C for 5 hrs	$H_{1.41}Li_{0.01}Mn_{1.65}O_4$	51.93	5710 (at pH 12) 2143 (at pH 10) 1000 (at pH 7)	powders	(*6*)
Li/Mn = 1.00 Autoclaved at 363-453 K for 12 hrs, β-MnO_2, calcined at 673 K for 120 hrs	($Li_4Mn_5O_{12}$)	60.9	6620 (at pH 10.1, 30°C)	1-D MnO_2 nanorods (20-140 nm x 0.8-4 mm)	(*7*)
LiOH + $Mn(NO_3)_2$ at 383K for 8 hrs in the presence of H_2O_2 Hydrothermally treated at 343-453 K for 8-48 hrs	($LiMn_2O_4$)	75.75	2300-2800 (at pH 10.1, 30°C)	1-D MnO_2 nanorods by soft process	(*8*)
Citric method Mn/Li = 1.25 At 150°C for 12 hrs, calcined at 350°C for 12 hrs	n.d. [b]	9.69 as MO form	5071 (at pH 12.0) 3143 (at pH 9.0) 1571 (at pH 6.0) in powder 1143 (at pH 12) in fabricated polyurethane	powders fabrication on polyuretane	(*9*)

Publication Date (Web): November 17, 2015 | doi: 10.1021/bk-2015-1197.ch009

Method	*Chemical formula*	*BET (m^2/g)*	*Q^a (mmol/kg)*	*Remarks*	*References*
γ-MnOOH was synthesized from $KMnO_4$ in ethanol by hydrothermal treatment, mixed with LiOH at 120°C, and then calcined at 400°C for 4 hrs	$H_{1.6}Mn_{1.6}O_4$	60.9	4400 (at pH 12) in powders 3800 (at pH 12) in PVC-HMO	powders fabrication in PVC membranes	(*10*)
Biogenic birnessite Mixing with Li^+ (Li/Mn = 1) Calcination at 500°C for 4 hrs	$H_{1.33}Mn_{1.67}O_4$	69	5100 (at pH 8.5, 25°C)	bio-templated fabrication	(*11*)

[a] *Q* is the amount of sorbed Li per unit weight of sorbent. [b] n.d., not described.

The SEM images of the solid products collected after 72 h incubation show that biogenic Mn oxide was formed in close proximity to the fungal hyphae (Figure 2a). When the Mn(II) concentration was increased to 1 mmol L^{-1}, the fungal hyphae were fully and uniformly covered and biogenic Mn oxides with a microtube morphology were observed (Figure 2b). When the Mn(II) concentration was increased to above 1.5 mmol L^{-1}, a large number of isolated particles with irregular shapes were observed (Figure 2c). This result indicates that bio-oxidation of Mn(II) and crystallization of biogenic Mn oxide preferentially occur on the surfaces of the fungal hyphae. At much higher Mn(II) concentrations, further crystallization of the newly formed Mn oxides did not occur on the surfaces of the hyphae after they were fully covered; however, homogeneous nucleation and crystal growth occurred in solution. Thus, at an appropriate Mn(II) concentration, fungal hyphae can serve as biotemplates to control the assembly of biogenic birnessite nanocrystals. Figure 2d–f shows the morphology of the solid products after incubation of the fungus in a scaled-up system of 10 L with 1 mmol L^{-1} Mn(II). The surfaces of the hyphae were fully and uniformly covered with flake-like nanocrystals (Figure 2d-f). Biogenic birnessite microtubes (BB-MTs) with uniform morphology were obtained.

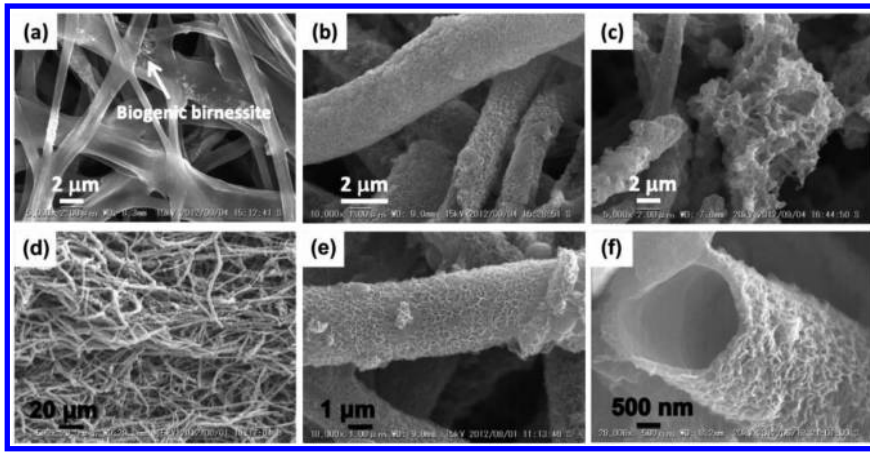

Figure 2. SEM images of biogenic birnessite after exposure of fungal hyphae to (a) 0.2 mmol L^{-1} Mn(II); (b) 1 mmol L^{-1} Mn(II); (c) 3 mmol L^{-1} Mn(II). (d,e,f) SEM images of BB-MTs at different magnifications. Reproduced with permission from ref. (11).

It can be also observed in Figure 2f that the inner tube surface is smooth. It can be expected that dissolved Mn(II) ions are accumulated on the polysaccharide compounds in extracellular periplasmic space, oxidized by H_2O_2, which is released by the fungus, through enzymatic reaction at neutral pH (*20*), resulting in the formation of poorly crystalline birnessite on the surface of the fungal hyphae. The thickness of biogenic birnessite can be estimated to 100-200 nm.

Preparation of LMO by Biogenic Mn Oxide

A schematic illustration of the synthesis of the Li ion-sieves is shown in Figure 3. BB-MTs were suspended in 20 mmol L^{-1} LiCl to form mixtures of different molar ratios. The mixed solutions were sealed in Teflon tubes, shaken at 100 rpm with a stroke of 25 mm at 25 °C for 12 h, and then dried at 80 °C for several hours. LMO microtubes (LMO-MTs) were obtained by calcination of the solid product in a crucible vessel at 300–700 °C for 4 h. The Li ion-sieve microtubes (HMO-MTs) were then obtained after washing the LMO-MTs with 0.1 mol L^{-1} HCl for 12 h.

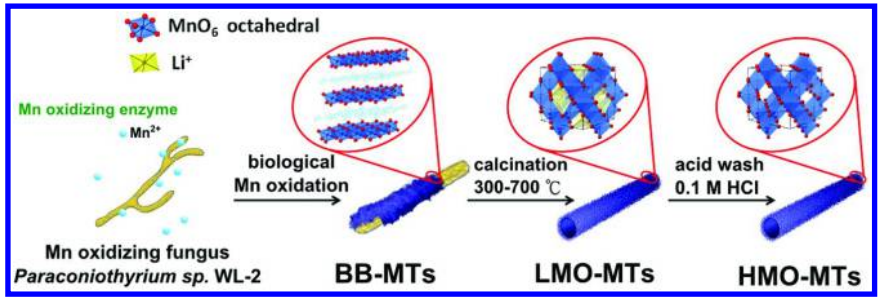

Figure 3. Schematic illustration of the synthesis of Li ion-sieves derived from biogenic birnessite. Biogenic birnessite is produced on the surface of the fungal hyphae, calcined at 300-700˚C, and washed by 0.1 M HCl. Although fungal hyphae in itself is decomposed after calcination, the micro-tube shape is maintained by crystalized LMO, even after acid washing. Reproduced with permission from ref. (11).

Effect of the Starting Materials on LMO-MT Formation

Well-defined LMO with small amounts of Mn_3O_4 was formed after calcination at 300 °C for 4 h (Figure 4a). This temperature is much lower than that reported in previous studies using hollandite, γ-MnO_2, β-MnO_2, γ-MnOOH, and $MnCO_3$ as the Mn precursors (*21–23*). When chemically synthesized birnessite (*24*) was treated under the same calcination conditions, the X-ray diffraction (XRD) pattern is almost unchanged, except for the additional peaks formed at *d* = 4.88 Å (Figure 4b), which may come from dehydrated birnessite. In a previous study, LMO was obtained from this synthetic birnessite after calcination at 450 °C for 8 h (*25*). The lower formation temperature may be attributed to the specific structure of biominerals. Firstly, the biogenic birnessite is poorly crystalline, which is influenced by the organic substances. The energy barrier accompanying lattice reconstruction of biogenic birnessite is much lower than that of the highly crystalline Mn oxides. Secondly, the birnessite structure provides edge-sharing MnO_6 octahedrons, which function as building blocks and are partially retained in the final product.

In Advances in the Environmental Biogeochemistry of Manganese Oxides; Sparks, et al.;
ACS Symposium Series; American Chemical Society: Washington, DC, 2015.

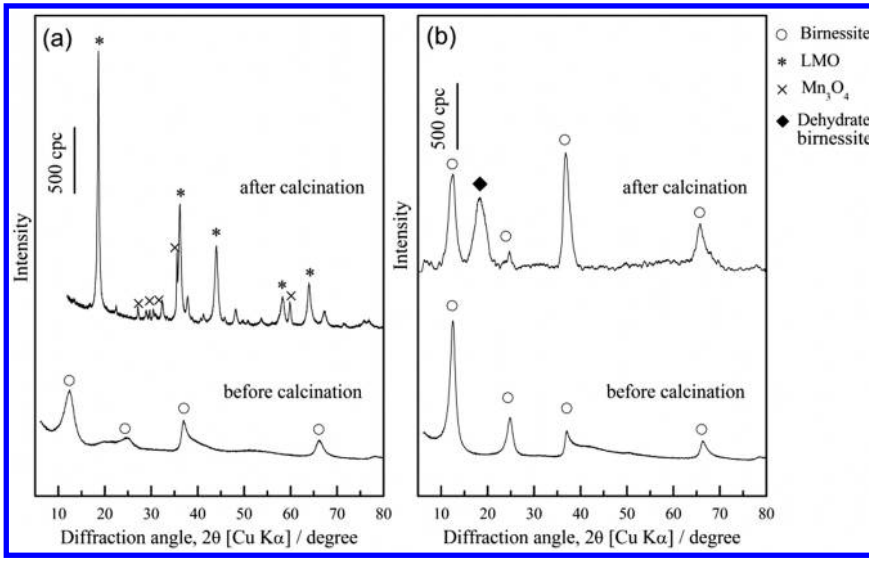

Figure 4. XRD patterns of (a) biogenic birnessite and (b) chemically synthesized birnessite before and after calcination at 300 °C for 4 h.

Effect of Temperature on the Structure of LMO-MTs

In situ XRD is a powerful technique for the observation of crystal growth and phase transition during calcination. To study the phase transition from BB to LMO in real time, a mixture of BB and LiCl with a Li/Mn molar ratio of 1:1 was mounted on a platinum plate and the XRD patterns were measured in situ during heating. Diffraction peaks assigned to the LMO spinel appeared at 300 °C (Figure 5a). The intensity of the LMO peaks gradually increased as the temperature was increased from 300 to 450 °C, while the intensity of the peaks assigned to LiCl gradually decreased. Formation of Li_2MnO_3 was observed at 600 °C. The expanded XRD patterns in the 2θ range of 42–45° showed that the diffraction peak assigned to the *400* plane in the LMO phase is right-shifted from 300 to 450 °C and then left-shifted between 450 and 700 °C (Figure 5b). LMO-MTs calcined for 4 h at different temperatures were then prepared for Rietveld analysis (Figure 6). LMO-MTs calcined at 300 °C contained 80.1% LMO spinel and 19.9% Mn_3O_4. When the calcination temperature was increased to 500°C, the weight fraction of LMO spinel increased to 92.8%, and the weight fraction of Mn_3O_4 decreased to 7.1%. Meanwhile, the lattice parameter (*a*) of the cubic spinel phase decreased from 8.25 to 8.17 Å, and the Mn occupancy decreased from 1 to 0.84. Basically, the lattice parameter of the spinel phase could be affected by the oxidation state of Mn in lattice, since the effective ion radii of octahedrally coordinated Mn(III) (0.645 Å) is larger than that of Mn(IV) (0.56 Å). According to XANES analysis, the consistent trend was observed with the Reitveld analysis. From elemental analysis, the Li/Mn molar ratio increased with calcination temperature. Thus, at elevated temperatures from 300 to 500 °C, Li^+ was gradually incorporated into the Mn oxide phase, and the spinel composition changed along the $Li_{1+x}Mn_{2-x}O_4$

spinel tie-line of the Li–Mn–O phase diagram from $LiMn_2O_4$ to $Li_{1.33}Mn_{1.67}O_4$. Decomposition of $Li_{1.33}Mn_{1.67}O_4$ occurred with the formation of Li_2MnO_3 and $LiMn_2O_4$ at temperatures higher than 600 °C. The content of the spinel phase sharply decreased from 66.9% to 56.6% and the content of Li_2MnO_3 increased. The lattice parameter of the spinel phase increased from 8.20 to 8.21, and the Mn occupancy increased from 0.87 to 0.94. The chemical formula of the LMO spinels prepared at each temperature is shown in Figure 6. It is evident that the calcination temperature not only affects the content but also the crystal structure of the LMO spinel.

HMO-MTs were prepared by acid washing the LMO-MTs with 0.1 mol L^{-1} HCl for 12 h. The XRD patterns of the spinel phase were unchanged except for a slightly decreased lattice parameter because of ion exchange of Li^+ with H^+. This result indicates that the structure of the LMO-MTs directly determines the structure of the HMO-MTs, which is important for Li^+ adsorption.

Effect of Temperature on the Morphology of LMO

The morphology of LMO prepared at temperatures from 300 to 700 °C was observed by SEM and transmission electron microscopy (Figure 7). At 300 °C, although the XRD pattern indicates that LMO is already formed (Figure 4), the SEM images are similar to those of the original biogenic birnessite (Figure 7a). Increasing the calcination temperature from 300 to 500 °C, the surface texture gradually became granular like (Figure 7b,c). Interestingly, the particles did not coarsen significantly. The estimated average particle size was less than 50 nm and the microtube morphology was kept intact. Significant coarsening of particles occurred at a calcination temperature of 600 °C (Figure 7d) and large amounts of block-shaped particles formed, and the tubes crumbled. The measured average particle size was ca. 220 nm at 600 °C, and increased to larger than 500 nm at 700 °C (Figure 7e). For all samples, the morphology was preserved after acid washing.

Adsorption of Li^+ on HMO-MTs

The sorption capacities of Li^+ on the HMOs were then determined at 25 °C with a pH of 8.5 (Figure 8). The sorption capacity of the HMO-MTs increased with increasing calcination temperature within the range of 300–500 °C. Although no significant difference in specific surface area was observed for the products calcined at lower temperatures (Table 2), LMO-MTs compositions are sensitive to the calcination temperature (Figure 6) and influence the sorption capacity of the corresponding HMO-MTs. Above 600 °C, the sorption density of Li^+ sharply decreased. Significant coarsening of the particles occurred at temperatures above 600 °C. Consequently, the specific surface area of HMO-MTs decreased from 71 $m^2\ g^{-1}$ at 300 °C to 10 $m^2\ g^{-1}$ at 700 °C. Therefore, the decreased sorption capacity of Li^+ at temperatures above 600 °C could be attributed to the smaller specific surface area as well as the smaller fraction of the HMO spinel phase.

In Advances in the Environmental Biogeochemistry of Manganese Oxides; Sparks, et al.;
ACS Symposium Series; American Chemical Society: Washington, DC, 2015.

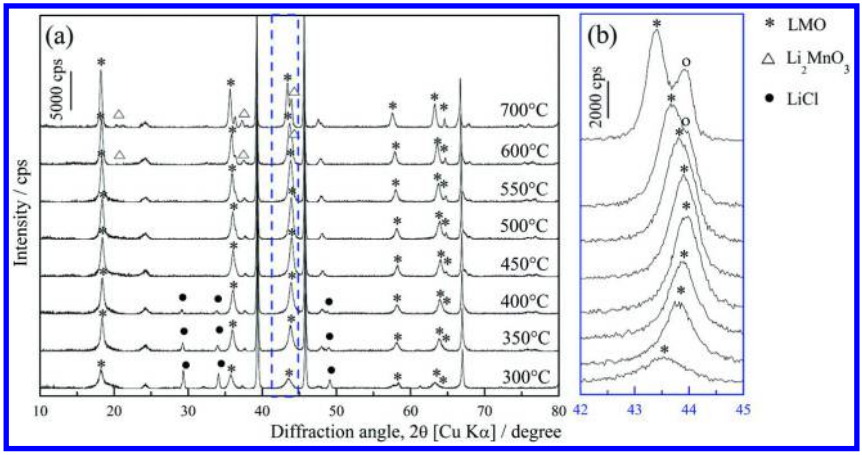

Figure 5. (a) In situ XRD patterns for biogenic birnessite after heating from 300 to 700 °C and (b) expanded in situ XRD patterns in the range 2θ = 42–45°. The unmarked peak arises from the platinum sample holder. Reproduced with permission from ref. (26).

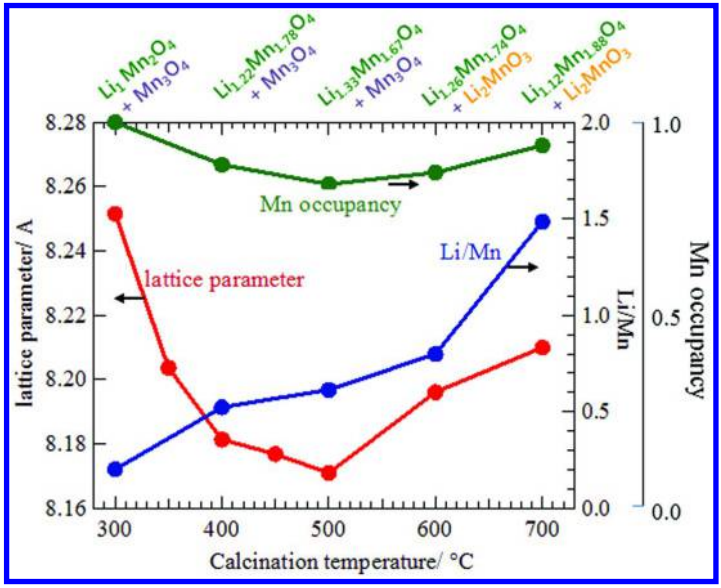

Figure 6. Effect of calcination temperature on the structural parameters obtained from Rietveld refinement. The Li/Mn molar ratio was determined by atomic absorption spectrometry.

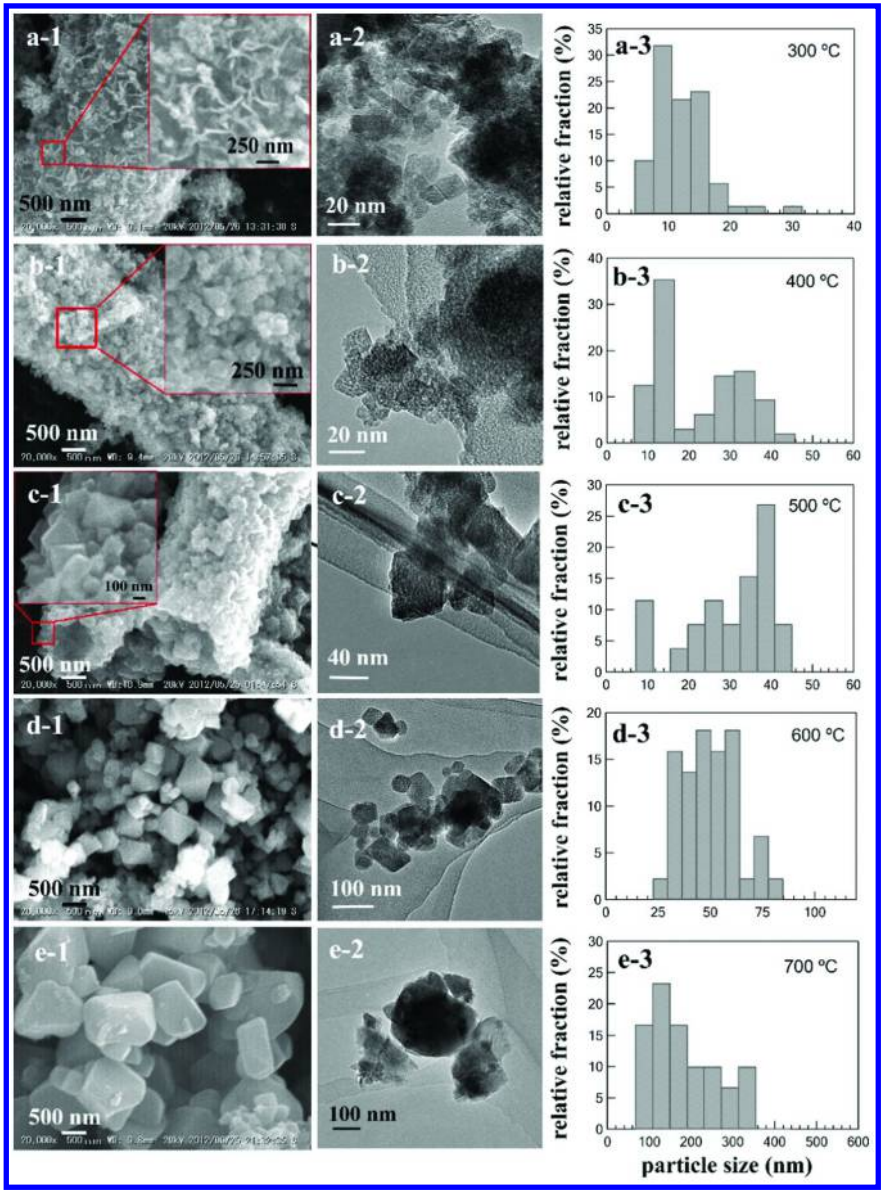

Figure 7. Effects of calcination temperature on the SEM (the first column) and TEM (the second column) morphologies and particle size distribution (the third column). Reproduced with permission from ref. (11).

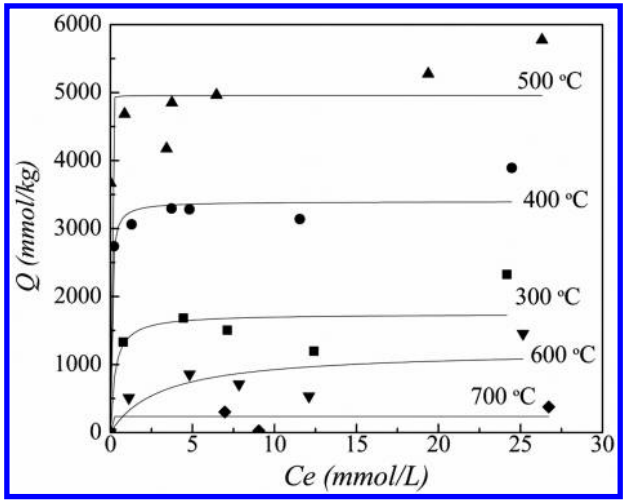

Figure 8. Adsorption isotherms of Li^+ on HMO-MTs prepared at different calcination temperatures.

Table 2. Sorption density of Li^+ on calcined products from 300 to 700 °C

Sample	*Calculated phase*		S_{BET} *(m²/g)*	Q [b] *(mmol/kg)*	Q_{spinel} [c] *(mmol/kg)*
	ID	*Fraction[a] (wt%)*			
HMO-MTs-300	HMO spinel	97.1 ± 0.2	71	1800	1853
	Mn_3O_4	2.9 ± 0.2			
HMO-MTs-400	HMO spinel	99.3 ± 0.1	64	3390	3414
	Mn_3O_4	0.7 ± 0.1			
HMO-MTs-500	HMO spinel	99.94 ± 0.03	69	5100	5105
	Mn_3O_4	0.06 ± 0.03			
HMO-MTs-600	HMO spinel	65.6 ± 0.3	22	850	1296
	Li_2MnO_3	34.4 ± 0.3			
HMO-MTs-700	HMO spinel	56.2 ± 0.1	10	370	658
	Li_2MnO_3	43.8 ± 0.1			

[a] All numbers are expressed as average ± standard deviations. [b] Q is the Li sorption capacity of HMO-MTs. [c] Q_{spinel} is the Li sorption capacity of the spinel phase, defined as the Q value divided by the weight fraction of the spinel phase.

Li^+-containing natural waters typically contain large amounts of other cations. In particular, high concentrations of Na^+ cause hypersalinity, resulting in significant mass transfer resistance. Therefore, the effect of Na^+ on the adsorption capacity of Li^+ was tested using simulated geothermal water containing 1000

mg L^{-1} Na^+ and 10 mg L^{-1} Li^+. As shown in Figure 9a, the uptake of Li^+ by HMO-MTs was 2835.2 mmol kg^{-1} in the absence of Na^+ and 2203.6 mmol kg^{-1} in the presence of Na^+, which is greater than the reference material prepared from the chemically synthesized birnessite (*25*). High concentrations of Na^+ do not significantly influence Li^+ adsorption by both HMO-synthetic and HMO-MTs. The high selectivity toward Li^+ ions is attributed to the structure of the lithium ion sieve. Ion exchange of Li^+ with H^+ takes place during acid washing, resulting in atomic holes of the same size as the Li^+ ion.

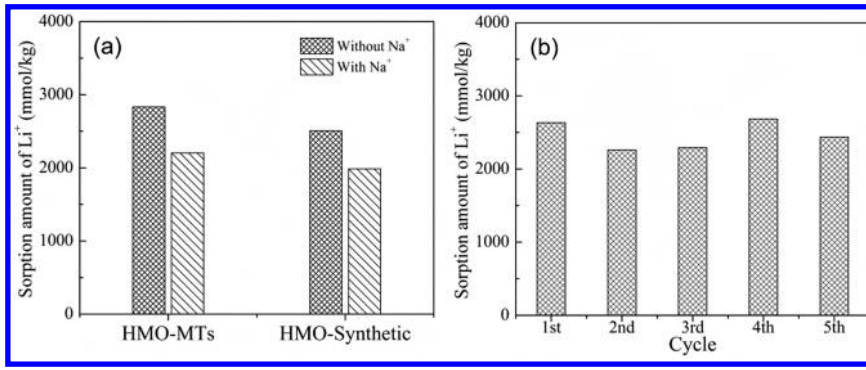

Figure 9. Selectivity and reuse performance. (a) Effect of a mixture of 1000 mg L^{-1} Na^+ and 10 mg L^{-1} Li^+. (b) Five cycles of adsorption/desorption of Li^+ with HMO-MTs. Reproduced with permission from ref. (25).

The adsorption density of Li^+ during different reuse cycles is shown in Figure 9b. The sorption capacity fluctuated slightly with increasing reuse cycle. This is attributed to the slight dissolution of Mn^{2+} during the extraction of Li^+ from LMO by acid washing. Li ion-sieves prepared from biogenic birnessite show a Li^+ sorption density of 2632 mmol kg^{-1} with 0.4 g L^{-1} sorbent and an initial Li^+ concentration of 20 mg L^{-1}. The sorption density remains above 85% after five cycles. This indicates that the prepared material possesses sufficient chemical stability to regenerate by acid washing after several rounds of adsorption of Li ions.

Conclusions

A microtube-type Li ion-sieve was synthesized using the Mn-oxidizing fungus *Paraconiothyrium* sp. WL-2 as a bio-oxidant and biotemplate, which showed good performance for Li^+ recovery in selectivity of Li^+ ions and repetition of adsorption / desorption. Micro scale fabrication of powdery adsorbents has been also achieved at the same time by using biotemplate. Although many works have been published from the geochemical perspectives due to the significant role of Mn oxides in biogeochemical cycling, utilization of this system in the material-oriented researches to control the organization of Mn oxide from nanoscale to microscale was firstly reported in the present work. The poorly

In Advances in the Environmental Biogeochemistry of Manganese Oxides; Sparks, et al.;
ACS Symposium Series; American Chemical Society: Washington, DC, 2015.

crystalline BB facilitates the transformation to highly crystalline LMO spinel at a relatively low temperature, compared with chemically synthesized precursor. The calcination temperature affected the LMO phase fraction and morphology, crystallinity as well as the chemical composition (i.e., the average oxidation state of Mn) of the product, all of which contribute to the adsorption capacity of Li^+ on HMO-MTs. We anticipate that this biotemplated material will be extended to a variety of applications.

References

1. Chitrakar, R.; Kanoh, H.; Miyai, Y.; Ooi, K. A new type of manganese oxide ($MnO_2{\cdot}0.5H_2O$) derived from $Li_{1.6}Mn_{1.6}O_4$ and its lithium ion-sieve properties. *Chem. Mater.* **2000**, *12*, 3151–3157.
2. Qi, F.; Kanoh, H. H.; Ooi, K. Manganese oxide porous crystals. *J. Mater. Chem.* **1999**, *9*, 319–333.
3. Ooi, K.; Miyai, Y.; Katoh, S.; Maeda, H.; Abe, M. Topotactic lithium insertion to λ-MnO_2 in the aqueous phase. *Langmuir* **1989**, *5*, 150–157.
4. Shi, X.; Zhou, D.; Zhang, Z.; Yu, L.; Xu, H.; Chen, B.; Yang, X. Synthesis and properties of $Li_{1.6}Mn_{1.6}O_4$ and its adsorption application. *Hydrometallurgy* **2011**, *110*, 99–106.
5. Feng, Q.; Kanoh, H.; Miyai, Y.; Ooi, K. Hydrothermal synthesis of lithium and sodium manganese oxides and their metal ion extraction/insertion reactions. *Chem. Mater.* **1995**, *7*, 1226–1232.
6. Wang, L.; Meng, C. G.; Ma, W. Study on Li^+ uptake by lithium ion-sieve via the pH technique. *Colloids Surf., A* **2009**, *334*, 34–39.
7. Zhang, Q.; Li, S.; Sun, S.; Yin, X.; Yu, J. Lithium selective adsorption on 1-D MnO_2 nanostructure ion-sieve. *Adv. Powder Technol.* **2009**, *20*, 432–437.
8. Zhang, Q.; Li, S.; Sun, S.; Yin, X.; Yu, J. $LiMn_2O_4$ spinel direct synthesis and lithium ion selective adsorption. *Chem. Eng. Sci.* **2010**, *65*, 169–173.
9. Ma, L.; Chen, B.; Chen, Y.; Shi, X. Preparation, characterization and adsorptive properties of foam-type lithium adsorbent. *Microporous Mesoporous Mater.* **2011**, *142*, 147–153.
10. Zhu, G.; Wang, P.; Qi, P.; Gao, C. Adsorption and desorption properties of Li+ on PVC-$H_{1.6}Mn_{1.6}O_4$ lithium ion-sieve membrane. *Chem. Eng. J.* **2014**, *235*, 340–348.
11. Yu, Q.; Sasaki, K.; Hirajima, T. Bio-templated synthesis of lithium manganese oxide microtubes and their application in Li^+ recovery. *J. Hazard. Mater.* **2013**, *262*, 38–47.
12. Zhang, Q.; Sun, S.; Li, S.; Jiang, H.; Yu, J. Adsorption of lithium ions on novel nanocrystal MnO_2. *Chem. Eng. Sci.* **2007**, *62*, 4869–4874.
13. Banfield, J. F.; Welch, S. A.; Zhang, H.; Ebert, T. T.; Penn, R. L. Aggregation-based crystal growth and microstructure development in natural iron oxyhydroxide biomineralization products. *Science* **2000**, *289*, 751–754.

14. Behrens, S.; Rahn, K.; Habicht, W.; Bohm, K. J.; Rosner, H.; Dinjus, E.; Unger, E. Nanoscale particle arrays induced by highly ordered protein assemblies. *Adv. Mater.* **2002**, *14*, 1621–1625.
15. Shenton, W.; Pum, D.; Sleytr, U. B.; Mann, S. Synthesis of cadmium sulphide superlattices using self-assembled bacterial S-layers. *Nature* **1997**, *389*, 585–587.
16. Braun, E.; Eichen, Y.; Sivan, U.; Ben-Yoseph, G. DNA-templated assembly and electrode attachment of a conducting silver wire. *Nature* **1998**, *391*, 775–778.
17. Douglas, T.; Young, M. Host-guest encapsulation of materials by assembled virus protein cages. *Nature* **1998**, *393*, 152–155.
18. Li, Z.; Chung, S.; Nam, J.; Ginger, D. S.; Mirkin, C. A. Living templates for the hierarchical assembly of gold nanoparticles. *Angew. Chem.* **2003**, *115*, 2408–2411.
19. Takano, K.; Itoh, Y.; Ogino, T.; Kurosawa, K.; Sasaki, K. Phylogenetic analysis of manganese-oxidizing fungi isolated from manganese-rich aquatic environments in Hokkaido, Japan. *Limnology* **2006**, *7*, 219–223.
20. Sasaki, K.; Konno, H.; Endo, M.; Takano, K. Removal of Mn(II) ions from aqueous neutral media by manganese-oxidizing fungus in the presence of carbon fiber. *Biotechnol. Bioeng.* **2004**, *85*, 489–496.
21. Sun, S.; Song, X.; Zhang, Q.; Wang, J.; Yu, J. Lithium extraction/insertion process on cubic Li-Mn-O precursors with different Li/Mn ratio and morphology. *Adsorption* **2011**, *17*, 881–887.
22. Feng, Q.; Miyai, Y.; Kanoh, H.; Ooi, K. Lithium extraction/insertion with spinel-type lithium manganese oxides. Characterization of redox-type and ion-exchange-type sites. *Langmuir* **1992**, *8*, 1861–1867.
23. Yang, X.; Kanoh, H.; Tang, W.; Ooi, K. Synthesis of LiMnO spinels with different morphologies and their ion adsorptivities after delithiation. *J. Mater. Chem.* **2000**, *10*, 1903–1909.
24. Villalobos, M.; Toner, B.; Bargar, J.; Sposito, G. *Geochim. Cosmochim. Acta* **2003**, *67*, 2649–2662.
25. Yu, Q.; Morioka, E.; Sasaki, K. Characterization of lithium ion sieve derived from biogenic Mn oxide. *Microporous Mesoporous Mater.* **2013**, *179*, 122–127.
26. Yu, Q.; Sasaki, K. In situ X-ray diffraction investigation of the evolution of a nanocrystalline lithium-ion sieve from biogenic manganese oxide. *Hydrometallurgy* **2014**, *150*, 253–258.

Chapter 10

Influence of Biomacromolecules on the Stability of Colloidal Manganese Dioxide

Xiaoliu Huangfu and Jun Ma*

State Key Laboratory of Urban Water Resource and Environment, School of Municipal and Environmental Engineering, Harbin Institute of Technology, Harbin 150090, China
***E-mail: majun@hit.edu.cn**

The stability of common manganese dioxide (MnO_2) colloids has great impact on their surface reactivity and therefore on the fates of these particles as well as the associated organism communities. In this work, MnO_2 stability was uncovered by the early stage aggregation kinetics of MnO_2 colloids in aqueous solution and the effects of biomacromolecules (i.e., alginate and bovine serum albumin).Markalbe aggregation was obtained in the presence of both mono- and divalent cations, and the the critical coagulation concentration concentrations were 28 mM $NaNO_3$ and 0.45 mM $Ca(NO_3)_2$. The Hamaker constant of MnO_2 colloids calculated by classical DLVO theory based on the experimental data in aqueous solution was about 7.84×10^{-20} J. Both macromolecules tested enhanced MnO_2 colloidal mobility greatly, and the stabilizing effects might mainly result from the steric repulsive forces which were introduced by organic layers adsorbed on MnO_2 colloidal surfaces. Nevertheless, the complexes formed by alginate and Ca^{2+} (>5 mM) enhanced MnO_2 colloidal aggregation due to a bridging role.

Introduction

It is well documented that the occurrence of manganese dioxide (MnO_2) colloids in aquatic systems (*1–3*). MnO2 colloidal surface reactions, such as adsorption/desorption and redox etc., may impact the fat and transport of both

In Advances in the Environmental Biogeochemistry of Manganese Oxides; Sparks, et al.;
ACS Symposium Series; American Chemical Society: Washington, DC, 2015.

natural and synthetic organic matter in the aquatic environment and related organism community once they are formed (*3*–*5*). However, MnO_2 colloids can also undergo aggregation in aqueous solution, and thus their surface reactivity may be changed (*6*–*8*). Thus, data on the MnO_2 colloidal stability and aggregation kinetics in aquatic environments are critical for understanding the fate and transport of themselves as well as associated contaminants.

Numerous studies have been conducted to examine the aggregation behavior of various nanomaterials, such as silica nanoparticles (NPs), carbon nanotubes, and TiO2 NPs in synthetic and/or natural waters. Numerous publications reported the aggregation behavior of various nanomaterials, such as silica nanoparticles (NPs) and TiO_2 NPs in natural waters (*9*–*11*). According to classical Derjaguin-Landau-Verwey-Overbeek (DLVO) theory, the energy barrier between colloids, strongly dependent upon solution chemistry (e.g., pH, ionic strength, and electrolyte ion valence), affected their aggregation (*11*). However, when macromolecular organic matter (e.g., humic substances (HS), polysaccharides, and proteins) was present, their interactions were much more complicated.

These macromolecules could stabilize colloidal particles due to the combining effects of the electrostatic, steric, and bridging forces induced by their adsorption on particle surfaces. Alginate stabilize NPs (e.g., SWNTs and hematite NPs) in the presence of Na^+ or low concentrations of Ca^{2+} (*10*, *12*), while in the presence of high concentrations of Ca^{2+}, alginate could increase their aggregation rates instead through increasing the measured particle diameters due to the bridging effect of alginate-Ca^{2+} complexes (*10*, *12*). Moreover, as an important biomacromolecule, protein could also stabilize colloids by increasing the steric repulsion between particles. For instance, bovine serum albumin (BSA) could enhance the stability of SWNTs colloids remarkably in the natural aquatic environments (*10*). A similar steric stabilization was also observed for TiO_2 colloids in the presence of fetal serum albumin and human serum albumin (*13*).

Theory

DLVO Interactions

The aggregation kinetics data of MnO_2 NPs in the presence of $NaNO_3$ were compared with DLVO theory. Accordingly, the attachment efficiency (α, obtained from experimental data) of aggregating nanoparticles which accounts for colloidal and hydrodynamic interactions is given by (*14*, *21*):

$$\alpha = \frac{1}{W} = \frac{\int_0^\infty \beta(h) \dfrac{\exp\left(\dfrac{V_A(h)}{k_B T}\right)}{(2a+h)^2} dh}{\int_0^\infty \beta(h) \dfrac{\exp\left(\dfrac{V_T(h)}{k_B T}\right)}{(2a+h)^2} dh} \quad (1)$$

In Advances in the Environmental Biogeochemistry of Manganese Oxides; Sparks, et al.;
ACS Symposium Series; American Chemical Society: Washington, DC, 2015.

where h is the surface-to-surface distance between two particles, a is the intensity-weighted radius of MnO_2 NPs measured by DLS (27.93 nm), k_B is Boltzmann constant, and T is the absolute temperature (298.15 K). The total interaction energy between the two particles ($V_T(h)$) is the sum of the van der Waals attraction ($V_A(h)$) and electrical double layer interaction ($V_{EDL}(h)$). The expression proposed by Gregory was used to calculate $V_A(h)$ (*15*):

$$V_A(h) = V_{VDW} = -\frac{A_{121}a}{12h\left(1+14\frac{h}{\lambda}\right)} \quad (2)$$

$V_{EDL}(h)$ was computed by the linear superposition approximation (LSA) expression (*16*):

$$V_{EDL} = 32\pi\varepsilon_0\varepsilon_r a\left(\frac{k_B T}{ze}\right)^2 \Gamma^2 \exp(-\kappa h) \quad (3)$$

where A_{121} is the Hamaker constant of the particle-water-particle, λ is the characteristic wavelength of the dielectric (assumed to be 100 nm), ε_0 is the vacuum dielectric permittivity, ε_r is the relative dielectric permittivity of solution for water (ε_r=78.5), z is the valence of bulk ions, 1 for sodium ions, e is the electron charge, Γ is the dimensionless surface potential for particles, and κ^{-1} is the Debye length. Γ function is given by:

$$\Gamma = \tanh\left(\frac{ze\psi}{4k_B T}\right) \quad (4)$$

where ψ is the surface potential. The dimensionless function $\beta(h)$ corrects for the hydrodynamic interaction between two approaching particles (*17*):

$$\beta(h) = \frac{6\left(\frac{h}{a}\right)^2 + 13\left(\frac{h}{a}\right) + 2}{6\left(\frac{h}{a}\right)^2 + 4\left(\frac{h}{a}\right)} \quad (5)$$

Ohshima's Soft Particle Theory

Theoretical analysis of Electrophoretic mobility (EPM) data by Ohshima's soft particle theory could define the characteristics of the adsorbed organic layers and further our understanding on the interactions between colloids. Because both biomacromolecules (Alginate and BSA) and MnO_2 colloids carry charges at various aqueous conditions, the EPM data can be interpreted according

In Advances in the Environmental Biogeochemistry of Manganese Oxides; Sparks, et al.;
ACS Symposium Series; American Chemical Society: Washington, DC, 2015.

to Ohshima's soft theory for a charged bare particle with a charged layer. The characteristics of adsorbed organic matter layers (layer thickness, d, soft parameter, λ_f and charged density, ZN) was obtained by fitting EPM data (μ_e) of MnO_2 NPs in the presence of biomacromolecules with Ohshima's soft theory:

$$\mu_e = \frac{\varepsilon_r \varepsilon_0}{\eta} \frac{\frac{\psi_0}{\kappa_m} + \frac{\psi_{DON}}{\lambda_f}}{\frac{1}{\kappa_m} + \frac{1}{\lambda_f}} f\left(\frac{d}{a}\right) + \frac{ZNe}{\eta \lambda_f^{\,2}} + \frac{8\varepsilon_r \varepsilon_0 k_B T}{\eta \lambda_f ze} \tanh \frac{ze\zeta}{4k_B T} \frac{e^{-\lambda_f d}/\lambda_f - e^{-\kappa_m d}/\kappa_m}{1/\lambda_f^{\,2} - 1/\kappa_m^2} \quad (6)$$

where η is the viscosity of water, ζ is the apparent Zeta potential of the bare particles calculated from EPM measurements based on Smoluchowski's formula, Z is the valance of the charged functional groups in the adsorbed layer, N is the number density of the charged groups, $f(d/a)$ is the function, varies according to layer thickness: 1 for a thin adsorbed layer relative to a core particle size and 2/3 for a thick layer, ψ_{DON} is the Donnan potential, κ_m is the effective Debye-Hückel parameter, and calculated as follows (*18*, *19*):

$$\psi_{DON} = \frac{k_B T}{ze} \sinh^{-1}\left(\frac{ZN}{2zn}\right) \quad (7)$$

$$\kappa_m = \kappa \left[\cosh\left(\frac{ze\psi_{DON}}{k_B T}\right)\right]^{1/2} \quad (8)$$

$$f\left(\frac{d}{a}\right) = \frac{2}{3}\left[1 + \frac{1}{2\left(1 + d/a\right)^3}\right] \quad (9)$$

where ψ_0 is the surface potential at the boundary between the charged adsorbed layers and the surrounding solution, and calculated as follows (*20*):

$$\psi_0 = \psi_{DON} - \frac{k_B T}{ze} \tanh \frac{ze\psi_{DON}}{2k_B T} + \frac{4k_B T}{ze} \tanh \frac{ze\zeta}{4k_B T} e^{-\kappa_m d} \quad (10)$$

where n is the concentration of bulk ions, Eq. 10 is valid when $\lambda_f d > 1$ and $\kappa d > 1$.

In Advances in the Environmental Biogeochemistry of Manganese Oxides; Sparks, et al.;
ACS Symposium Series; American Chemical Society: Washington, DC, 2015.

Impacts of Biomacromolecules

Characteristics of Aqueous MnO_2 Colloids

MnO_2 colloids were synthesized by reduction of $KMnO_4$ by $Na_2S_2O_3$ method. $KMnO_4$ solution was rapidly stirred with a magnetic stirrer, and the solution was purged with N_2 at the same time. 30 min late, the stoichiometric amount of $Na_2S_2O_3$ solution was added drop-wise. The brown MnO_2 colloids were formed and continuously stirred over 12 hours. Maximum absorption peaks was obtained at the wavelengths of 215 and 365 nm through the UV-vis spectra (Figure 1) of colloidal suspensions. The MnO_2 colloidal sizes exhibited a narrow distribution with the peak width at half-maximum of 11.12 nm (Figure 2). The diameters of 24-105 nm with an average value of 55.86±0.26 nm (n=30) was observed in the DLS measurements. The diameters obtained by *in situ* DLS measurements were slightly smaller than that of TEM result. of freshly prepared MnO_2 colloids determined by were slightly greater than the one (Figure 3). MnO_2 aggregates showed an irregular structure. The absolute Zeta potential (ζ potential) of these colloids was about -42mV in the presence of 10 mM $NaNO_3$ at pH 6 and 25°C.

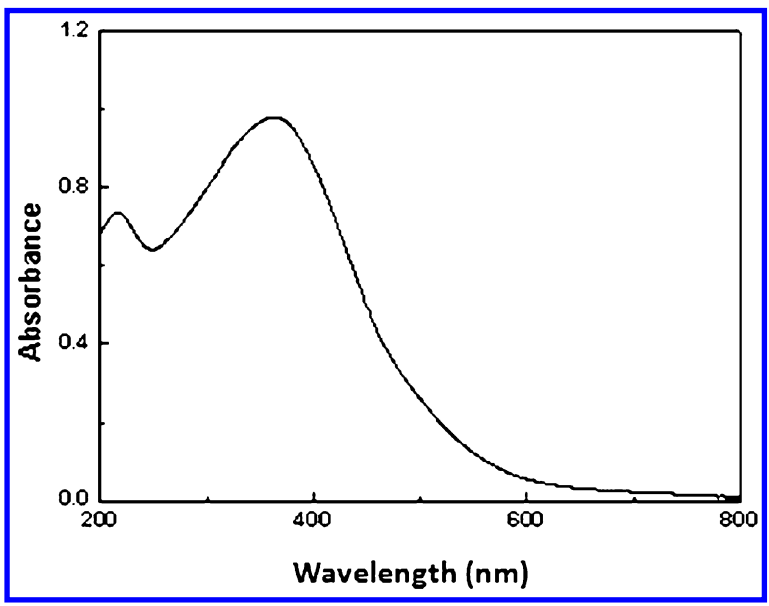

Figure 1. UV-vis spectra of MnO_2 colloids dispersed in Milli-Q water (0.1mM MnO_2, pH 6, and 25°C).

In Advances in the Environmental Biogeochemistry of Manganese Oxides; Sparks, et al.;
ACS Symposium Series; American Chemical Society: Washington, DC, 2015.

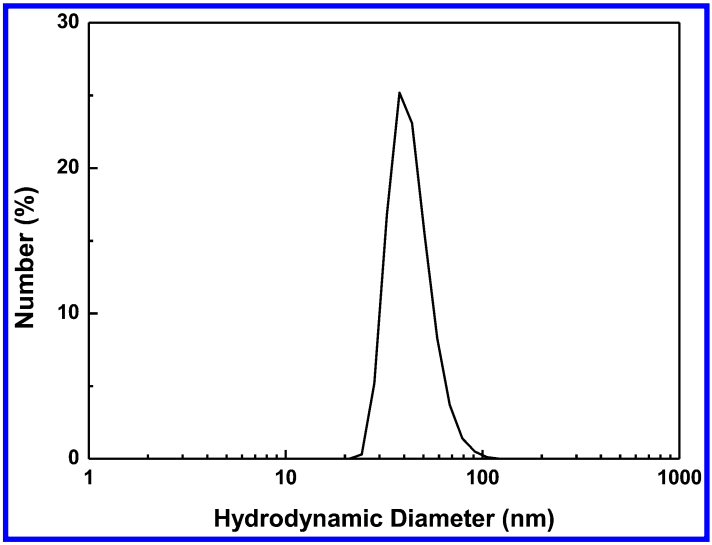

Figure 2. Representative number-weighted hydrodynamic diameter distribution of MnO_2 colloids (0.1mM MnO_2, pH 6, and 25°C).

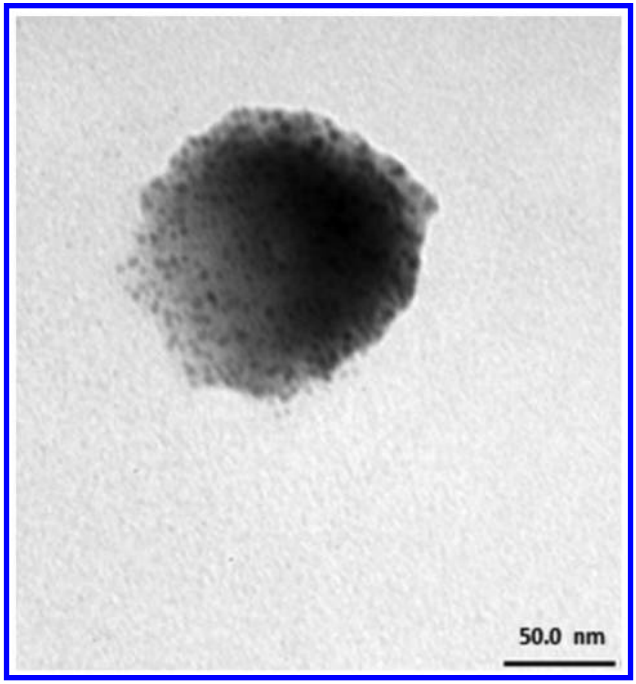

Figure 3. Representative TEM micrograph of MnO_2 aggregates (pH 6 and 25°C).

DLVO-type interactions were observed in the presence of monovalent and divalent cations (Figure 4). As can be seen in Figure 4a, the increase of the electrolyte concentration resulted to a corresponding increase in the aggregation rate at relatively low concentration regime (i.e., < 20 mM), in the presence of $NaNO_3$. However, no change was detected for MnO_2 colloidal aggregation rate at higher concentration regime (30 and 500 mM). The similar observation was also obtained for aggregation behavior of MnO_2 colloids in the presence of $Ca(NO_3)_2$ (Figure 4b).

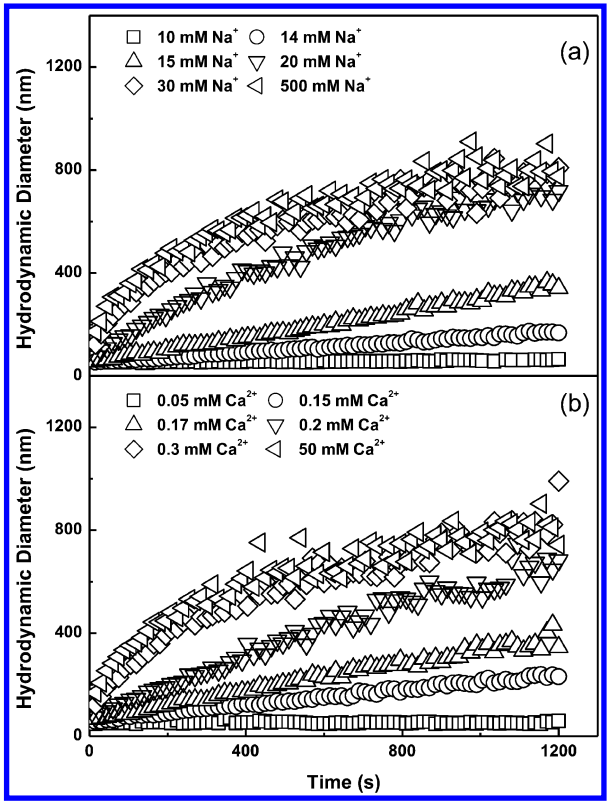

Figure 4. Aggregation profiles of MnO_2 colloids (0.03mM) in various electrolyte solutions: a) $NaNO_3$; b) $Ca(NO_3)_2$ at pH 6 and 25°C (21).

Representative α values as a function of electrolyte concentrations are presented in Figure 5. At low concentration regime of $NaNO_3$, defined as reaction-limited (slow) aggregation regime ($\alpha<1$), any increase of $NaNO_3$ concentration provided more Na^+ to shield the negative surface charge, and led to corresponding increase of α value. When the concentration of $NaNO_3$ was high enough (defined as diffusion-limited (fast) aggregation regime), further increase of $NaNO_3$ concentration had ignorable effect on the attachment efficiency ($\alpha=1$).

The critical coagulation concentration (CCC) for the MnO_2 colloids prepared in this study was ~28 mM for $NaNO_3$ (Figure 5). Two distinct regimes were also observed in the presence of $Ca(NO_3)_2$. As can be seen in Figure 5, the CCC values were about 0.4 mM $Ca(NO_3)_2$, which was much lower than that of $NaNO_3$.

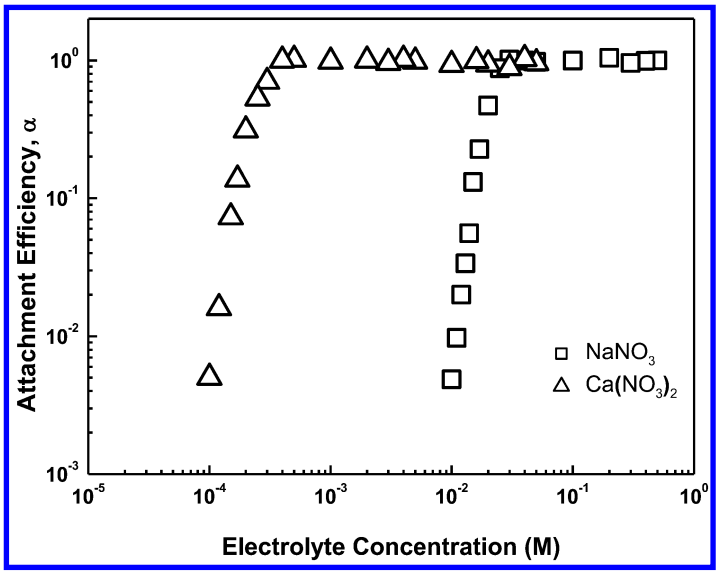

Figure 5. Attachment efficiencies of MnO_2 colloids (0.03mM MnO_2) as a function of $NaNO_3$ and $Ca(NO_3)_2$ concentration at pH 6 and 25°C (21).

The EPM measurements showed that the charges of MnO_2 colloids in the presence of $Ca(NO_3)_2$ were considerably less negative than those in $NaNO_3$ (Figure 6), consistent well with the results of aggregation experiments (Figure 5). According to classical DLVO theory, the different aggregation behaviors of MnO_2 colloids in different electrolyte solution might result from higher charge density in the diffuse layer for divalent ions versus monovalent (at the same molarity), as well as more likely specific surface complexes formation for the divalent cations, divalent electrolyte is more effective in reducing the energy barrier for colloids than monovalent ion.

The calculated Hamaker constant of MnO_2 NPs, 7.84×10^{-20} J, seems reasonable in the range of values reported in literatures for metal oxide NPs (e.g., 5.57×10^{-20} J for cerium dioxide (CeO_2) NPs (*22*) and 26×10^{-20} J for rutile (TiO_2) NPs (*23*)). Since, DLVO theory always assumes a uniform distribution of the surface charge on NPs, the remarkable agreement between fitted classical DLVO curve and experimental data (R^2=0.9998) also suggests that the charge is homogeneously distributed on the surface of the MnO_2 colloids (Figure 7) (*10*).

In Advances in the Environmental Biogeochemistry of Manganese Oxides; Sparks, et al.;
ACS Symposium Series; American Chemical Society: Washington, DC, 2015.

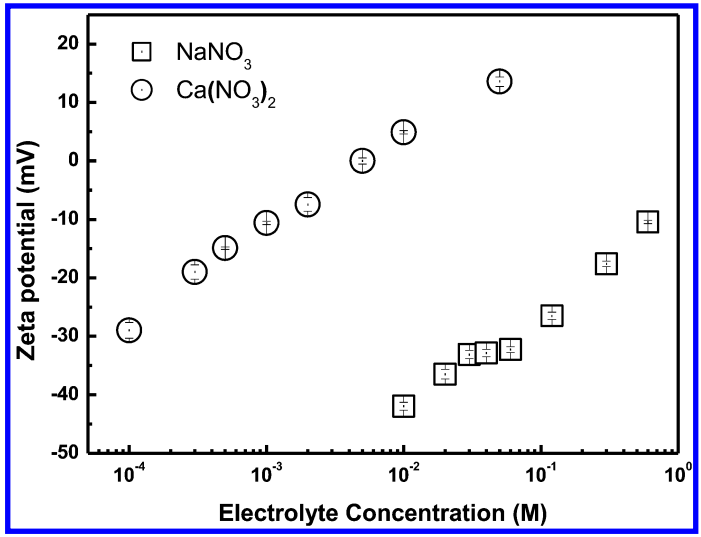

Figure 6. Zeta potential of MnO_2 (0.1mM MnO_2) colloids as a function of $NaNO_3$ and $Ca(NO_3)_2$ concentration at pH 6 and 25°C (21).

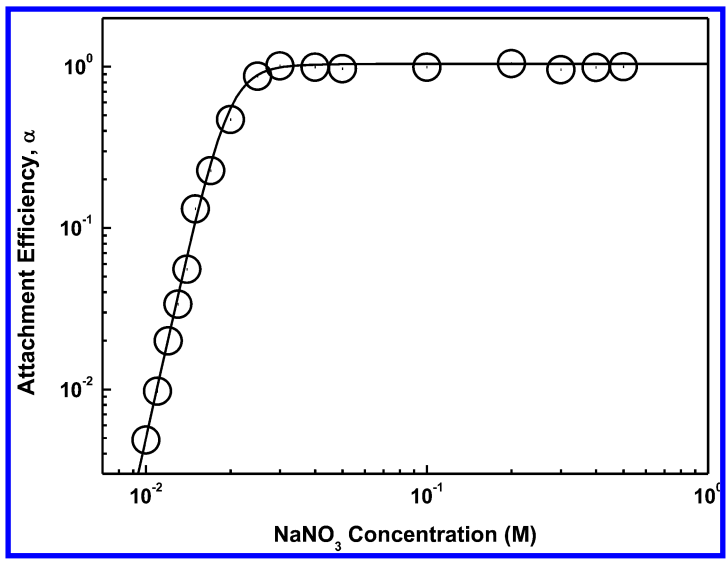

Figure 7. Theoretical classical DLVO prediction and experimentally derived attachment efficiencies of MnO_2 NPs as a function of $NaNO_3$ concentration (0.03mM MnO_2, pH 6, and 25°C) (21).

The values of MnO_2 colloidal attachment efficiency in the presence of $NaNO_3$ and alginate were lower (Figure 8). Similarly, as can be seen in Figure 8, alginate hindered MnO_2 colloidal aggregation at low $Ca(NO_3)_2$ concentration. Steric repulsive force resulting from the adsorption of alginate on the particles should be responsible for the increase of engineered NPs stability (*10*).

The Zeta potential of MnO_2 colloids in the presence of 2mg/L alginate was also determined (Figure 9) and data might confirm steric stabilizing mechanism (*10*). The theoretically calculated thicknesses of adsorbed layer according to Ohshima's Soft Particle Theory was ~24.3 nm (Table 1). The calculated EPMs accorded with the experimental data very well (Figure 10). The adsorbed layer on MnO_2 NP surface may also reveal the steric repulsion between particles (*10*).

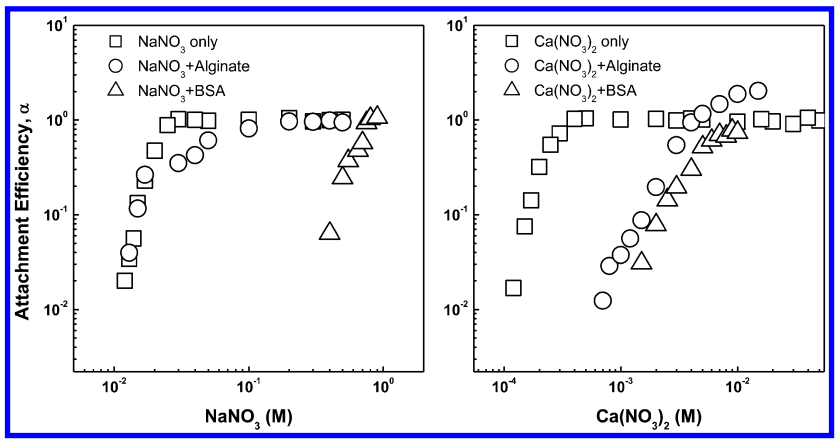

Figure 8. Aggregation attachment efficiencies of MnO_2 colloids as a function of electrolyte concentration in the presence of alginate or BSA (0.03mM MnO_2, 2mg/L alginate or BSA, pH 6, and 25°C) (21).

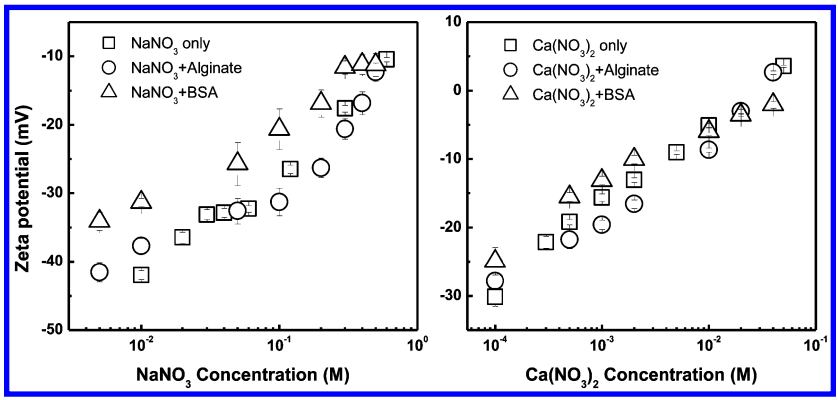

Figure 9. Zeta potential of MnO_2 colloids as a function of electrolyte concentration in the presence of alginate and BSA (0.1mM MnO_2, 2mg/L alginate or BSA, pH 6, and 25°C) (21).

In Advances in the Environmental Biogeochemistry of Manganese Oxides; Sparks, et al.;
ACS Symposium Series; American Chemical Society: Washington, DC, 2015.

Table 1. Adsorbed layer thickness (d) estimated by fitting EPM data with the Ohshima's soft particle theory (experimental conditions: 0.1mM MnO_2, 2mg/L alginate or BSA, pH 6, and 25°C).

Biomacromolecules	*d (nm)*	R^2
Alginate	24.3	0.91
BSA	38.9	0.98

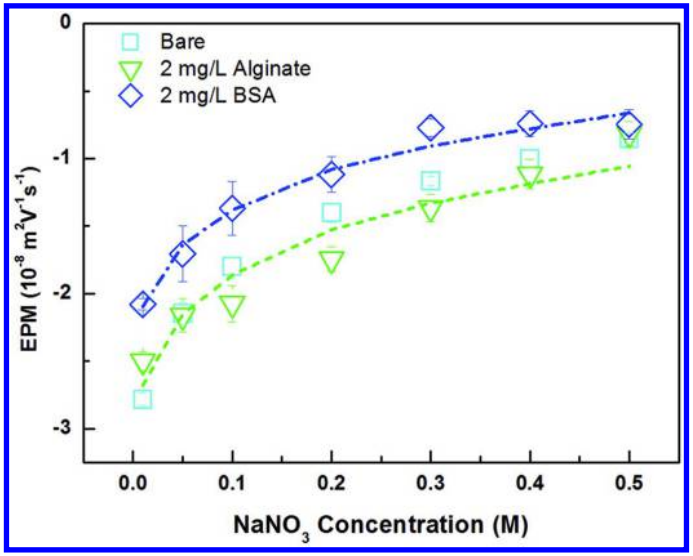

Figure 10. The best-fit theoretical EPM data of MnO_2 NPs in the presence $NaNO_3$ with the Ohshima's soft particle theory (connected by dashed lines) (experimental conditions: 0.1mM MnO2, 2mg/L alginate or BSA, pH 6, and 25°C) (21).

However, in the case of high Ca^{2+}, the enhancement of MnO_2 colloidal aggregation in the presence of alginate was observed (Figure 11). The aggregation rate was constant at concentration of 5 mM and 10 mM $Ca(NO_3)_2$ without alginte. The aggregation rate was increasing with 2mg/L alginate. Over a wide region of Ca^{2+} concentration, MnO_2 colloidal Zeta potential values did not change obviously in the presence of alginate (Figure 9), demonstrating that the enhancement of the aggregation kinetics did not attribute to the decrease of electrostatic repulsive energy. Therefore, aggregation behavior of MnO_2 colloids might be consistent with the bridging mechanism.

The measured particle diameter was enlarged due to alginate polymers bridging on the surface of alginate coated NPs via calcium complexation (*10*). TEM measurement in Figure 12 confirmed this bridging mechanism for MnO_2 colloids.

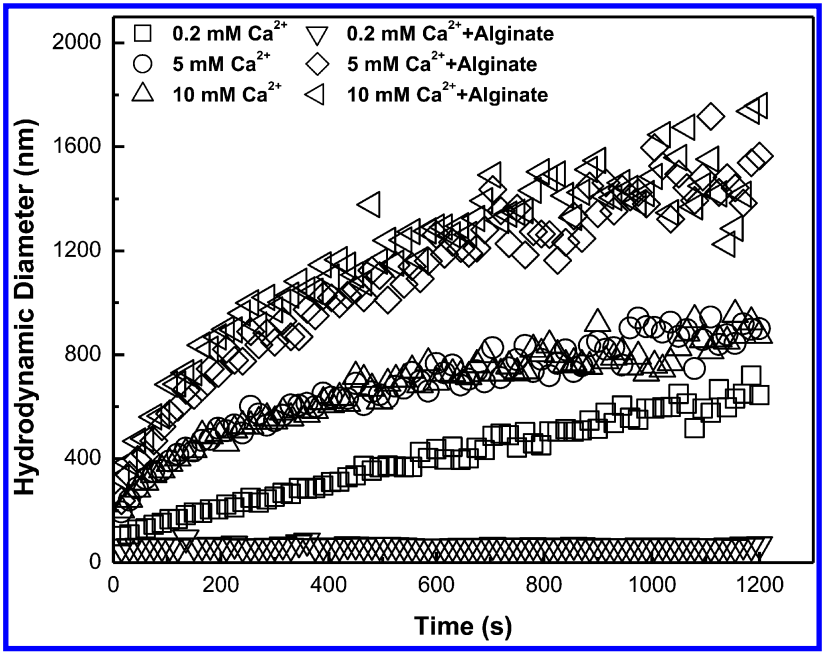

Figure 11. Aggregation profiles of MnO_2 colloids (0.03mM MnO_2) in various concentrations of $Ca(NO_3)_2$ solutions in the absence and presence of 2 mg/L alginate at pH 6 and 25°C (21).

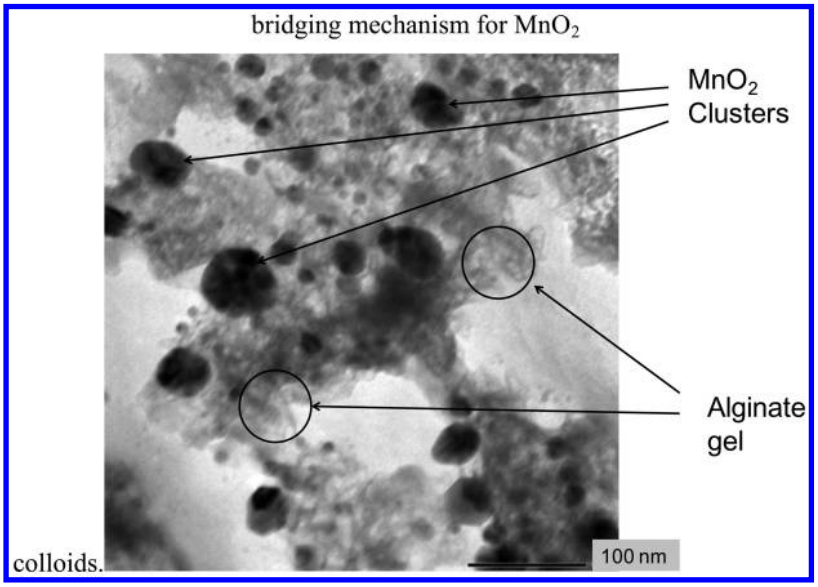

Figure 12. Representative TEM image for MnO_2 colloids (0.03mM MnO_2) in the presence of 2 mg/L alginate and 10 mM $Ca(NO_3)_2$ at pH 6 and 25°C (21).

As can be seen in Figure 8, a significantly enhanced stability of MnO_2 colloids was observed in the presence of BSA, much more strong than alginate. Zeta potential values showed in Figure 9 indicated that the surface charges of MnO_2 particles in the presence of BSA did not change apparently. Moreover, the electrostatic repulsive forces between BSA (with isoelectric point of 4.8) and MnO_2 particles were reduced compared to that between alginate (with isoelectric point of ~4.0) and MnO_2 NPs, and thus BSA could be adsorbed readily on the particles. Therefore, the steric repulsive forces resulting from the adsorption of BSA on the particles may play a primary role in retarding MnO_2 colloidal aggregation rate. Additionally, the globular architecture of BSA molecules also induced longer-steric repulsive forces compared with alginate (*10*). The adsorbed layer thickness of BSA on the surface of MnO_2 NPs was greater than that of alginate (Table 1).

Conclusions

The stability of MnO_2 colloids under the influence of two model biomacromolecules (i.e., alginate and BSA) was obtained. Generally, higher stability of MnO_2 colloids was observed. BSA stabilized MnO_2 colloids much efficient than alginate. Nevertheless, in the presence of alginate and high concentration of $Ca(NO_3)_2$, a polymer via calcium and alginate may enlarge the measured hydrodynamic diameter of MnO_2 colloids.

References

1. Ferreira, J. R.; Lawlor, A. J.; Bates, J. M.; Clarke, K. J.; Tipping, E. *Colloids Surf., A* **1997**, *120*, 183–198.
2. Lienemann, C. P.; Taillefert, M.; Perret, D.; Gaillard, J. F. *Geochim. Cosmochim. Acta* **1997**, *61*, 1437–1446.
3. Herszage, J.; dos Santos Afonso, M.; Luther, G. W. *Environ. Sci. Technol.* **2003**, *37*, 3332–3338.
4. Villalobos, M.; Bargar, J.; Sposito, G. *Environ. Sci. Technol.* **2005**, *39*, 569–576.
5. Yang, K.; Lin, D. H.; Xing, B. S. *Langmuir* **2009**, *25*, 3571–3576.
6. Wang, C. Y.; Groenzin, H.; Shultz, M. J. *J. Am. Chem. Soc.* **2005**, *127*, 9736–9744.
7. Zhang, H. Z.; Penn, R. L.; Hamers, R. J.; Banfield, J. F. *J. Phys. Chem. B* **1999**, *103*, 4656–4662.
8. Tseng, Y. H.; Lin, H. Y.; Kuo, C. S.; Li, Y. Y.; Huang, C. P. *React. Kinet. Catal. Lett.* **2006**, *89*, 63–69.
9. Abe, T.; Kobayashi, S.; Kobayashi, M. *Colloids Surf., A* **2011**, *379*, 21–26.
10. Saleh, N. B.; Pfefferle, L. D.; Elimelech, M. *Environ. Sci. Technol.* **2010**, *44*, 2412–2418.
11. French, R. A.; Jacobson, A. R.; Kim, B.; Isley, S. L.; Penn, R. L.; Baveye, P. C. *Environ. Sci. Technol.* **2009**, *43*, 1354–1359.
12. Chen, K. L.; Mylon, S. E.; Elimelech, M. *Langmuir* **2007**, *23*, 5920–5928.

13. Allouni, Z. E.; Cimpan, M. R.; Hol, P. J.; Skodvin, T.; Gjerdet, N. R. *Colloids Surf., B* **2009**, *68*, 83–87.
14. McGown, D. N. L.; Parfitt, G. D. *J. Phys Chem* **1967**, *71*, 449–450.
15. Gregory, J. J. *J. Colloid Interface Sci.* **1981**, *83*, 138–145.
16. Gregory, J. J. *J. Colloid Interface Sci.* **1975**, *51*, 44–51.
17. Honig, E. P.; Roeberse, G.; Wiersema, P. H. J. *J. Colloid Interface Sci.* **1971**, *36*, 97–109.
18. Phenrat, T.; Kim, H. J.; Fagerlund, F.; Illangasekare, T.; Tilton, R. D.; Lowry, G. V. *Environ. Sci. Technol.* **2009**, *43*, 5079–5085.
19. Phenrat, T.; Saleh, N.; Sirk, K.; Kim, H. J.; Tilton, R. D.; Lowry, G. V. *J. Nanopart. Res.* **2008**, *10*, 795–814.
20. Ohshima, H. *Adv. Colloid Interface Sci.* **1995**, *62*, 189–235.
21. Huangfu, X.; Jiang, J.; Ma, J.; Liu, Y.; Yang, J. *Environ. Sci. Technol.* **2013**, *47*, 10285–10292.
22. Karimian, H.; Babaluo, A. A. *J. Eur. Ceram. Soc.* **2007**, *27*, 19–25.
23. Wang, Y. M.; Forssberg, E.; Pugh, R. J. *Int. J. Miner. Process.* **1992**, *36*, 93–105.

Subject Index

In Advances in the Environmental Biogeochemistry of Manganese Oxides; Sparks, et al.; ACS Symposium Series; American Chemical Society: Washington, DC, 2015.

N

P

In Advances in the Environmental Biogeochemistry of Manganese Oxides; Sparks, et al.; ACS Symposium Series; American Chemical Society: Washington, DC, 2015.

S

In Advances in the Environmental Biogeochemistry of Manganese Oxides; Sparks, et al.; ACS Symposium Series; American Chemical Society: Washington, DC, 2015.

W

In Advances in the Environmental Biogeochemistry of Manganese Oxides; Sparks, et al.;
ACS Symposium Series; American Chemical Society: Washington, DC, 2015.